Klaus Halbach, "Matrix Representation of Gaussian Optics," American Journal of Physics, vol. 32, no. 2, pp. 90-108 (February 1964).

LBL-PUB-754

VOLUME 1

The Art and Science of Magnet Design

A Festschrift in Honor of Klaus Halbach

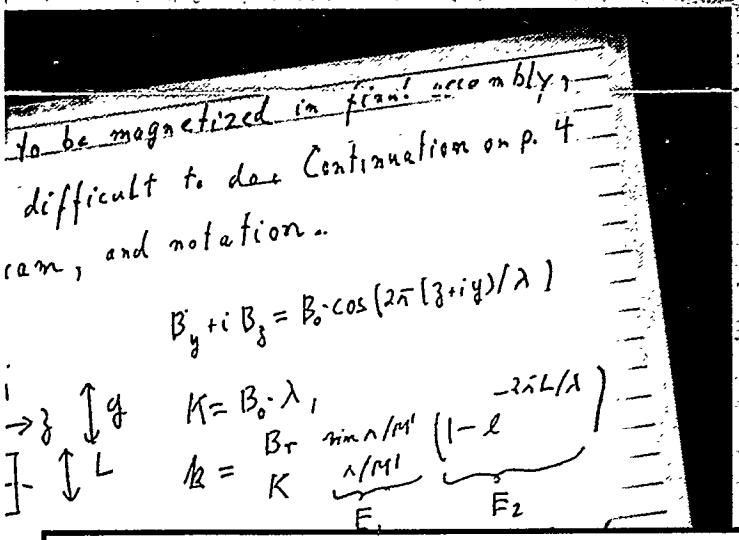

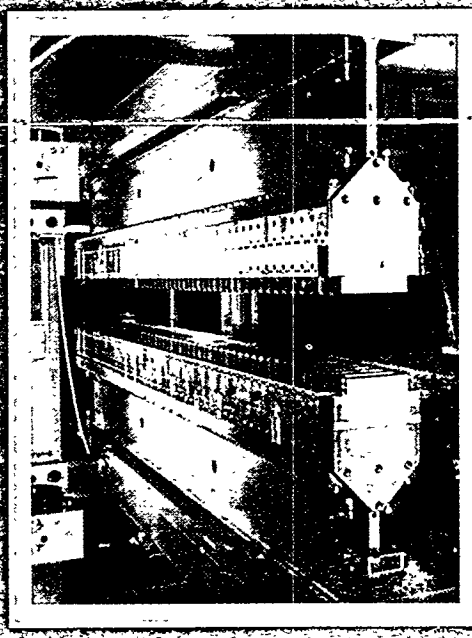

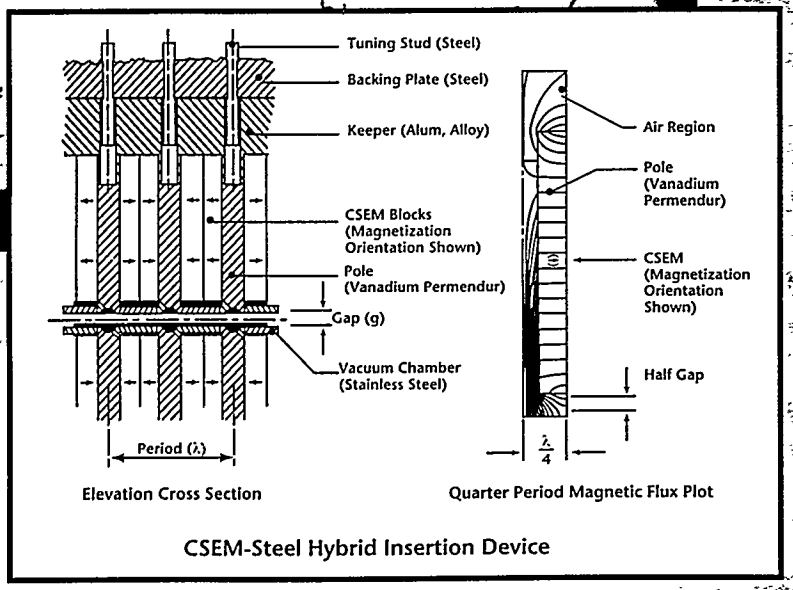

CSEM-Steel Hybrid Insertion Device

February 1995
Lawrence Berkeley Laboratory
University of California
Berkeley, CA 94720

Klaus Halbach, "Berechnung linearer, realisierbarer Netzwerke zur Erzielung optimaler Signal/Rauschverhältnisse," Helvetica Physica Acta, vol. 26, no. 1, pp. 65-74 (January 1953). ◦ Klaus Halbach, "Modulation-Effect Corrections for Moments of Magnetic Resonance Line Shapes," Physical Review, vol. 119, no. 4 (August 1960). ◦ Klaus Halbach and William R. Baker, "Plasma Gun Aspects of an E x B System," The Physics of Fluids Supplement (1964).

This is the first of two volumes published in conjunction with the Halbach Symposium on Magnet Technology held at Lawrence Berkeley Laboratory on February 3, 1995, in honor of Klaus Halbach's 70th birthday.
Volume 2 (LBL PUB 755) contains a compilation of fifth-seven notes written by Dr. Halbach selected from his collection of over 1650 such documents.

VOLUME 1

The Art and Science of Magnet Design

A Festschrift in Honor of Klaus Halbach

February 1995
Lawrence Berkeley Laboratory
University of California
Berkeley, CA 94720

Prepared for the U.S. Department of Energy under Contract DE-AC03-76SF00098

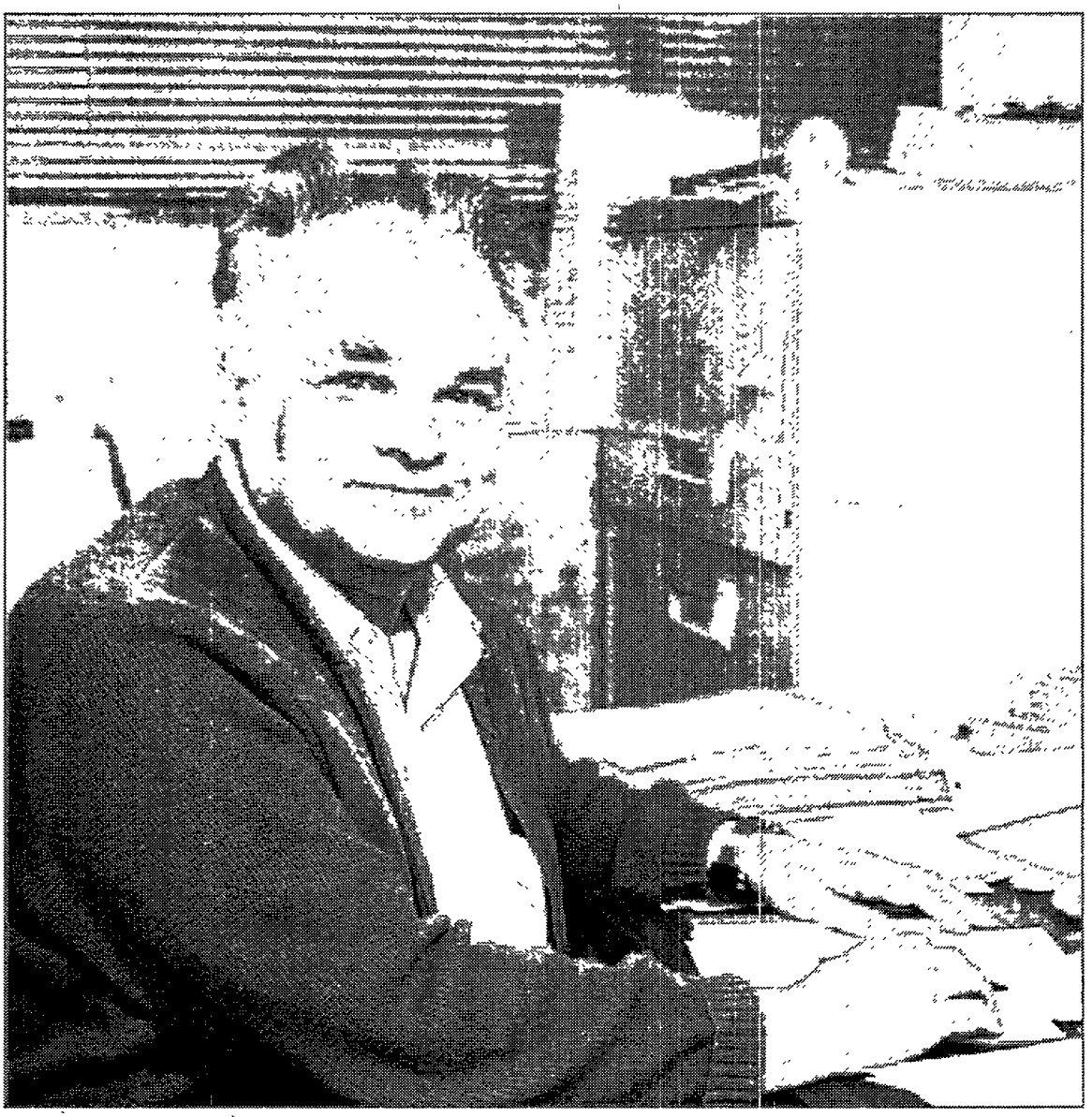

Klaus Halbach

Preface

To honor Klaus Halbach on his 70th birthday, his colleagues and students have assembled this Festschrift, a collection of technical papers and personal remembrances written expressly for the Halbach Symposium and dedicated to him. The topics presented offer but a hint of the diversity of Klaus' scientific career, so we have included this biographical sketch and gallery of photographs to provide the proper perspective. Klaus worked in nuclear physics, nuclear magnetic resonance, plasma physics, and magnet physics, and showed us, by his late contributions to magnet design, that one's physics career need not be over by age 30.

It all started on February 3, 1925, in the town of Wuppertal in the German state of Rhineland-Westphalia. This innovative town was the first to develop a social retirement system (1830's -- later adopted by Bismarck for all of Germany), and was the site of the first elevated commuter monorail system (1900) which Klaus used to ride to and from school. He was actually not a star student in the Gymnasium, but was motivated to study mathematics on his own. By age 15, Klaus had decided to become an applied physicist despite having never met such a person!

Klaus' family owned a business that made silk ribbons for use in clothing. After he joined the Luftwaffe in 1943, Wuppertal was heavily damaged by Allied bombing and the resulting firestorm. Fortunately his family survived, and they moved their business to the small village of Grenzach in Baden, on the German side of the border near Basel, Switzerland. Klaus met the daughter of the town doctor while he was there on military leave, and he and Ruth were married in March of 1945. Klaus was trained as a fighter pilot but he never saw combat. He was captured by American forces near Munich in 1945 and sent to a POW camp. After the war ended, he returned to his wife in Grenzach.

At this point Klaus had the good fortune to be admitted to the University of Basel. In addition to the academic benefits, it allowed him to obtain essential food for his newborn daughter Terry when there was very little in Germany. He studied in Basel for 8 years, which included both instruction and hiking in the mountains with his professors. The relationships were personal and formal at the same time; one always addressed the professor as "Herr Professor," even while hiking. The only significant requirement for a PhD was one full length publication in a prestigious journal. Unfortunately, when Klaus had

done the research for a paper in nuclear physics, an American published the result first, so Klaus had to start on a new thesis. He switched to nuclear magnetic resonance, built a complete NMR apparatus, including magnets, power supplies, RF system and detector, and published his (mostly theoretical) work in 1954. Felix Bloch, who shared with Edward Purcell the 1952 Nobel for the development of NMR, was then the director of CERN and Klaus had a chance to present his work to him in Geneva. When Bloch later returned to Stanford, he offered Klaus a position as a research associate there. In the meantime, Klaus became a Privatdozent at the University of Fribourg, Switzerland, where he continued to work on NMR.

He came to Stanford in 1957 and worked as a theorist under Felix Bloch. They would meet several hours per week and assist each other with their respective problems. Klaus recalls that Bloch was uncommonly generous, as on the infrequent occasions when Klaus had a better approach to a problem and Bloch would acknowledge that fact with praise. In 1959 Bloch switched his interest to superconductivity, and Klaus decided to switch into magnetic fusion. Bloch arranged for him to work for six months in the fusion group at LBL. After this, Klaus returned briefly to Fribourg and started a fusion group there. But in October 1960, thanks to help from Bill Baker and Wolf Kunkel, he returned to LBL where he has been ever since.

At LBL Klaus was placed in charge of a homopolar plasma generator project, with a budget of the order of a million (1994) dollars per year. It was at this time he first worked with Ron Holsinger, a mechanical engineer and programmer who was later to become Klaus' son-in-law. He and Klaus developed the computer optimization program PISA, and later POISSON, MIRT, and SUPERFISH, which are among Klaus' most lasting achievements. Though he is associated with these numerical methods, Klaus still insists that real understanding comes from analytical physics methods.

While Klaus was still working on the homopolar generator, Albert Ghiorso and the late Bob Main brought him to the HILAC project in 1965 to work on the Omnitron proposal. This completed his migration from nuclear physics, NMR, and plasma physics, to accelerator physics—his fourth career. In 1969, he wrote one of his most influential papers, "Perturbation Effects in Iron Dominated Multipoles" [Nucl. Inst. & Methods 74, p. 147 (1969)] in which he calculated tables of perturbation effect coefficients that are used to this day in the design of accelerator magnets. This paper contains the key to much of the work that he did afterwards, namely deriving a mathematically

complicated conformal transformation by looking at the underlying physics appropriately. In this particular case, it was the conformal transformation that maps the interior of an ideal two dimensional quadrupole onto a circular disk.

In the late 1970s, Klaus was given a special account by LBL director Andy Sessler to free him to write papers on his past work. In 1979 Klaus had the celebrated inspiration of the iron free permanent magnet undulator, described by Herman Winick elsewhere in this volume. He also continued to consult for various research groups, but this was not a satisfactory time to Klaus who had always preferred to work with a team. So it was with great pleasure that he was tapped by the next LBL director Dave Shirley for a role in the development of synchrotron radiation instrumentation, and later in the Advanced Light Source. Parallel to his work on accelerator (and other) magnets, Klaus also worked on beam position monitors and some optical problems. The first paper on the latter topic was a 1964 paper on Gaussian optics in light systems, a paper that has been used at many universities as the textbook on that topic.

The first iron free permanent magnet undulator was built for SSRL and tested on Beamline 7 in December 1980. Klaus was appointed a consulting professor at SSRL in 1983, where he assisted with the design of a 5 GeV light source whose eventual realization was the APS at Argonne. In 1987 he received the U.S. Accelerator School Prize for Achievement for Accelerator Physics and Technology, and in 1990 he was elected a Fellow of the American Physical Society.

The rest is history. Klaus became the leading light in the development of pure permanent magnet and hybrid wigglers, undulators, free electron lasers, as well as the electromagnets for storage ring x-ray sources. He developed the permanent magnet versions of quadrupole and higher order multipole magnets, and consulted on many storage ring and insertion device projects all around the world. Though he accepted early retirement from LBL in 1991, he continues to work in magnet design and accelerator design internationally, and has taught an entire generation of scientists and engineers the essential art and science of magnet design.

The Halbach Festschrift Editorial Board
Roger Carr
Brian Kincaid
Ross Schlueter

A peek into the past. . .

Klaus and Ruth in Grenzach (Ruth's home town) in about 1950.

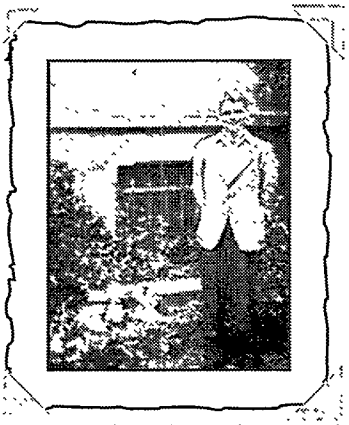

At age 12 (1937) in Wuppertal, Germany by the house where he grew up.

At Stanford Village in 1957 with Ruth and their neighbor, Guy Poorman.

While a graduate student in physics at the University of Basel (1952).

Talking with Forrest Boley, a physicist in the magnetic fusion group, at LBL in 1961.

With his son-in-law Ron Holsinger in the early 1960s.

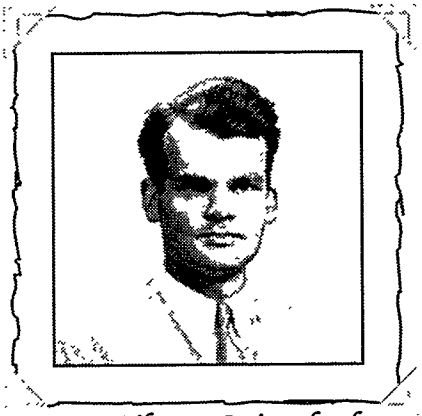

In Fribourg, Switzerland at age 30 (1955).

With his sisters Gerda (left) and Ilse, and brother Wolfgang in 1977.

Ruth and Klause in Berkeley in 1967.

With his daughter Terry in about 1965.

With Herman Winick and the first undulator designed and built based on Halbach's idea of using permanent magnets in insertion devices. The undulator was installed in the SPEAR storage ring at Stanford in 1980.

Some of Klaus' Projects. . .

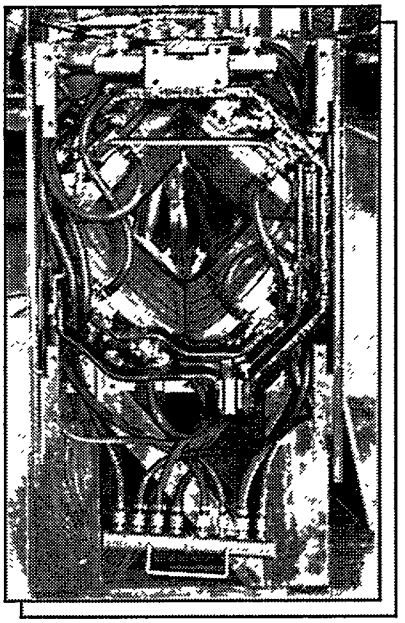

1975 - This PEP I quadrupole was built under the guidance of Klaus and his perturbation theory was used to determine the mechanical tolerances necessary to achieve the high field quality required for this design.

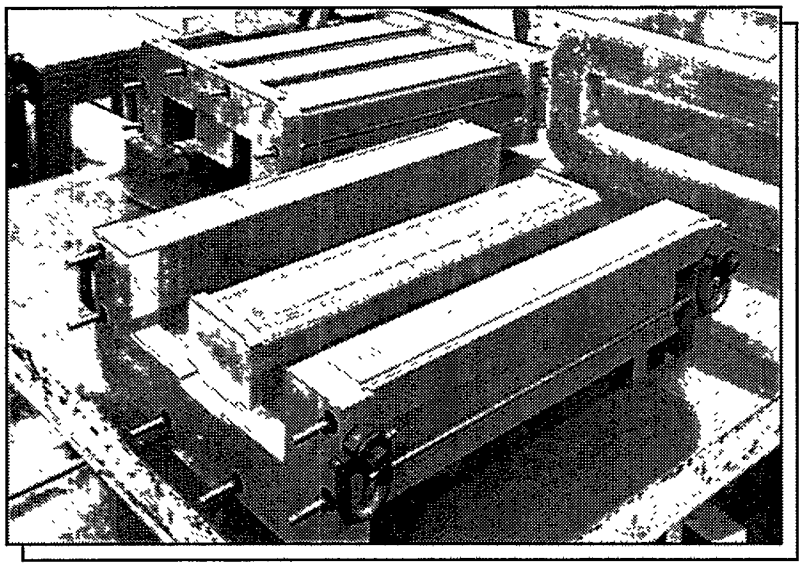

1967 - This Omnitron gradient magnet was one of the first magnets designed using the MIRT code (one of the codes in the POISSON family).

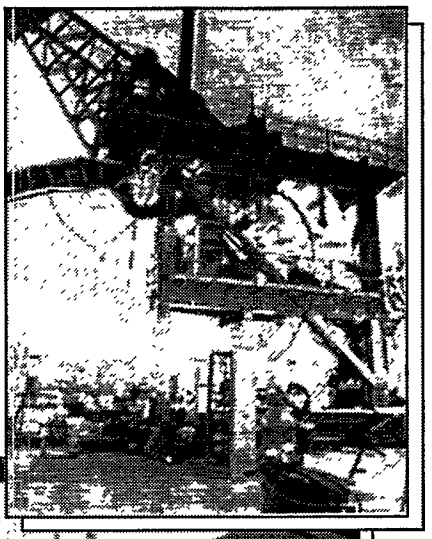

1972 - Work underway on the High Resolution Spectrometer at Los Alamos National Laboratory. Klaus conceived of the idea of putting correction windings in slots in the backside of the poles to produce very uniform fields in wide aperture magnets. (Inset) At project completion in 1977.

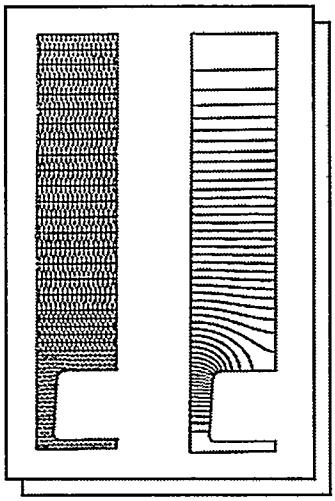

1976 - A SUPERFISH drift tube linac problem. Klaus was instrumental in developing the SUPERFISH code, a computer program for evaluation of rf cavities with cylindrical symmetry.

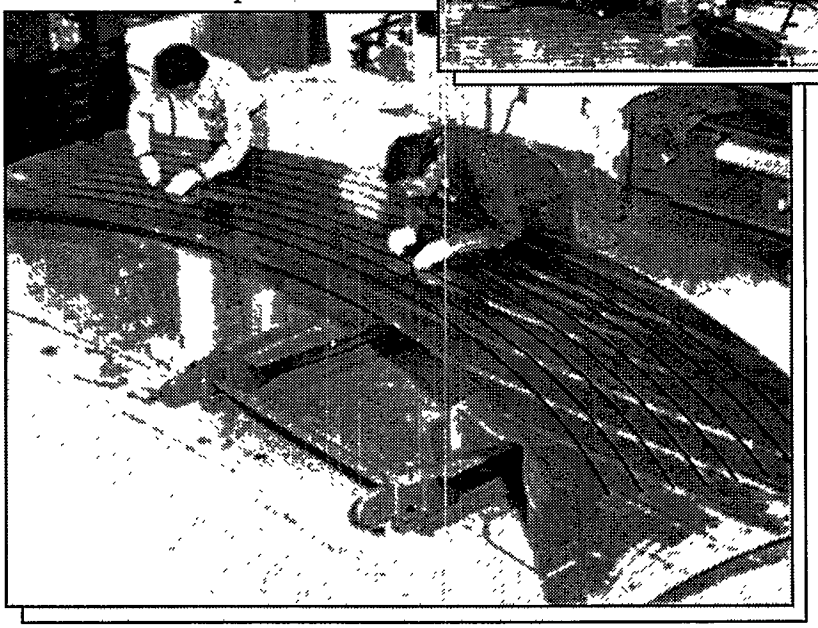

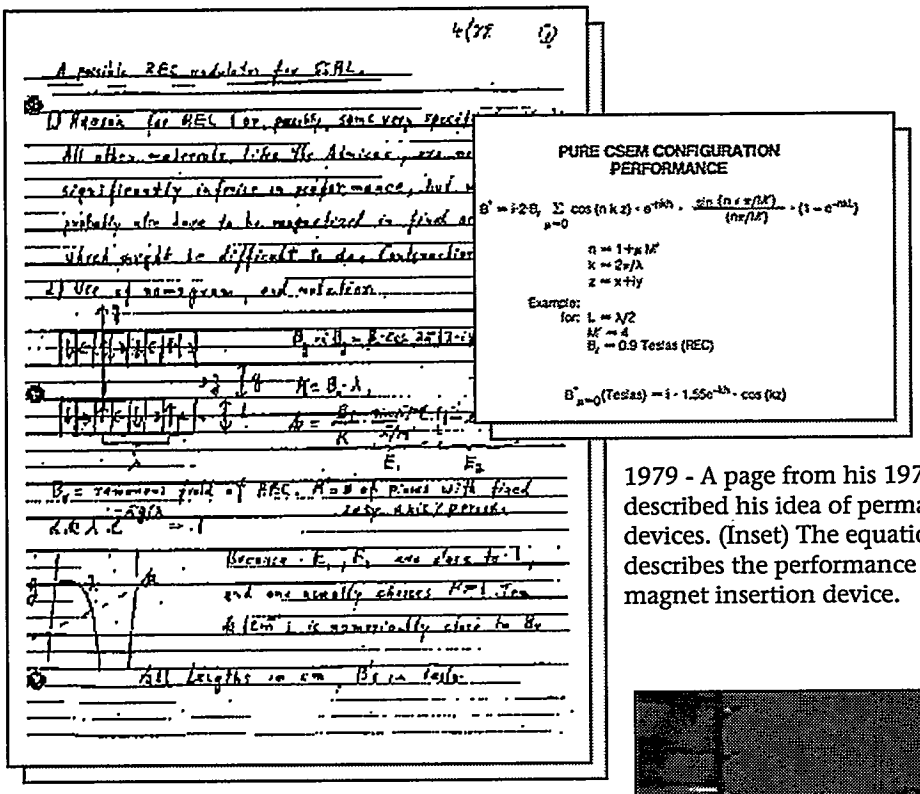

PURE CSEM CONFIGURATION
PERFORMANCE

$$B^{*}_{\mu=0} = 2B_r \sum_{\mu=0} \cos(n\,k\,z) \cdot e^{-nkh} \cdot \frac{\sin(n\,\pi/M)}{(n\pi/M)} \cdot (1 - e^{-nkL})$$

$n = 1 + \mu M$
$k = 2\pi/\lambda$
$z = x + iy$

Example:
for: $L = \lambda/2$
$M = 4$
$B_r = 0.9$ Teslas (REC)

$$B^{*}_{\mu=0}(\text{Teslas}) = i \cdot 1.55 e^{-kh} \cdot \cos(kz)$$

1979 - A page from his 1979 logbook on which he described his idea of permanent magnet insertion devices. (Inset) The equation derived by Klaus that describes the performance of a pure permanent magnet insertion device.

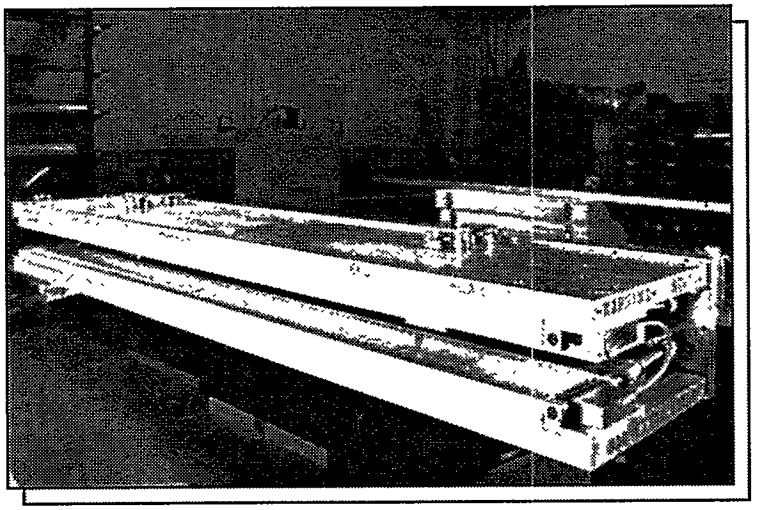

1980 - The first undulator based on Klaus' idea to use permanent magnets was installed in the SPEAR storage ring at Stanford in late 1980, the result of a joint effort of LBL and SSRL. The undulator is still in operation at the Synchrotron Radiation Center in Wisconsin.

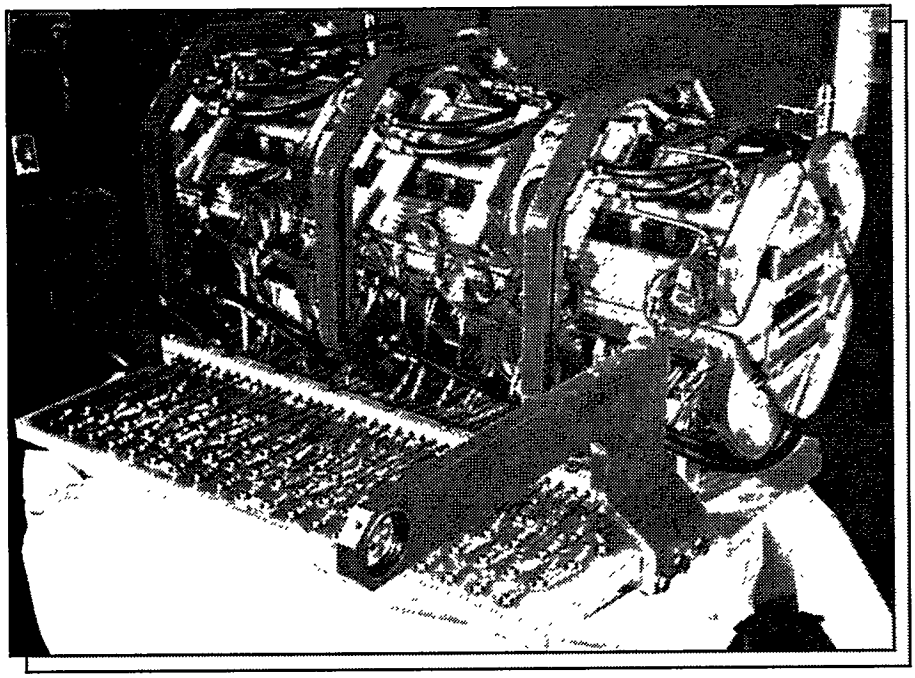

1983 - The concept for this electromagnetic wiggler was developed by Klaus for the Electron Laser Facility (ELF) at Livermore. An early experimental free-electron laser, ELF confirmed the "exponential gain regime," where the signal grows at a rate that increases as the signal increases.

1983 - The 54-pole hybrid wiggler LBL constructed for SSRL was featured on the cover of Physics Today. Another Halbach innovation, the hybrid uses samarium-cobalt to produce the magnetic flux in the steel pole pieces—achieving simultaneously a high magnetic field with a short period.

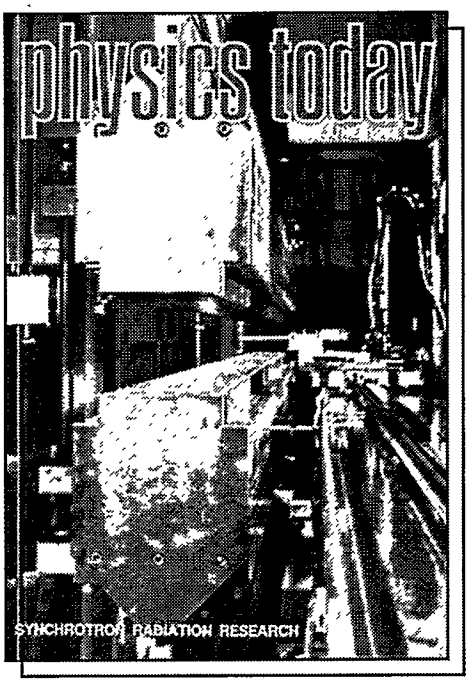

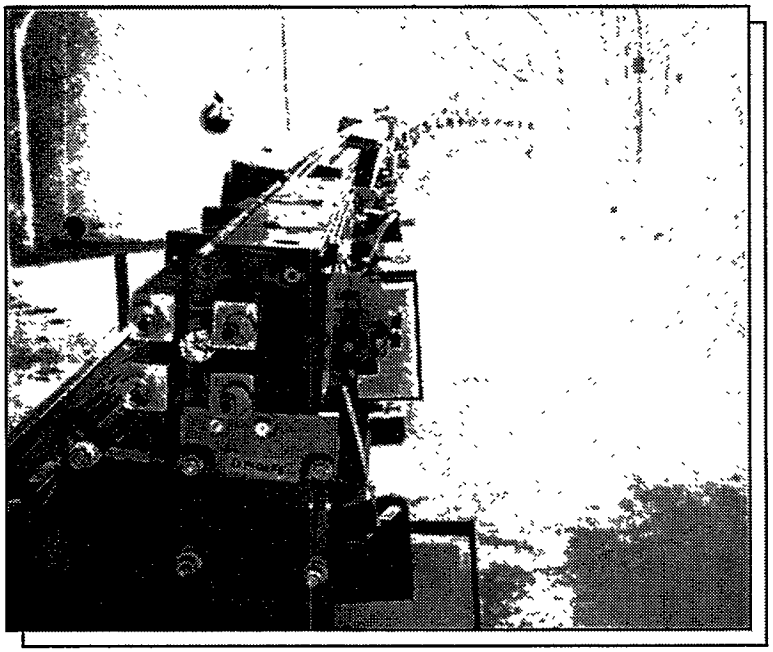

1985 - Arc magnets designed by Klaus' group at LBL installed in the Stanford Linear Collider (SLC).

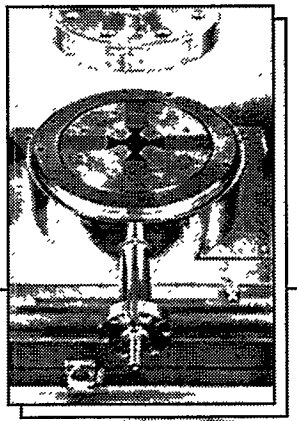

1984 - Klaus came up with the concept for the first adjustable hybrid drift type magnet which provides the adjustability needed to focus different beams in heavy ion linacs. The one shown here was built as a "proof of principle" device for use in a linac for ion radiotherapy treatment. (Inset) A later version from 1987.

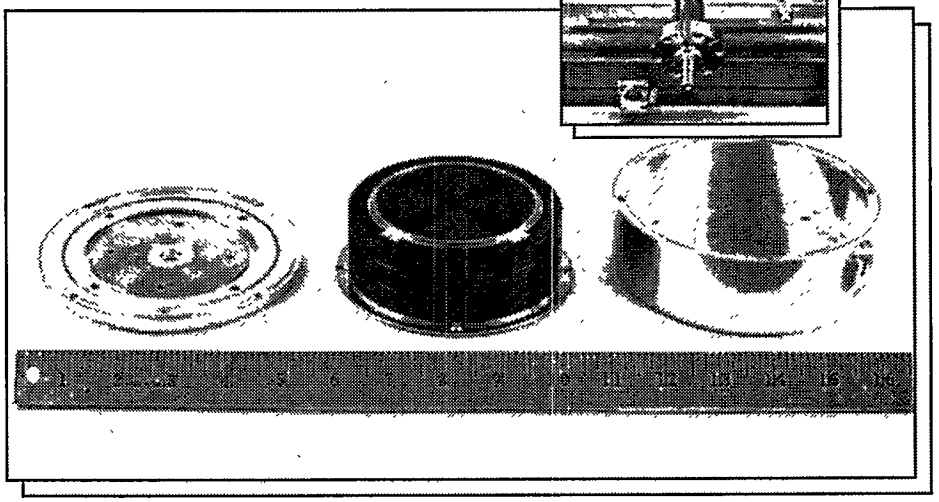

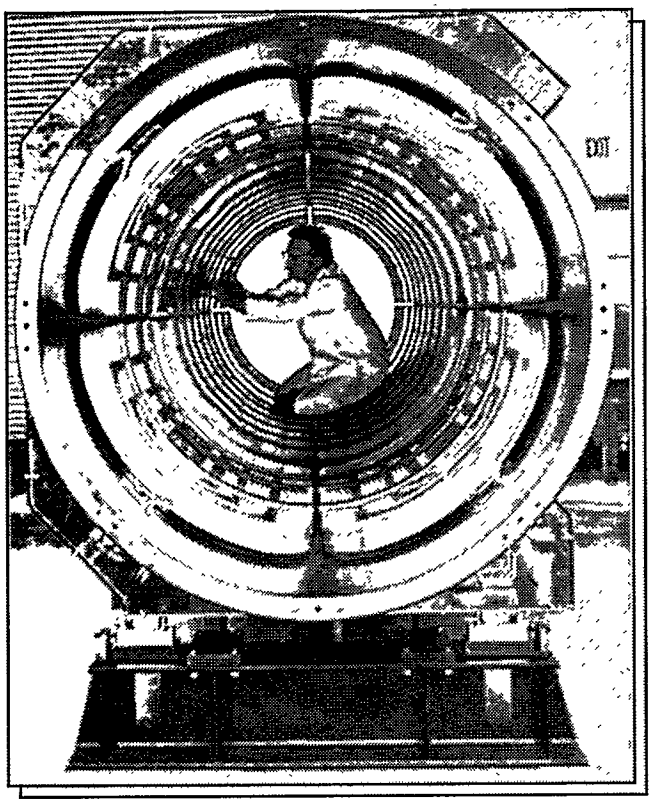

1987 - A large bore quadrupole built at Los Alamos. A coil dominated magnet inside a cylindrical iron yoke, it was part of a star wars project to focus large beams of electrons into outer space.

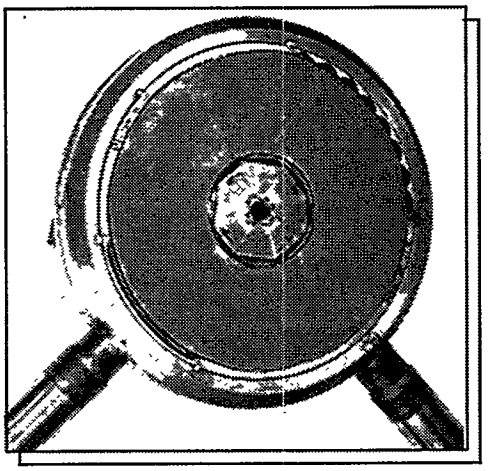

1988 - Another Halbach concept was the laced quadrupole, which uses permanent magnet material to reduce saturation in the poles thus allowing electromagnetic excitation to result in higher gradient operation.

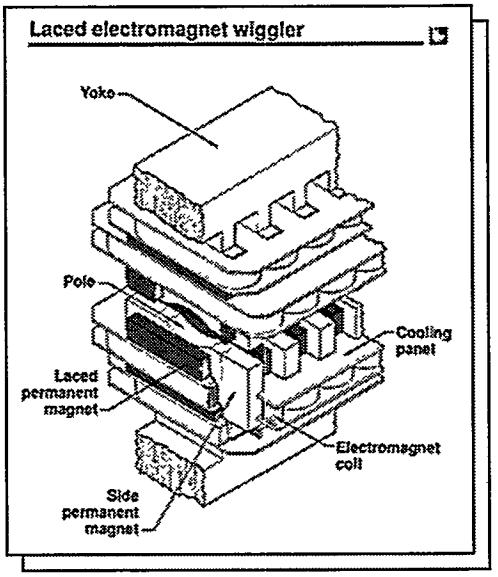

1989 - His laced permanent magnet concept was used in the design of the laced electromagnet wiggler built at Lawrence Livermore. This type of wiggler had applications in star wars and in electron cyclotron heating in tokamaks (a confinement system for fusion).

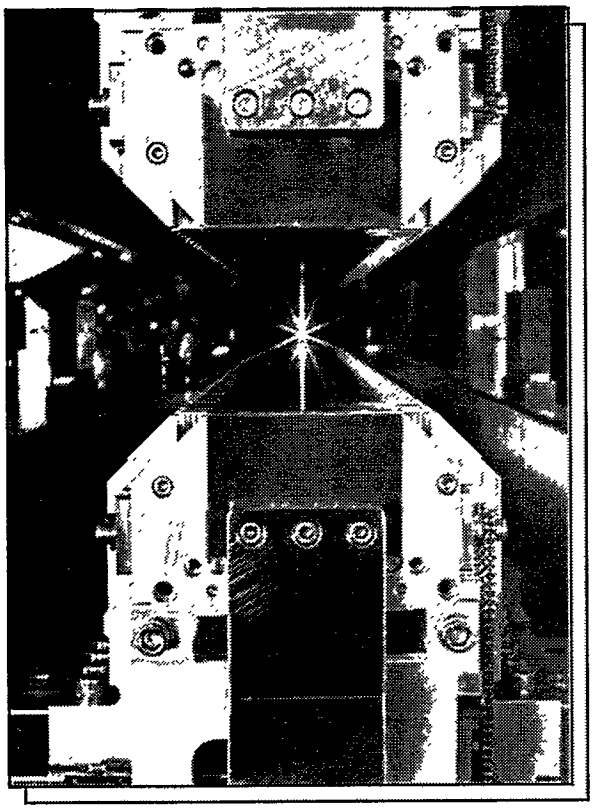

1992 - The ALS 8-cm-period undulators have a magnetic structure based on Klaus' 3D hybrid theory.

Table Of Contents

A Short History of WOLF

William S. Cooper

Klaus was a physicist in the LBL fusion energy group when I joined it as a graduate student in 1959. I ultimately also became a staff member of the group, and Klaus ultimately left it, to pursue magnet design. In the Fall of 1970, we were asked to develop a neutral beam injector for the Livermore 2X experiment; the goal was to deliver 10 A of D^0 at 20 keV to the plasma, which required the development of a large area ion source and a multiple aperture electrostatic accelerator capable of accelerating 16 A of D^+ ions, both considerable extensions of the then current technology.

I volunteered to design the accelerator, and began looking for a suitable design code. I couldn't find one--in those days the codes did not deal correctly with the problem of "extraction" of ions from the ion source plasma, and the design of this type of accelerator was largely done by trial and error. So I went to Klaus, as I often did when I had a tough problem, to see if it might be possible to adapt his PISA optimization program, which had already made a big impression on me, to electrostatic accelerator design. He agreed; many of the necessary elements had already been developed in applying PISA to magnet design, such as a flexible triangular mesh and a Poisson solver for it. Calculating ion trajectories through this mesh would be particularly simple, as the electric field in a triangle was taken as uniform, resulting in a simple parabolic trajectory through a triangle. In fact the trajectory calculation only amounted to evaluating formulas to determine the trajectory parameters when the ion crossed from one mesh triangle into another!

I went to Ken Fowler, at the time head of the Livermore fusion program, and he agreed to give us an additional $20k for this project. I provided overall guidance, Klaus worked out the physics and his usual "clever tricks,"[1] and Steve Magyary did the programming. The program to calculate ion trajectories, with space charge, was called "FLOW." The convention at the time was to invert the name of a program when it was combined with PISA for optimization (the magnet code "TRIM" became "MIRT," etc.); that is how FLOW became WOLF.

FLOW was running in short order, in only a few months as I recollect, and Steve incorporated it into PISA. The result was WOLF, a very sophisticated ion optics program, then and even now. Of course it correctly handled the ion space charge, and also treated electrons near the plasma sheath edge (as a Boltzmann distribution, not as particles). It could simulate a finite ion temperature, and by generating a fine mesh near the edges of electrodes, the aberrations that these edges generated could be calculated. WOLF let us determine what physics was important and what was not in the accelerator design process, which took some time. The optimization features were remarkable--WOLF could vary the ion current density, and electrode shapes, positions, and potentials to optimize the final beam properties. It could also deform the plasma sheath edge, which we chose as the ion emitting surface, to generate a realistic plasma "meniscus." By 1974

we had used WOLF to design an accelerator, our group had made and operated it, and we were able to compare predicted and experimental results.[2] We continued to use the program very successfully; the accelerators in the neutral beam systems still in use on the TFTR (Princeton Plasma Physics Laboratory) and DIII-D (General Atomics) tokamaks were designed with WOLF. The original program only handled two dimensional electrostatic problems ("slot" electrodes), but WOLF was later extended, particularly by Chun Fai Chan, to include magnetic fields and circularly symmetric apertures as well.

Two advantages of using a good optimization program really stand out. Klaus has discussed these, but I want to add my comments as well, drawing from my experience in using WOLF. First, when WOLF converged to a solution, there wasn't any point in wasting time looking for a better one. There wasn't one, within the constraints that the program had been given for optimization. It was exhilarating to watch WOLF chug along, reducing the "test sum" (a measure of the performance of the system, the quantity that was being minimized) at every iteration. WOLF removed the temptation to try just one more thing, in the hope that I could improve the performance of a very complex nonintuitive and nonlinear system. Second, WOLF could sometimes find solutions that had never occurred to me. One example I will never forget. I gave WOLF a problem with an excess number of accelerator electrodes, and was surprised to see that it was able to get more current through the structure by increasing the potential on alternate electrodes, while decreasing the intermediate ones. What in the world was it doing? Then it dawned on me--WOLF had discovered electrostatic strong focusing! I tried to patent the idea, but I was too late--someone else had beaten WOLF and me to it.

Working with Klaus has always been a joy, an inspiring and sobering experience. I am thankful to have had the opportunity.

References:

1. Klaus Halbach, "Mathematical Models and Algorithms for the Computer Program "WOLF," LBL-4444 (December, 1975).

2. William S. Cooper, Klaus Halbach, and Steven B. Magyary, "Computer-Aided Extractor Design," in Proceedings of the Second Symposium on Ion Sources and Formation of Ion Beams, Berkeley, Calif., 22-25 October, 1974; LBL-3399.

A Compact Permanent Magnet Cyclotrino for Accelerator Mass Spectrometry

A. T. Young, D. J. Clark, W.B. Kunkel, K.N. Leung, and C.Y. Li
Lawrence Berkeley Laboratory
University of California
Berkeley, California 94720 USA

Abstract

We describe the development of a new instrument for the detection of trace amounts of rare isotopes, a Cyclotron Mass Spectrometer (CMS). A compact low energy cyclotron optimized for high mass resolution has been designed and has been fabricated. The instrument has high sensitivity and is designed to measure carbon-14 at abundances of $< 10^{-12}$. A novel feature of the instrument is the use of permanent magnets to energize the iron poles of the cyclotron. The instrument uses axial injection, employing a spiral inflector. The instrument has been assembled and preliminary measurements of the magnetic field show that it has a uniformity on the order of 2 parts in 10^4.

I. INTRODUCTION

Accelerator mass spectrometers (AMS) are currently being used very successfully for the detection and measurement of trace elements and for the determination of isotopic abundance ratios. Continuing advances in the state of the art are accompanied by steady growth in diversity and scope of the applications, as is apparent from the proceedings of periodic international topical conferences.[1] The present status and outlook have been well summarized by J. Davis, who mentions novel uses of AMS, e.g. in industry and even in forensic work, in addition to the usual archeological, geoscientific, environmental, and biomedical applications.[2] In connection with the latter in particular, Davis points out that there is an increasing need for the development of smaller machines, optimized for ^{14}C and ^{3}H, and specialized for medical work.

The one disadvantage of the AMS method is that the equipment tends to be large and expensive. The most common devices used are tandem accelerators, yielding energy doubling, provided the particles in question can start out as negative ions. On the other hand, smaller, low-energy cyclotrons for use in mass spectrometry have been under development for some time, at various locations.[3-5] Particularly successful has been the effort by Chen et al., at Fudan University in China, which included a number of sophisticated refinements.[6] However, this machine is still fairly large.

In this paper, we describe a small low-energy cyclotron, a "cyclotrino," designed to accelerate ^{14}C ions, for biological research and for medical

applications. It differs from all other cyclotrons in that its magnetic field is derived from an assembly of judiciously placed permanent magnets. The resulting loss in variability of the field strength causes no problems, since the instrument is intended to be optimized only for one single ion mass. The advantage of this design lies in the gain in compactness and simplicity of operation. No coils or power supplies and no cooling are required for the magnet. This greatly reduces the utility requirements for the spectrometer system as a whole. This reduction and the small size and weight are make the system "portable" or "transportable," conceivably permitting utilization in medical studies in hospitals, or for environmental monitoring in trucks or airplanes.

The term "Cyclotrino" was introduced in the 1980s by R.A. Muller and co-workers,[7] who also proposed the use of permanent magnets at the time but failed to obtain funding.[8] The realization of the present device is a result of recent increases in demand for specialized machines combined with the participation of our local expert on magnet design, Klaus Halbach.

II. CMS DESIGN

A. System Considerations

The physical principle behind using a cyclotron as a mass spectrometer is the fact that only particles of the correct charge-to-mass ratio will be accelerated in the device. Each particle makes many orbits in the cyclotron, and with each orbit the mass discrimination increases. The overall size of the machine is dictated by the species to be measured, the injection energy of the ion, and the mass resolution needed. For ^{14}C, a mass resolution of about 1800 is needed to separate ^{14}C from ^{13}CH. The resolution of a CMS is described by[9]

$$R \approx 3 \times n \times H, \qquad (1)$$

where n is the number of orbits the particles make before extraction and H is the harmonic of the fundamental cyclotron frequency that the accelerating RF is operating on. For ^{14}C in a 1 T field, the fundamental frequency is 1 MHz. H might be 15, so that the minimum number of orbits would be 40. With modest energy gain per turn, ≤500 V, it is possible to achieve this figure with an extraction radius of ≤ 9 cm. We have conservatively designed the instrument for an extraction radius of 12 cm, corresponding to an energy of 50 keV.

Figure 1 shows a schematic diagram of the LBL CMS system. To improve the performance over existing devices, changes are being made in the ion source and the injection system. This will lead to enhanced sensitivity and increased sample throughput. The magnetic field of the cyclotron is produced by permanent

magnets rather than electromagnets. Particles emerging from the accelerator are detected using a microchannel plate detector.

Figure 1. Schematic diagram of the LBL Cyclotrino.

B. Ion Source and Injection System

The ion source typically used in AMS is a cesium sputter ion source. However, we have experimented in the use of a magnetic multicusp source for this project.[10] In these devices, negative ions from gas phase precursors are formed directly in the discharge plasma. Recent experiments have shown that C^- can be formed in these sources as well.[11] Further research is necessary to optimize this type of source for C^- production. If successful, it will provide a simple to operate, high throughput source of negative ions without the need for the graphitization process used with sputter ion sources.

After production, the ions are transported to the cyclotron where they are injected axially using a spiral inflector, an electrostatic channel which twists or "tilts" as it guides the ions down the axis of the machine and into the midplane. The inflector geometry has been optimized so that the emittance of the ion beam coming out of the inflector matches the acceptance of the cyclotron.

C. Magnet Design

A novel aspect of the cyclotron design is the use of permanent magnets to produce the magnetic field. This has two advantages. First, the overall size and weight of the magnet structure are reduced, as the magnet coils and power supplies are eliminated. Second, the electrical power and cooling requirements of the instrument are minimized. With permanent magnets, the CMS will be transportable and could be placed aboard aircraft, small boats, or in field locations. Their use will also reduce operational costs. The magnetic field in the midplane is 1 T. For high mass resolution, the orbits need to be isochronous; a flat magnetic field uniform to about 2 parts in 10^4 must therefore be maintained.

Under the guidance of Klaus Halbach, a conceptual design for the magnet was developed. Figure 2 shows a sketch of the device that Klaus produced for one of the early design meetings. Magnet material is placed in contact with the iron pole pieces. The iron concentrates and directs the magnetic flux to the pole faces. For one pole, the magnets are oriented so that the magnetization vector points toward the pole face. For the other pole piece, the magnets are oriented so that the magnetization points away from the pole face. A magnetic flux return ("yoke") connects the magnets to complete the circuit. The midplane of the accelerator is placed between these poles.

From this conceptual design, calculations were performed to optimize the geometry. Initially, a program which analytically calculated the indirect and direct magnetic fluxes from various candidate configurations was used to define the dimensions of the magnets, poles, and yoke. The computer program

POISSON was then used to verify and optimize this solution. Figure 3 shows the final geometry adopted. Note the similarity between it and the original sketch of the cyclotrino. Some differences can be noted, for example, the accelerator's radius increased, resulting in an increase in pole radius and magnet material.

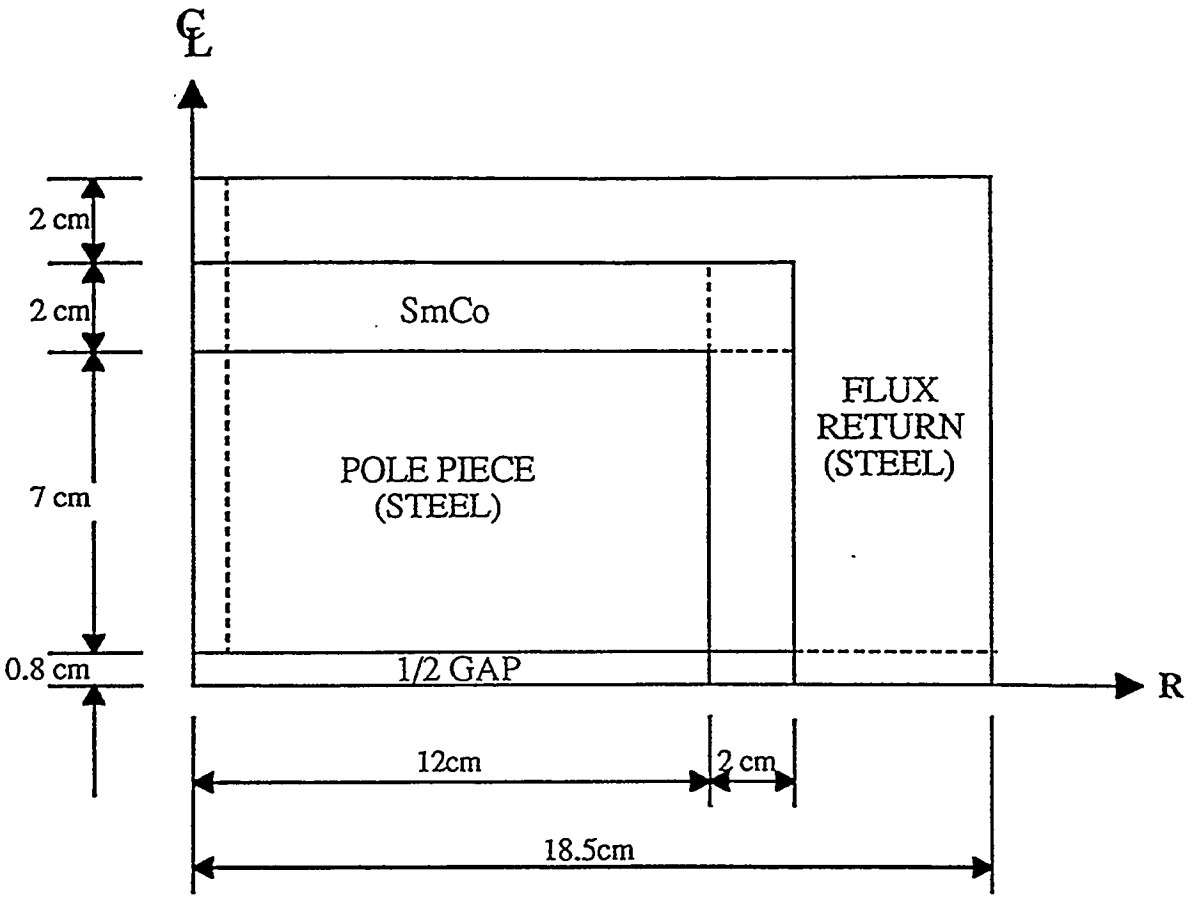

Figure 2. The original cyclotrino magnet conceptual design proposed by Klaus Halbach. The figure is a side view of one quadrant of the cylindrically symmetric instrument.

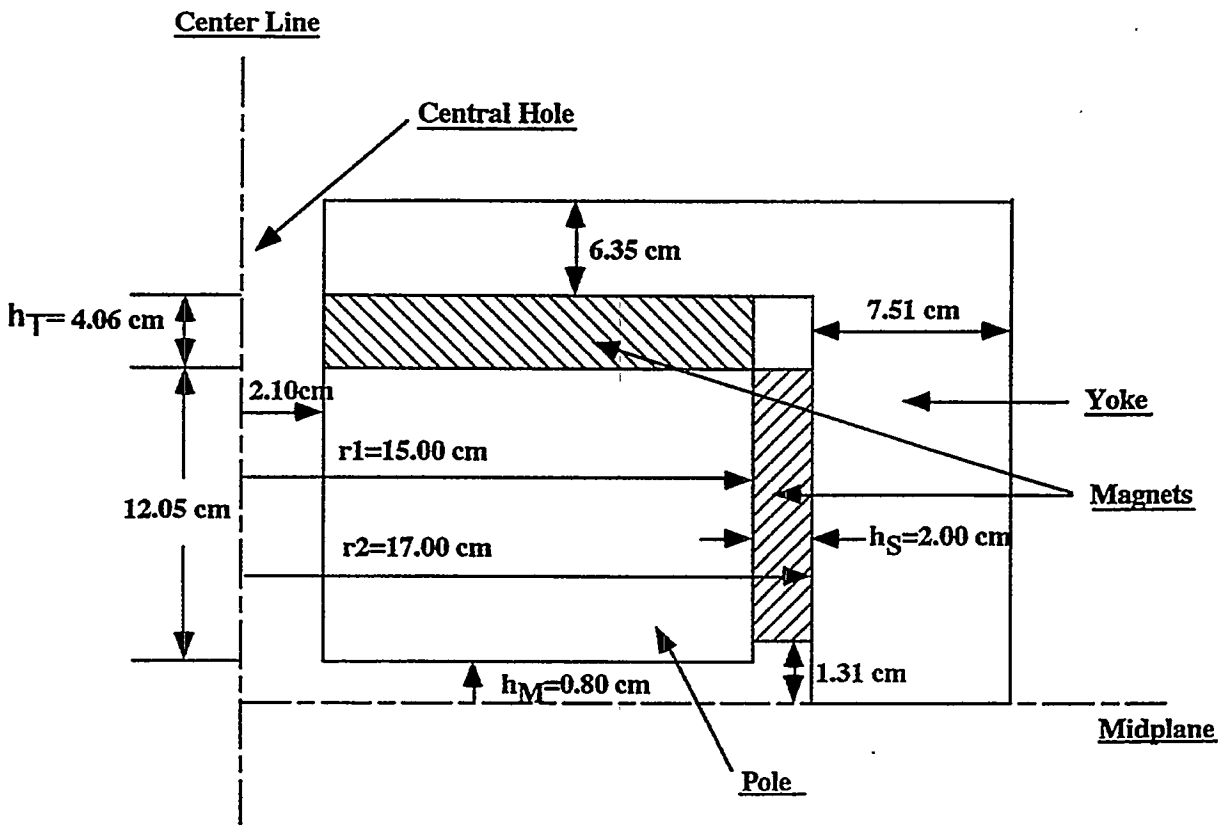

Figure 3. The final design of the cyclotrino. Most of the changes with respect to Figure 2 came as a result of an increase in the cyclotrino radius.

III. INSTRUMENT PERFORMANCE

The final design parameters of the cyclotrino are listed in Table 1. Of crucial importance is the quality of the magnetic field. After assembly, measurements of the magnetic field were made. These are shown in Figure 4. As can be seen, within the acceleration region between 5 cm and 12 cm, the field is flat to within $\pm$ 3 parts in 10^4. This small deviation was anticipated in the POISSON calculations, and can be corrected by trimming and adjusting the position of the radial magnets. With this correction, the field should be within tolerance throughout the acceleration region.

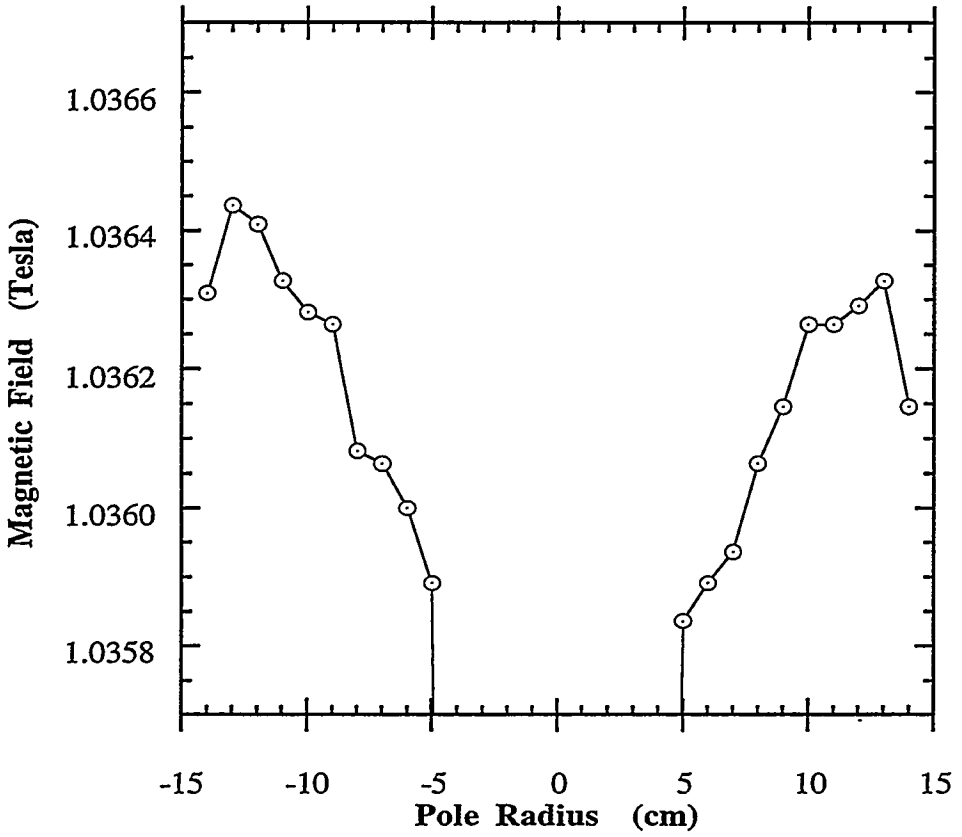

Figure 4. Measurement of the magnetic field in the cyclotron across a diameter. The field is flat to within ± 3 x 10^{-4} between 5 cm and 12 cm radius.

Parameter	Description
Ion source	Magnetic multicusp
Species	Carbon 14
Injector type	Spiral inflector
Injection energy	5 keV
First orbit radius	4 cm
Extraction radius	12 cm
Extraction energy	< 50 keV
Pole face radius	15 cm
Pole gap	1.6 cm
Magnetic Field	1 T
Field Source	SmCo Magnets

Table 1. Cyclotron design parameters.

Figure 5 is a photograph of the completed instrument with Klaus, the authors, and many of the people involved in the project. Further optimization of this prototype design can also be envisioned. For example, reductions in the pole and yoke radii may be possible, leading to an even smaller machine.

IV. CONCLUSIONS

Cyclotron mass spectrometry (CMS) is a potentially powerful analytical technique with applications ranging from studies of global warming constituents to the biological metabolism of pollutants and pathogens. A permanent magnet cyclotrino has been designed and constructed to demonstrate a system which would be cost-effective and readily available. Initial measurements of the magnetic field show that the field uniformity is within expectations.

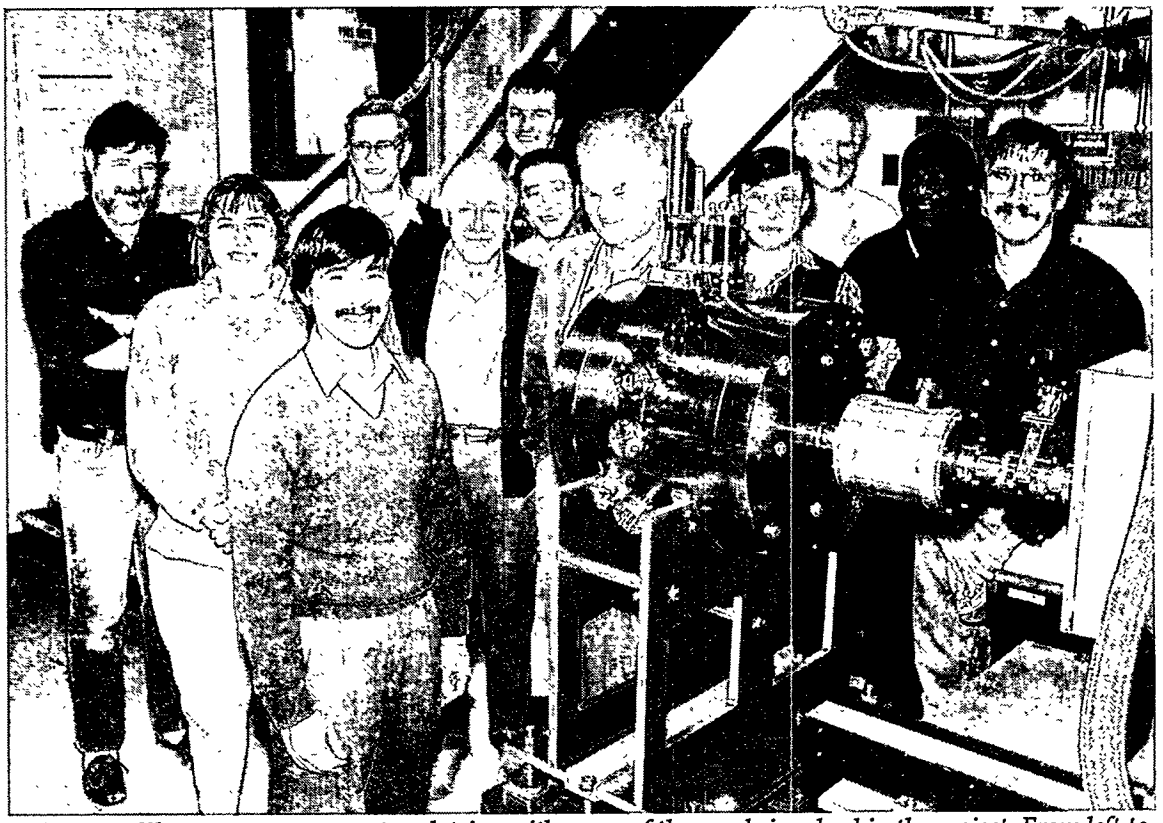

Figure 5. The permanent magnet cyclotrino with many of the people involved in the project. From left to right are: Glenn Ackerman, Mary Stuart, Anthony Young, Dave Clark, Wulf Kunkel, Luke Perkins, Ka-Ngo Leung, Klaus Halbach, Chaoyang Li, Tom McVeigh, Al Rawlins, and Steve Wilde.

The authors sincerely thank the many people who helped make this project a success. These include: Kirk Bertsche, Chun-Fai Chan, Rich Muller and J.X. Yu for their scientific guidance; Russ Wells, Mary Stuart, Ross Schlueter, and Al Rawlins for superb engineering; and Steve Wilde, Larry Mills, Don Williams, Glenn Ackerman, and Tom McVeigh for their efforts to construct and install the instrument. Bruce Milton of TRIUMF graciously helped in obtaining and running some of the ion trajectory codes, and Wes Bethel of the Information and Computing Sciences Division of LBL provided assistance with computer-generated graphics. Finally, the authors acknowledge the contribution of Klaus Halbach, who provided the inspiration behind the permanent magnet system.

This work is supported by the U.S. Department of Energy, Office of Basic Energy Sciences, Division of Advanced Energy Projects, under contract No. DE-AC03-76SF00098

V. REFERENCES

1. Proc. 6th Int. Conf. on AMS, Canberra-Sydney, Australia, 1993. Published in Nucl. Instr. and Meth. B 92 (1994) pp 1-524.
2. J.C. Davis, ibid. pp.1-6.
3. K.J. Bertsche et al., Nucl. Instr. and Meth. B 29 (1987) 105.
4. M.B. Chen et al., Nucl. Instr. and Meth. A 278 (1989) 402.
5. K.M. Subotic et al., Nucl. Instr. and Meth. B 50 (1990).
6. M.B. Chen et al., Nucl. Instr. and Meth. B 92 (1994) 213.
7. J. Goldhaber, LBL News Magazine, vol. 7 (Spring/Summer 1982) p. 22.
8. R.A. Muller, private communication.
9. K.M. Subotic, J. Physics G - Nucl. and Part. Physics 17S, S363.
10. Leung, K.N., Anderson, O.A., Chan, C.F., Cooper, W.S., deVries, G.J., Hauck, C.A., Kunkel, W.B., Kwan, J.W., Lietzke, A.F., Purgalis, P., and Wells, R.P., Rev. Sci. Instru. 61 (1990) 2378.
11. K.N. Leung, D.A. Bachman, D.S. McDonald, and A.T. Young, Proceedings of the 13th International Conference on Cyclotrons and Their Applications, Vancouver, Canada, 1992, p. 312.

A Study of the Suitability of Ferrite For Use in Low-Field Insertion Devices

Kenneth Johnson and William V. Hassenzahl

ABSTRACT

Most insertion devices built to date use rare-earth permanent-magnet materials, which have a high remanent field and are more expensive than many other permanent-magnet materials. Low-field insertion devices could use less-expensive, lower performance magnetic materials if they had suitable magnetic characteristics. These materials must be resistant to demagnetization during construction and operation of the insertion device, have uniform magnetization, possess low minor-axis magnetic moments, and have small minor field components on the surfaces. This paper describes an investigation to determine if ferrite possesses magnetic qualities suitable for insertion device applications. The type of ferrite we investigated, MMPA Ceramic 8 from Stackpole Inc., was found to be acceptable for insertion device applications.

INTRODUCTION

Insertion devices [1,2,3] are used with electron storage rings to produce photon beams. The insertion devices' magnetic fields accelerate electrons in a direction transverse to their forward velocity, which causes them to emit synchrotron radiation. Spectral requirements for the emitted radiation [4] impose requirements on the emittance of the electron beam in the storage ring [5] and the quality of the magnetic field in the insertion device [3]. This in turn determines the requirements for the magnitude and variation of the remanent field B_r of the magnetic blocks used to produce the accelerating magnetic field. A permanent magnet block having dimensions typical of those used for some of the Lawrence Berkeley Laboratory (LBL) Advanced Light Source (ALS) undulators is shown in Fig. 1. Each block is placed at a precise location in the magnetic structure and has a fixed orientation. Producing the ideal magnetic field depends on achieving the proper alignment between the local and average magnetization vector and the reference coordinates determined by the block geometry. Insertion devices, in

particular those in which the field is produced and shaped entirely by the magnetic material, require high quality magnetic blocks that must:

1. Be resistant to demagnetization due to contact with other pieces of permanent magnet material and with high-permeability metals

2. Have uniform magnetization throughout their volume

3. Be magnetized parallel to a specific axis, with low minor-axis components of magnetization, and

4. Have small local minor-axis surface field components on the minor faces, particularly those that are closest to the electron beam.

Resistance to demagnetization assures a predictable magnetization state or operating point during operation of the complete insertion device. Several steps in fabrication may expose the block to high external fields and other demagnetizing forces. Hybrid insertion devices use high-permeability metals to concentrate the flux and produce higher and better controlled magnetic fields in the region of the electron beam. The blocks in these devices are always in contact with high permeability materials.

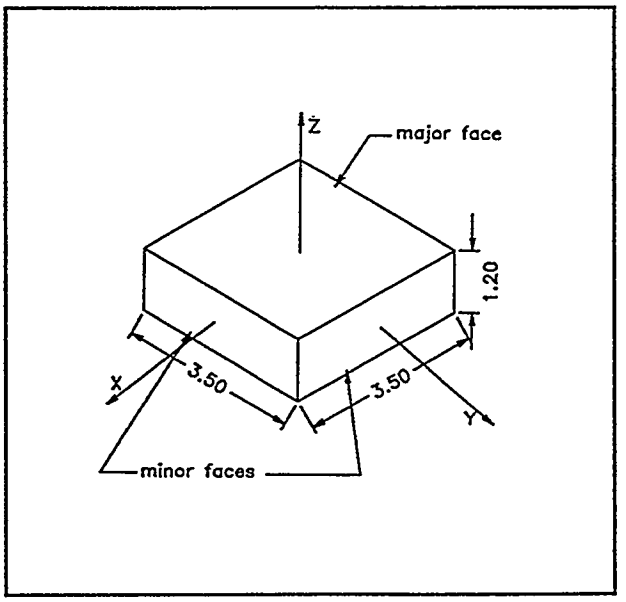

Figure 1. Ferrite block and reference coordinates (dimensions in centimeters).

Providing uniform magnetization in a direction parallel to the major axis throughout the block's volume will assure small minor axis field components and allow proper orientation during insertion device construction. Local field components perpendicular to the minor faces of the block, in particular the face closest to the electron beam, degrade the quality of the magnetic field in this area and thus affect the synchrotron radiation produced by the insertion device. Blocks that have low minor-axis surface field components minimize this effect.

High-field hybrid insertion devices utilize the high remanent fields obtainable in rare-earth permanent magnets. For example, Neodymium-Iron-Boron (Nd-Fe-B), which has a B_r of 11,800 gauss and is very resistant to external temperatures and fields, contributes to the performance of the ALS insertion devices. One tesla fields are routinely achieved and 2 T is possible in long period devices. The materials selected for the blocks in these insertion devices have been investigated to determine that they meet the requirements mentioned above. Lower fields may be acceptable in insertion devices for other applications. These devices can be constructed with rare-earth materials by just using smaller quantities than are required for the high-field devices. However, low field insertion devices may be less expensive and easier to construct using less expensive materials with lower remanent fields. We evaluated the suitability of ferrite for use as permanent-magnet blocks in a low-field insertion device by verifying that ferrite possesses the relevant magnetic qualities.

EVALUATION OF A FERRITE BLOCK

Sample Block

To test this material we procured an unmagnetized sample of the ferrite MMPA Ceramic 8 from Stackpole Inc. Block SP1, with dimensions 1.2 x 3.5 x 3.5 cm, which is similar to those of the ALS U5.0 [3], was cut from this sample. Block SP1 was magnetized in a direction parallel to the Z-axis by applying a field of 20 kOe. The applied field was produced in the 1.2 cm gap of an iron yoke wrapped with 800 turns of wire carrying 25 amperes. Verification that the block was saturated by the magnetizing procedure was obtained by measuring the dipole moment of SP1 (or volume averaged magnetization) at its operating point in air, and comparing this value to the remanent field specified by the manufacturer (see Table 1).

Block Magnetic Field and Orientation

The block characteristics were determined in the Helmholtz-coil magnetic-moment measurement system [6] developed for the ALS. Results are shown in Table 1. The volume averaged magnetization is less than the maximum possible remanent field by about 6%. Since the demagnetizing-field in air, H_{d_air}, reduces the effective magnitude of B_r, the moment of a block measured in this system is always less than the maximum.

Thus we conclude that the block was saturated during the magnetizing procedure. Table 1 also verifies that the magnetization was parallel to the desired axis of the block. The transverse components are quite small and the volume averaged magnetization vector given in Table 1 has an angle of only 0.685° with respect to the major-axis. This misorientation is well within the 3° range acceptable for the U5.0 blocks. The actual misorientation for the U5.0 blocks was less than 1°.

TABLE 1.

Manufacturer's specifications for MMPA Ceramic 8.

$B_r = 3850$ gauss

$H_c = 3050$ gauss

Energy Product = 3.4×10^6 gauss·oersted

Measured magnetization (volume averaged) after magnetizing block.

$M_z(H_{d\_air}) = -3639 \pm 1$ gauss

$M_x(H_{d\_air}) = 35 \pm 3$ gauss

$M_y(H_{d\_air}) = -26.7 \pm 0.1$ gauss

Resistance to Demagnetization

Resistance to demagnetization by external fields is characterized by the coercivity, H_c, specified in Table 1 for MMPA Ceramic 8 ferrite. Demagnetization due to contact with a high-permeability metal was measured by comparing the volume averaged magnetization of the block before and after measurement of surface fields in a high-permeability flux shunt [7]. This device, sometimes called an iron maiden, clamps the major surfaces of the magnetic block in a high permeability Ni-Fe yoke. Contact with the high permeability ($\mu \approx 60{,}000$ at low H_c) Ni-Fe moves the operating point of the ferrite block by decreasing the internal demagnetizing field magnitude, ($H_d < H_{d\_air}$). In particular, removal of the block from the Ni-Fe maiden could partially demagnetize the block and place all or part of the material at a lower operating point, i.e., on an inner hysteresis loop. As shown in Table 2, ferrite block SP1 was not affected by this process, indicating adequate resistance to demagnetization during contact with magnetic materials.

TABLE 2.

Change in volume averaged magnetization due to contact with Ni-Fe.

$(|M_i(H_{d\_air})_{final}| - |M_i(H_{d\_air})_{initial}|)$

$(i = x, y, \text{or } z)$

delta $M_z = +10 \pm 1$ gauss

delta $M_x = +4 \pm 6$ gauss

delta $M_y = 0.0 \pm 0.1$ gauss

Surface Field Components

Measurement of the minor-axis surface field component was performed while the block was clamped inside the Ni-Fe flux shunt. A small search coil was used to scan the minor surfaces of the block. The resulting minor-surface field profiles are shown in Figs. 2 and 3. Note that the local field has a maximum value of only 0.8% of the measured remanent field, B_r.

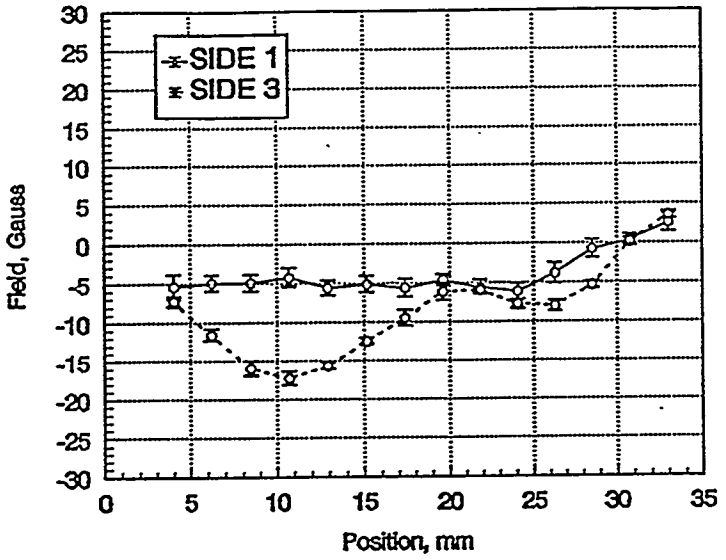

Figure 2. Minor-surface field profile for surfaces perpendicular to the x axis.

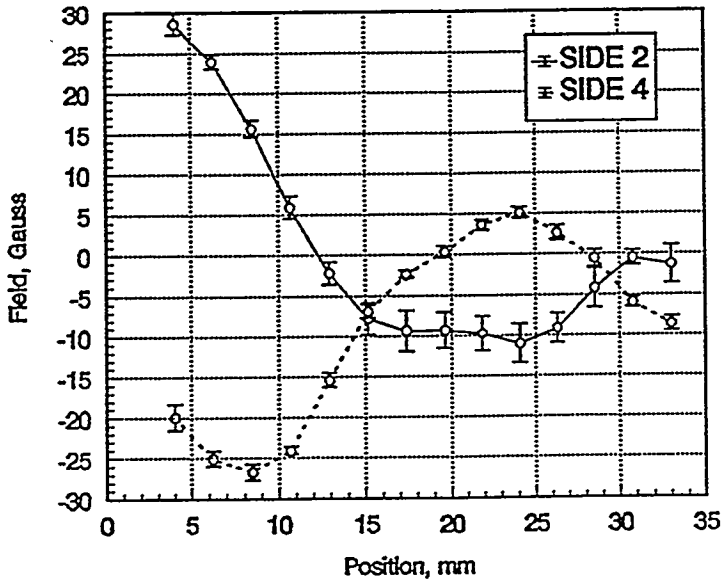

Figure 3. Minor field profile for surface's perpendicular to the y axis.

Limit of Applicability

The demagnetizing field, H_{d_air}, increases with decreasing geometric ratio [8] (geometric ratio = length (or transverse dimension) to height). Since the geometric ratio for block SB1 is 0.343, demagnetization should not occur in blocks using this type of ferrite and having geometric ratios greater than 0.343.

CONCLUSION

The MMPA Ceramic 8 ferrite block studied possessed adequate resistance to demagnetization, and small, local, minor-axis surface-field components. These magnetic qualities suggest this type of ferrite is a suitable permanent magnetic material for use in low-field insertion devices. Because resistance to demagnetization is dependent on block geometry and thinner blocks might be indicated for some applications, further investigation should be performed if blocks with geometric ratios significantly less than 0.343 are proposed.

REFERENCES

[1] Halbach K., "Permanent Magnet Undulators", In Proc. 1982 Bendor FEL Conference, and Journal de Physique, **44**, p C1-211 (1983).

[2] Halbach, K., "Insertion Device Design"' 16 Lectures presented from Oct. 1988 to March 1989, Lawrence Berkeley Laboratory Report, V-8811-1.1-16, (1989).

[3] U5.0 Undulator Conceptual Design Report, Lawrence Berkeley Laboratory Report, PUB-5256, (1989).

[4] Kincaid, B. M., "Random Errors in Undulators and Their Effects on Radiation Spectrum", J. Opt. Soc. Am. B, **2**, 1294, (1985).

[5] "An ALS Handbook", Rev. 2, Lawrence Berkeley Laboratory Report PUB-643, (1989)

[6] S. Marks, et al, ALS Insertion Device Block Measurement and Inspection,

[7] U5.0 Undulator Conceptual Design Report, Lawrence Berkeley Laboratory Report, PUB-5256, (1989).

[8] Richard M. Bozorth, Ferromagnetism, D. Van Nostrand Co. Inc., 1955.

BIG KARL and COSY
Examples for High Performance Magnet Design taught by "Papa Klaus"

U. Bechtstedt, Georg. P.A. Berg[a], U. Hacker, A. Hardt[b], W. Hürlimann[c], R. Maier, S. Martin, J. Meissburger[d], J. G.M. Römer[e], P. v. Rossen, and T. Sagefka

Institut für Kernphysik, Forschungzentrum Jülich, KFA, D-52425 Jülich, Germany
a) Indiana University Cyclotron Facility, Bloomington, Indiana 47 408
b) Fachhochschule Aachen Jülich, D-52428 Jülich
c) Colenco, Power Consulting Ltd. CH-5405 Baden, Switzerland
d) Institut für angewandte Mathematik, Forschungzentrum Jülich, KFA, D-52425 Jülich, Germany
e) Leybold-Heraeus GmbH, D-50968 Köln

Introduction

The past decades have seen a tremendous development in nuclear, middle, and high energy physics. This advance was in a great part promoted by the availability of newer and more powerful instruments. Over time, these instruments grew in size as well as in sophistication and precision. Nearly all these devices had one fundamental thing in common — magnetic fields produced with currents and iron. The precision demanded by the new experiments and machines did bring the magnet technology to new frontiers requiring the utmost in the accuracy of magnetic fields. The complex properties of the iron challenged innumerable physicists in the attempt to force the magnetic fields into the desired shape. Experience and analytical insight were the pillars for coping with those problems and only few mastered the skills and were in addition able to communicate their intricate knowledge.

It was a fortuitous situation that we got to know Klaus Halbach who belonged to those few and who shared his knowledge contributing thus largely to the successful completion of two large instruments that were built at the Forschungszentrum Jülich, KFA, for nuclear and middle energy physics. In one case the efforts went to the large spectrometer named BIG KARL [1] whose design phase started in the early 70ties. In the second case the work started in the early 80ties with the task to build a high precision 2.5 GeV proton accelerator for cooled stored and extracted beams known as COSY-Jülich [2].

Designing BIG KARL

The accurate observation of the momenta of ejectiles after a scattering process constitutes one of the most powerful tools for nuclear structure studies. In connection with the isochronous cyclotron JULIC [3] this research had to be carried to higher energies and created the need to design a high resolution spectrometer with large acceptance and a momentum range fitted to the envisioned physics. The mass-energy product mE/q^2 had to be in the range of 540 u·MeV and was significantly larger then the current systems in use for these studies. Scaling a well known design of that time like the Q3D [4] resulted unfortunately in a device to big and with a price tag that was out of reach. Therefore, it was necessary to conceive a new design. It came to be a QQDDQ structure and the spectrometer was named BIG KARL reminding with its name to Karl L. Brown, one of the key persons in the design process. The important new

consideration in this design was the phase space matching within the dipoles allowing to shrink considerably their gap and thus the cost for manufacturing. In terms of expenditure this new design meant a tremendous savings compared to scaling up the the Q3D as depicted in figure 1. Included in this estimate is besides others the cost for iron, copper, power supplies, primary power, cooling, and machining.

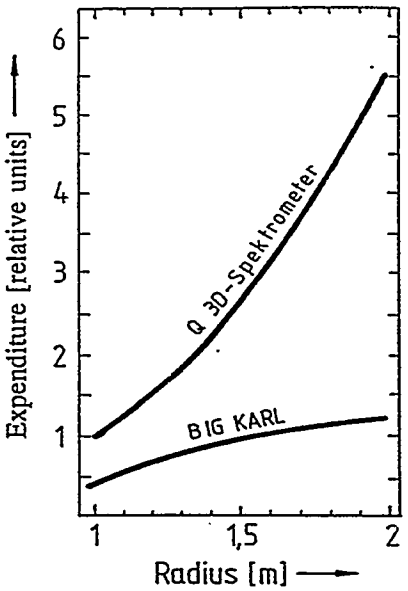

Fig. 1 Relative expenditure for Q3D-type spectrometer and BIG KARL-type spectrometer versus the central radius and correspondingly different energy-mass products.

The next major hurdle that had to be passed was the design of the magnets themselves which had to break new ground in terms of energy resolution. The reason for this is that studying nuclear states at higher energies has one inherent difficulty. On a relative scale those states are spaced closer together and thus demand a higher precision of the magnetic fields and a significant better correction of residual optical aberrations. It is here where the expertise and experience of Klaus Halbach came into play. The shape of the magnetic fields in the dipole needed to be formed in a highly controlled way to counter the aberration of the system that would have been detrimental towards the demanded resolution. To remedy this problem Klaus Halbach proposed a special type of correction windings [5] that gave the necessary freedom for manipulating the field shape and thus allowing for the desired field corrections.

The basic design consists of a certain number of conductors that are embedded in grooves machined in the surface of the upper and lower yoke where the pole pieces are attached. Their curvature is identical to the radius on which they act and they are arranged symmetrical to the magnetic midplane. At the transition from iron to air the currents in these conductors cause a change in the tangent magnetic field component H_t. This led to the name H_t-winding for this type of correction coil. An overview of their layout is given in fig. 2, which shows a front view of the first dipole. The upper part is shown as cross section while the lower part shows a front view with the correction coils going around the yoke.

Much more detail can be seen in fig. 3 showing the cross section through the pole piece and part of the upper yoke of a model magnet that had been used to study in depth the properties

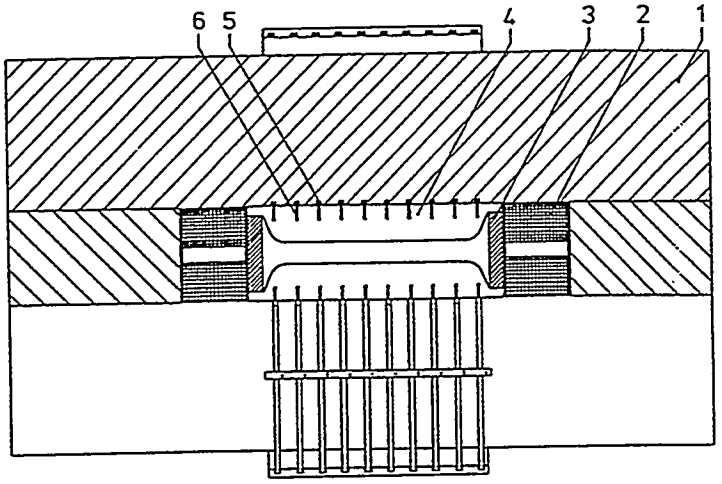

1 yoke, 2 main coil, 3 vacuum chamber, 4 pole piece, 5 H_t-winding, 6 H_t-slot

Fig. 2 Front view with cut away view of the upper part of dipole 1 of BIG KARL.

and the handling of the H_t-Windings.

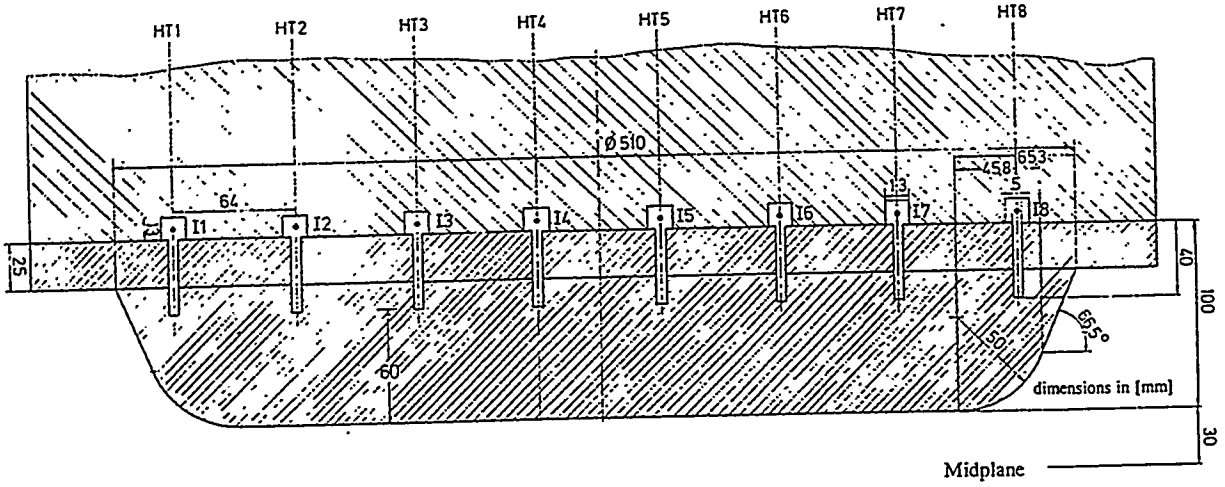

Fig. 3 Model magnet with H_t-Windings and pole form analog to the dipoles of BIG KARL.

It reveals the sophistication that had to be applied to achieve the required field quality. The upper yoke carries grooves in which the windings of the H_t-winding are placed. The pole piece is engraved with 40 mm deep grooves to force the magnetic field lines to the vertical direction enhancing thereby the uniformity of the field.

The gradient profile for the x-direction of this model magnet is depicted in figure 4. One of the H_t-windings, in this case HT4, was fed with currents of different polarity and magnitude. For each measurement the magnet had been cycled in a well prescribed way through saturation. With this procedure a field reproducibility of 10^{-5} was obtained [5]. Many of the observed effects can be understood within the frame of the orthogonal analog model described in ref. [5].

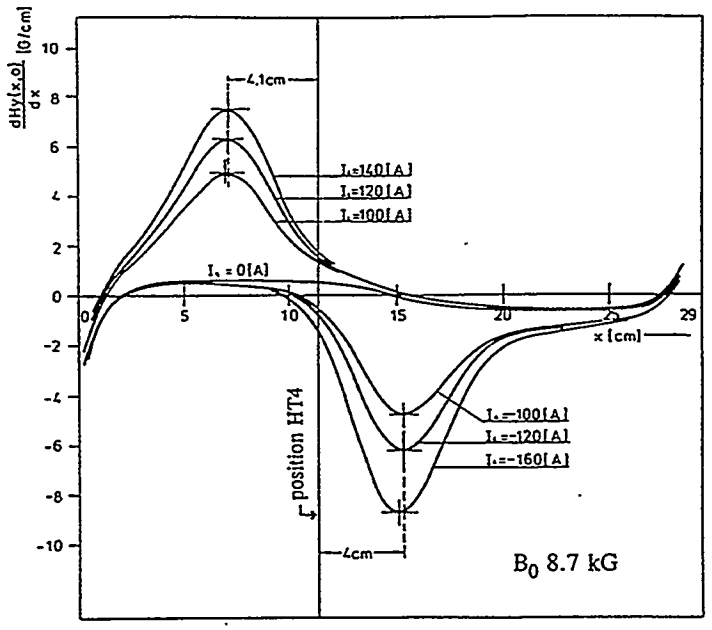

Fig. 4 Gradient profile measured in the model magnet for a set of correction currents applied to H_t-4.

In this model magnetic properties are set in correspondence to certain electrical properties. This allows in many cases to study the behavior of magnetic systems by creating the corresponding structure on conductive paper and measuring the electrical properties.

The corrective action of the H_t-currents depends on the relative permeability and, hence, on the magnitude of the main field. The higher its value the smaller the effect of those currents limiting this correction method at higher fields.

Complementary, the effect of H_t-currents has been studied in parallel via POISSON calculations [7]. The deformation of the field lines caused by a H_t-current is visualized in fig. 5 for a H-type dipole magnet similar to the ones used in the spectrometer. Taking into account the finite mesh

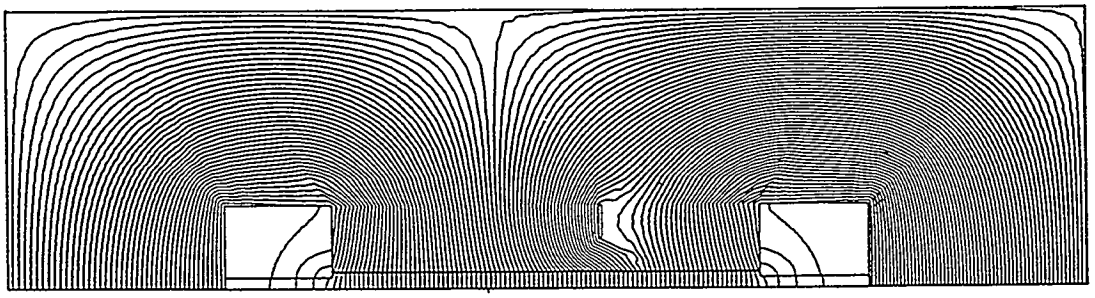

Fig. 5 Result of a POISSON calculation showing the effect of an H_t-current of 120 A. Mean field is 8.8 kG.

structure, gradient curves extracted from those calculations are in reasonable agreement with the measurement. Of course, for the precision needed in a spectrometer an accurate measurement of the field distribution was indispensable.

A field map of the homogeneous range of dipole D1 of the spectrometer is lain down in fig. 6. Shown is, in a blown up scale, a small window of the magnetic induction B, covering a range of approximately 10 Gauss at a level of 8770 Gauss. The characteristic small bump

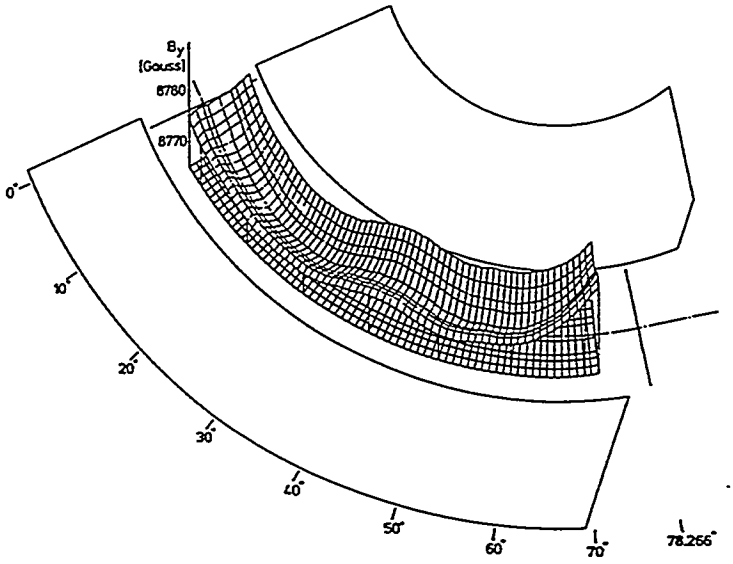

Fig. 6 Field map of the first spectrometer dipole.

in the middle of the dipole is due to the split structure of the upper and lower yoke. The mechanical design had to resort to such a construction as otherwise it would not have been possible to assemble the large dipole magnets on site. The small azimuthal variation of the field is not detrimental to the ionoptical quality of the dipole. More important and of excellent quality is the radial uniformity of the field.

The dipole fringe field region is another critical point for the final resolution of a spectrometer. Besides the Rogovski shape of the pole pieces field clamps are used to shape the entrance and exit fields. They enable the shaping the entrance in exit curvature for minute corrections and result in a quite stable position of the virtual field boundary over a large field range. Their mechanical shape and the corresponding field is graphed in fig. 7.

Handling of the H_t-Windings

Adjusting the currents of the H_t-windings for optimal resolution is a non trivial task. It is of course possible to adjust calculated field forms within a specified range. But when it comes to high resolution spectroscopy the calculated field form may not give the best result. Examples of radial field shapes generated in the first dipole are shown in figures 8 and 9.

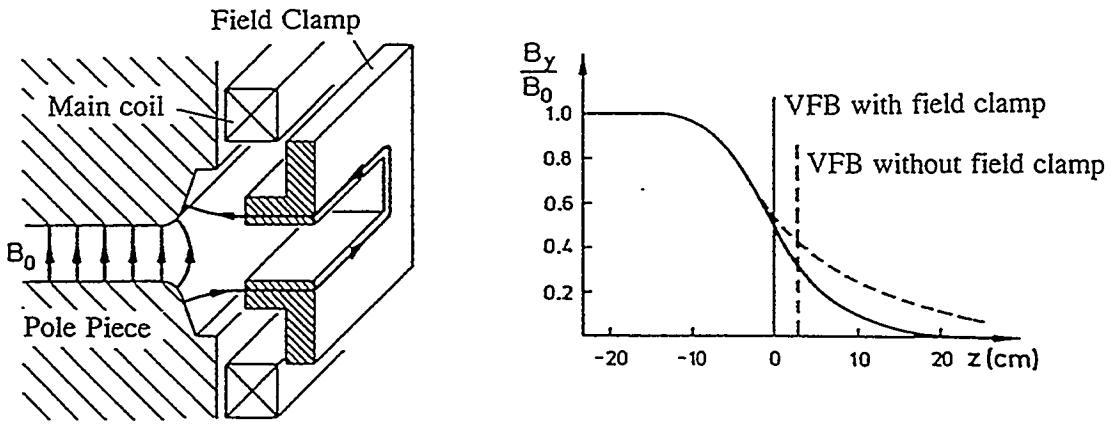

Fig. 7 Shape of the fringe field at the entrance of dipole 1.

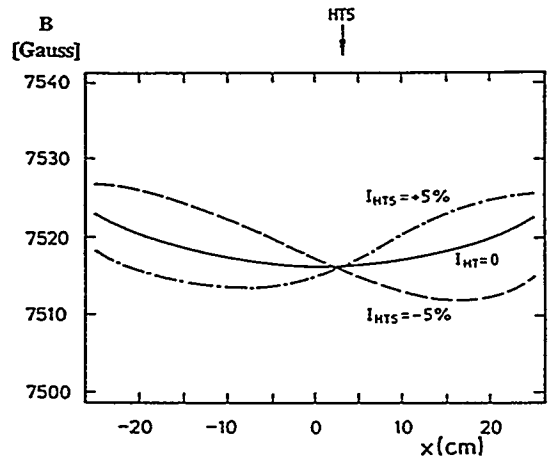

Fig. 8 Field deformation through a single H_t-current.

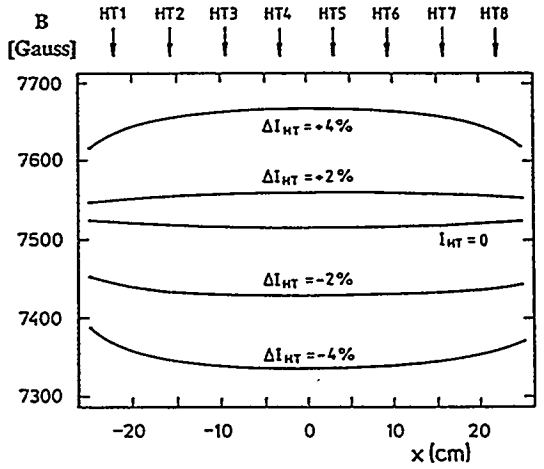

Fig. 9 Field distribution applying H_t-currents with a linear rise respectively fall versus radius.

The first case shows the effect of a 50 A current through a single H_t-winding. It leads approximately to an indexed dipole field. This effect is enhanced and the field form improved when supplying the same current to all H_t-conductors. This field shape results in a focussing respectively defocussing of the particles. Different to this a current distribution with a linear rise respectively fall versus radius is used in the other case, giving a quadratic field term that would modify the second order aberrations for the focussed particles.

To get best result in a real experiment one starts with an approximate field setting. To speed up the optimization process one uses a target of suitable thickness and a reaction having a high cross section and several exited stated that allow to judge the variation of the line width along the focal plane. To study the focussing properties one narrows the entrance slits such

that only a small angular band is accepted. The entrance slits are moved to different angle positions and for each position a spectrum is acquired. The movement of the line centers is measured and fed into the program "MATRIX" [8] that calculates the main residual second order effects $T_{122}$and T_{126} according to TRANSPORT [9] notation. In addition it computes the line broadening due to those components and suggest changes for the settings of the H_t-currents using a matrix formalism. One important feature of the ion optical design of BIG KARL is that those two components can be adjusted reasonably well due to a certain decoupling between the two dipoles. Therefore, after few iterations one arrives at the optimum correction. To obtain a reproducible setting one needs to "cycle" the dipole magnets. In this procedure the magnets are driven into saturation raising the current with a slope low enough to keep the Eddy currents small. After a period of 10 minutes the current is lowered with the same slope to the desired value. After such a procedure it may be necessary to make some small final adjustments to the H_t-currents. Once such a field form has been established it can be adjusted with great reproducibility lowering significantly the time needed to set up the fields in the spectrometer in future runs.

The performance obtained after such an optimization is illustrated with the spectrum in figure 10 which is a deuteron spectrum of the reaction $^{109}Ag(p,d)^{108}Ag$ with an incident proton energy of 25 MeV [10].

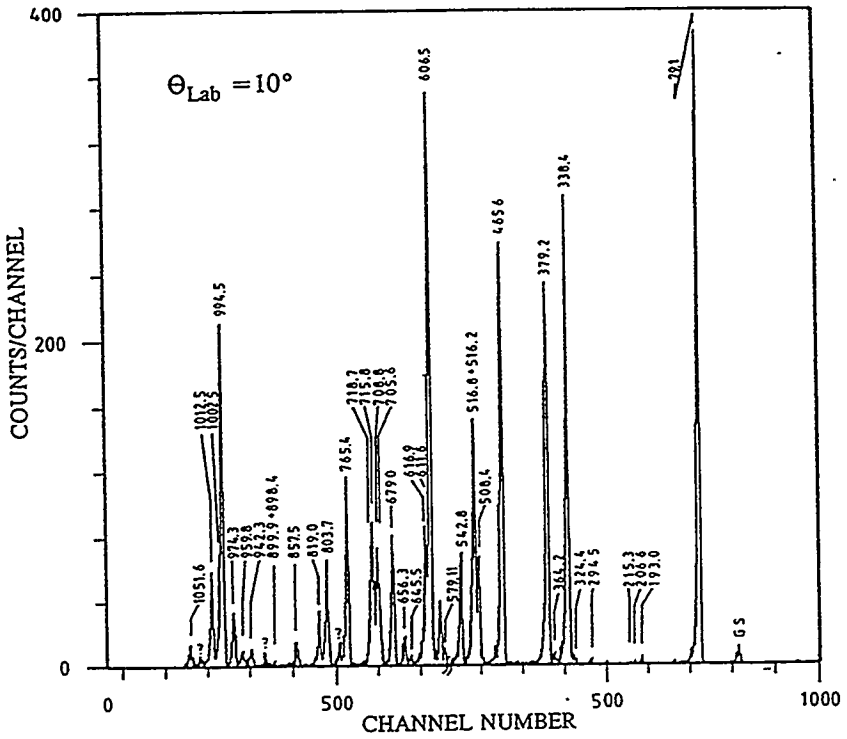

Fig. 10 Deuteron spectrum measured with BIG KARL. Excitation energies are shown in keV.

An energy resolution of 4 keV was obtained which corresponds to a momentum resolution of $0.8 \cdot 10^{-4}$, a number which is well within the design goal. Numerous nuclear studies that have been performed over the years with the spectrometer BIG KARL enriched the knowledge in this field. Even with the advent of COSY the spectrometer has not ceased to serve as an important experimental tool in future experiments.

Designing Quadrupole Magnets for COSY Using Conformal Mapping

The proton synchrotron and storage ring COSY is accelerating protons from 40 MeV at injection up to energies of 2.5 GeV. Besides a large number of quadrupoles due to the race track design with telescopic straight sections the large energy range requires large apertures of the beam pipe and, hence, large apertures of the quadrupole magnets to allow for the storage of up to 10^{11} protons at the low injection energy. In addition, one needs a very good field distribution in those magnets to obtain the best beam quality possible.

The COSY quadrupole magnets were specified to provide maximum gradients of 7.6 T/m and a good field region with a high linearity of B_y within ± 100 mm horizontally and ± 20 mm vertically, keeping within this area the cumulated multipole contribution well below a few percent. The aperture radius of the quadrupoles was chosen to be 85 mm, which means that the good field region had to extend beyond that. To limit the width of the poles and thus the cost and power requirement, these had to be supplied with appropriate longitudinal shims.

Klaus Halbach taught us that the best way to design multipole magnets with high precision is to map them into dipole geometry by means of conformal mapping, optimize the dipole and then transform back to the multipole geometry. The transformation used to map a quadrupole is:

$$z = x + iy \text{ (real geometry)} \dashrightarrow w = u + iv \text{ (dipole geometry)}$$
$$\text{with } w = 1/2r_0z^2 \quad r_0 \text{ aperture radius} \qquad (1)$$

Using this mapping technique the horizontal width of the good field region in the quadrupole is transformed to 58.8 mm in the dipole geometry. Now another principle of Klaus Halbach came into play, the design of the pole width of a dipole magnet with shims using his overhang formula:

$$\text{overhang} = \epsilon \cdot h \quad \text{with} \quad h\text{: half gap height}$$

$$\epsilon = 0.39 - 0.14 \cdot \ln(p) \qquad p = 100 \cdot \Delta B / B \qquad (2)$$

A required homogeneity for the dipole field of 10^{-4} gives an $\epsilon = 1.035$. With $h = 42.5$ mm the overhang necessary to give the desired homogeneity is 44 mm. So one ends up with the edge of the pole in dipole geometry at $w = (103.0;42.5)$ and the transformation back to quadrupole geometry yields $z = (135.0;26.7)$ for the end point of the hyperbola. Figure 11 shows a fieldline plot of the dipole geometry with a shim calculated with POISSON [7]. The corresponding transformed quadrupole computed with the same program is given in figure 12.

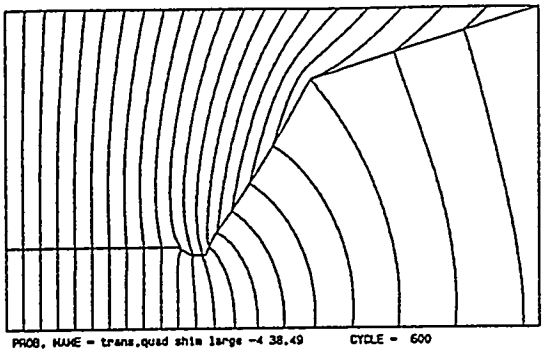

Fig. 11 Field lines in dipole geometry.

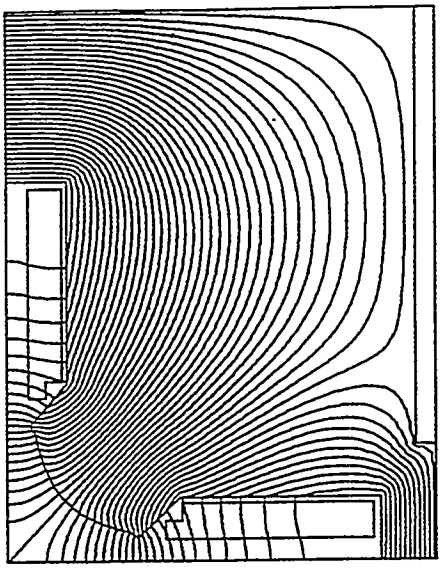

Fig. 12 Field lines in the transformed quadrupole geometry.

The COSY quads have been built with a pole contour designed that way and the field of the first prototype magnet was mapped carefully with a hall probe prior to mass production. The field map in the midplane of the quadrupole is displayed in figure 13 whereas figure 14 shows a cut through this map in the centre of the magnet. It turned out that even at a gradient of 8.4 T/m which is well above the specified value of 7.6 T/m the linearity of B_y is surprisingly good within the required horizontal range of ± 100 mm. The performance of the quadrupoles

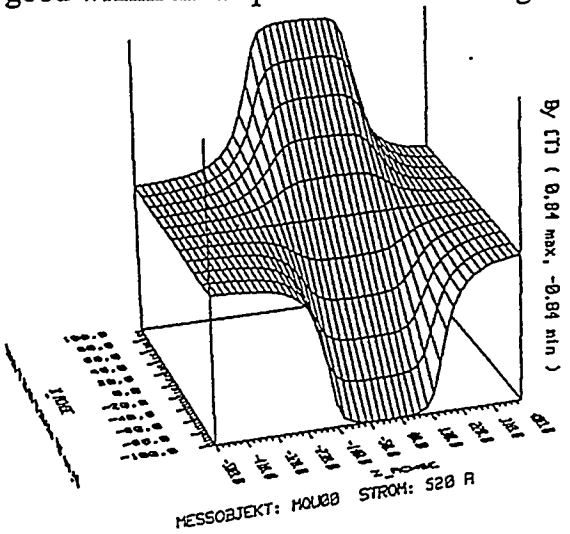

Fig. 13 Field map in the midplane of quadrupole, field gradient is 8.4 T/m.

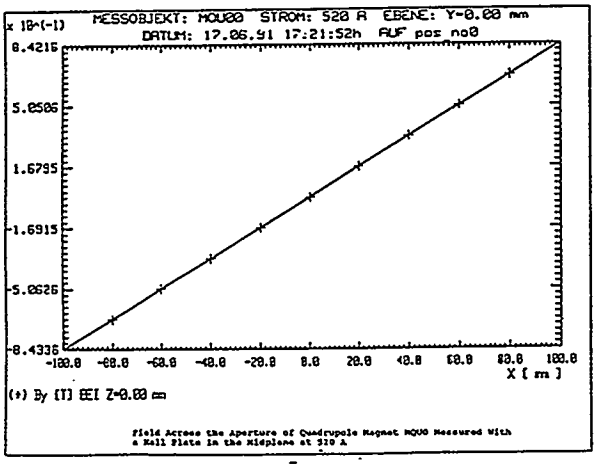

Fig. 14 B_y versus horizontal position in COSY-quadrupole, field gradient is 8.4 T/m.

designed according to the techniques sketched above yielded excellent results, so we may conclude that we followed Klaus Halbach's way and it worked.

Acknowledgement

We are surely indebted to many people who have made significant contributions to the successful completion of BIG KARL and COSY. But at this place and this time it is our wish to express foremost our deep gratitude to Klaus Halbach who has been freely sharing his knowledge and inspired us with many new ideas. He has been a good friend and mentor to many of us and certainly communicated his enthusiasm for the intricate beauty of magnets, their fields, and their applications.

References

[1] S. Martin et al., "The QQDDQ Magnet Spectrometer "BIG KARL" ",Nucl. Instr. and Meth. 214 (1983) 281.

[2] COSY-Team, "Studie zum Bau eines kombinierten Kühler-Synchrotron-Rings an der KFA Jülich, Forschungszentrum Jülich, Jül-Spez-242 (1984)
R. Maier et al., "Status of COSY", Proceedings of the Fourth European Particle Accelerator Conference, London (1994)

[3] L. Aldea et. al, Proc. 9th Int. Conf. on Cyclotrons and their Application, Caen (France).(1991) p. 103

[4] H. A. Enge and S. B. Kowalski, Proc. 3rd Int. Conf. on Magnet Technology, Hamburg (1970) p. 366

[5] K. Halbach, Nucl. Instr. and Meth. 107 (1973) 515

[6] A. Abdel-Gawad, "Untersuchung zu Bau eines hochauflösenden Magnetspektrometers und Modellmessungen zur Wirkungsweise von Feldkorrekturströmen in Eisen", Forschungszentrum Jülich, Jül-1329 (1976)

[7] A.M. Winslow,"Numerical Solution of the Quasilinear Poisson Equation in a Nonuniform Triangle Mesh", Journal of Computational Physics, Vol. I (1966) 149

[8] W. Hürlimann, Dissertation, Jül-Spez. 104, Forschungszentrum Jülich (1981)

[9] K.L. Brown and S.K. Howry, Stanford Linear Accelerator Center, SLAC-91 (1970), NAL-91 (1973)

[10] G.P.A. Berg et al.,Proc. Int. Conf. on Spin Excitations in Nuclei, Telluride (1982)

Calculated and Measured Fields in Superferric Wiggler Magnets

Eric B. Blum and Lorraine Solomon
National Synchrotron Light Source
Brookhaven National Laboratory
Upton, New York 11973

Introduction

Although Klaus Halbach is widely known and appreciated as the originator of the computer program POISSON for electromagnetic field calculation, Klaus has always believed that analytical methods can give much more insight into the performance of a magnet than numerical simulation. Analytical approximations readily show how the different aspects of a magnet's design such as pole dimensions, current, and coil configuration contribute to the performance. These methods yield accuracies of better than 10%. Analytical methods should therefore be used when conceptualizing a magnet design. Computer analysis can then be used for refinement.

A simple model is presented for the peak on-axis field of an electromagnetic wiggler with iron poles and superconducting coils. The model is applied to the radiator section of the superconducting wiggler for the BNL Harmonic Generation Free Electron Laser. The predictions of the model are compared to the measured field and the results from POISSON.

Superconducting Magnet Design and Measurement

The undulator magnet described here is the radiator stage of a three stage (modulator, dispersive, and radiator) superconducting undulator, presently under construction at the National Synchrotron Light Source for use at the Accelerator Test Facility.[1] The undulator will be used in a high-gain, harmonic generation FEL experiment, and triples the input frequency of a 10.4 μm CO_2 seed laser with a 30 MeV electron beam. The modulator stage (12 periods of 26 mm, 0.81 Tesla) modulates the electron beam energy, the tunable dispersive section (12 cm long, 0.3–1.2 Tesla) converts this energy bunching into spatial bunching, and the radiator (84 periods of 18 mm, 0.54 Tesla) extracts the energy in the beam. The strength of the magnetic field is tapered along the length of the radiator by reducing the magnet current.

The magnet yokes for all three stages of the undulator are machined out of ground, low carbon steel blocks. The magnet design for all three stages is very similar. Here we will restrict the discussion to the radiator magnet

shown in fig. 1. It is made of six contiguous 25 cm long sections, each consisting of an upper and lower magnet yoke. A series of 28 slots is precision machined to ±10 μm tolerance into the 25 cm long yokes. Kapton wrapped superconducting wire is wound within these slots. This tolerance results in peak field variations on the order of ±0.1% when the magnetic field in the iron is not saturated. These field errors increase with saturation, but level off at about 0.35%. The increase in error with excitation is likely due to inhomogeneities in the iron. As the iron saturates and its permeability decreases, the contribution of coil placement errors to the peak field errors increases. The radiator magnets exhibit no training, and the quench current of 180 A is significantly higher than the 90 A operational current.

The main magnet winding is continuous, with each slot wound in the reverse direction from its neighbors. The pole faces of the radiator sections are parabolically shaped for transverse focusing (fig. 1). For the results described here the magnet gap in the flat region of the poles is 6 mm, making the maximum gap in the curved region 8 mm. In addition to the main magnet winding, there are trim windings on both ends of each yoke to control the entrance and exit beam trajectory. The winding scheme of the radiator magnets permits field tapering while allowing sorting and interchangeability between the

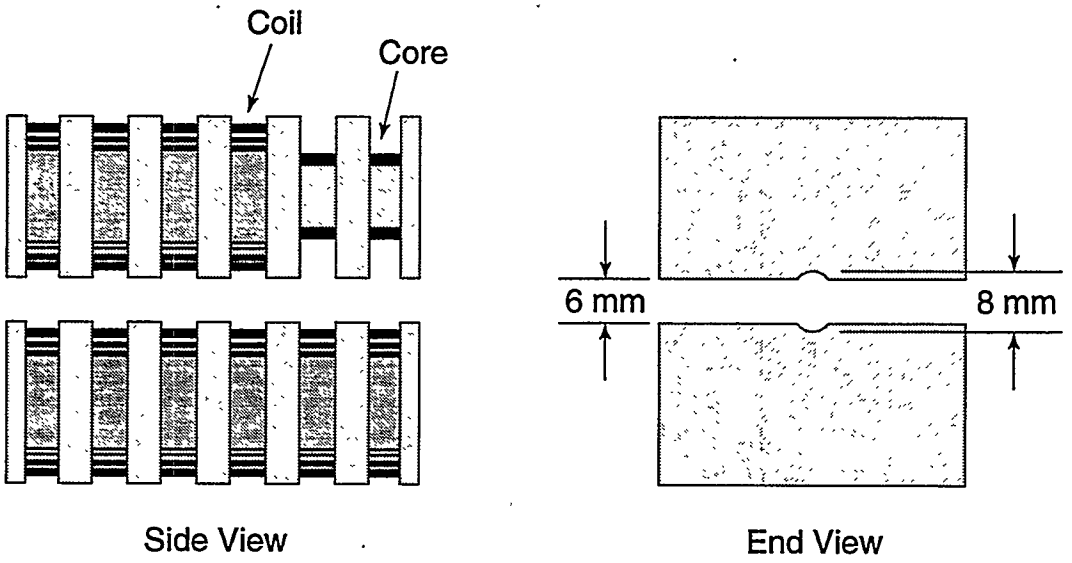

Fig. 1. Simplified drawing of the iron yokes and superconducting coils from the harmonic generation wiggler magnet. Only 7 poles are shown although the actual magnet has 29. Two of the coils are omitted from the drawing of the upper yoke to show the central core. The poles at each end are half-thickness.

various magnet sections. The radiator magnets are wound with a binomial current pattern[2] which nominally results in a net displacement but no steering, in the absence of saturation.

The full length magnet is housed in a 2.5 m long cryostat. The magnet structure is of the cold bore, cold yoke type, and is cooled by pool boiling helium at 4.4 K. Electron strip line monitors are located at the entrance and exit of the cold mass assembly.

The radiator magnets are tested in 50 cm long units. The magnet gap is set by a precision ground spacer. A Hall probe array is guided by the spacer. An in-situ Helmholtz coil permits Hall probe calibrations during testing at cryogenic temperatures, a necessary feature for analysis. The Hall probe array position is computer driven. Measurements are taken as a function of magnet excitation current. The first and second field integrals are used to determine the trim currents required for minimal beam steering.

Theory

We present a simple 2D analytical model for the peak on-axis field B_0 of a superconducting electromagnetic wiggler magnet with iron poles. The current dependence of the field is well described by its behavior in two limiting cases. At low current we assume that the iron is infinitely permeable. Using a model first presented by Klaus Halbach in 1986[3], we calculate B_0 as well as the maximum field in the pole B_M as functions of the current through the coil I. When B_M reaches B_S, the saturation induction of the iron, we assume that the iron is totally saturated and makes no additional contribution to the magnetic field. Above this point we model the wiggler as an air core magnet made from superconducting coils with an additional, constant contribution due to the field from the saturated poles. From the two limiting cases we obtain a piecewise, linear model of the on-axis field versus current with a change in slope at the point where the iron saturates.

Only the upper half of a quarter period section, illustrated schematically in fig. 2, is needed to model the properties of the periodic structure of the wiggler. Half of a coil of full width D_1 and half of an iron pole of full width W are shown. The period of the magnet is

$$\lambda = 2(W + D_1). \tag{1}$$

The half-gap of the magnet is called h.

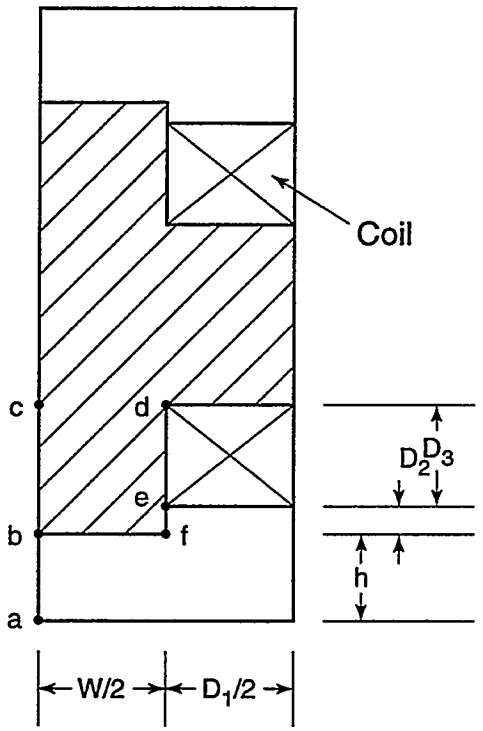

Fig. 2. Quarter period cross-section of the upper pole of the wiggler showing the dimensions used in the calculations.

By Ampere's law, the pole tip field is related to the current in the coil I by the expression

$$B_0 = \frac{\mu_0 NI}{2hf_1} \tag{2}$$

where N is the number of turns in the coil. The factor

$$f_1 = \frac{\int_0^h B_y dy}{B_0 h} > 1 \tag{3}$$

accounts for the increase in field from the midplane to the pole. The integral is evaluated along the line a b in fig. 2 . It can either be found analytically or from a single POISSON run with infinitely permeable iron and arbitrary current.

Except for the enhancement at the sharp outside corner, the highest field in the iron is along line c d . The flux through c d is

$$\overline{B}W = B_0 W f_2 + \mu_0 NI \frac{D_2}{D_1} f_3 + \tfrac{1}{2}\mu_0 NI \frac{D_3}{D_1}, \tag{4}$$

where $\overline{B}$ is the average field along the line. The terms on the R.H.S of eqn. (4) represents the flux through b f, f e, and e d, respectively. A linear increase in field along e d is assumed. The numbers f_2 and f_3 are greater than 1 and account for the excess flux at the sharp corner of the pole. They can be defined and evaluated as described for f_1 in eqn. (3).

We say that the iron is completely saturated when $\overline{B} = B_S$, the saturation inductance. Substituting eqn. (2) for B_0 in eqn. (4), and solving for I, we predict that the magnet will saturate at a current

$$I_S = \frac{2B_S W}{\mu_0 N\left(\frac{W}{h}\frac{f_2}{f_1} + 2\frac{D_2}{D_1}f_3 + \frac{D_3}{D_1}\right)}. \tag{5}$$

The magnetic field at saturation $B_{0,S}$ is found by substituting this result into eqn. (2).

At currents above I_S, the maximum midplane field is

$$B_0 = B_{0,S} + B_{0,coil}\,, \tag{6}$$

where the first term on the R.H.S. is the contribution from the saturated iron and the second is from the coils alone. Although we can calculate the field due to the magnet coils from first principles we instead use Klaus Halbach's results for pure permanent magnet wigglers.[4] Klaus has shown that magnetic materials like samarium cobalt and neodymium-iron-boron can be modeled by current sheets and calls them "current sheet equivalent materials" (CSEM). Consequently, we model the coils by permanent magnet blocks with a remanent field

$$B_r = \mu_0 N(I - I_S)/D_1, \tag{7}$$

and use Klaus' formulas for the magnetic field of a pure CSEM wiggler:

$$B^*(z) = 2iB_r \sum_{\nu=0} \cos(nkz)\,e^{-nkh'}\left(1 - e^{-nkL}\right)\sin(n\varepsilon\pi / M')/(n\pi / M'), \tag{8}$$

where, referring to fig. 3,

$$z = x + iy, \tag{9}$$

$$B^* = B_x - iB_y, \tag{10}$$

$$n = 1 + \nu M', \tag{11}$$

$$k = 2\pi / \lambda, \tag{12}$$

and M' is the number of blocks per half period of the wiggler. In our case, $M' = 2$,

$$h' = h + D_2, \tag{13}$$

and

$$\varepsilon = 2D_1 / \lambda. \tag{14}$$

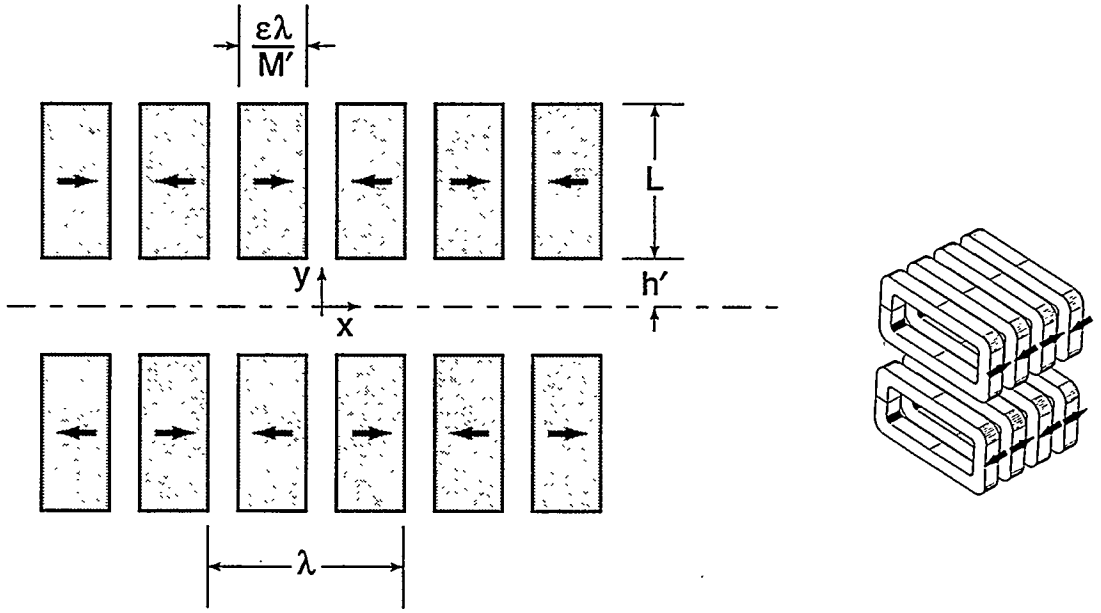

Fig. 3. Arrangement of CSEM blocks used in the unit permeability model of the wiggler. The inset drawing shows the wiggler coils with arrows indicating the equivalent remanent field direction.

We find $B_{0,coil}$ by evaluating eqn. (8) at $x=y=0$. Retaining only the first term in the expansion and substituting in eqn. (7) we find that in the unit permeability limit, the maximum midplane field is

$$B_0 = B_{0,S} + \frac{4\mu_0 N}{\pi D_1}(I - I_S)e^{-kh'}\left(1 - e^{-kL}\right)\sin(\varepsilon\pi/2). \tag{15}$$

We have now developed a piecewise linear model of the peak midplane field of the wiggler magnet. Eqn. (2) shows the behavior below I_S and eqn. (15) shows the behavior at higher currents. We will apply this model to the harmonic generation wiggler magnet in the next section and compare it to the POISSON and experimental results.

Harmonic Generation Wiggler Results

Table 1 lists the dimensions of the harmonic generation wiggler that we used in the model. The half gap h is the distance from the midplane to the top of the recess in the pole shown in the end view in fig. 1. The values of the correction factors f_1, f_2, and f_3, were obtained from the POISSON calculations described. The saturation induction B_S was set to 1.8 T based on our experience with similar calculations for other types of iron core magnets.

Table 1

Data and Results From The Harmonic Generation Wiggler Calculation

l (mm)	18.04
h (mm)	4.00
W (mm)	4.52
D_1 (mm)	4.50
D_2 (mm)	1.13
D_3 (mm)	3.21
L (mm)	17.2
N	68
B_S (T)	1.8
f_1	1.24
f_2	2.07
f_3	1.32
I_S (A)	48.5
$B_{0,S}$ (T)	0.418

Fig. 4 compares the results from the model with the measured data for the magnet and with a POISSON calculation for the geometry pictured in fig. 3 using the dimensions in Table 1. The agreement between the two-limit model and POISSON calculations is better than 4% at all currents. Both do an excellent job of predicting the measured data (better than 3%) when the iron is fully saturated (above 50 A). At low currents, when the magnetic field is dominated by the iron, both the model and the POISSON results show the general performance of the magnet but differ from the measured results by as much as 20%. This is because the 2D geometry of both POISSON and the model can not fully account for the curved pole surface of the magnet. Nevertheless, the model and the POISSON predictions are equally accurate in this range.

Examining the assumption of a 1.8 T maximum field in the iron at saturation, we see, surprisingly, that POISSON predicts greater than 2 T at the top of the pole at $I_S = 48.5$ A. Although the model predicts the dependence of B_0 on current as well as POISSON, it does not accurately predict the fields in the iron. It is possible that extending the model to finite permeability of the iron may improve this but because we are interested in the field in the magnet gap we have not done so.

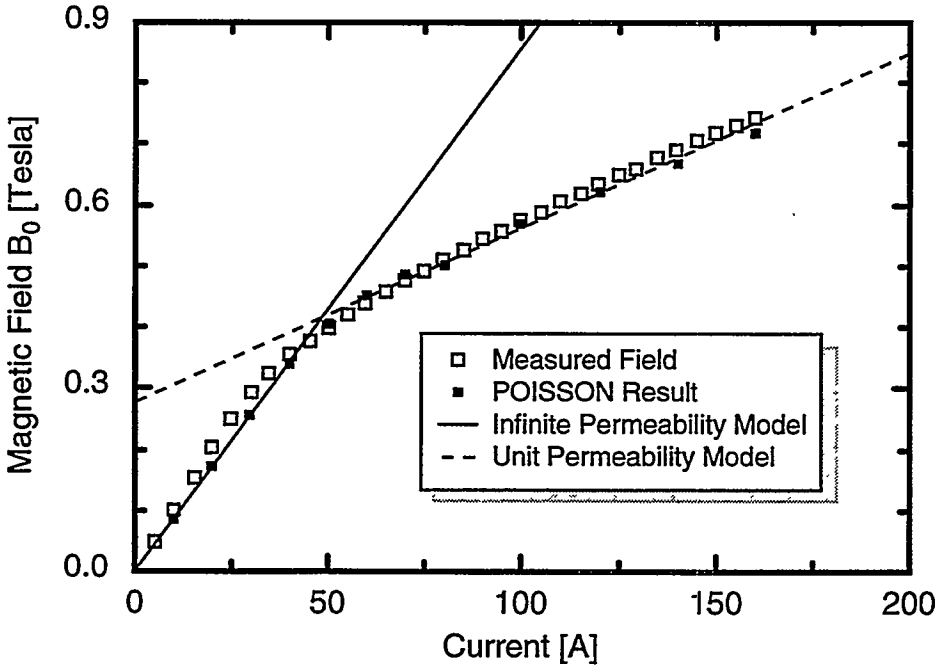

Fig. 4. Comparison of model and POISSON results with measured field.

Conclusions

We have presented a simple, straightforward analysis of the peak mid-plane field of a superferric wiggler magnet as a function of the current in the magnet coils. The model is just as accurate as POISSON in predicting the performance of the BNL harmonic generation wiggler magnet. The analytic formulation of the model make it easy to see the effect of the varying magnet dimensions on performance. By comparison, a series of POISSON runs is needed to evaluate each change in geometry.

Acknowledgments

First and foremost, we thank Klaus Halbach for his reviews and discussions of the harmonic generation wiggler. Klaus also suggested the two-limit model in a casual conversation with one of the authors (E.B.). This paper would never have been written without him.

The harmonic generation wiggler magnet and cryostat were built by Grumman Corporation. Their work is greatly appreciated. We also thank Gerhard Ingold, William Graves, and the NSLS staff for assistance with testing and measurements.

This work was performed under the auspices of the U.S. Department of Energy, under contract DE-AC02-76CH00016.

References

1. L.H. Yu, *Phys. Rev A* **99** (1991) 5178;
I. Ben-Zvi, et. al., *Nucl. Inst. and Meth. in Phys. Res.* **A318** (1992) 208;
G. Ingold, et. al., *Proc. 1993 Particle Accelerator Conference* , 1439;
L. Solomon, W.S. Graves, and I. Lehrman, *Proc. 1994 FEL Conference.*

2. K. Halbach, *Nucl. Inst. and Meth. in Phys. Res.* **A250** (1986) 95.

3. K. Halbach, *Nucl. Inst. and Meth. in Phys. Res.* **A250** (1986), 115.

4. K. Halbach, *Nucl. Inst. and Meth.* **169** (1980), 1.

Comparison Of Conventional and Novel Quadrupole Drift Tube Magnets Inspired by Klaus Halbach

Ben Feinberg
Lawrence Berkeley Laboratory
University of California
Berkeley, CA 94720

Abstract

Quadrupole drift tube magnets for a heavy-ion linac provide a demanding application of magnet technology. A comparison is made of three different solutions to the problem of providing an adjustable high-field-strength quadrupole magnet in a small volume. A conventional tape-wound electromagnet quadrupole magnet (conventional) is compared with an adjustable permanent-magnet/iron quadrupole magnet (hybrid) and a laced permanent-magnet/iron/electromagnet (laced). Data is presented from magnets constructed for the SuperHILAC heavy-ion linear accelerator, and conclusions are drawn for various applications.

Introduction

A number of constraints make the design and construction of quadrupole drift tube magnets for a heavy-ion linac a demanding application of magnet technology. The available space is severely limited by the size of the drift tubes, and the magnets must be cooled to dissipate the strong radio-frequency (RF) heating as well as the heat generated by the energizing current (if any). In addition, for a heavy-ion linac where many different ions (with different charge-to-mass ratios) must be accelerated, the focusing field strength must be variable and the maximum field gradient as high as possible.

The initial solution to this problem was the development of the tape-wound quadrupole electromagnet, which maximizes the volume of copper and relies on edge cooling.[1] The next solution investigated was the hybrid adjustable quadrupole, which energizes conventional iron pole-pieces with sets of stationary and rotatable permanent magnets rather than a coil.[2] The third solution, the laced quadrupole, uses unconventional iron pole-pieces energized by a tape-wound coil, and introduces permanent-magnet material to reduce the level of saturation in the pole-pieces, thus achieving higher fields.[3] The pros and cons of each choice will be presented, backed by data from actual magnets.

Magnet Principles

The basic features of the conventional tape-wound magnet are shown in Figure 1. The coil consists of two layers of copper tape, cut as shown in Figure 2, and wound circumferentially about the magnet with insulation between the layers. The arrows show the current path, which forms closed loops about each pole-piece, thus producing a quadrupole field. The coil fills the annular region between the flux return yoke and the beam tube, maximizing the amount of copper to carry current. It is potted in high-temperature epoxy, and freon is pumped around the edges of the magnets, cooling the coil from the edges in. This cooling method limits the axial length of the quadrupoles, since the heat must be removed by conduction to the edge of the coil. Note that the coil surrounds the pole pieces along almost the entire radial extent, thus limiting the axial length of the poletips.

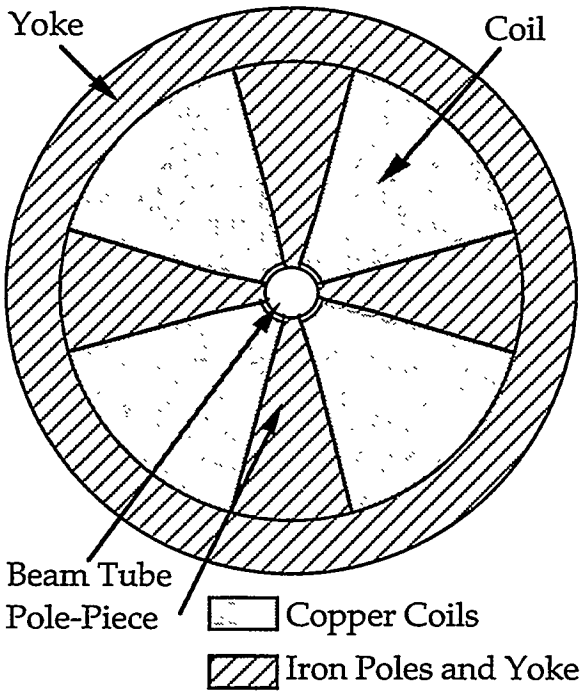

Figure 1—Schematic of the conventional tape-wound quadrupole. The poles determine the shape of the magnetic field and are energized by the copper coils. The return flux is carried by the iron yoke.

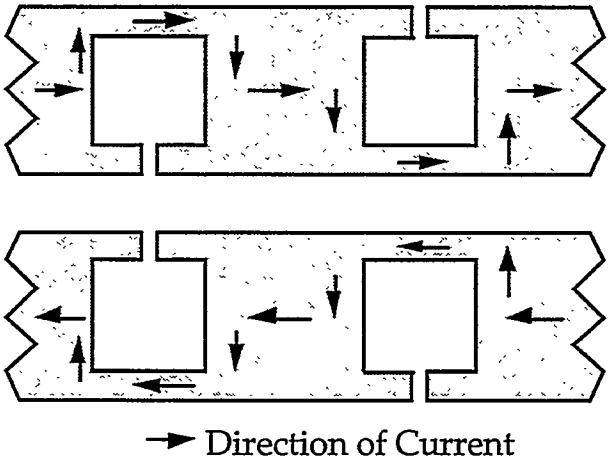

Figure 2—Diagram of the bi-filar windings forming the coil of the tape-wound quadrupole. The current forms a closed loop, of the correct polarity for a quadrupole, around each of the magnet poles.

The hybrid quadrupole magnet is shown in Figure 3. This magnet relies on permanent magnets (samarium cobalt) to energize the poles, which provide the requisite quadrupole shape. Each pole is surrounded by fixed permanent magnets which either add or subtract flux. On the outer circumference, a rotatable iron ring has permanent magnets attached to its inner surface. Rotating this ring either adds to the flux in each pole, or subtracts from the flux, thus providing adjustability. In this magnet, cooling is only needed to remove the heat generated by the strong RF fields, since there are no electromagnet coils.

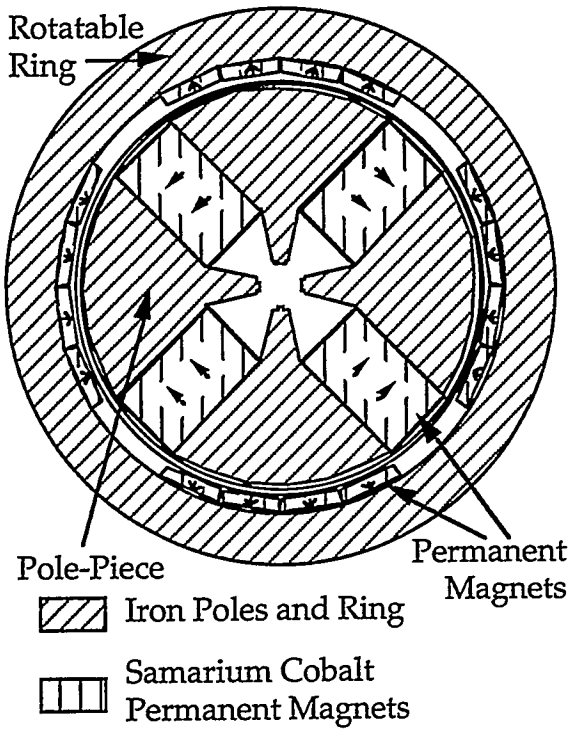

Figure 3—Schematic of the hybrid rotatable quadrupole magnet. The permanent magnets in the interior energize the pole-pieces, while the magnets attached to the outer iron rings rotate to adjust the strength of the magnetic field. Note that there are actually two axially separated outer rings (only one of which is shown), rotating in opposite directions, to ensure that no net torque is introduced.

The third type of magnet to be described, the laced quadrupole, is shown in Figure 4. This magnet is basically a conventional tape-wound quadrupole, with permanent magnets added between the poles to reduce the flux in the iron. The flux added by the permanent magnets is carried by a closed path in the iron; it does not add to the field in the gap. The reduction of flux in the poles, however, allows a longer pole tip than in a conventional quadrupole, and also for a reduction in the cross-sectional area of the poles. More copper can thus be added to each turn (see the thin area above or below each pole in Figure 3), allowing the current to be increased. These two effects, the longer pole tip and the higher current, both add to the focusing strength, which is the product of the field gradient and the effective length.

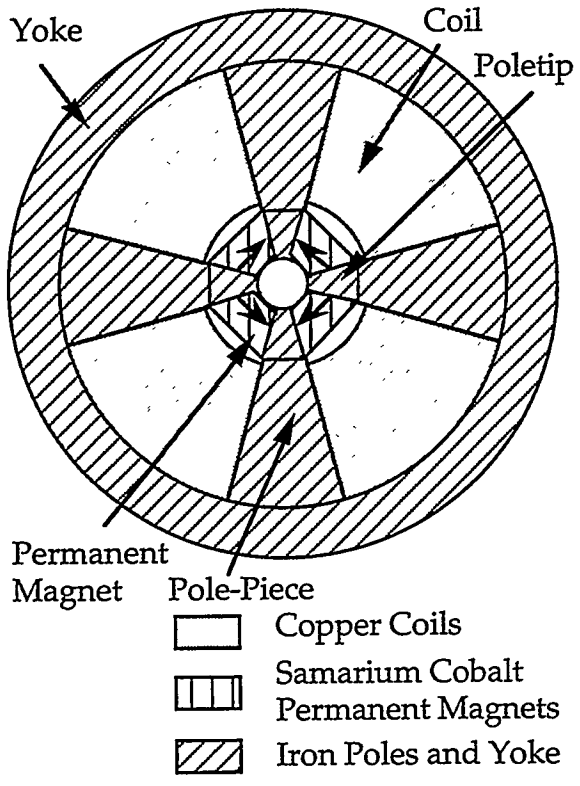

Figure 4—Schematic of the laced quadrupole. The permanent magnets reduce the flux in the poles by adding flux to oppose the flux generated by the coils. Note that the flux generated by the permanent magnets remains entirely in the iron, and makes no contribution to the field in the gap.

Measurements

Conventional drift-tube quadrupoles have been used in the SuperHILAC heavy-ion linear accelerator at Lawrence Berkeley Laboratory for many years. The magnets in the upstream section of the accelerator (prestripper) have been divided into six groups. The members of each group all have the same dimensions, with only the axial length of the drift tube shell increasing downstream along the axis of the accelerator. Failures were observed in the larger magnets in the prestripper, due to overheating of the epoxy potting. A hybrid quadrupole was constructed as a proof-of-principle replacement magnet. This magnet was the size of the largest group to test the forces required to rotate the adjusting rings. Figure 5 shows a comparison between a conventional magnet and the proof-of-principle hybrid magnet.

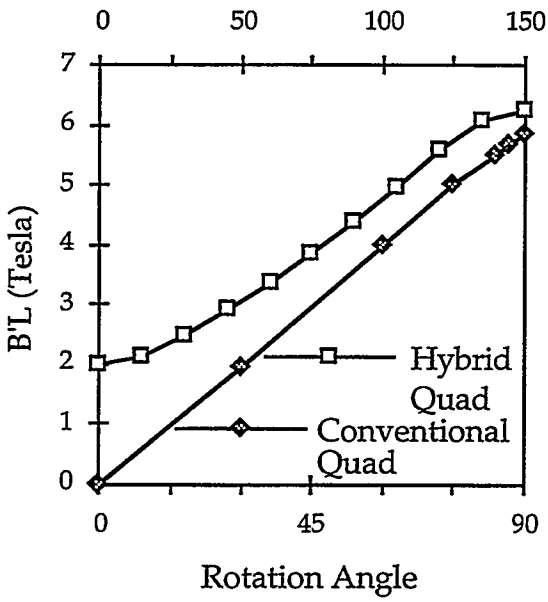

Figure 5—Comparison of the hybrid quadrupole with the conventional tape-wound quadrupole. The hybrid quadrupole was not fully optimized to maximize the field strength.

Note that the hybrid magnet field strength is adjustable over a factor of three, with a long linear section in the middle of the range, providing the needed adjustment for accelerating various heavy ions. While the hybrid quadrupole shows only a 7% increase in focusing strength over the conventional quadrupole, this proof-of-principle magnet was designed to test the mechanical arrangement and was not optimized for the highest possible strength. Since the reliability of the hybrid quadrupole depends on the mechanical arrangement for rotation, the magnet was cycled repeatedly for 105,000 cycles to test its reliability. No problems with the mechanical system were found during or after this test.

Figure 6 shows the comparison between a conventional magnet and the laced quadrupole. Twenty-three of these laced quadrupoles were constructed to replace the smallest two groups of magnets in the prestripper of the SuperHILAC. These groups were chosen because they have the smallest aperture, and thus the beam transmission is enhanced the most by the higher focusing strength available from the laced quadrupoles. As seen, the magnets deliver about a 20% increase in maximum focusing strength, which improves the transmission of the heaviest ions by up to a factor of two.

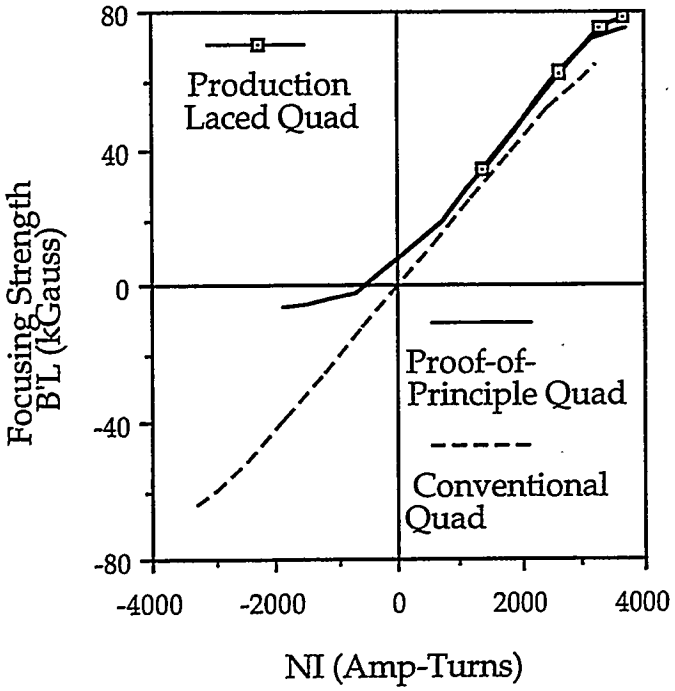

Figure 6—Comparison of the laced quadrupole with the conventional tape-wound quadrupole. The production laced quadrupole was optimized to increase the field strength.

Another point of comparison are the error fields for each type of quadrupole. Figure 7 presents the magnitude of the first harmonic, n = 3, as a percentage of the fundamental, graphed as a function of field strength. In both the laced and the hybrid quads errors due to unequal excitation of opposite poles introduce odd harmonics, that are usually avoided in the conventional quadrupole by wrapping the poles in equal numbers of turns connected in series. Note that the magnets demonstrate a sextupole error field of less than 0.36% This is acceptable for a quadrupole in the heavy-ion linac, where the specifications called for errors less than 0.5% for any one harmonic, and less than 1% overall. As can be seen from the Figure, the error fields are relatively insensitive to the exact type of magnet. They are more dependent on the fabrication of the poles and the sorting of the permanent magnet blocks for the hybrid and the laced quadrupoles.

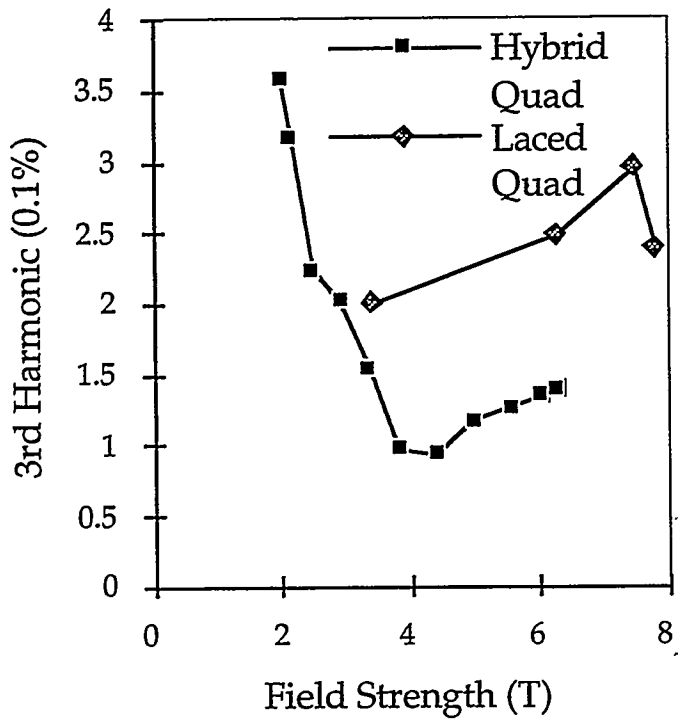

Figure 7—Graph of the ratio of the third harmonic multipole to the fundamental as a function of the field strength.

Discussion

Both the laced quadrupole and the hybrid quadrupole form more powerful alternatives to the conventional quadrupole for the heavy-ion linac drift tube magnets. When optimized for focusing strength, each is capable of approximately a 20% increase in strength compared to the tape-wound quadrupole. A point that should be noted, however, is that each of these quadrupoles using permanent magnets is polarized; the polarity is fixed upon construction and cannot be reversed by changing the polarity of the power supply, as with a tape-wound quadrupole. If the polarity cannot be specified in advance, the tape-wound quadrupole may offer a more flexible, but weaker focusing strength, option. The hybrid quadrupole utilizes a mechanical rotation system, requiring a motor with appropriate controls, while the laced quadrupole requires a power supply, enhanced cooling, and controls similar to that required by the conventional tape-wound quadrupole. In the case of the SuperHILAC prestripper, the availability of the existing magnet power supplies, control system, and cooling system strongly favored the use of the laced quadrupole as a replacement for the conventional quadrupole, since no new motors or controls would be required. If a new heavy-ion linac were to be constructed, the relative construction and operating costs of each solution would need to be carefully weighed.

Conclusion

The laced quadrupole and the hybrid quadrupole provide acceptable replacements for the conventional tape-wound drift tube quadrupole where focusing strength and adjustability are required. The choice of the technology will generally be driven by the compatibility and cost of the control and adjustment system, since the performance of each magnet is similar. Each performs significantly better than the tape-wound quadrupole, and each should therefore be considered in the construction of a heavy-ion linac.

---

[1] Robert M. Main, Klaus Halbach, Patrick Kennedy, Roland Yourd, Albert Watanabe, and Daniel Kolody, "High Gradient Magnetic Drift Tube Quadrupoles", 1968 Proton Linear Accelerator Conference Proceedings, May 1968, BNL 50120 (C-54), 52 (1968).

[2] K. Halbach, "Conceptual Design of a Permanent Quadrupole Magnet with Adjustable Strength", Nuclear Instruments and Methods, **206**, 353 (1983); B. Feinberg, J. Tanabe, K. Halbach, G. Koehler, and M.I. Green, "Adjustable Rare Earth Quadrupole Drift Tube Magnets", 1987 Particle Accelerator Conference Proceedings, March 1987, IEEE 87CH2387-9, Vol. 3, 1419 (1987).

[3] K. Halbach, "Magnet Innovations for Linacs", 1986 Linear Accelerator Conference Proceedings, June 1986, SLAC-Report-303, 407 (1986); B. Feinberg, G.U. Behrsing, K. Halbach, J.S. Marks, M.E. Morrison, and D.H. Nelson, "Laced Permanent Magnet Quadrupole Drift Tube Magnets", 1989 Particle Accelerator Conference Proceedings, March 1987, IEEE 89CH2669-0, Vol. 1, 375 (1989).

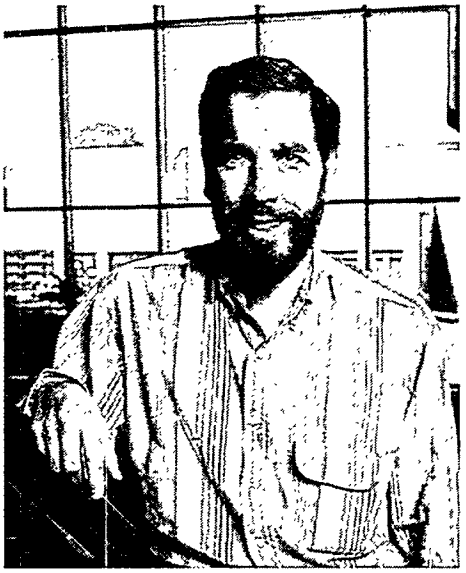

Concept of Quasi-Periodic Undulator
- Control of Radiation Spectrum -

Shigemi Sasaki
Department of Synchrotron Radiation Facility Project
Japan Atomic Energy Research Institute
Tokai-mura, Naka-gun, Ibaraki 319-11, Japan

A new type of undulator, the quasi-periodic undulator (QPU) is considered which generates the irrational harmonics in the radiation spectrum. This undulator consists of the arrays of magnet blocks aligned in a quasi-periodic order, and consequentially lead to a quasi-periodic motion of electron.

A combination of the QPU and a conventional crystal/grating monochromator provides pure monochromatic photon beam for synchrotron radiation users because the irrational harmonics do not be diffracted in the same direction by a monochromator.
The radiation power and width of each radiation peak emitted from this undulator are expected to be comparable with those of the conventional periodic undulator .

Introduction

Conventional undulators which have ever been built have periodic magnetic structures so that the relativistic electrons have sinusoidal orbit in the device to emit sharply peaked radiation. The motion of electrons in an undulator leads to a generation of rational harmonics of radiation such as the third and fifth harmonics in addition to the fundamental radiation unless the deflection parameter K is infinitesimally small.

For many user's experiments, monochromatic radiation from an undulator is very useful, however a mixing of the higher harmonics is not welcome because it causes a increment of noise ratio. The higher harmonics of radiation are usually removed by using a total reflection mirror which absorbs the radiation above the critical energy at a given reflection angle. The other way to remove the higher harmonics is to detune a double crystal monochromator so as to utilize the wider Darwin width of the fundamental reflection. However, these conventional techniques are somewhat difficult to use in the hard x-ray region because of a very small critical angle of total reflection and a very narrow Darwin width even for the fundamental radiation.

Recently, an undulator which suppresses higher harmonics by introducing intentional phase error in periodic structure or by adding a horizontal magnetic field has been proposed in order to avoid the higher harmonic contamination.[1-4] From a different viewpoint , we proposed a new type of undulator which never generates the rational higher harmonics but generates the irrational ones.[5,6]

The idea came up from an analogy between an equation of x-ray scattering by matter and that of synchrotron radiation. The intensity of x-ray diffracted by a one-dimensional scatterer is [7]:

$$I(q) = \left| \int_{-\infty}^{\infty} \rho(r) \exp(-2\pi i q r)\, \mathrm{d}r \right|^2 , \tag{1}$$

where $\rho(r)$ electron density of scatterer. On the other hand, the spectral angular intensity distribution of synchrotron radiation is [8]:

$$\frac{\mathrm{d}^2 I}{\mathrm{d}f\, \mathrm{d}\Omega} = \left| \int_{-\infty}^{\infty} F(r_\mathrm{n}) \exp\{-2\pi i (f/c) r_\mathrm{n}\}\, \mathrm{d}r_\mathrm{n} \right|^2 , \tag{2a}$$

$$F(r_\mathrm{n}) = \left(\frac{[\mathbf{n} \times (\mathbf{n} - \dot{\mathbf{r}}/c) \times \ddot{\mathbf{r}}/c\,]}{\dot{r}_\mathrm{n}(1 - \dot{r}_\mathrm{n}/c)^2} \right) \exp(2\pi i f t) , \tag{2b}$$

$$r_\mathrm{n} = \mathbf{n} \cdot \mathbf{r}. \tag{2c}$$

Here, we neglected the coefficient for simplicity.

As we see above, equations (1) and (2a) have the same form. Therefore, we realize that we can treat the radiation from a quasi-periodic undulator as the same manner with the diffraction from one-dimensional quasi-crystal.

Creation of quasi-periodicity

One of the ways for creating a one-dimensional quasi-periodic lattice is to project the two-dimensional periodic lattice points in a window onto a line inclined with an irrational gradient against an axis of two-dimensional lattice. Figure 1 shows an example of the two-dimensional square lattice with the nearest neighbor distance of a, in which open and full circles refer to the scattering centers of positive and negative contribution for x-ray or electron, respectively. Then, we draw a line through the origin with an irrational gradient of $\tan\alpha$ with respect to the x-axis.

In order to produce a quasi-periodic array of scattering centers, we next draw a window AA'BB' inclined with the slope of $\tan\alpha$ as shown in Fig. 1.

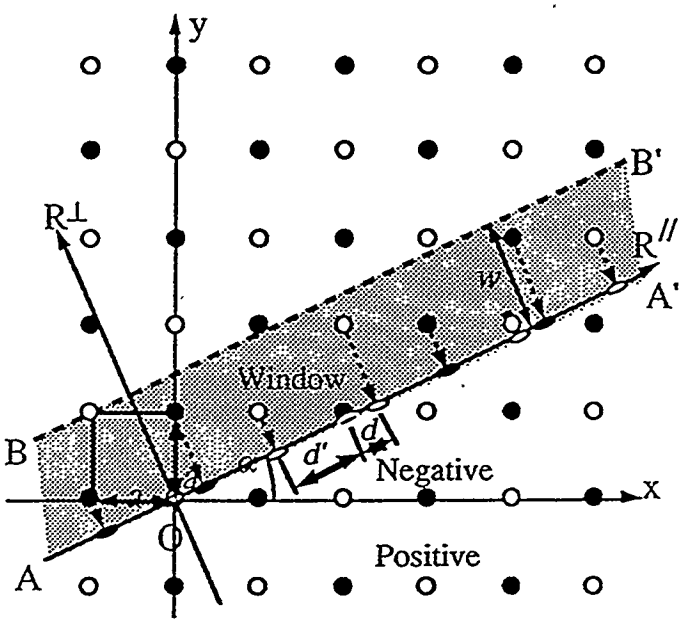

Fig. 1 Creation of one-dimensional quasi-periodic lattice from a 2D square lattice consists of positive and negative scattering centers. A quasi-periodic 1D lattice is created on the AA' line.

In this example, we selected an irrational inclination of $\tan\alpha=1/\sqrt{5}$. Then, we project the lattice points contained in the window onto the inclined axis AA'(hereafter we refer to this axis as R//). From Fig. 1, we find intuitively that the points projected onto R// have coordinates of (R_i//, 0)'s with two kinds of inter-site distances, $d=a\sin\alpha$ and $d'=a\cos\alpha$ having a ratio of

$$\frac{d'}{d}=\frac{1}{\tan\alpha} \tag{3}$$

The points are aligned in an aperiodic fashion defined by

$$R_i^{//} = ia\cos\alpha + a\,(\sin\alpha-\cos\alpha)\left[\frac{i\tan\alpha}{1+\tan\alpha}+1\right] \tag{4}$$

for the ith point, where [z] stands for the greatest integer less than z.

As we realize from equations (1) and (2), the intensity in each equation is given by the square of the Fourier transform of the function $\rho(r)$ or $F(r_n)$. Therefore, the intensity distribution in q-space (reciprocal space) or in f-space (frequency space) is determined in a simple way by assuming the position of +/- scatterer described in eq. (4). Figures 2(a) and (b) show the Fourier transform of the structure in Fig. 1 and the intensity distribution as a function of q.

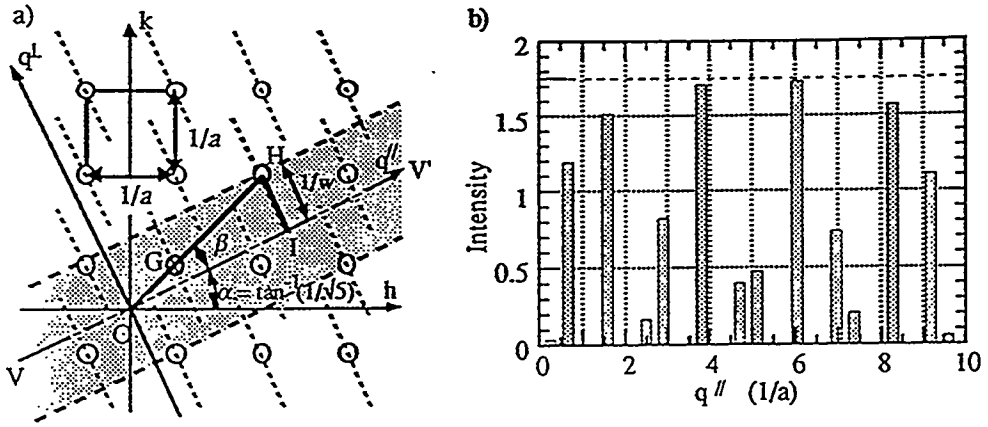

Fig. 2(a) Fourier transform of the structure described in Fig. 1, and (b) the intensity distribution along the line VV' ($q^{//}$-axis).

Real magnet configuration of QPU

Figure 3 shows the example of a part of the QPU magnet structure. Arrows in the magnet blocks represent the directions of magnetization. A magnet block isolated from its neighbors is thinner by a factor of 0.7 to reduce the strength of the on-axis magnetic field to the same magnitude as the other non-isolated regular magnet blocks. The magnets at the most left end and those at the most right end (which are not shown in Fig. 3) are thinner by a factor of 0.65 for the purpose of the end correction. In this example, we chose $\sqrt{5}$ for an irrational number (and consequently $d'/d=\sqrt{5}$) in order to avoid including rational harmonics in the spectrum. The order of magnet alignment was determined by eq. (4).

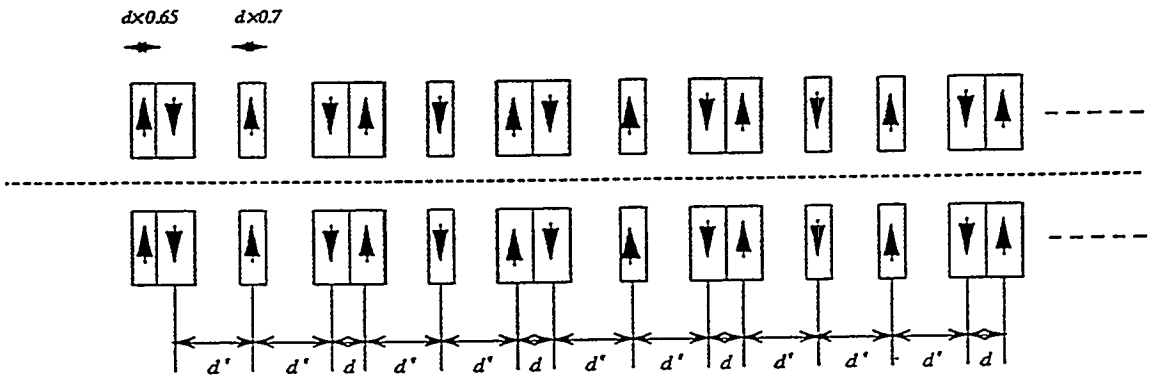

Fig. 3 Magnetic structure of QPU. An arrow in each magnet block represents the direction of magnetization. The magnets in a row are aligned in a quasi-periodic order. $d'/d=\sqrt{5}$.

Spectral radiation from QPU

We calculated the spectral angular power density emitted from the QPU in Fig. 3 by using eq. (2). The number of magnetic poles was set to be 100 including both end-magnets and the total length about 3.8 m. The inter-pole distances d and d' were 20.41 mm and 45.64 mm, respectively. Figure 4(a) shows the radiation spectrum at the gap of 30 mm. Broken lines indicate the positions of fundamental, third and fifth harmonics of corresponding periodic undulator with the same number of poles and the same length. As we clearly see in this figure, there is no rational harmonic peak.

Radiation spectrum from a conventional periodic undulator is shown in Fig. 4(b) for the sake of comparison. This undulator gives an energy of fundamental peak similar to the lowest energy of radiation peak from QPU. By comparing Figure 4(a) with Figure 4(b), we can see that there is no notable difference between two devices in respect to the peak heights and the widths except the irrationality in peak positions.

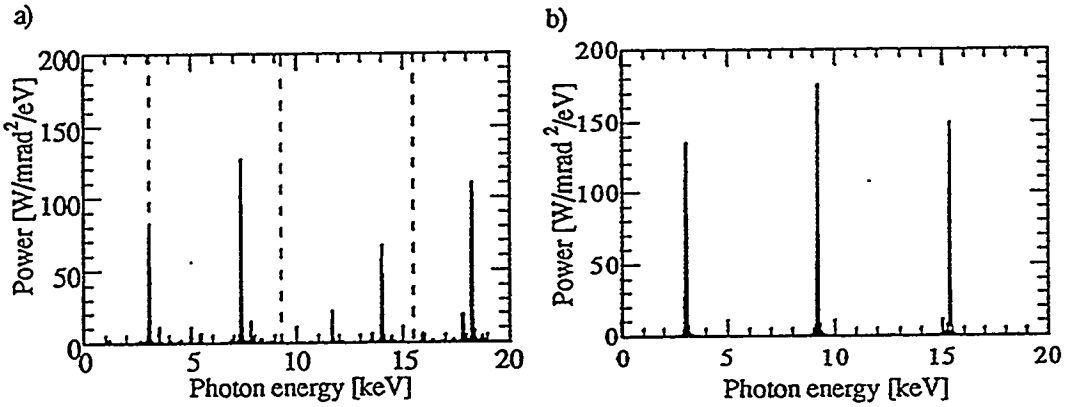

Figure 4 (a) Spectral angular power density from QPU. N_{pole}=100, gap=30 mm, electron beam = 8 GeV, 100 mA. (b) Spectral angular power density from conventional undulator, N_{pole}=100, K=1.8, electron beam = 8 GeV, 100 mA.

Discussions

We proposed a very different idea from the conventional undulator to suppress the rational higher harmonics. By analogy with diffraction from a quasi-crystal, the quasi-periodic arrays of magnets in an undulator were supposed to be capable of generating irrational higher harmonics, i.e. suppressing rational harmonics.

We calculated the radiation spectra from QPU by using eq. (2) in the case of $d'/d=\sqrt{5}$ with realistic magnet sizes and structures. The calculation was successful to prove the basic idea of QPU. However, the analysis of basic equations is not sufficient and the way of derivation of radiation spectrum from a fundamental equation is not elegant in this paper. We will publish more detailed treatment elsewhere. [10]

We inserted spacers between the magnetic segments to produce longer inter magnet distance. These spacers do not generate the magnetic field, i.e. do not contribute to emit the radiation. This means that, if the total length of the device is the same with the conventional one, the QPU is less effective in regard to the total radiation power. This disadvantage may be recovered to some extent by changing the inclination, $\tan\alpha$, to some different value.

An advantage of QPU is of course the generation of irrational harmonics in spectrum. With a combination of crystal/grating monochromator, we will be able to use purely monochromatic radiation in wide energy range since any higher harmonic radiation from QPU does not contaminated by rational harmonics if $\tan\alpha$ is carefully chosen.

Acknowledgments

The author would like to thank Shinya Hashimoto of JASRI for allowing him to write this paper by single author. He also express many thanks to Masaru Takao and Hideki Kobayashi for their collaboration and fruitful discussions.

References

[1] B. Kincaid : SPIE Proceedings 582 (1985) 72.
[2] R. P. Walker : Nucl. Instr. and Meth. A335 (1993) 328.
[3] G. Dattoli, G. Voykov : Phys. Rev. E 48 (1993) 3030.
[4] V. M. Popik, N. A. Vinokurov : Nucl. Instr. and Meth. A331 (1993) 768.
[5]. Hashimoto, S. Sasaki : JAERI-M Report 94-055 (1994); to be published in Nucl. Instr. and Meth.
[6] S. Sasaki, S. Hashimoto, H. Kobayashi, M. Takao, and Y. Miyahara : Proc. Int'l Conf. on Synchrotron Radiation Instrumentation, Stony Brook, July, 1994.
[7] A. Guinier : "X-ray diffraction in crystals, imperfect crystals and amorphous bodies", Freeman, 1963.
[8] J. D. Jackson : Classical Electrodynamics, 2nd. ed. (Wiley, New York, 1975).
[9] D. Levine, P. J. Steinhardt : Phys. Rev. B (1986) 596.
[10] M. Takao and S. Sasaki : to be published.

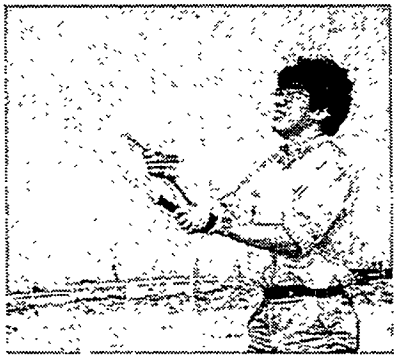

Dear Klaus

Egon Hoyer

I feel very fortunate to have had the opportunity to have been associated with you for the past 27 years. You have been an inspiration to me, teacher, colleague, and friend.

Our association started with the Omnitron project in 1967. It was on this project where you began the development of the POISSON family of magnetic design codes. One of the first applications of this code was on the Omnitron gradient magnet where Ted Scalise and I implemented the MIRT (one of the codes in the POISSON family) designed pole contour into the gradient magnet design which was built and tested at its 60 Hz frequency and shown to meet the design requirements. On this project, we also designed a 1.6 kG, 0.5 mm thick, DC septum magnet with a current density of 165,000 A/in^2 in the septum. It was on this assignment that you taught me how to calculate the field errors of the septum using complex variable techniques. We built the device and the central error fields measured on the low field side of the septum were just what we had calculated. However, the end fields were not what we had expected on the low field side of the septum so you went away and developed the concept of the "extended septum" and the "Halbach Ditch." The extended septum extends beyond the return conductors which allowed currents to flow in these extended conductors which reduced the septum end fields. The "Halbach Ditch" further reduced septum end fields by burying the return conductors in the core of the yoke which extends the core thus giving the magnet field clamps. We of course remember when Director Ed McMillan came to visit our project and while observing our septum magnet one of the stainless steel cooling tubes sprung a leak and squirted him in the eye! I remember his mild mannered response which was something to the effect that "the leak is just an engineering detail that will be taken care of."

About this time, you were given a Koralle sailboat from Germany by the manufacturer who was a long time friend of yours. The understanding that you had was he would get some photos of the boat being sailed on San Francisco Bay. Ron Yourd and I remember sailing this 13 foot craft on the ocean side of the Golden Gate where the swells were running so high that we lost visual contact from out companion power boat. It was scary.

The next project that we worked on together, in the early seventies, was the High Resolution Spectrometer (HRS) which still is located in Experimental Area C at LAMPF. On this project you developed the concept of Ht windings, which allows achieving very uniform fields over very wide magnet apertures, and how large magnets behave during fields changes (eddy current effects). The Ht winding concept allows the tangential field component of the pole surface to be controlled when coils placed in slots behind the pole surface are energized. I remember one of my assignments was to build a test setup of this idea in one of the large Bevatron H magnets to show feasibility. When you and I carried out the tests you were ecstatic as to how well it worked. The ultimate test of this concept was demonstrated in "Big Karl," located at Kernforschungsanlage Juelich, where field integral uniformity of one part in 100,000 was achieved in this very large spectrometer magnet.

It was during the HRS project where I helped you quit smoking and we had our wonderful backpack trip through the Tetons. I remember the last cigarette you smoked this side of Twin Bridges, California on our tune up trip to Desolation Valley, in preparation to going to the Tetons. On this trip, I also remember your being upset with me for leading us down Horsetail Falls, which required using a rope for safety after I assured you that we wouldn't need a rope on the trip as well as the horrible dinner we had after the trip at the Blue Bell Cafe in Placerville. Some of the experiences on the Teton trip are worth remembering. At the beginning of the Teton trip, I was thinking you were getting cold feet when you asked the ranger about Hurricane Pass because you had read that the pass can be dangerous. I think you asked the ranger if you could get killed but I was relieved that he responded by saying that you might only be maimed. The first evening of the trip in Granite Canyon was amusing. I remember you yelling out "Oh God" - well, you had sat on a log and gotten pitch all over your pants and then we watched you struggle to get it off. After this first day, you were pretty pooped and began to downsize your load. I remember Ron getting the sleeping bag liner right away - a few years later Ron got the backpack. When you started to cut away the section of the map that we had already covered, to lighten your load, I was sure we weren't going to turn back. At dinner that night, the LASL contingent, Ron, Denny, Naby and Mike, surprised us by showing up with neckties. In the middle of the trip, the crossing of Hurricane Pass proved to be uneventful and provided a spectacular view. The last night's dinner at Solitude Lake was Ham Romano and after cooking it the ham was bad so we had to bury the dinner. My fly fishing ability was then put to a true test and I came up with ten good sized Cutthroat trout which were had for both dinner and the following breakfast. This trip was the beginning of a series of backpack trips for some of us. In subsequent years we went to the Sierra, the Unitas, the San Juans, the Marble Mountains and the Wind River Range.

In 1979, you came to me and asked me who I would recommend in the engineering department to build a new kind of magnetic structure. I looked at all the possible candidates and found that most everybody wasn't available so I volunteered myself after getting permission from Ken Mirk, for whom I was currently working for, to work on this new endeavor. This event was a turning point in my career and the new magnetic structure was to become the LBL/SSRL Undulator, the first pure permanent undulator. The project, from concept to completed device was accomplished in less than a year. We had our difficulties too - I had opted to only put adhesive on the backs of the permanent magnets and after the structure was assembled the REC blocks began to "pop up." Fortunately, the fix was easy - the adhesive was "troweled" between the blocks and between the keepers and blocks. To test out this new device, it was placed in one of the wiggler beamlines at SSRL. To do this, the in place electromagnet wiggler magnet was outfitted with a structure that allowed the wiggler magnet to be split in the middle to allow the undulator to be inserted in its place. I remembered we worked hard to deliver the undulator by October 1980 but unfortunately the wiggler splitting mechanism was a half inch too small so testing was delayed until December while the mechanism was modified.

The follow on to the undulator was the Beamline VI project which was a joint effort between LBL, SSRL and EXXON. By this time you had developed the hybrid concept, where steel is combined with permanent magnet material (e.g., REC) in the magnetic structure of insertion devices, which was used for the now famous "54 pole wiggler" (actually, the 7 cm period, 27 period device has 55 full field poles) with its variable gap vacuum chamber. This project got underway in early 1981 and the completed device was installed in the SPEAR ring in 1983. During this time, with the wiggler and associated beam line under design and construction, we were involved in the initial conceptual design of the ALS and the first reviews. It was an exciting time.

In the mid-eighties we went on to build the BLX Wiggler, a joint project between LBL, LLNL and SSRL, another hybrid configured insertion device where we used Nd-Fe-B as the permanent magnet material. Tests showed that this 12.85 cm period device, at its extreme, produced peak fields of 2.35 T at a 8 mm gap!

Your sixteen lecture series given in 1988-1989 (LBL V 8811-1.1-16) is a classic where you presented your hybrid 3-D theory as well as many of the concepts you had developed over the years. This is an invaluable reference for me. The 3-D hybrid theory would go on to be the basis of the insertion device designs for the ALS. The quality of the ALS undulators we have built reflects the error analysis theory you developed for these hybrid structures.

Most recently, at the Permanent Magnet Synchrotron Workshop, I had the opportunity to learn about your newest ideas about building complete storage rings with permanent magnet dipoles, quadrupoles, etc. It has been interesting to help in developing the practical realization of these latest ideas.

In conclusion, I think what has made the projects that we have worked on together successful has been our teamwork; you developed the ideas and I led the implementation of those ideas. I felt that it was always imperative that you made the decisions when matters involved theory and you let me make the hardware decisions. I feel indebted to you for giving me these opportunities and enriching my life.

Egon

The start of the Teton backpack trip in July 1971. From left: Egon Hoyer, Ron Yourd, Dan Salomon, Mike Thompson, Denny Roeder, Klaus Halbach.

Hurricane Pass, Teton National Park. From left: Klaus Halbach, Naby Tanaka, Dan Salomon, Mike Thompson, Ron Yourd, Denny Roeder.

Klaus at Donner Lake (July 1971).

FIELD ERRORS IN HYBRID INSERTION DEVICES[†1]

Ross D. Schlueter
Lawrence Berkeley Laboratory
1 Cyclotron Road, MS 46-161
Berkeley, CA 94720, USA[‡2]

Abstract

Hybrid magnet theory as applied to the error analyses used in the design of Advanced Light Source (ALS) insertion devices is reviewed. Sources of field errors in hybrid insertion devices are discussed.

1 Introduction

Klaus Halbach is well known for originating and developing permanent magnet (PM) technology for accelerator magnets, including insertion devices (IDs). An equally important contribution, though perhaps less glamorous, is his pioneering work in error analyses, both their theoretical calculation and effects, applicable to these accelerator magnets, again including IDs [1,2]. Hybrid IDs, employing both permanent magnet material and soft iron, were pioneered at LBL and have since become popular in synchrotron sources worldwide. Recently several outside requests have been received to set forth the error analysis theory used in the design of these devices. That follows herein. Implications for resulting mechanical tolerances and permanent magnet block quality specifications are already described in the various ALS ID conceptual design reports [3-7].

Yet another immense contribution of Klaus's is his mentorship of numerous scientists and engineers and the "little-boy-excitement" he transmits to those that work with him in the field of accelerator magnet design and technology. This paper is dedicated to Klaus Halbach in appreciation for both the broad training graciously tendered and the little-boy-excitement for the subject he has infused in me.

2 Permanent Magnets: Passive Materials with Active Terms

In directions parallel and perpendicular to the magnetization of a permanetly magnetized material the induction B is related to the field H by, respectively

$$B_{\|} = \mu_{\|} H_{\|} + B_r \quad \text{and} \quad B_{\perp} = \mu_{\perp} H_{\perp}, \tag{1}$$

where B_r is the remanent field and μ is the differential permeability. Vectorially the $B - H$ relation may be expressed

$$\vec{B} = \hat{\mu}\vec{H} + \vec{B}_r \qquad \text{or} \qquad \vec{H} = \hat{\gamma}\vec{B} - \vec{H}_c, \tag{2}$$

[1†] This work was supported by the Director, Office of Energy Research, Office of Basic Energy Sciences, Materials Science Div., of the U.S. Dept. of Energy under Contract No. DEAC03-76SF00098.
[2‡] E-mail: ross@lbl.gov, Fax: 510-486-4873.

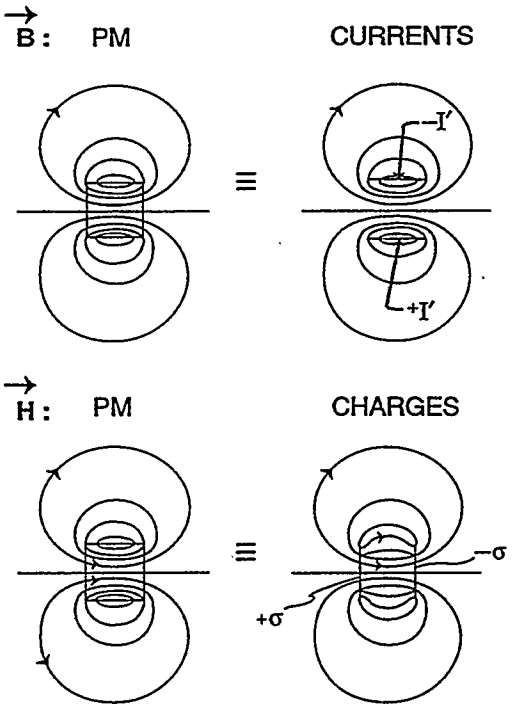

Figure 1. Plots of (a) B and (b) H for a homogeneously magnetized PM block in free space and for equivalent current or charge sheet models.

where H_c is the coersive force and $\hat{\gamma} \equiv \hat{\mu}^{-1}$. In a current-free, time-independent region, it follows from Maxwell's equations $\vec{\nabla} \times \vec{H} = 0$ and $\vec{\nabla} \cdot \vec{B} = 0$. Thus the divergence of Eq. (2a) and the curl of Eq. (2b) yield, respectively,

$$\vec{\nabla} \cdot \hat{\mu}\vec{H} = -\vec{\nabla} \cdot \vec{B}_r \equiv \rho_{eq} \quad \text{or} \quad \vec{\nabla} \times \hat{\gamma}\vec{B} = -\vec{\nabla} \times \vec{H}_c \equiv \jmath_{eq} \tag{3}$$
$$\text{with } \vec{\nabla} \times \vec{H} = 0 \qquad \text{with } \vec{\nabla} \cdot \vec{B} = 0,$$

where ρ_{eq} and $\jmath_{eq}$ are equivalent charge and current densities, respectively. The PM material thus can be represented as a passive material of permeability $\hat{\mu}$ or $\hat{\gamma}^{-1}$ with active source terms ρ_{eq} or j_{eq}. For a homogeneously magnetized PM block $\vec{\nabla} \cdot \vec{B}_r$ and $\vec{\nabla} \times \vec{H}_c$ are zero everywhere except at surfaces parallel and perpendicular, respectively, to the block magnetization, giving rise to surface charge sheets $\sigma \equiv \rho_{eq}\delta = \pm B_r$ [G] or current sheets $I' \equiv \jmath_{eq}\delta = \pm H_c$ [G], respectively, where δ is the infinitesimal sheet thickness. Figure 1a,b plot B and H, respectively for a homogeneously magnetized PM block and for either equivalent current or charge sheets, respectively. The remaining quantity, H or B, can be obtained from the $B - H$ relation, e.g., Eq. (2). The high strength Nd-Fe-B, Sm-Co, and ferrite PMs used in accelerator magnets exhibit permeabilities $\mu \simeq 1.04$, thus it is often convenient to model these with $\pm B_r$ charge sheets separated by effectively free space.

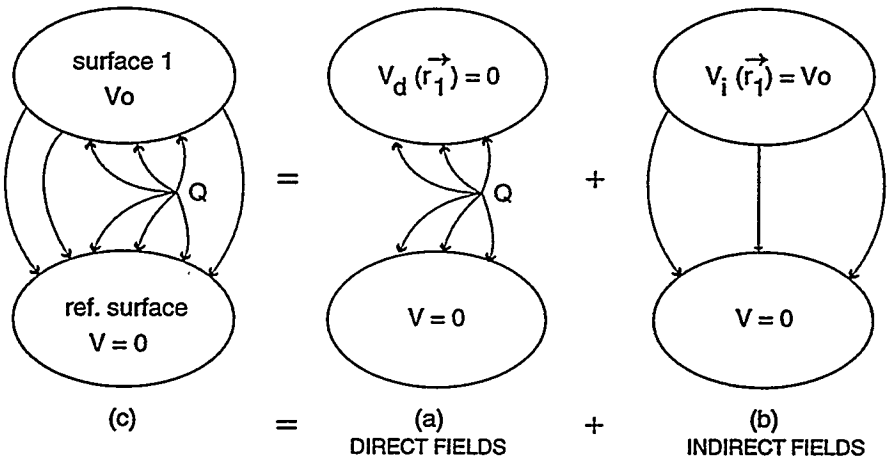

Figure 2. Hybrid solution for two infinite μ bodies in the presence of a point charge Q: (c) the total solution, (a) the direct field component, (b) the indirect field component.

3 Hybrid Magnets: Zero Reluctance Volumes with Iso-Scalar Potential Field Shaping Surfaces passing Zero Net Flux

A hybrid magnet can be modeled by charge sheets at appropriate PM surfaces and by iso-scalar potential surfaces enclosing the reluctance-free soft iron. Imagine a single point charge Q near two iso-scalar potential surfaces. A field solution can be constructed that satisfies Maxwell's equations in space outside the iron and has net flux $\Phi_1 = 0$ entering surface 1 on scalar potential V_0. (The other is a reference surface pegged to a scalar potential $V = 0$, without loss of generality.) As shown by Fig. 2, this solution, (c), is a superposition of two solutions, (a) and (b), to Maxwell's equations outside the iron. The first solution, (a), comprises the direct flux emanating from the point charge being deposited on either of the two surfaces, both of whose surfaces are on iso-scalar potential contours V=0. The second solution, (b), comprises the indirect flux arising from assumed different scalar potentials of the two surfaces, in the absence of all sources (charges). In fact, the equilibrium scalar potential $V = V_0$ that surface 1 assumes is that required to satisfy $\int_{a_1} \vec{B} \cdot d\vec{a}_1 = 0$, where a_1 is the area of surface 1, i.e., no net flux enters the iron.

In the first solution, (a), the direct flux deposited on surface 1, $\Phi_{1_d} = fQ$, $(0 \leq f \leq 1)$, where f, the fraction of Q deposited on surface 1, is readily obtained from the geometry of the second solution, (b): f is merely the scalar potential at the location of the charge (in its absence) normalized with respect to the potential of surface 1, i.e., $f = V_i(\vec{r}_Q)/V_0$. The remainder, $(1 - f)Q$ is deposited on the reference surface. That this is so is somewhat intuitive; the source in a vacuum region near two zero potential surfaces is analogous to a voltage divider. A rigorous proof is given in Appendix A.

In the second solution, (b), the indirect flux into surface 1, $\Phi_{1_i} = -V_0 c_2$, where V_0 is still unknown and where the "capacitance" c_2, is a constant of proportionality

readily determined from the geometry alone by solving the boundary value problem, (b), with any assumed value of V_0.

Finally, in the combined solution, (c), the net flux crossing surface 1 is zero, which determines the value of the equilibrium scalar potential V_0:

$$\Phi_{1_i} + \Phi_{1_d} = 0 \quad \Longrightarrow \quad V_0 = Qf/c_2. \tag{4}$$

Zero net flux across the reference surface is likewise achieved when the necessary complimentary negative point charge $-Q$ is added to the model. For a dipole then, the direct flux deposited on surface 1 is

$$\Phi_{1_d} = Q(V_i(\vec{r}_Q + \vec{\delta r}_Q) - V_i(\vec{r}_Q))/V_0 = -Q\vec{\delta r}_Q \cdot \vec{H}_i(\vec{r}_Q)/V_0, \tag{5}$$

and for a PM block, with $Q\vec{\delta r}_Q = |B_r|a_{PM}\vec{\delta r}_Q = \vec{B}_r dv$, the direct flux deposited on surface 1 is

$$\Phi_{1_d} = -\int \vec{B}_r \cdot \vec{H}_i dv/V_0. \tag{6}$$

The total solution to a hybrid system then, consists of solving a boundary problem and integrating over the charge distribution modeling the PM material to obtain f (or equivilently Φ_{1_d}) and c_2.

Applying this theory to a hybrid ID design, let surface 1 be that of a soft iron undulator pole and the reference surface be the zero scalar potential surface consisting of the ID midplane and the vertical planes midway between adjacent poles. Then c_2V_0 is the indirect flux leaving the pole sitting on scalar potential V_0. The design of a hybrid ID entails selecting the pole tip shape that produces the desired [indirect-flux-induced] field distribution, then determining the pole scalar potential required to achieve the desired field strength, and finally designing the rest of the iron and [direct-flux-generating] PM to produce this potential. It should be noted that in a hybrid design the PM is positioned so the direct flux goes where one desires, i.e., either to/from an energized pole or from/to a non-critical portion of a zero scalar potential surface, thus leaving only indirect flux in the "business region". Detailed hybrid theory analytical calculation for accelerator magnet design (including IDs) is an interesting subject in itself, but is not treated here.

4 Partitioning of the Capacitance c_2

Here we are interested in the integrated error flux that the electron beam sees. It is thus incumbent on us to determine both how much direct flux and how much indirect flux crosses the midplane in the region underneath the pole-width-envelope where the field is invariant in the transverse direction. For this reason, though not for the hybrid ID design itself, it is necessary to partition the capacitance c_2, as shown below. (Partitioning of c_2 is likewise integral to analytical design of ID ends and calculation of error propagation through the ID.)

The hybrid theory introduced in the preceeding section may be rigorously extended to systems with multiple isopotential surfaces. Here we take advantage of inherent

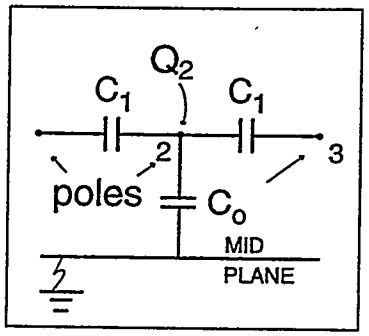

Figure 3. ID circuit model.

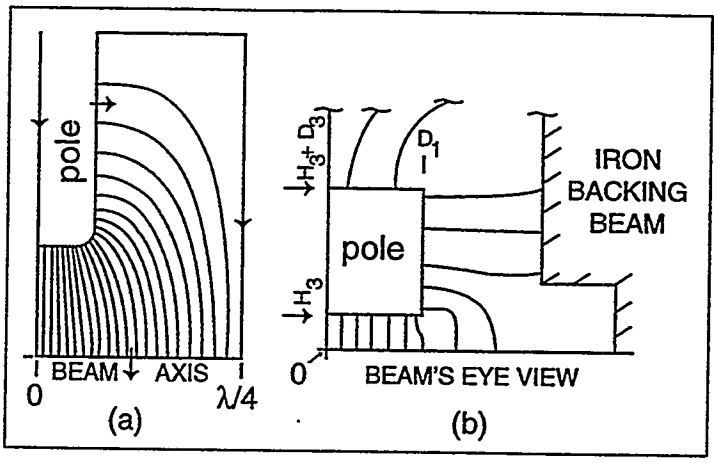

Figure 4. (a) 2-D and (b) fringe flux to ID reference surface for determination of capacitance c_0.

ID symmetries allowing simple partitioning of the capacitance c_2. Figure 3 shows an electrical analog of an undulator where the nodes are poles, with the reference ground on $V = 0$ being the ID midplane.

For $+,-,+,-$ pole excitation, the PM-induced charge Q_2 into pole #2 on $+V_0$ leaves the pole as indirect flux to either pole #1 or pole #3, both on potential $-V_0$ or to to the midplane on $V = 0$. The direct flux Q_2 is then given by

$$Q_2 = V_0(c_0 + 4c_1). \tag{7}$$

We already know from the hybrid design, which assumes $+,-,+,-$ pole excitation, that the direct flux entering a pole is equal to the indirect flux leaving, which in turn is proportional to the pole potential V_0, via the capacitance c_2. The c_2 then can be partitioned as follows:

$$\Phi_d(= Q_2) = -\Phi_i = c_2 V_0 \quad \Longrightarrow \quad c_2 = c_0 + 4c_1. \tag{8}$$

With c_2 known from the [analytical or numerical] solution of a boundary value problem, it remains to calculate either c_1 or c_0. Consider a fictitious $+,+,+,+$ pole excitation, where all poles lie on isopotential $V = V_2$. In this case there is no net flux pole-to-pole and 100% of the charge Q into pole #2 leaves the pole as indirect flux to the midplane on $V = 0$:

$$Q = V_2 c_0. \tag{9}$$

Two parts contribute to c_0 as shown in Fig. 4a,b: (a) The 2-D portion in the region underneath the pole-width-envelope where the field is invariant in the transverse direction is given by

$$c_{0_f}/4 = [A(\lambda/4, 0) - A(0, 0)]D_1/V_2, \tag{10}$$

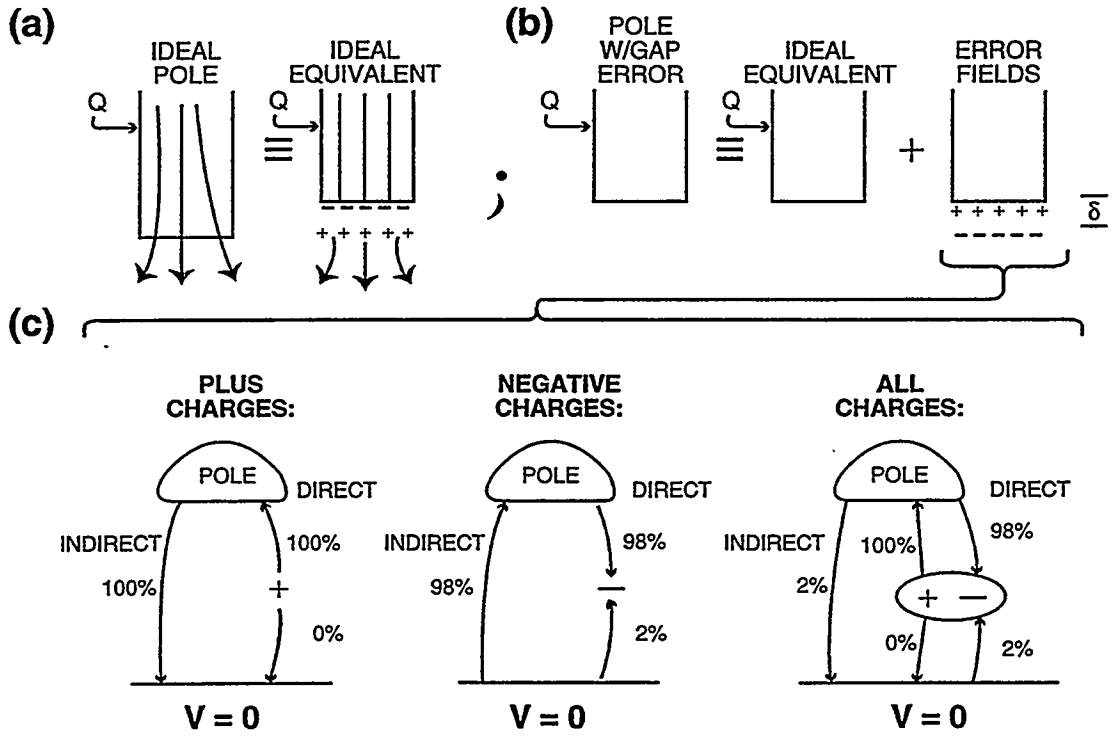

Figure 5. Modeling iron displacement with charge sheet equivalents: (a) an ideal pole, (b) a shortened pole, (c) direct and indirect error flux from positive and negative charge sheets.

where coordinates are in the z-y plane, A is the 2-D magnetostatic vector potential ($\nabla \times A = B$), λ is the ID period, and D_1 is the pole half-width in the transverse direction; (b) The fringe flux at the side and top surfaces of the pole is given by

$$c_{0_s}/4 = [A(0, H_3 + D_3) - A(D_1, 0)][\lambda/4]/V_2, \tag{11}$$

where coordinates are in the x-y plane, H_3 and D_3 are the half-gap and pole height, respectively. The nearby iron backing beam must be considered part the the zero scalar potential reference surface. To be rigorous one must modify the c_{0_s} calculation to account for an excess voltage drop associated with the fact that the pole does not extend axially to $\lambda/4$. Also one could include capacitances between non-adjacent poles. Both these are relatively minor effects.

5 ID Error Sources and Their Effect on Integrated Field Errors

An ideal pole energized by charge Q and an energized charge sheet ideal equivalent recessed pole with charge sheets separated by the recessed amount δ yield identical flux distributions, as shown in Fig. 5a. An energized pole exhibiting a gap error thus, can be modeled by superposing to an energized ideal equivalent recessed pole an unenergized recessed pole with charge sheets of the opposite polarity, as shown in Fig. 5b. The decomposition of the error fields is shown in Fig. 5c for the plus charges

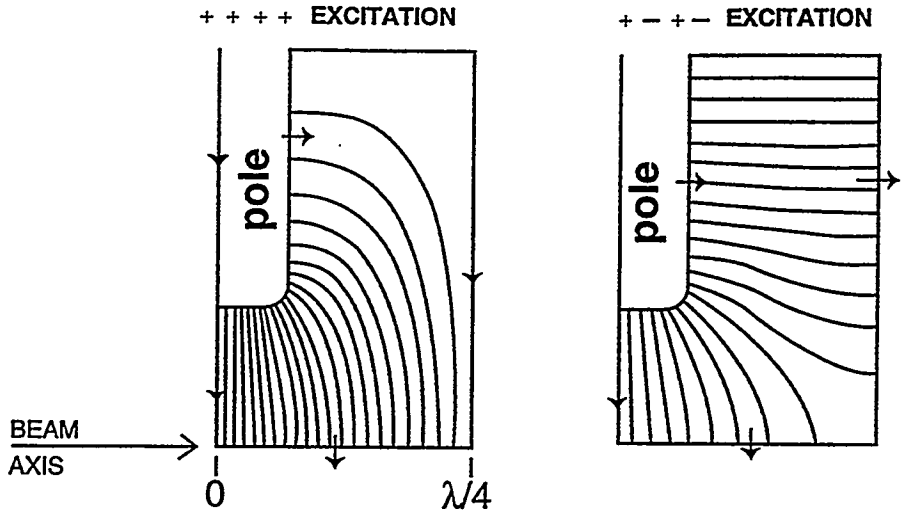

Figure 6. A quarter-period ID model with adjacent pole excitation patterns of: (a) +,+,+,+, and (b) +,−,+,−

and for the negative charges separately. The direct error flux going to the midplane, Q_0 is all from the negative charges. It may be calculated following the argument set forth in section 3: The magnitude of the charge density $q^- = B_{+-+-}$, where B_{+-+-} is the field at the location r_{q^-} for the $+,-,+,-$ pole excitation shown in Fig 6a. The f, the fraction of q^- that goes directly to the midplane, found by putting all poles on zero scalar potential and the midplane on V_2, is just $f = V_i(r_{q^-})/V_0 = B_{++++}\delta/V_0$, where B_{++++} is the field at the location r_{q^-} for the $+,+,+,+$ pole excitation shown in Fig 6b, and δ is the half-gap error. Error flux to the midplane is thus

$$Q_0 = \delta \int B_{+-+-}(s) B_{++++}(s) ds / V_2, \tag{12}$$

where ds is along the charge sheet.

From Fig. 5c, an equal amount of direct flux (100% of the + charges and 98% of the − charges in this hypothetical example shown) but of opposite polarity $-Q_0$ goes to the poles. Indirect fields must deposit this flux on the midplane, but only a fraction $c_{0_f}/(c_{0_f}+c_{0_s})$ is seen by the electron beam, per the argument of the preceding section. Thus the net flux that the electron beam sees is

$$Q_{beam} = Q_0(1 - [c_{0_f}/(c_{0_f} + c_{0_s})]) = Q_0 c_{0_s}/(c_{0_f} + c_{0_s}). \tag{13}$$

Various error sources are depicted in Fig. 7. Pole thickness error is modeled analogously, following the pole gap error method. Spacing between the PM and the pole is analogously modeled with a perfectly sized PM block and a superimposed PM block sliver of thickness δ and with magnetization in the opposite direction as the ideal PM block. An easy axis orientation error of angle α is modeled as charge sheets of charge density $\pm B_r \sin\alpha$ at the top and bottom of the PM block, respectively. Where two adjacent PM blocks are mismatched in strength, there is are error charge sheets of

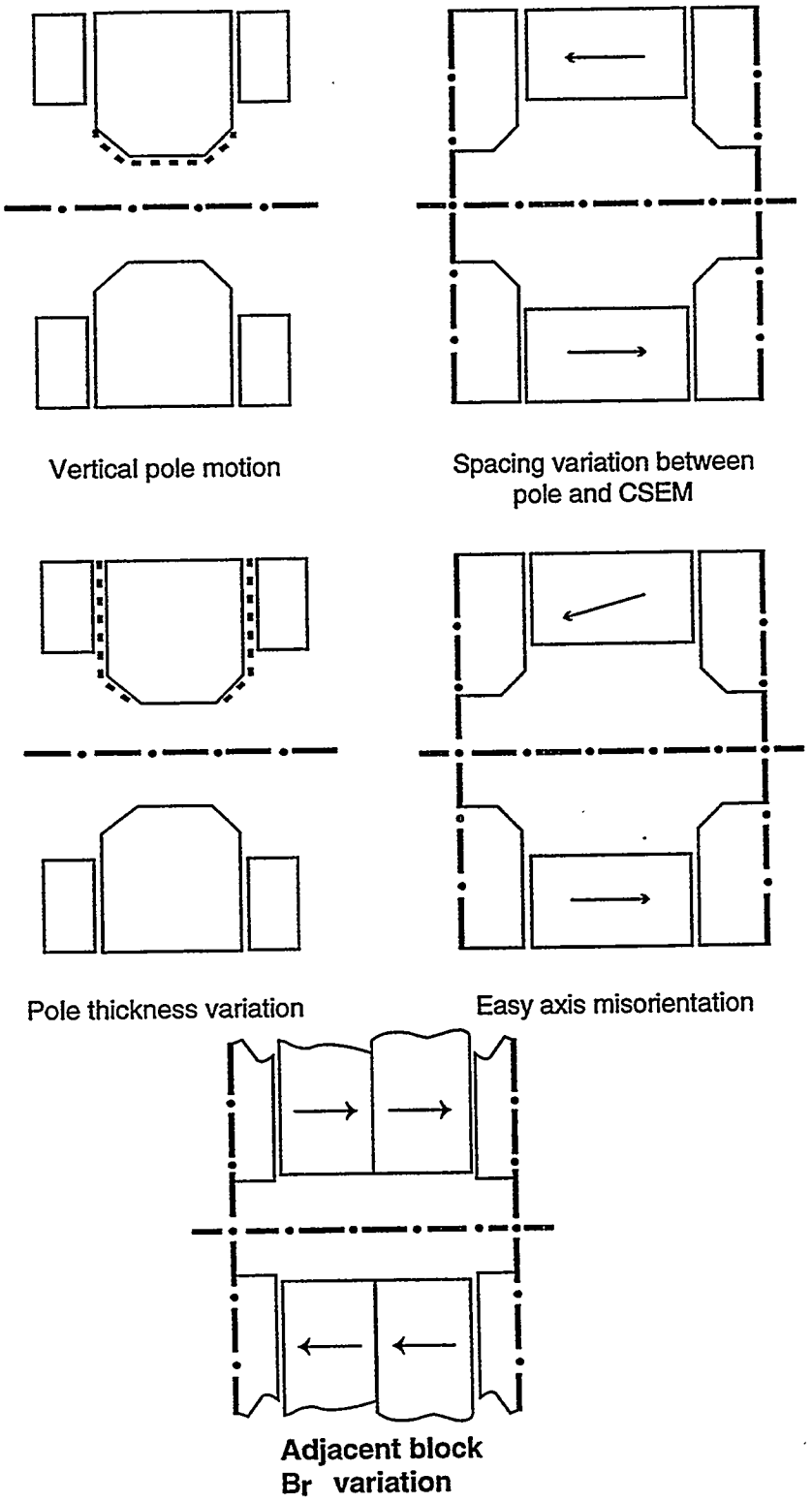

Figure 7. Various Hybrid ID error sources.

strength $\pm(B_{r_1} - B_{r_2})$. Chips in PM blocks, oversized PM blocks, and inhomogeneities in PM blocks can also be handled analogously. The relative iomportance of these error sources varies with the geometry, field strengths, etc. Notice that whenever there is an error charge sheet, there is a corresponding error sheet of opposite charge, usually adjacent to a pole, where a feature is or should have been. It should be noted that the only reason there is net flux to the beam is because of three-dimensional effects; if c_{0_s} were zero, $Q_{beam} \longrightarrow 0$ too! Implications for tolerances and PM quality specifications have been discussed at length in the various ALS ID conceptual design reports.

The theory described in this paper is quite general, and is good for all hybrid designs, error analyses, or whenever one wishes to determine out how much of a charge winds up on a given surface.

6 Acknowledgements

I am happy to acknowledge Klaus Halbach's original work on the hybrid theory and his guidance in applying the fundamentals to the ALS IDs described herein.

7 References

1. K.Halbach, *ID Design*, Law. Berk. Lab. Rep. V-8811-1.1-16 (1989).
2. K.Halbach, *3-D Hybrid Theory*, Law. Berk. Lab. Rep. LSBL-034. (1989).
3. *U5.0 Conceptual Design Report*, Law. Berk. Lab. Pub-5256 (1989).
4. *U8.0 Conceptual Design Report*, Law. Berk. Lab. Pub-5276 (1990).
5. *W16.0 Conceptual Design Report*, Law. Berk. Lab. Pub-5288 (1991).
6. *U10.0 Conceptual Design Report*, Law. Berk. Lab. Pub-5390 (1994).
7. *EW20.0 Conceptual Design Report*, Law. Berk. Lab. Pub-5400 (1995).

8 Appendix A

The $f = V_i(\vec{r}_Q)/V_0$. Proof: consider $I \equiv \int(V_i\vec{B}_d - V_d\vec{B}_i)\cdot d\vec{a}$, where $d\vec{a}$ is over all surfaces enclosing the total volume that is not iron. On the reference surface: $V_d = 0, V_i = 0$; on surface 1: $V_d = 0, V_i = V_0$; and at infinity $V\vec{B} \longrightarrow 0$ faster than $a \longrightarrow \infty$. Thus, one expression for I is

$$I = V_0\Phi_{1_d}. \tag{14}$$

Alternatively, I can be expressed

$$I \equiv \int(V_i\vec{B}_d - V_d\vec{B}_i)\cdot d\vec{a} = \int \vec{\nabla}\cdot d(V_i\vec{B}_d - V_d\vec{B}_i)dv =$$

$$\int(V_i\vec{\nabla}\cdot\vec{B}_d - V_d\vec{\nabla}\cdot\vec{B}_i + \vec{H}_d\cdot\vec{B}_i - \vec{H}_i\cdot\vec{B}_d)dv = \int V_i(\vec{r})\rho_{eq}(\vec{r})dv, \tag{15}$$

since $\vec{\nabla}\cdot\vec{B}_d = \rho_{eq}$, $\vec{\nabla}\cdot\vec{B}_i = 0$, and $\vec{H}_d\cdot\vec{B}_i = \vec{H}_i\cdot\vec{B}_d$. The latter can be shown:

$$\vec{H}_d\cdot\vec{B}_i = \mu_0(\vec{H}_{i_\parallel}+\vec{H}_{i_\perp})\cdot(\mu_\parallel\vec{H}_{d_\parallel}+\mu_\perp\vec{H}_{d_\perp}) = \mu_0(\mu_\parallel\vec{H}_{i_\parallel}\vec{H}_{d_\parallel}+\mu_\perp\vec{H}_{i_\perp}\vec{H}_{d_\perp}) = \vec{H}_i\cdot\vec{B}_d. \tag{16}$$

Equating the two expressions for I gives $\Phi_{1_d} = \int V_i(\vec{r})\rho_{eq}(\vec{r})dv/V_0$, which for a point charge Q reduces to $\Phi_{1_d} = V_i(\vec{r}_Q)Q/V_0 = fQ$.

Field of a Helical Siberian Snake

Alfredo Luccio
Brookhaven National Laboratory
Upton, NY 11973-5000

Introduction

To preserve the spin polarization of a beam of high energy protons in a circular accelerator, magnets with periodic magnetic field, called Siberian Snakes are been used[1]. Recently, it was proposed to build Siberian Snakes with superconducting helical dipoles[2]. In a helical, or twisted dipole, the magnetic field is perpendicular to the axis of the helix and rotates around it as we proceed along the magnet. In an engineering study of a 4 Tesla helical snake[3], the coil geometry is derived, by twisting, from the geometry of a cosine superconducting dipole.

While waiting for magnetic measurement data on such a prototype, an analytical expression for the field of the helix is important, to calculate the particle trajectories and the spin precession in the helix. This model will also allow to determine the optical characteristics of the snake, as an insertion in the lattice of the accelerator. In particular, one can calculate the integrated multipoles through the magnet and the equivalent transfer matrix.

An expression for the field in the helix body, i.e. excluding the fringe field was given in a classical paper by Blewett and Chasman[4]. An alternate expression can be found by elaborating on the treatment of the field of a transverse wiggler[5] obtained under the rather general conditions that the variables are separable. This expression exactly satisfies Maxwell's div and curl equations for a stationary field

$$\nabla \cdot \mathbf{B} = 0, \quad \nabla \times \mathbf{B} = 0. \tag{1}$$

This approach is useful in what it will allow one to use much of the work already done on the problem of inserting wigglers and undulators in the lattice of a circular accelerator[6].

Superposition of Wigglers

A general expression for a field of a transverse wiggler that exactly satisfy Eqs. (1) can be found, assuming that the variables are separable. let the field on axis be directed along the vertical (y) axis

$$B_y(x,y,z) = B_0 X(x) Y(y) \sum_m \sin(mkz), \tag{2}$$

and apply Maxwell equations (1). From curl **B** = 0, obtain

$$\begin{cases} B_x = \dfrac{\partial X}{\partial x}\left(\int Y dy\right)\sum_m \sin(mkz) \\ B_z = X\left(\int Y dy\right)\sum_m mk\cos(mkz) \end{cases} \tag{3}$$

From div = 0 and, by differentiating with respect to y, obtain two formally identical set of equations, for each harmonic m of the field

$$\begin{cases} \dfrac{\partial^2 X(x)}{\partial x^2} - m^2 k_x^2 X(x) = 0 \\ \dfrac{\partial^2 Y(y)}{\partial y^2} - m^2 k_y^2 Y(y) = 0 \end{cases} \tag{4}$$

with

$$k_x^2 + k_y^2 = k^2. \tag{5}$$

The general integral of Eqs. (4) that obey the symmetry requirements for a transverse wiggler, is

$$\begin{cases} B_x = B_0 \dfrac{k_x}{k_y} \sum_m \mathrm{Sh}(mk_x x)\mathrm{Sh}(mk_y y)\sin(mkz) \\ B_y = B_0 \sum_m \mathrm{Ch}(mk_x x)\mathrm{Ch}(mk_y y)\sin(mkz) \\ B_z = B_0 \dfrac{k}{k_y} \sum_m \mathrm{Ch}(mk_x x)\mathrm{Sh}(mk_y y)\cos(mkz) \end{cases} \tag{6}$$

A general helical dipole can be obtained by the superposition of many infinitesimal transverse wigglers, continuously rotated by an angle θ around the axis z. Using the transformation between rotated frame (primed quantities) and laboratory (unprimed)

$$\begin{cases} B_x = B_{x'}\cos\theta - B_{y'}\sin\theta \\ B_y = B_{x'}\sin\theta + B_{y'}\cos\theta \end{cases} \qquad \begin{cases} x' = x\cos\theta + y\sin\theta \\ y' = -x\sin\theta + y\cos\theta' \end{cases} \tag{7}$$

the components of the field, obtained by the integral sum of many infinitesimal transverse sinusoidal wigglers, that exactly satisfy Maxwell's, are found

$$\begin{cases} b_x^{(m)} = \dfrac{B_x^{(m)}}{B_0} = b_1^{(m)}\sin(mkz) + b_2^{(m)}\cos(mkz) \\ b_y^{(m)} = \dfrac{B_y^{(m)}}{B_0} = b_3^{(m)}\sin(mkz) + b_4^{(m)}\cos(mkz), \\ b_z^{(m)} = \dfrac{B_z^{(m)}}{B_0} = b_5^{(m)}\sin(mkz) + b_6^{(m)}\cos(mkz) \end{cases} \tag{8}$$

with

$$\mathbf{b}^{(m)} = \frac{1}{\sqrt{2}}\begin{pmatrix} -a_1^{(m)} + \dfrac{k_x}{k_y}a_2^{(m)} \\ a_3^{(m)} - \dfrac{k_y}{k_x}a_4^{(m)} \\ a_3^{(m)} + \dfrac{k_x}{k_y}a_4^{(m)} \\ a_1^{(m)} + \dfrac{k_y}{k_x}a_2^{(m)} \\ -\dfrac{k}{k_x}a_5^{(m)} \\ \dfrac{k}{k_y}a_6^{(m)} \end{pmatrix}, \qquad \mathbf{a}^{(m)} = \begin{pmatrix} \int \mathrm{Ch}(mu')\mathrm{Ch}(mv')\sin\theta\, d\theta \\ \int \mathrm{Sh}(mu')\mathrm{Sh}(mv')\cos\theta\, d\theta \\ \int \mathrm{Ch}(mu')\mathrm{Ch}(mv')\cos\theta\, d\theta \\ \int \mathrm{Sh}(mu')\mathrm{Sh}(mv')\sin\theta\, d\theta \\ \int \mathrm{Sh}(mu')\mathrm{Ch}(mv')\, d\theta \\ \int \mathrm{Ch}(mu')\mathrm{Sh}(mv')\, d\theta \end{pmatrix}, \tag{9}$$

$$\begin{cases} u' = u\cos\theta + v\sin\theta \\ v' = -u\sin\theta + v\cos\theta \end{cases} \qquad \begin{cases} u = k_x x \\ v = k_y y \end{cases} \tag{10}$$

On axis, the field is

$$\begin{cases} B_x = B_0 \sum_m \sin(mkz + \phi^{(m)}) \\ B_y = -B_0 \sum_m \cos(mkz + \phi^{(m)}), \qquad \tan\phi^{(m)} = \dfrac{\sin\theta_2^{(m)} - \sin\theta_1^{(m)}}{\cos\theta_2^{(m)} - \cos\theta_1^{(m)}}, \\ B_z = 0 \end{cases} \tag{11}$$

(θ_1 and θ_2 are, for each harmonic, the rotation angle of the first and last infinitesimal wiggler, respectively, limits of the integrals over θ).

Explicit expressions for the products of hyperbolic functions in the a coefficients of Eq. (9) are found using the identities[7]

$$\begin{cases} e^{z\cos\theta} = I_0(z) + 2\sum_{k=1}^{\infty} I_k(z)\cos k\theta \\ e^{z\sin\theta} = I_0(z) + 2\sum_{k=0}^{\infty}(-1)^k I_{2k+1}(z)\sin(2k+1)\theta + 2\sum_{k=1}^{\infty}(-1)^k I_{2k}(z)\cos 2k\theta \end{cases}, \tag{12}$$

so that the field of an helix can be expressed in trigonometric series with coefficients containing the modified Bessel functions I_n . Defining $c = \cos\theta$, $s = \sin\theta$, obtain

$$\begin{cases} \mathrm{Sh}(muc)\mathrm{Ch}(mvs) = 2\sum_{i=1}^{\infty}(-1)^i \sum_{k=-\infty}^{\infty}(-1)^k I_{2k-1}(mu) I_{2k-2i}(mv)\cos(2i+1)\theta \\ \mathrm{Ch}(muc)\mathrm{Sh}(mvs) = 2\sum_{i=1}^{\infty}(-1)^i \sum_{k=-\infty}^{\infty}(-1)^k I_{2k}(mu) I_{2i+2k+1}(mv)\sin(2i+1)\theta \\ \mathrm{Ch}(muc)\mathrm{Ch}(mvs) = \frac{1}{2}\left[I_0(mu)I_0(mv) - 2\sum_{k=1}^{\infty}(-1)^k I_{2k}(mu) I_{2k}(mv) \right] \\ \qquad\qquad +2\sum_{i=1}^{\infty}(-1)^i \sum_{k=-\infty}^{\infty}(-1)^k I_{2k}(mu) I_{2i+2k}(mv)\cos 2i\theta \\ \mathrm{Sh}(muc)\mathrm{Sh}(mvs) = \sum_{i=1}^{\infty}(-1)^i \sum_{k=-\infty}^{\infty}(-1)^k I_{2k+1}(mu) I_{2k-2i+1}(mv)\sin 2i\theta \end{cases} \tag{13}$$

Expansion. Trajectory. Integrated multipoles.

An expansion in u, v of Eq. (8) is useful to evaluate analytically the multipole content of the field along a particle trajectory, and the transfer matrix of the magnet. Consider only the first harmonic ($m = 1$) and the important case

$$k_x = k_y = k/\sqrt{2} \tag{14}$$

To second order in u and v, in the particular case of a right handed helix and field vertical at helix entrance

$$\theta_1 = \pi/4, \quad \theta_2 = 3\pi/4 \ , \tag{15}$$

it is

$$\begin{cases} b_x \approx \left[-1-\frac{1}{3}\left(2u^2+v^2\right)\right]\sin kz + \frac{2}{3}uv\cos kz \\ b_y \approx -\frac{2}{3}uv\sin kz + \left[1+\frac{1}{3}\left(u^2+2v^2\right)\right]\cos kz \\ b_z \approx -\sqrt{2}\left[v+\frac{1}{3}\left(u^2v+\frac{2}{3}v^3\right)\right]\sin kz - \sqrt{2}\left[u+\frac{1}{3}\left(\frac{2}{3}u^3+uv^2\right)\right]\cos kz \end{cases} \tag{16}$$

The equation for the trajectory in a stationary field is

$$\frac{\mathrm{d}\beta}{\mathrm{d}t} = \beta \times \Omega \tag{17}$$

with the definitions

$$\Omega = \frac{e\mathbf{B}}{m\gamma}, \quad \beta = \frac{\mathbf{v}}{c}, \quad \gamma = \frac{E}{mc^2} = \frac{1}{\sqrt{1-\beta^2}} \tag{18}$$

By integration of Eq. (17) the para-axial trajectory is found

$$\begin{cases} x = x_0 + \left(x'_0 - \frac{\Omega_0}{k}\sin\phi_0\right)z - \frac{\Omega_0}{k^2}\left[\cos(kz+\phi_0) - \cos\phi_0\right] \\ y = y_0 + \left(y'_0 + \frac{\Omega_0}{k}\cos\phi_0\right)z - \frac{\Omega_0}{k^2}\left[\sin(kz+\phi_0) - \sin\phi_0\right] \end{cases} \tag{19}$$

Let us now calculate the integrated field along this trajectory, using the expansion for the field components. The integrals will be a function of the particle initial position and angle. In the simplifying assumptions

$$\begin{aligned} &kL = 2\pi \\ &x'_0 = \frac{\Omega_0}{k}\sin\phi_0 = -\frac{\Omega_0}{\sqrt{2}k}, \\ &y'_0 = -\frac{\Omega_0}{k}\cos\phi_0 = \frac{\Omega_0}{\sqrt{2}k} \end{aligned} \tag{20}$$

with L the length of the helix, we obtain to second order in x_o, y_o

$$\begin{cases} \int b_x dz = -\frac{1}{48\pi^2}(\Omega_0 L)^2 L - \frac{1}{12}\Omega_0 L x_0 \\ \int b_y dz = -\frac{1}{48\pi^2}(\Omega_0 L)^2 L + \frac{1}{12}\Omega_0 L y_0 \end{cases} \tag{21}$$

This Eq. shows that the quadratic terms, in $x_0^2, x_0 y_0, y_0^2$, vanish.
A numerical example (Siberian Snakes for RHIC, at injection[8]) is

$$\gamma = 25, \quad B = 4\,T, \quad L = 2\,m$$
$$\Omega_0 L = 0.0978, \quad \frac{1}{12}\Omega_0 L = 8.15\,10^{-3}, \quad \frac{1}{12\pi^2}(\Omega_0 L)^2 L = 8.08\,10^{-5}\ m$$

Numerical integration. LTB Equation. Example of a Siberian Snake for RHIC.

The helical field (9) has been calculated numerically and the result expressed as an expansion of the form[9]

$$b_i = \sum_{j,k=0}^{N} b_{ijk} x^j y^k \ . \tag{22}$$

The result shows a substantial sextupole and decapole contribution to the transverse field plus x-y coupling, but no quadrupole or octupole (similar results are obtained with a Blewett-Chasman field). From the numerical calculation of

the trajectories of a distribution of particles in phase space, the resulting transfer matrix for a helical dipole was derived by least squares fitting. The results can also be represented fairly well with a first order analytical matrix[10].

The rotation of the proton spin in a helical snake, consisting of four right-handed 4-Tesla helices of one period each, has been also calculated by simultaneous numerical integration of the BMT Equation[11] (s is the unitary 3-dimensional spin vector)

$$\frac{\mathrm{d}\mathbf{s}}{\mathrm{d}t} = C_1 \mathbf{s} \times \Omega + C_2 (\beta \cdot \Omega) \mathbf{s} \times \beta \tag{23}$$

with the definitions

$$C_1 = 1 + G\gamma; \quad C_2 = -\frac{G\gamma^2}{1+\gamma}; \quad G = \tfrac{1}{2} g - 1; \quad g = 5.58 \text{ (proton)} \tag{24}$$

The results for a proposed Siberian Snake for RHIC are shown in Fig. 1.

References

[1] Ya. S. Derbenev and A.M. Kondratenko, JETP 35 (1972) 230; *Part. Accel* 8 (1978) 115

[2] E.A. Perevedentsev, V. Ptitsin and Y. Shatunov , informal communication also reported by Yu M. Ado and E. A. Ludmirsky in *Acceleration of Polarized Protons in the Fermilab Tevatron*, Progress Report of the SPIN collaboration, August 1, 1994

[3] R. Gupta, E.Willen (Brookhaven), Private Communication

[4] J.P. Blewett and R. Chasman, *J. Ap. Phys*, 48, No.7 (1977) p.2692

[5] S. Krinsky, in *Wiggler Meeting* (A.Luccio, A.Reale, S.Stipcch editors), Frascati, June 29-30, 1978, p.95.

[6] E.g. A.Luccio and S.Krinsky, in *Free -Electron Generators of Coherent Radiation*, Vol.8, Addison-Wesley, Reading 1982, p.181.

[7] M.Abramowitz and I.A.Stegun, *Handbook of Mathematica Functions*, U.S.D.of Commerce, (1964), p.376

[8] T. Roser, presented to "Spin '94", Bloomington, Indiana, Sept. 15-22, 1994

[9] A. Luccio, Brookhaven AGS/AD/Tech.Note No.399, August 15, 1994

[10] E.D.Courant, Private Communication.

[11] V.Bargmann, L.Michel, and V.L.Telegdi, *Phys. Rev. Letters* 2(1959) p.435. See also: J.D.Jackson, *Classical Electrodynamics*, Wiley, New York, 2.nd edition (1962) p.556

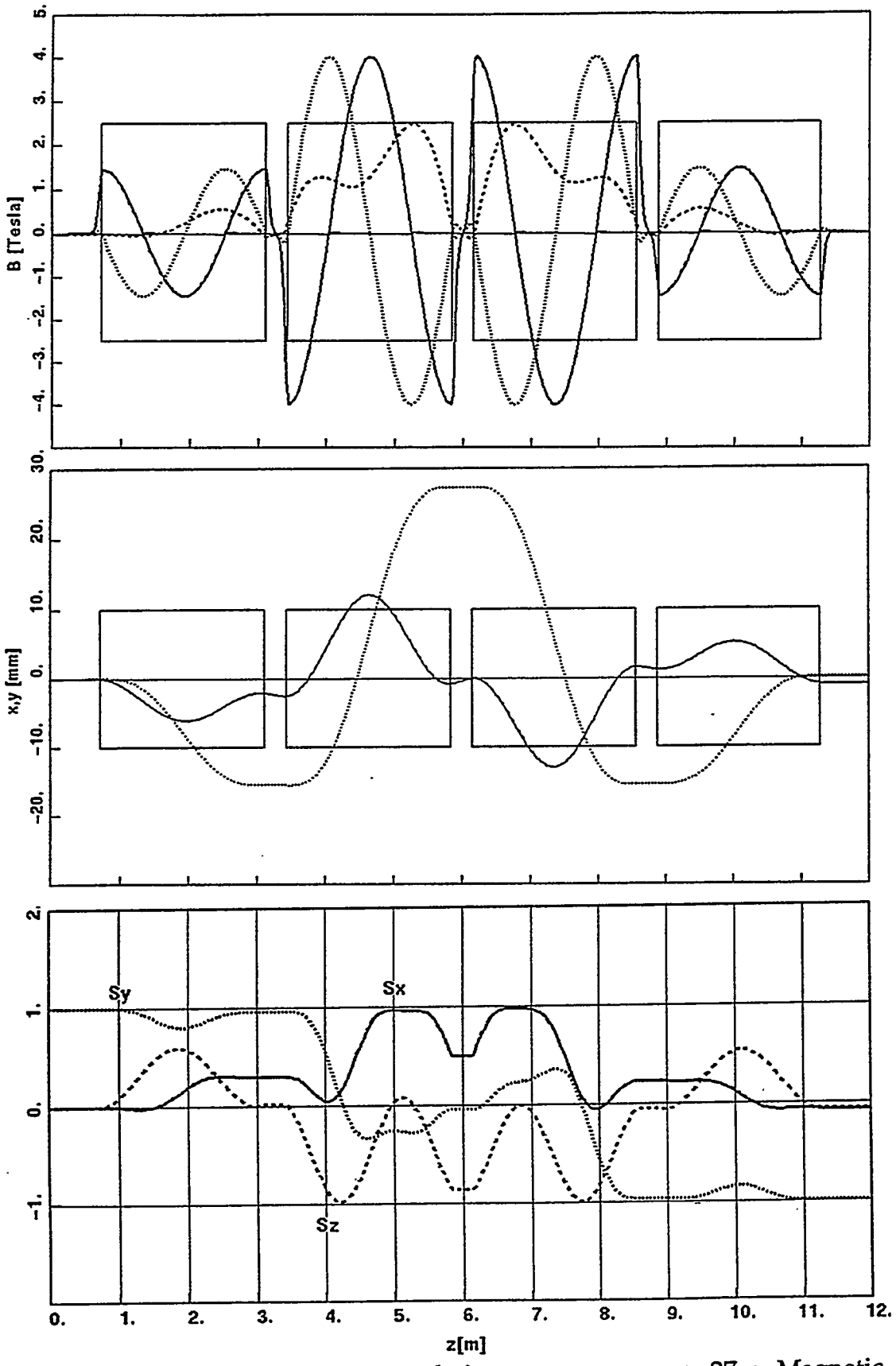

Fig. 1. A Siberian Snake for RHIC at relative proton energy $\gamma = 27$. a- Magnetic field (z-component -dotted- X10); b- Trajectories; c- Spin components.

Alfredo Lucero
1994

Halbach Arrays in Precision Motion Control

David L. Trumper and Mark E. Williams
Mechanical Engineering Department
Massachusetts Institute of Technology
Cambridge, MA 02139

Abstract

The Halbach array was developed for use as an optical element in particle accelerators. Following up on a suggestion from Klaus Halbach, we have investigated the utility of such arrays as the permanent magnet structure for synchronous machines in cartesian, polar, and cylindrical geometries. Our work has focused on the design of a novel Halbach array linear motor for use in a magnetic suspension stage for photolithography. This paper presents the details of the motor design and its force and power characteristics.

1 Introduction

With the advent of rare earth magnetic materials which combine high remanence and coercive force, new application areas have opened for synchronous permanent magnet machines. Typically, such machines use periodic permanent magnet structures wherein the magnetization vector is directed purely normal to the machine air gap. The magnitude of this magnetization alternates periodically as a function of the dimension parallel to the machine air gap.

An interesting alternative to this conventional solution, which has not yet been widely used in synchronous machines, is the magnet array geometry introduced by Halbach for use in particle accelerator optical elements and advanced synchrotron light sources. In this geometry, the magnetization vector in the array has both gap-normal and gap-tangential periodic components.

The purpose of this paper is to demonstrate that the Halbach array is highly applicable for magnetic excitation in synchronous machines. To this end, we present the geometry of Halbach arrays in cartesian, polar, and cylindrical coordinates. We also present the design of a cartesian linear motor which has been optimized for use in conjunction with a class of high-precision magnetic suspension stages for photolithography. The paper gives analytical solutions for this motor's fields, forces, commutation structure, and power dissipation; and develops results for the power-optimum thickness of the stator windings. Finally, we suggest that an equivalent Halbach geometry electromagnet may find utility in areas such as magnetically levitated trains.

2 Overview of Halbach arrays

For the present purposes, the Halbach array has the following advantages: The fundamental field is stronger by 1.4 than with a conventional array, and thus the power efficiency of the motor is doubled. The array does not require an iron backing sheet, and so can be bonded directly to non-ferrous substrates such as aluminum or ceramic which may have desirable structural properties. The magnetic field is more purely sinusoidal than that of a conventional magnet array, resulting in a simple control structure. Finally, the array has very low back-side fields, and thus requires less shielding in low-field applications.

The key concept of the Halbach array [1,2] is that the magnetization vector should rotate as a function of distance along the array so as to maximally aid the desired field distribution. In fact if the vector rotates continuously, the field on one side of the array will be identically zero, while the field strength on the other side of the array is doubled relative to an array with a sinusoidally varying purely vertical magnetization. The choice of the direction of rotation determines which side of the array is the strong side and which is the weak side.

While the ideal case calls for continuous rotation, in practice it is not possible to construct magnetic material with a continuously rotating easy axis, nor to magnetize this material in the proper pattern if it could be constructed. Thus practical implementations of Halbach arrays are assembled from blocks of magnetic material which are each uniformly magnetized in a desired axis. By proper choice of the block magnetic axes, a close approximation of the ideal case can be achieved. As mentioned previously, the Halbach arrays have geometries useful for synchronous machines in cartesian, polar, and cylindrical coordinates. These correspond to magnet arrays for planar linear, cylindrical rotary, and cylindrical linear motors, respectively.

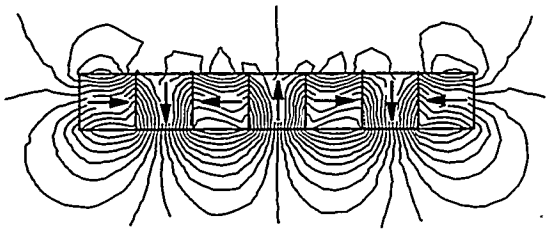

Figure 1: Cartesian Halbach array.

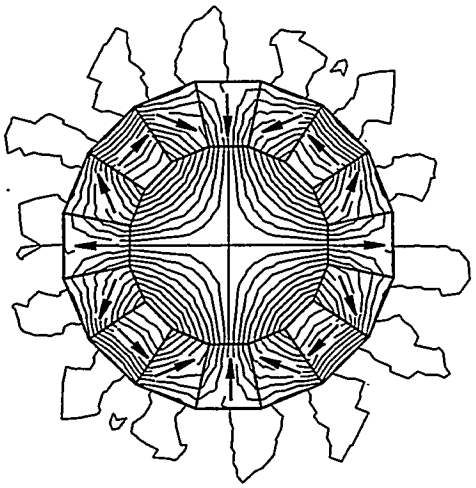

Figure 2: Interior Halbach quadrupole.

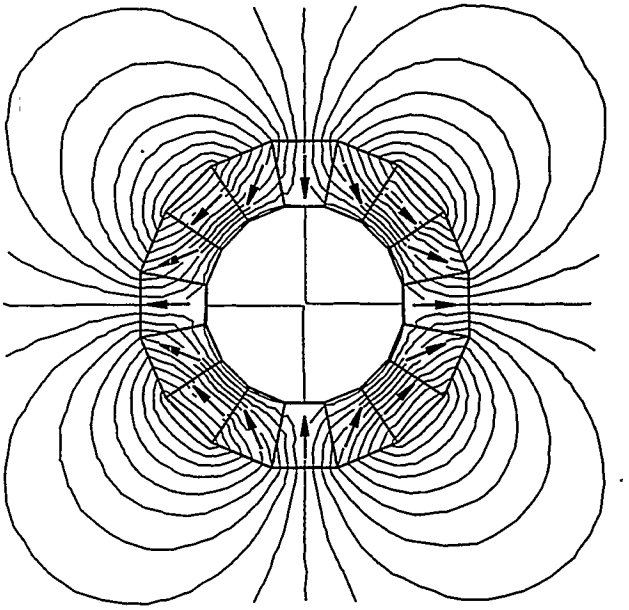

Figure 3: Exterior Halbach quadrupole.

The finite element solution of the field pattern for a section of cartesian Halbach array is shown in Fig. 1. The arrows in each block indicate the direction of magnetization. This particular array uses four blocks per period, with the magnetization axis rotating by 90 degrees in each subsequent block. Further, the array thickness is equal to one quarter of the spatial period and thus this array is easily fabricated, since the blocks are identical and are simply rotated as the array is assembled. We later show that the fundamental field on the strong side of this array is within 90% of the field of the ideal array in which the rotation is continuous. Thus this is the magnet array we have adopted for the linear motor which drives our magnetic bearing stage.

Finite element solutions of the field patterns for two polar Halbach quadrupole arrays are shown in Figs. 2 and 3. The arrows in each block indicate the direction of magnetization. These particular arrays use eight blocks per period, with the magnetization axis rotating by 45 degrees in each subsequent block relative to the radius vector through the block center. Note that the only difference between the two arrays is in the direction of rotation of the magnetization vector. In Fig. 2 the vector rotates clockwise as the array is traversed in the clockwise sense, and the field is concentrated on the *inside* of the array; in Fig. 3 the vector rotates in the opposite direction and the field is concentrated on the *outside* of the array. Dipoles and higher-order multipoles can also be constructed in this geometry by choice of the number of rotations of the magnetization vector encountered in one circuit around the annulus. In particle accelerators, such arrays are used for focusing and otherwise manipulating the particle beam. To a motor designer it is clear that this polar array can be used as either the rotor or stator of a rotary synchronous machine.

The geometry of a magnet array suited to a cylindrical linear motor is shown in cross-section in Fig. 4. As shown in the figure, the magnetization rotates about a vector tangent to the cylinder, and is constant in r-θ direction and magnitude as a function of the azimuthal coordinate. The fabrication of this motor requires two types of permanent magnets which are in the shape of identical annuli, i.e., one with axial magnetization and one with radial magnetization. Both can be readily fabricated. In this case, the controlled motion is along the axis of the tube, and the stator takes the form of annular coils arranged axially along the surface of a cylinder. Such a motor can be made to be highly efficient since both cross-axis fringing fields and winding end-turns are eliminated, due to the fact that there is no transverse boundary. Again, by choice of the direction of magnetization rotation, the working field of this cylindrical array can be located on either the outside or inside of the tube, as dictated by a particular design application. When viewed in a transverse section, the field pattern for this motor is similar to that of the cartesian array and thus is not shown herein.

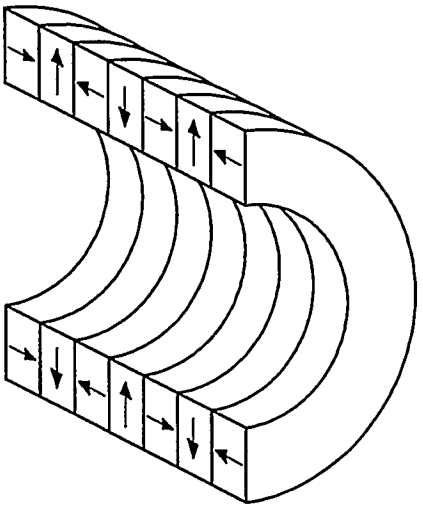

Figure 4: Cylindrical Halbach array in cross-section.

3 Magnetic bearing stage for photolithography

The authors have previously reported on the design of a magnetic bearing stage for precision motion control in photolithography [3–5]. The function of a photolithography stage is to position a semiconductor wafer in six degrees of freedom so as to align a die site on the wafer with the image plane of the lithographic lens in order to expose subsequent circuit layers in precise alignment. The stage must provide 200 mm travel[1] in the plane of the wafer (X and Y axes) so that any portion of the wafer can be positioned under the lens, and must also provide approximately 300 μm travel normal to the wafer for fine focusing. In current lithography systems each die site is locally levelled and rotationally aligned to the image plane, so the stage must also provide milliradian-scale rotations. The stage must be able to rapidly move from die-site to die-site (typically 20 mm apart) and thus fast settling is important. Our design goal is to step 20 mm and settle to the required precision in under 200 msec. At a particular die site, the stage position must be maintained with a standard deviation better than 10 nm during the approximately 300 msec die-site exposure time. Thus both high speed and high precision are required.

A magnetic bearing stage is advantageous in this application, since the small focus and rotational alignment motions can be supplied for "free" given that the stage is in suspension. The magnitude of the required motions is also compatible with the constraint that the magnetic bearing air gap not vary too much (i.e., motions at the air gap should be less than about 1 mm) in order to obtain high power efficiency from the actuators.

It is possible to envision stages which have a "flying-puck" design in which a single moving part is suspended and controlled over the complete range of motion [3]. However, the actuator size and packaging constraints of such a design result in a stage which is excessively large and is inefficient in power and in the use of magnetic materials.

A more efficient design which we have adopted utilizes crossed axes, in which the base axis is a conventional mechanical linear slide (Y axis) which carries a magnetic bearing linear slide (X axis). This design yields a much more efficient motor structure and packaging factor.

Such a crossed-axis design takes advantage of the typical operation of a lithography machine. In normal operation, the stage is rastered in X across 10–20 die sites before a single step is made in Y in order to move to the next row of die sites. Thus the throughput performance of the machine is dominated by the X-positioning stage and depends much less upon the Y-positioning stage. Since the crossed-axis design allows a simple magnetic bearing structure and yields better performance and power efficiency, this is the design which we have adopted.

Given a crossed-axis design, the remainder of this paper focuses on the requirements of the X-positioning stage. These are travel of 200 mm in the X-axis, travel of 300 μm in the Y and Z axes, and milliradian-scale rotation about all three axes. These requirements have been addressed through the design of a linear magnetic bearing stage which is constrained in five degrees of freedom by variable reluctance magnetic bearings, and driven in the sixth degree of freedom by a permanent magnet linear motor. The magnetic bearing controls translations in Y and Z and rotations about all three axes. This bearing is described in [3–5] and will not be discussed further here. The use of a Halbach array in the design of the linear motor provides the focus for this paper.

To provide an indication of the positioning performance achievable with such a stage, Fig. 5 shows the X-axis step response of our first-generation magnetic linear bearing [5]. In this figure, the bearing is commanded to take a 200 nm step in the X-axis. The feedback in this axis is via a plane mirror laser interferometer, and the linear motor is digitally-controlled by a '386-based PC housing a laser interferometer interface card and analog output card. The 5 nm quantization of the interferometer is visible in the figure.

The bearing control is presently implemented in analog electronics; subsequent versions now in construction will use digital control in the bearing axes as well. The

[1]While for convenience some dimensions are given in other than meters, all variables in analytical expressions are in SI units.

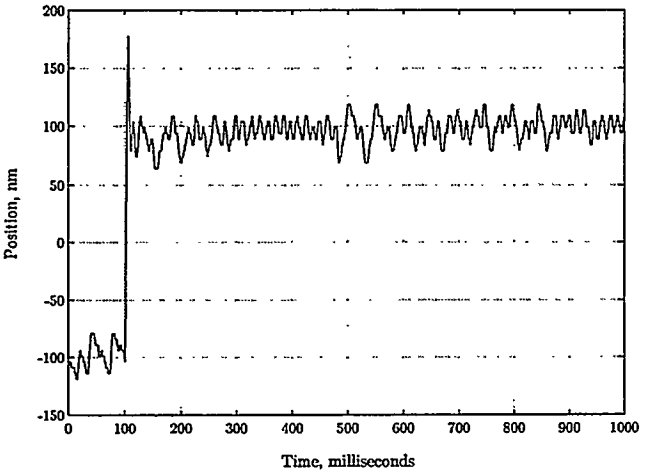

Figure 5: X-axis step response (200 nm) of first-generation linear magnetic bearing stage. Vertical axis is 50 nm per division; horizontal axis is 100 msec per division.

step response shows that we can achieve the required settling time and position precision. However, due to bearing nonlinearities, we are as yet unable to demonstrate the required acceleration necessary to achieve a 20 mm/200 msec step-and-settle time. Additionally, the motor used in this experiment uses a conventional magnet array with pure normal magnetization, and thus is not as power efficient as a similar motor using a Halbach magnet array. These limitations are to be corrected in a second-generation stage which is now in fabrication. The motor for this stage is described in more detail below.

4 Design issues

While a Halbach array is applicable for many permanent magnet machine designs, it is particularly suited to the linear magnetic bearing stage which we have designed. To demonstrate this suitability, it is necessary to understand the issues which must be addressed by the linear motor design and to understand those features which are unique to the magnetic bearing application. These are as follows:

1. No lateral loading of linear magnetic bearing; zero force at zero current; no cogging.
2. Low total power dissipation with no power dissipation on platen; low resistance thermal path from stator to air.
3. Stator wires in fixed frame, thus no need for leads onto moving platen.
4. Independently controllable levitation and drive forces with equal control authority in both degrees of freedom; wide-bandwidth, linear control.
5. Motor electromechanics analytically tractable, so analytical optimization of geometry and analytical derivation of control laws are possible.
6. Motor form factor compatible with system packaging.
7. Motor able to accommodate 300 μm changes in air gap with little loss in force capability; axial travel of 200 to 300 mm.

With respect to item 1, it is highly desirable that the linear motor exert no extraneous forces on the linear bearing. That is, when the motor control currents are zero, the linear motor forces in all axes should be zero. This is in contrast with a conventional linear motor which, if it uses iron, may exert significant off-axis forces due to the attraction of the permanent magnets to the iron in the stator. The requirement in our case for low extraneous forces is due to the limited force capabilities of the magnetic bearing and to the requirement that the bearing dissipate a minimum of power. Any side loads on the bearing result in unacceptable power dissipation or overloading of the magnetic bearing. Thus any motor structure must be either balanced (two-sided), or if single-sided, then the stator must be iron-free so that it is not strongly attracted to the permanent magnet array. The requirement for no cogging (item 1) greatly eases the task of precision control, and again suggest an ironless motor design. It is easier to package a planar single-sided motor as opposed to a more conventional slotted linear motor (item 6), since a slotted motor requires greater stage height and weakens the stage with respect to resonant modes. Additionally, a planar single-sided motor with the stator windings on the fixed base presents a large-area thermal path out of the machine (item 2). Higuchi [6] has constructed a two-sided variable reluctance linear motor for a magnetic suspension semiconductor wafer transporter. However this design is difficult to package in a lithography machine. A single-sided variable reluctance motor such as used in a Sawyer motor [7] has unbalance forces approximately ten times as large as the lateral force capability of the motor and thus requires an air bearing to counterbalance these forces. However, the use of a planar air bearing eliminates the ability to move normal to the motor air gap and thus eliminates the capability of the stage to provide focus motions. Thus the variable reluctance linear motor structure has been eliminated from consideration. An induction machine of necessity dissipates power on the moving stator and thus is not considered further. On the basis of the design considerations stated above we have chosen to develop the permanent magnet linear motor which is discussed in detail in the following section.

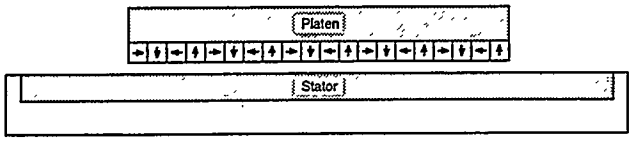

Figure 6: Cross section through linear motor. Not to scale.

5 Linear motor design and analysis

A simplified cross section of the second generation magnetic bearing stage is given in Fig. 6 in order to show the motor geometry. The linear motor consists of a 250 mm long cartesian Halbach array on the bottom surface of the moving platen, and a surface-wound stator of 500 mm length on the top surface of the stator base. This base is to be carried by the Y-stage, although the details are not discussed here. The motor has a depth of 150 mm into the paper.

In order to analyze the motor, we first study several possible magnet arrays and solve for their associated fields. The result is that the Halbach array field is a factor of $\sqrt{2}$ stronger than that of a conventional magnet array. We next solve for the fields due to the stator windings and then apply superposition to give the fields in the presence of both the stator and the Halbach array. Once the fields are known, the Maxwell stress tensor is used to solve for the normal and lateral motor forces, under the assumption of a two-phase sinusoidally-distributed stator. Inverting this analytical solution for the motor force yields the motor commutation laws which are used in the digital controller. Following this, the motor power dissipation is analytically determined and a power-optimal stator thickness is derived. Finally, the expected performance characteristics of our linear motor are presented.

5.1 *Analytical preliminaries*

To calculate the fields and thus the electromagnetic forces, the motor is idealized as a two-dimensional structure as shown in Fig. 7. Here the motor is assumed to have a depth of w into the paper and to extend indefinitely in the $\pm z$ direction. Edge effects in the y-direction are ignored in this analysis so that a two-dimensional model is applicable. The stator is fixed in the laboratory frame x, y, z (Y-slide motions are ignored herein). The primed coordinate frame x', y', z' is fixed in the layer of magnetization, and is displaced from the unprimed frame by the vector $(x_0+\Gamma)\bar{i}_x+z_0\bar{i}_z$. Throughout the following analysis vector quantities are represented by an overbar.

The magnetization layer is of thickness Δ, and within this layer the magnetization is represented by the Fourier

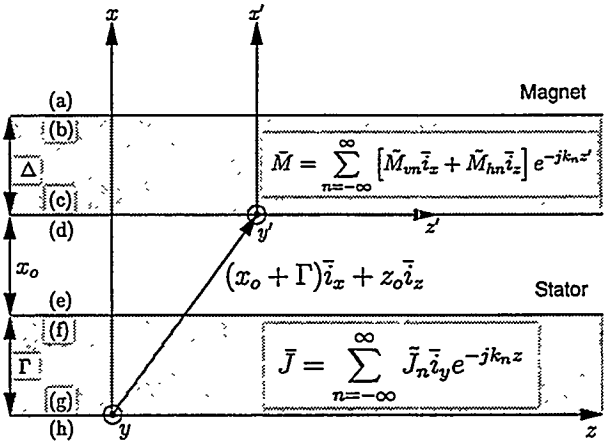

Figure 7: Idealized model for linear motor.

series

$$\overline{M}=\sum_{n=-\infty}^{\infty}\left[\tilde{M}_{vn}\bar{i}_x+\tilde{M}_{hn}\bar{i}_z\right]e^{-jk_nz'} \qquad (1)$$

Here $\tilde{M}_{vn}$ and $\tilde{M}_{hn}$ are the complex amplitudes of the n^{th} vertical and horizontal Fourier magnetization components, respectively. Assuming that the spatial period of the array is l, then $k_n = 2\pi n/l$ is the wavenumber of the n^{th} Fourier component.

The stator layer is of thickness Γ, and within this layer the current density is represented by the Fourier series

$$\overline{J}=\sum_{n=-\infty}^{\infty}\tilde{J}_n\bar{i}_y e^{-jk_nz} \qquad (2)$$

Here $\tilde{J}_n$ is the complex amplitude of the n^{th} current density component. Note that the stator current is purely y-directed and is assumed constant in x within the layer, although the analysis could be extended to address current densities which vary with x.

Letters (a), (b),...,(h) indicate the top and bottom surfaces of the four boundaries. Throughout this analysis, quantities with a tilde are the complex amplitudes of Fourier components; these represent temporal variations in both amplitude and spatial (z) phase. Variables with a superscript a,b,...h represent a quantity evaluated on the corresponding boundary. The notation and analytical approach used herein follow [8], chapters 2, 3, and 4.

5.2 *Cartesian magnet arrays*

In this section we compare the fields of four possible magnet array topologies shown in Fig. 8. The top row of the figure shows topologies for the ideal Halbach array (A)

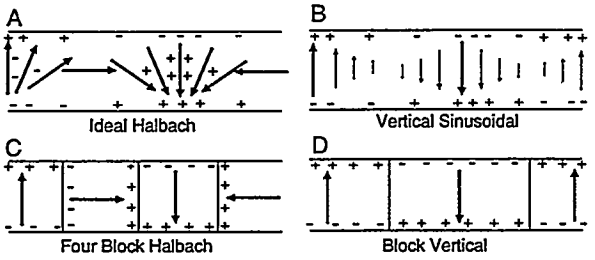

Figure 8: Four possible cartesian magnet arrays.

and the vertical sinusoidal array (B) where the magnetization varies sinusoidally with the lateral dimension. It is not practical to fabricate either of the arrays in the top row. The bottom row shows a cartesian Halbach array with four blocks per period and thus ninety degree rotations per block (C) and a conventional magnet array with alternating vertical magnetized blocks (D). The figure also shows the magnetic charge $\rho_m = -\nabla \cdot \mu_0 M$ associated with each geometry. Note that the Halbach arrays have charge within the layer associated with the spatially varying horizontal component of magnetization as well as the magnetic surface charge associated with the termination of vertical magnetization in all four arrays.

In order to compare the arrays, we assume that the magnetic material has a peak magnetization of M_0. Further, since the stator contains no iron, once the magnetic scalar potential ψ due to the magnet array is known on the upper (a) or lower (d) boundary it is known throughout the corresponding half-space, and thus the associated fields are also known. Thus it is reasonable to compare the array field strength through the value of the scalar potential on boundaries (a) and (d). Using the analysis presented in Appendix A, we can show that the fundamental components of the potentials of the four arrays are as follows:

$$\begin{aligned} \psi^d_{1A} &= F(M_0,\Delta,k_1,z') & \psi^a_{1A} &= 0 \\ \psi^d_{1B} &= \tfrac{1}{2}F(M_0,\Delta,k_1,z') & \psi^a_{1B} &= -\psi^d_{1B} \\ \psi^d_{1C} &= \tfrac{2\sqrt{2}}{\pi}F(M_0,\Delta,k_1,z') & \psi^a_{1C} &= 0 \\ \psi^d_{1D} &= \tfrac{2}{\pi}F(M_0,\Delta,k_1,z') & \psi^a_{1D} &= -\psi^d_{1D} \end{aligned} \tag{3}$$

where $F(M_0,\Delta,k_1,z') \equiv -(M_0/k_1)(1-e^{-k_1\Delta})\cos k_1 z'$ is introduced to emphasize that this function is common to all four arrays.

The first thing to notice is that the Halbach arrays have zero fundamental on the upper surface, whereas the vertical arrays have vertically antisymmetric fields. The highest potential magnitude is for the ideal Halbach array (A), whereas the vertical sinusoidal array (B) is weaker than (A) by a factor of 2. However, the block Halbach array (C) has a potential which is within $2\sqrt{2}/\pi$ or about 90% of the ideal case (A). Further, the block Halbach array (C) is stronger than the block vertical array (D) by a factor of $\sqrt{2}$. For the ideal Halbach array (A) it can be further shown that there are no higher Fourier components on either surface. In the case of the block Halbach array (C), the next component on the strong side (d) above the fundamental is $n = 5$, whereas for the block vertical array (D), an $n = 3$ component is present. Thus the Halbach array yields a more purely sinusoidal field, which simplifies the task of commutation. As a final point, the term $(1-e^{-k_1\Delta})$ appearing in $F(M_0,\Delta,k_1,z')$ is approximately equal to 0.8 for $\Delta = l/4$. Thus the block array which uses identical square magnets has a field strength within 80% of that obtainable from an infinite thickness array. Since the block Halbach array provides the highest fields for the arrays which can be fabricated, it is solely considered in the subsequent motor analysis.

5.3 *Stator fields*

Since we intend to use the Maxwell stress tensor to solve for the motor forces, it is only necessary to know the system fields along one air-gap boundary. For the present purposes boundary (d) is chosen. There are several approaches to solving for these stator fields; since this is a conventional problem, only the end results are given. Specifically, the complex amplitude of the n^{th} component of the vertical field on boundary (d) due to the stator is

$$^{S}\tilde{H}^d_{xn} = \frac{j\tilde{J}_n}{2k_n}e^{-\gamma_n x_0}(1-e^{-\gamma_n \Gamma})e^{-jk_n z_0} \tag{4}$$

Similarly the horizontal component is

$$^{S}\tilde{H}^d_{zn.} = \frac{-\tilde{J}_n}{2\gamma_n}e^{-\gamma_n x_0}(1-e^{-\gamma_n \Gamma})e^{-jk_n z_0} \tag{5}$$

where $\gamma_n \equiv |k_n|$. Making use of $z' = z - z_0$, these complex amplitudes are expressed with respect to the primed frame. That is, we choose to consider boundary (d) as fixed in the magnet and thus in the primed frame.

5.4 *Total fields*

Given the potentials driven by the magnet array which were determined in section 5.2, the magnetic field is solved for as $\overline{H} = -\nabla\psi$. Evaluating these fields on boundary (d) gives the complex amplitudes on the boundary which are due to the magnet, i.e., $^{M}\tilde{H}^d_{xn}$ and $^{M}\tilde{H}^d_{zn}$. The total complex amplitudes at the boundary are then given by $\tilde{H}^d_{xn} = {}^{S}\tilde{H}^d_{xn} + {}^{M}\tilde{H}^d_{xn}$, or upon expanding

$$\begin{aligned} \tilde{H}^d_{xn} &= \frac{j\tilde{J}_n}{2k_n}e^{-\gamma_n x_0}(1-e^{-\gamma_n \Gamma})e^{-jk_n z_0} \\ &\quad +(\tilde{M}_{vn} - j\frac{\gamma_n}{k_n}\tilde{M}_{hn})(1-e^{-\gamma_n \Delta})/2 \end{aligned} \tag{6}$$

and by $\tilde{H}^d_{zn} = {}^S\tilde{H}^d_{zn} + {}^M\tilde{H}^d_{zn}$, or upon expanding

$$\tilde{H}^d_{zn} = \frac{-\tilde{J}_n}{2\gamma_n} e^{-\gamma_n x_0}(1 - e^{-\gamma_n \Gamma}) e^{-jk_n z_0} + (-j\frac{k_n}{\gamma_n}\tilde{M}_{vn} - \tilde{M}_{hn})(1 - e^{-\gamma_n \Delta})/2. \quad (7)$$

5.5 *Motor forces*

As presented in [8], the stress tensor for magnetically-linear materials associated with the Korteweg-Helmholtz force density is

$$T_{ij} = \mu H_i H_j - \frac{\mu}{2} H_k H_k \quad (8)$$

using the Einstein summation convention where since the k's appear twice in the same term they are to be summed from one to three. The force acting on a volume of the magnet array is given by the integral of the stress tensor over the surface of the volume. For a spatially-periodic structure, the integration is simplified if the volume encloses an integer number of periods. In this case the components on the z-faces of the volume cancel due to symmetry. We can consider the upper surface of the volume to extend to infinity, where the fields are zero and thus the only contribution is along the bottom surface which we take to lie on boundary (d).

If the lower surface encloses an integer number of periods and is of area A, then the x-directed force acting on the enclosed section of magnet array is given by

$$F_x = -A\langle T^d_{xx}\rangle_z = -\frac{A\mu_0}{2}\langle H^d_x H^d_x - H^d_z H^d_z\rangle_z, \quad (9)$$

and the z-directed force acting on the enclosed section of magnet array is given by

$$F_z = -A\langle T^d_{xz}\rangle_z = -A\mu_0\langle H^d_x H^d_z\rangle_z, \quad (10)$$

where the angle bracket expression $\langle\cdot\rangle_z$ indicates the spatial average of the quantity enclosed by the brackets. The minus sign appears because the bottom surface has an outwardly-directed normal in the $-x$-direction. A useful identity is the spatial averaging theorem ([8], section 2.15)

$$\left\langle \sum_{n=-\infty}^{\infty} \tilde{A}_n e^{-jk_n z} \sum_{m=-\infty}^{\infty} \tilde{B}_m e^{-jk_m z} \right\rangle_z = \sum_{n=-\infty}^{\infty} \tilde{A}_n \tilde{B}_{-n} = \sum_{n=-\infty}^{\infty} \tilde{A}_n \tilde{B}^*_n \quad (11)$$

where the last step holds if the Fourier series represents a real function since the components must then possess conjugate symmetry.

Although the analysis can be carried out more generally, in the following we assume that the stator currents are sinusoidally distributed with a fundamental period of l and thus that $\tilde{J}_n$ is equal to zero for $n \neq \pm 1$. Specifically, we let $\tilde{J}_1 = J_a + jJ_b$, and $\tilde{J}_{-1} = J_a - jJ_b$. That is, $2J_a$ is the peak phase A current density and $2J_b$ is the peak phase B current density. The above assumption is reasonable since it is primarily the fundamental field components which are responsible for force production. Further, in application, the spatial currents are driven to resemble a sinusoid and thus the assumption is accurate for our purposes. Under this assumption, applying (11) to (9) and (10), and using (6) and (7) yields, after some algebra, the forces acting on one spatial period of the magnet array as

$$\begin{bmatrix} F_{x\lambda} \\ F_{z\lambda} \end{bmatrix} = \mu_o M_o G e^{-\gamma_1 x_o} \begin{bmatrix} -\sin\gamma_1 z_o & \cos\gamma_1 z_o \\ \cos\gamma_1 z_o & \sin\gamma_1 z_o \end{bmatrix} \begin{bmatrix} J_a \\ J_b \end{bmatrix} \quad (12)$$

where $F_{x\lambda}$ and $F_{z\lambda}$ are the x-directed and z-directed forces per spatial wavelength, respectively. Here $\mu_o M_o$ is the remanence of the permanent magnets ($\simeq 1.2$ T for neodymium-iron-boron). The constant

$$G = \frac{\sqrt{2}wl^2}{\pi^2}(1 - e^{-\gamma_1 \Gamma})(1 - e^{-\gamma_1 \Delta}) \quad (13)$$

contains the effects of the motor geometry. The x_0 and z_0 dependencies have been explicitly retained since these variables represent motion of the magnet array relative to the stator.

In an implementation, densities J_a and J_b are established by two sinusoidally-distributed windings which we can model as having a peak turns density of η_0 turns per meter squared and terminal currents I_a and I_b, respectively. In this case, $J_a = I_a\eta_0$ and $J_b = I_b\eta_0$. However, for present purposes, the analysis will be carried out in terms of current densities.

For the purposes of control, the motor commutation laws are derived by inverting (12) to yield

$$\begin{bmatrix} J_{as} \\ J_{bs} \end{bmatrix} = \frac{e^{\gamma_1 x_o}}{\mu_o M_o G N_m} \begin{bmatrix} -\sin\gamma_1 z_o & \cos\gamma_1 z_o \\ \cos\gamma_1 z_o & \sin\gamma_1 z_o \end{bmatrix} \begin{bmatrix} F_{xd} \\ F_{zd} \end{bmatrix}, \quad (14)$$

where N_m is the number of spatial periods l of the magnet array which interact with the stator. Here F_{xd} and F_{zd} are signals that exist within the controller and represent the forces the controller is requesting to act on the entire motor in the x and z directions respectively. The signals J_{as} and J_{bs} are the current densities which are calculated to achieve the desired forces. These are scaled to take account of the winding density η_0 before being output to set the phase currents I_a and I_b, which are assumed to be controlled by current drive amplifiers. If the analytical model (12) is accurate, then the commutation laws (14) linearize and decouple the plant. The

controller which sets F_{xd} and F_{zd} is then a simple decoupled lead/lag compensator. In practice, since the bearing controls all lateral displacements, we have been setting $F_{xd} = 0$ (open-loop control) and only actively controlling lateral motion through F_{zd}. Thus in our present experiments the controller is single-input–single-output. The performance which can be achieved by such a control strategy was shown earlier in Fig. 5.

5.6 *Power dissipation*

In precision machines, power dissipation is a key factor due to the fact that materials change dimensions significantly even with small temperature variations. Thus a focus of our design efforts has been to build a highly power-efficient machine. One advantage of an analytical solution for the motor force characteristics is that this solution allows us to also analytically determine the force-power characteristics. This solution makes clear how the motor should be designed and scaled to maximize power efficiency. With this solution in hand, we can further derive a power-optimal thickness Γ for the stator.

The power dissipation density in a region of conductivity σ carrying a current density J is J^2/σ. Thus the power density in the stator is $P_{ds} = [(J_a - jJ_b)e^{j\gamma_1 z} + (J_a + jJ_b)e^{-j\gamma_1 z}]^2/\sigma$. This expression is averaged on z and then mutliplied by the volume of one spatial period to yield $P_\lambda = 2wl\Gamma(J_a^2 + J_b^2)/\sigma$, where P_λ is defined as the power dissipation per wavelength in the working region of the motor. By (14), the current density term $(J_a^2 + J_b^2)$ can be expressed in terms of the commanded forces. This allows us to solve for the total motor power dissipation P_t as

$$P_t = \frac{3N_s\pi^4\Gamma e^{2\gamma_1 x_0}(F_{xd}^2 + F_{zd}^2)}{N_m^2\sigma(\mu_0 M_0)^2 wl^3(1 - e^{-\gamma_1\Gamma})^2(1 - e^{-\gamma_1\Delta})^2} \quad (15)$$

where N_s is the total number of spatial periods l in the stator. The factor of three appears because we assume that the motor dissipates three times more power than that given by the ideal calculation, due to non-ideal packing factor in the windings, significant winding length in the end turns, and to fringing fields.

Note that this expression is independent of motion in z and depends upon the sum of the squares of the commanded forces. Note also that the power dissipation drops as the square of the permanent magnet remanence. Thus we design with high-remanence magnetic material. We can also see clearly here the confirmation of the result stated earlier, i.e., that since the Halbach array yields a field stronger by $\sqrt{2}$ relative to a conventional magnet array, the power efficiency of the motor is doubled.

Power grows exponentially with x_0, and thus it is important to run the motor at a small air gap. However, the problem is not severe, since the characteristic dimension to which x_0 is compared in the exponent is l. For instance if $l = 50$ mm, then at an air gap of $x_0 = 0.5$ mm, the power dissipation is only 14% higher than at zero air gap. Thus the motor force is not sensitive to vertical focusing motions, and the design satisfies our earlier-stated criteria (item 7).

We solve for the power optimal stator thickness as follows. The term in (15) that depends on Γ is $\Gamma/(1 - e^{-\gamma_1\Gamma})^2$. Setting the partial of this term with respect to Γ equal to zero yields a transcendental equation $1 + 2\gamma_1\Gamma = e^{\gamma_1\Gamma}$. Solving this numerically yields the minimum power solution $\gamma_1\Gamma \simeq 1.25$. Now, since $\gamma_1 = 2\pi/l$, we find $\Gamma \simeq l/5$ as the power optimal stator thickness.

As another way to minimize power, consider the motor scaling laws in power and force. Specifically, since power increases as the square of current and force increases linearly with current, if the motor area is increased by a factor of n, then the power required to achieve a given force is reduced by this factor. This result is apparent in (15), since if N_m and N_s are scaled by n, then the motor power dissipation P_t drops by this same factor. Following this reasoning, we have designed a large motor which takes advantage of the significant planar area available on the bottom surface of the lithography stage. This motor is described in more detail below.

5.7 *Example motor design*

As an example of the achievable performance, consider a motor with the following specifications: magnet area: 0.15 m wide by 0.25 m long, stator area: 0.15 m wide by 0.5 m long, $w = 0.15$ m, $l = 0.05$ m (five spatial periods in magnet array, $N_m = 5$, ten spatial periods in stator, $N_s = 10$), $\Gamma = l/5$ (power optimum), $\Delta = l/4$ (square magnet blocks), $x_0 = 2.5 \times 10^{-4}$ m, $\sigma = 5.6 \times 10^7$ S/m (copper), and $\mu_0 M_0 = 1.2$ T (NdFeB magnets). Substituting these values into (15) yields a motor power coefficient of about 2.6×10^{-3} W/N^2. For example, at 50 N force, the motor dissipates a total of 6.5 W.

To put this result in context, consider a 200 msec step-and-settle time with a 15 kg platen. Under this assumption, we calculate a power dissipation of 2.3 W while the stage is moving. Since the stage is held fixed for more than half the time while an exposure is in progress, the average power will be lower than 1.1 W. We estimate that given the low-resistance thermal path out of the stator, the winding temperature will rise less than 0.1° C. This shows that the motor meets the criteria for low power (item 2).

6 Maglev train electromagnets

Since permanent magnets can be thought of in terms of equivalent current sheets, there exists an electromagnetic

analog of the Halbach array, in which circulating currents with proper orientation replace the rotated permanent magnet blocks. Such an electromagnetic array has the advantage that its field can be constrained primarily to one side of the array. This topology has potential use in systems where low fields on the back side of the electromagnet are important, for instance in the superconducting electromagnets of maglev trains. Since there is no fundamental field on the back side of the array, and since the higher harmonics decay rapidly with distance from the array, it should prove far easier to shield the passenger compartment of a maglev train which uses a Halbach-type electromagnet vis-a-vis one which uses a conventional magnet [9]. This issue bears further study and can be addressed using analyses similar to those given herein.

7 Conclusions

This paper has presented the design of synchronous permanent magnet motors utilizing the Halbach array topology. The design of a cartesian linear motor has been developed in depth. This motor is optimized for use with a novel magnetic suspension linear bearing which is designed for photolithography. We have demonstrated that the motor is highly power efficient and have presented the key motor design constraints and performance characteristics. A second-generation magnetic suspension stage using this motor design is currently in construction. The insight obtained from studying the Halbach permanent magnet array geometry may prove useful in other applications such as maglev trains.

Acknowledgments

The authors wish to thank Klaus Halbach for his valuable suggestions regarding the suitability of his array designs for linear motors. This work has been supported by a grant from the GCA Unit of General Signal and through the first author's Presidential Young Investigator Award (NSF #DDM-9158054).

Bibliography

[1] Halbach, K., "Design of Permanent Multipole Magnets with Oriented Rare Earth Cobalt Material," Nuclear Instruments and Methods, 169, 1980, pp. 1–10.

[2] Halbach, K., "Physical and Optical Properties of Rare Earth Cobalt Magnets," Nuclear Instruments and Methods, 187, 1981, pp. 109–117.

[3] Trumper, D.L., "Magnetic Suspension Techniques for Precision Motion Control," Ph.D. Thesis, Dept. of Elec. Eng. and Comp. Sci., M.I.T., Camb., Mass., Sept., 1990.

[4] Trumper, D.L., and Slocum, A. H., "Five-Degree-of-Freedom Control of an Ultra-Precision Magnetically-Suspended Linear Bearing," NASA Workshop on Aerospace Applications of Magnetic Suspension Technology, Hampton, VA, Sept. 25–27, 1990.

[5] Trumper, D.L., and Queen, M.A., "Precision Magnetic Suspension Linear Bearing," NASA Int. Symp. on Mag. Susp. Tech., Hampton, VA, Aug. 19–23, 1991.

[6] Higuchi, T., and Kawakatsu, H., "Development of a Magnetically Suspended Stepping Motor for Clean-Room Transportation and Sample Handling," 11th Int. Conf. on Mag. Lev. Sys. and Linear Drives (Maglev '89), July 7-11, 1989, Yokohama, Japan, pp. 363–368.

[7] Sawyer, B.A., "Magnetic Positioning Device," U.S. Patent #3,376,578, Apr. 2, 1968.

[8] Melcher, J.R., *Continuum Electromechanics*, MIT Press, Camb., Mass., 1981.

[9] Tanaka, T., "Change in the Coil Distribution of Electrodynamic Suspension System, NASA Int. Symp. on Mag. Susp. Tech., Hampton, VA, Aug. 19–23, 1991, pp. 813–825.

Appendix A: Field Solution Details

This section provides the details which support the magnet array comparison presented in section 5.2. Given the magnetization (1), we seek a solution for the scalar potential ψ on the boundaries (a)–(d). Since superposition applies, the stator windings are ignored throughout the remainder of this appendix.

In the follwing, we assume that the potentials and fields are given by a Fourier series, i.e.,

$$\psi = \sum_{n=-\infty}^{\infty} \tilde{\psi}_n e^{-jk_n z'} \tag{16}$$

and

$$\overline{H} = \sum_{n=-\infty}^{\infty} \left[\tilde{H}_{xn}\bar{i}_x + \tilde{H}_{zn}\bar{i}_z\right] e^{-jk_n z'}. \tag{17}$$

The vertical component of magnetization terminates abruptly on the upper and lower boundaries and is constant in the volume; this creates surface charges on the upper and lower boundaries

$$\sigma_s^b = -\bar{n}\cdot[\mu_0\overline{M}^a - \mu_0\overline{M}^b] = \mu_0 \sum_{n=-\infty}^{\infty} \tilde{M}_{vn} e^{-jk_n z'} \tag{18}$$

and $\sigma_s^c = -\sigma_s^b$, respectively, where $\bar{n}$ is the surface unit normal. These surface charges are addressed through the jump conditions

$$\begin{aligned} \tilde{H}_{xn}^a - \tilde{H}_{xn}^b &= \tilde{M}_{vn} \\ \tilde{H}_{xn}^c - \tilde{H}_{xn}^d &= -\tilde{M}_{vn} \end{aligned} \tag{19}$$

and thus do not affect the solution within the magnetization layer.

Since the magnetization has a spatially-varying horizontal component, the volume contains a polarization

charge given by

$$\rho_m = -\nabla \cdot \mu_0 M = \mu_0 \sum_{n=-\infty}^{\infty} jk_n \tilde{M}_{hn} e^{-jk_n z'}. \quad (20)$$

Within the volume we seek a solution satisfying $\nabla \times \overline{H} = 0$, and thus $\overline{H} = -\nabla\psi$. Thus it also holds that

$$\tilde{H}_{zn} = jk_n \tilde{\psi}_n. \quad (21)$$

The field must additionally satisfy

$$\nabla \cdot \mu_0 \overline{H} = -\nabla \cdot \mu_0 \overline{M}. \quad (22)$$

Since the volume contains charge, we take the approach of determining a particular solution $\overline{H}_p = -\nabla\psi_p$ and a homogeneous solution $\overline{H}_h = -\nabla\psi_h$ where $\nabla \cdot \mu_0 \overline{H_p} = -\nabla \cdot \mu_0 \overline{M}$ and $\nabla \cdot \mu_0 \overline{H_h} = 0$.

In light of (20)–(22) the volume charge imposes the constraint on the particular solution

$$\tilde{\psi}_{pn} = \frac{j\tilde{M}_{hn}}{k_n}. \quad (23)$$

If we further consider that the total boundary potentials $\tilde{\psi}_n^b$ and $\tilde{\psi}_n^c$ are given, then the homogeneous solution is used to match these potentials, i.e.,

$$\begin{aligned} \tilde{\psi}_{hn} &= (\tilde{\psi}_n^b - \frac{j\tilde{M}_{hn}}{k_n}) \frac{\sinh k_n x'}{\sinh k_n \Delta} \\ &\quad -(\tilde{\psi}_n^c - \frac{j\tilde{M}_{hn}}{k_n}) \frac{\sinh k_n (x' - \Delta)}{\sinh k_n \Delta} \end{aligned} \quad (24)$$

Within the magnetization layer $\tilde{\psi}_n = \tilde{\psi}_{pn} + \tilde{\psi}_{hn}$. Then, since $H_x = -\partial\psi/\partial x'$, we find that

$$\begin{aligned} \tilde{H}_{xn} &= -k_n (\tilde{\psi}_n^b - \frac{j\tilde{M}_{hn}}{k_n}) \frac{\cosh k_n x'}{\sinh k_n \Delta} \\ &\quad +k_n (\tilde{\psi}_n^c - \frac{j\tilde{M}_{hn}}{k_n}) \frac{\cosh k_n (x' - \Delta)}{\sinh k_n \Delta}. \end{aligned} \quad (25)$$

Evaluating (25) at $x' = 0$ and $x' = \Delta$ yields

$$\begin{aligned} \begin{bmatrix} \tilde{H}_{xn}^b \\ \tilde{H}_{xn}^c \end{bmatrix} &= k_n \begin{bmatrix} -\coth k_n \Delta & \frac{1}{\sinh k_n \Delta} \\ -\frac{1}{\sinh k_n \Delta} & \coth k_n \Delta \end{bmatrix} \begin{bmatrix} \tilde{\psi}_n^b \\ \tilde{\psi}_n^c \end{bmatrix} \\ &\quad +j \begin{bmatrix} \frac{\cosh k_n \Delta - 1}{\sinh k_n \Delta} \\ -\frac{\cosh k_n \Delta - 1}{\sinh k_n \Delta} \end{bmatrix} \tilde{M}_{hn}. \end{aligned} \quad (26)$$

This result gives the *transfer relation* between the complex amplitudes of the boundary potentials $\tilde{\psi}_n^b$ and $\tilde{\psi}_n^c$ and the normal magnetic field $\tilde{H}_{xn}^b$ and $\tilde{H}_{xn}^c$ given the volume source $\tilde{M}_{hn}$. The first term on the right represents the homogeneous solution and the second term on the right represents the particular soultion. This transfer relation may be used to represent any region with a Fourier-transformable horizontal magnetization which is not a function of the vertical coordinate.

Since the bounded spaces at (a) and (d) are half-infinite, the transfer relations of [8], pg. 2.33, simplify to

$$\begin{aligned} \tilde{H}_{xn}^a &= \gamma_n \tilde{\psi}_n^a \\ \tilde{H}_{xn}^d &= -\gamma_n \tilde{\psi}_n^d. \end{aligned} \quad (27)$$

Further, since the boundaries are current-free, the potential is continuous, i.e.,

$$\begin{aligned} \tilde{\psi}_n^a &= \tilde{\psi}_n^b \\ \tilde{\psi}_n^c &= \tilde{\psi}_n^d. \end{aligned} \quad (28)$$

Equations (19), (26), (27), and (28) form a set of eight equations in eight unknowns which allow us to solve for the desired potentials on boundaries (a) and (d). After some manipulation, the result is

$$\tilde{\psi}_n^a = \frac{\tilde{M}_{vn}}{2\gamma_n}(1 - e^{-\gamma_n \Delta}) + \frac{j\tilde{M}_{hn}}{2k_n}(1 - e^{-\gamma_n \Delta}) \quad (29)$$

and

$$\tilde{\psi}_n^d = \frac{-\tilde{M}_{vn}}{2\gamma_n}(1 - e^{-\gamma_n \Delta}) + \frac{j\tilde{M}_{hn}}{2k_n}(1 - e^{-\gamma_n \Delta}). \quad (30)$$

All that remains is to determine the Fourier components associated with each magnet array. These are given by the analysis integrals

$$\tilde{M}_{vn} = \frac{1}{l} \int_0^l M_v e^{jk_n z'} dz' \quad (31)$$

and

$$\tilde{M}_{hn} = \frac{1}{l} \int_0^l M_h e^{jk_n z'} dz' \quad (32)$$

where M_v and M_h are the vertical and horizontal components of the magnetization within the array. Carrying out this analysis and then substituting into (29) and (30) yields the results given in section 5.2.

Halbach Array Motor/Generators
A Novel Generalized Electric Machine

B. T. Merritt, R. F. Post, G. R. Dreifuerst, D. A. Bender
Lawrence Livermore National Laboratory

Introduction

For many years Klaus Halbach has been investigating novel designs for permanent magnet arrays, using advanced analytical approaches and employing a keen insight into such systems. One of his motivations for this research was to find more efficient means for the utilization of permanent magnets for use in particle accelerators and in the control of particle beams. As a result of his pioneering work, high power free-electron laser systems, such as the ones built at the Lawrence Livermore Laboratory, became feasible, and his arrays have been incorporated into other particle-focusing systems of various types. This paper reports another, quite different, application of Klaus' work, in the design of high power, high efficiency, electric generators and motors. When tested, these motor/generator systems display some rather remarkable properties. Their success derives from the special properties which these arrays, which we choose to call "Halbach arrays," possess.

In August 1979, K. Halbach submitted a paper[1] entitled "Design of Permanent Multipole Magnets with Oriented Rare Earth Cobalt Material." In this paper, he presented a novel method of generating multipole magnetic fields using non-intuitive geometrical arrangements of permanent magnets. In subsequent publications [2-4], he further defined these concepts. Of particular interest to one of the authors (RFP) was the special magnet array that generated a uniform dipole field. In 1990 Post proposed the construction of an electric machine (a motor/generator) using a dipole field based on K. Halbach's array of permanent magnets. He further proposed that such a system should be employed as an integral part of "an electromechanical battery" (EMB), i.e., a modular flywheel system to be used as a device for storing electrical energy, as an alternative to the electrochemical storage battery.

This paper reviews Halbach's theory for the generation of a dipole field using an array of permanent magnet bars, presents a simple analysis of a family of novel "ironless" electric machines designed using the dipole Halbach array, and describes the results obtained when they were tested in the laboratory.

The Dipole Array

Although electric machines can be constructed using multipole fields based on the techniques introduced by K. Halbach, the dipole field offers some unique advantages for the construction of a high speed electric machine. Figure 1 shows an end view of a dipole Halbach array. Shown in the figure are the directions of magnetization of the bars and one quadrant of the computed lines of force produced by the array. Note the highly uniform field inside the array, and the near-cancellation of the field outside the array.

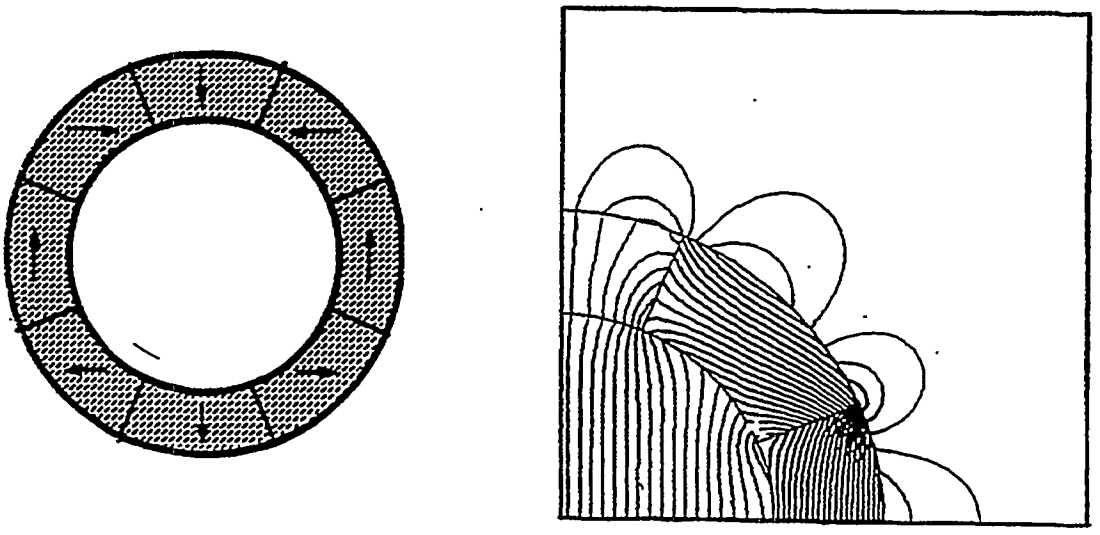

Figure 1. Cross Section and Field Lines of Halbach Array

Except near the ends of the array, or very near its inner surface, the dipole field inside a such an array is given by the expression derived by Halbach:

$$B_0 = B_r \; C_N \; \ln(r_2 / r_1) \qquad (1)$$

with r_1 and r_2 indicating the inside and outside radius of the magnet array, respectively, and B_r representing the remanent field of the permanent magnet material. If M is the number of segments in the magnet,

$$C_N = \mathrm{Sin}(2\pi/M)/(2\pi/M) \qquad (2)$$

giving $C_N = 0.90$ for M = 8 and $C_N = 0.97$ for M = 16. These equations are derived in reference 2.

When Equations (1) and (2) are compared with a computer code using the correct remanent field of the magnets, the code results agree within a percent or two of the analytical result. Arrays constructed using the high-field material, NdFeB, have measured fields that are found to be within a few percent of the predicted values.

Figure 2 is a field plot of a dipole field constructed using an eight segment Halbach array. The permanent magnets used for this dipole were ceramic; the field values measured are uniform to about three percent. The values for the field strength are those measured inside the Halbach array cylinder; the field decreases somewhat near the ends of the magnet array. See references for a detailed discussion and calculation of this decrease.

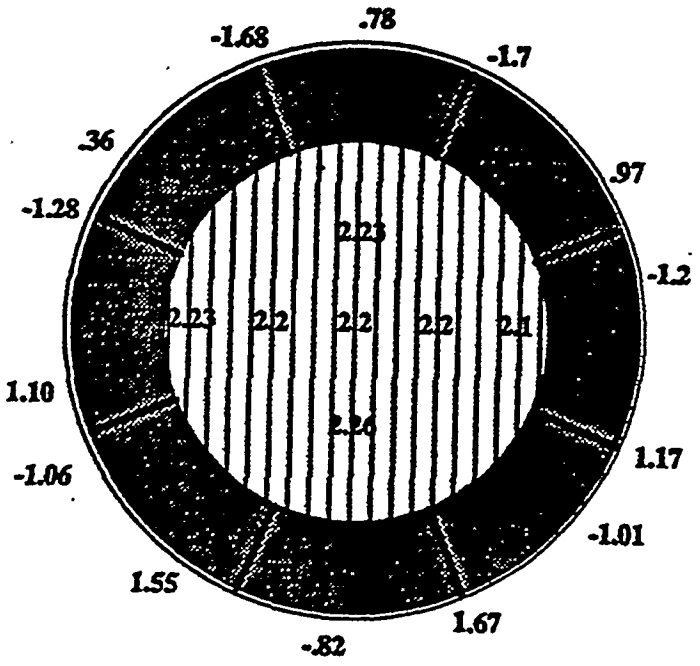

Figure 2. Measured Values of Halbach Array Field

Construction of the Generalized Motor/Generator

The design of a motor/generator using a dipole Halbach array is simplicity itself. Furthermore, since there are no iron laminations used in the design the theoretical prediction of the properties of such motor/generators is equally simple.

In order to construct a motor/generator, all that is required is to insert a single or multi-phase winding down the axis of the dipole field and provide relative motion between the field and the winding(s). Relative rotation then generates an EMF in the winding that is linearly related to the product of the

rotation speed and the amount of flux intercepted by the winding. In the case of a generator, the work performed in sustaining the relative motion between the windings and the field is transformed directly into ac electrical energy that flows out of the machine. Conversely, ac electrical energy flowing into the winding, if at the proper frequency and phase, is transformed into mechanical work that causes a relative motion between the windings and the field. At this point it is important to note that only a relative motion between the windings and the field is required; electric machines having either the windings or the Halbach array in motion could be constructed. There are advantages to each type depending upon the application.

Figure 3 shows a three phase winding inserted into the Halbach array field. Single phase or higher phase number machines can also be constructed. This paper concentrates on the three phase machine in which the dipole Halbach array surrounding the winding is rotating. This configuration has been employed by us in the application for which it was first proposed, electromechanical batteries (flywheel energy storage modules).

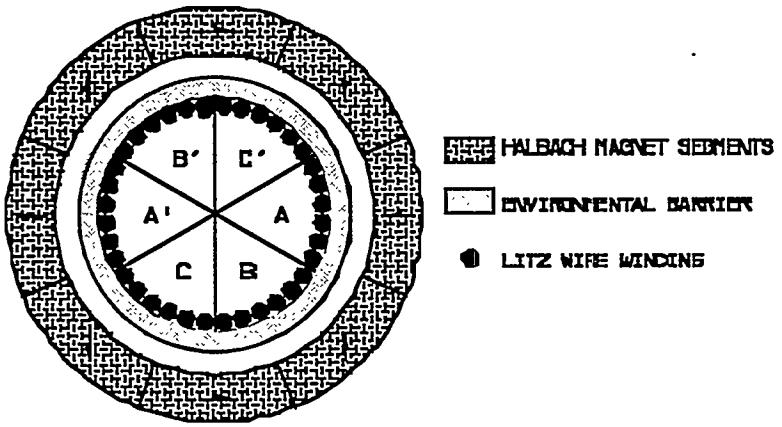

Figure 3. Halbach Array with Three Phase Winding

In order to calculate the induced EMF, consider first the simple case of a single turn winding. Assume for the moment that the winding is stationary and that the Halbach field, due to the relative motion, is given by

$$B(t) = B_0 \, \mathrm{Cos}(\omega t) \qquad (3)$$

Owing to the linearity of the system the induced EMF is given exactly by

$$V(t) = d\Phi/dt, \qquad (4)$$

where Φ is simply given by the product of the dipole magnetic field strength and the area, A, intercepted by the windings (with a small correction, usually

of order 10 to 20 percent, depending on the relative length of the windings and the magnets) for the fall-off of the field strength near the ends of the magnet array.

This expression then reduces to

$$V(t) = B_0 A\omega \, Sin(\omega t) \qquad (5)$$

where A is the area of the winding, i.e., its length multiplied by its transverse width, and w is the rotational velocity in radians per second.

For the case of multiple turns per winding, the voltage becomes

$$V(t) = K N B_0 \, \omega \, Sin(\omega t) \qquad (6)$$

where N is the number of turns and K is a geometric constant, close to unity, that accounts for the fact that the winding now has some physical width that spans an arc along the circumference of the cylinder upon which the windings are attached. This constant is readily calculated; it accounts for the relative decrease in magnetic field since a particular turn is no longer exactly aligned with the reference direction for the magnetic field. For such a turn the correction factor is equal to $\cos\beta$, where β is the angle between the reference for the magnetic field, usually zero, and the angle at which a particular turn resides. For a distributed winding with angular spread α (i.e. its two sides intercept a fraction $2\alpha/2\pi$ of the circumference), upon performing the average over this spread the factor K is given by the following expression:

$$K = 2 \, Sin(\alpha/2)/\alpha \qquad (7)$$

If $\alpha = 30°$, for example, $K = 0.989$.

Figure 4 is a schematic of the electric machine. It is to be interpreted on a per phase basis for machines having multiple phases. Note that this representation contains only linear elements, and also note that the value of magnetic field B_0 , that is to be used in calculating the induced voltage, is that of the Halbach array. In this ironless system, and for all feasible values of the winding currents, there is no "back reaction" between the stator windings and the inducing magnetic field. There is, of course, an effect of the winding inductance on the output voltage as well as the usual resistive drop. However, since the system is ironless, inductances are low, and with good design, the resistive drops are also low. As will be shown, not only is the power output very high, but the efficiency is also typically much higher than that of an iron-core machine of comparable physical size.

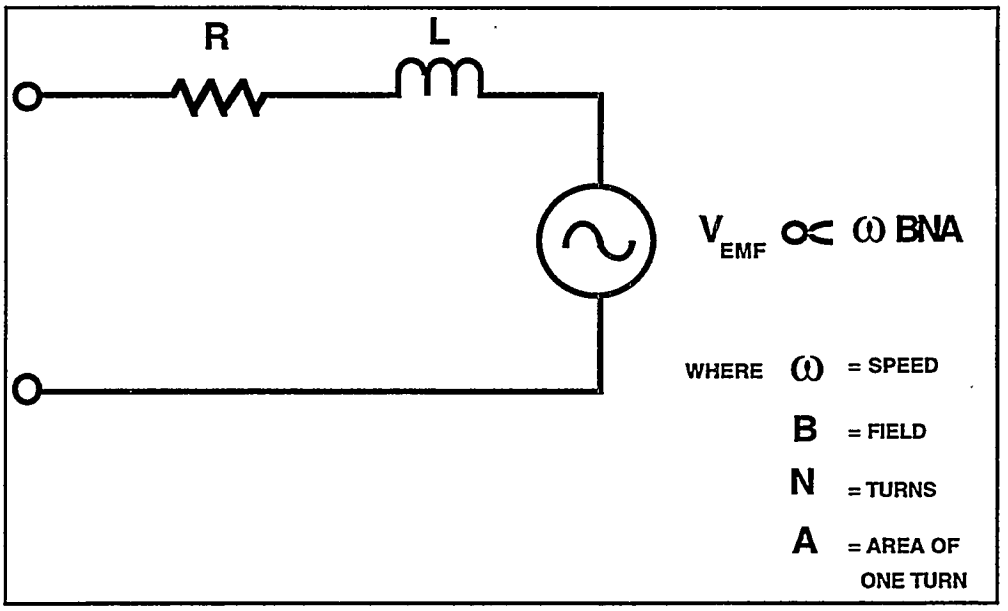

Figure 4. Equivalent Circuit for Electric Machine, per Phase Basis

The equations for torque are also straightforward. Consider again the case of a single turn winding and only one phase. The vector force on a conductor is given by

$$\mathbf{F} = 2I(\mathbf{L} \times \mathbf{B}) \tag{8}$$

where I is the current in the conductor, **L** is the vector path along the conductor and **B** is the vector magnetic field. The torque is then

$$\mathbf{T} = \mathbf{r} \times \mathbf{F}, \tag{9}$$

where **r** is the radius.

For a single turn rectangular winding with longitudinal length L, in a dipole field, the magnitude of the peak torque becomes

$$T = 2\,r\,L\,I\,B_0 \tag{10}$$

and for the multiple turn case, the peak torque becomes

$$T = 2\,r\,L\,I\,B_0\ K\,N, \tag{11}$$

where K is the geometric factor as before and N is the number of turns.

Owing to the complete linearity of this ironless system these simple equations form an adequate basis for the design of motor/generator systems employing a dipole Halbach array. We will later discuss the circuit-related

factors that must be employed in order to calculate the output power and the efficiency of such generators. Again, as noted, the absence of iron in the magnetic circuit means that only simple air-core inductances and winding resistances must be taken into account to calculate these quantities.

If the rms output voltage of each of the 3-phase windings is V_0, the winding inductance is L_0, and its resistance is R_0, then the output power of each phase into a resistive load with resistance R_L is given by the equation:

$$P = \frac{(V_0)^2}{R_L}\left\{\frac{1}{[1+(R_0/R_L)]^2+(\omega L_0/R_L)^2}\right\}, \text{ Watts/phase} \qquad (12)$$

The efficiency is then given by the expression:

$$\eta = \frac{R_L}{R_0 + R_L} \qquad (13)$$

Advantages

A fundamental advantage of a machine of this type has already been mentioned. That is, the fact that the machine can be constructed without the use of magnetic material other than the permanent magnets. There is no need for laminations or back iron. This has two major advantages. First the conventional core loss and eddy current loss in the laminations or back iron does not exist. The only loss in the machine will be losses in the windings. The second advantage is since there is no back iron or laminations required, the machine is inherently lightweight.

The uniform field also results in several important advantages. Since the field is truly uniform, the machine design is no longer constrained by the airgap size. This offers the opportunity to solve other system issues. For example, in the modular EMB application, it allows a vacuum barrier to be placed between the windings and the Halbach array without appreciable degradation of machine performance.

The field uniformity of the dipole Halbach array has another, very important result for the extraction of very high peak powers over short time scales. Conventional generators employing narrow gaps and iron laminations have a problem that is not encountered here. In such systems, where the drag torque caused by the power is a function of the gap spacing, there can exist a strong tendency to drive the rotating system into so-called "whirl" instability. Contrast this with our situation. Since the field is uniform, the torque is not a function of the displacement of the windings relative to the field (the windings only "know" that they are in a uniform rotating field, origin

"unknown"). Thus the potential, from this source, for whirl instability does not exist.

As mentioned earlier, the major loss mechanism in this type of machine is the losses in the windings. These losses can be minimized by increasing the amount of copper in the windings. There is a trade-off between the efficiency of the machine and the size of the winding. There is also a potential loss due to eddy currents in the conductors; since the field is always present, eddy currents will be induced in the conductors due to the relative motion between the windings and the field. This latter loss is easily controlled to low levels, i.e. a few watts, by the use of Litz wire.

Motor Types

Halbach array electric machines could be constructed in a conventional manner, whereby the Halbach array is stationary and the windings rotate within the array. As we have mentioned for use in our modular EMBs, the Halbach array machine has been constructed "inside out", with the windings stationary and the magnet array rotating around the windings. There are advantages to both types of construction; specific applications drive the choice.

In a conventional machine configuration, the Halbach array machine would look physically much like a dc machine; that is, the armature is on the rotor and the field is stationary. Such a machine could be operated as either a dc or ac device. If one uses slip rings to bring out the windings, the machine could be characterized as an ac machine. However, if now an electronic commutation circuit is added, the Halbach array machine can be characterized as a dc machine. If one desired, one could use a mechanical commutation as well.

The inherent advantage of this construction technique is that the inertia of the rotor is dominated solely by the mass of the windings since there are no laminations required. One can therefor envision the construction of a very high speed low inertia machine.

If the machine is configured, as we have done, in an "inside-out" geometry, the windings are stationary and readily accessible. Again, the machine can be characterized as either an ac or dc machine. The primary advantage of the inside-out construction is that it is readily adapted to evacuated systems (such as in our EMB) since there is no need for slip rings.

Our specific application, the EMB

As noted earlier, the impetus for the development of this new type of electric machine was our application to modular electromechanical batteries.[5,6,7] The EMB battery consists of a high-speed flywheel with an integral motor/generator suspended on magnetic bearings and in an evacuated housing. For practical use, a set of power electronics is coupled to this module. The flywheel and its motor/generator is a means for energy storage and extraction; the power electronics conditions electrical energy, both for adding energy to and extracting energy from the flywheel. Since the goal is to mimic a battery, the input/output voltage to the power electronics is typically dc, although ac-based systems can also be contemplated, using so-called cycloconverters, or the multi-phase devices called matrix converters. A sketch of the electromechanical battery is given in Figure 5.

As can be seen in Figure 5, the Halbach array machine is an integral part of the flywheel construction. The array of magnets is designed into the rotor; the mass of the magnets is used advantageously to keep the composite material in compression. The advantages listed above are also utilized in this design. The outer diameter of the stator windings are typically a centimeter smaller than the inner diameter of the Halbach array magnets. In this space, a thin vacuum barrier is placed, still allowing for a substantial clearance between the array and the barrier. This clearance simplifies the design of the bearing/suspension system, which need not constrain the radial displacements of the rotor assembly to the fraction-of-a-millimeter tolerances that would be required in a conventional iron-core machine.

We conclude this section with a summary of the design parameters of one of the modular EMBs that we have constructed.

Table 1. Electromechanical Battery Parameters

Useful Energy (100% to 50% speed)	0.6 kW-hr
Max Speed	84,000 RPM
Peak Power	50 kW
Open Circuit Voltage	151 Vrms/phase at max speed
Halbach Array Length	18 cm
Halbach Array Outer Diameter	10.5 cm
Halbach Array Inner Diameter	7 cm
Winding - Turns/phase	6
Conductor size	1700 strand, #40 Litz
Inductance per phase	7.4 microhenries
Resistance per phase	10.8 milliohms

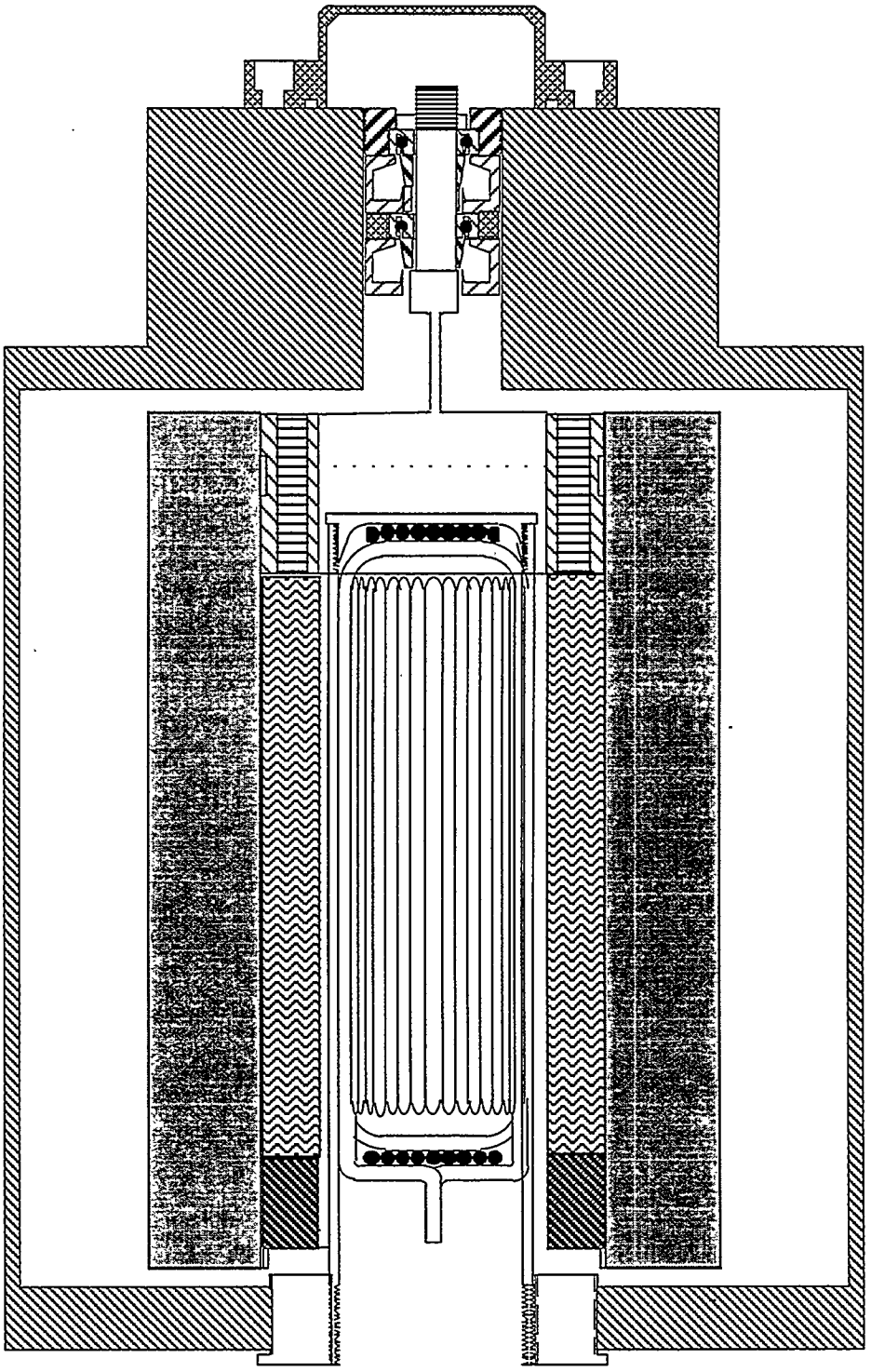

Figure 5. Electromechanical Battery

Using these data and equations (12) and (13) we can calculate the power output and the efficiency of this generator. We assume that the power from each of the three phases is summed independently in calculating the output power, and we ignore the eddy current losses in the Litz wire (it is of order

one or two Watts). In the table below the power and efficiency are calculated as a function of the load resistance (the same for each of the three phases) and at full speed (84,000 RPM). As will be seen at or below the design power the efficiencies are very high.

Table 2. Generator Efficiency Versus Output Power

R_L (Ohms)	Power (kW)	Efficiency
3.0	23	0.9964
2.5	27	0.9957
2.0	34	0.9946
1.5	45	0.9929
1.0	66	0.9893

Drive Circuitry

Although the Halbach array machine can be operated as either an ac or dc machine, there are advantages to operate it as a dc machine. The primary advantage is that the drive circuitry can use a simple 120° gating waveforms. Normally, in an ac machine, elaborate PWM techniques are used to generate sinusoidal waveforms in order to minimize harmonics that can cause losses in the laminations. Since the Halbach array machine does not have laminations this is no longer of concern. The resulting drive can then be greatly simplified, since in this case a simple rectangular wave is very nearly as efficient in driving the rotor as would be a pure sine wave.

In our specific application, energy is transferred into and out of the flywheel on a routine basis. In order to add energy to the flywheel, the power electronics treat the Halbach array machine as an electronically commutated dc motor, as the voltage is raised across the motor, the speed of the motor increases. A schematic of the power electronics for spin-up is given in Figure 6. The electronic commutation is provided by six IGBTs connected to the three phases of the machine. The dc voltage to the commutating bridge is controlled by the "buck" regulator formed by one IGBT, an inductor, and diode. The IGBTs in the commutation bridge also serve as an overcurrent protection scheme. The lower IGBT in each leg can be pulse width modulated to control the current in the windings. The switching frequency for this modulation is about 20 kHz, while the electronic commutation needs to accommodate frequencies up to 1400 Hz to achieve 84,000 RPM operation. This protection is not for the windings but for the power semiconductors.

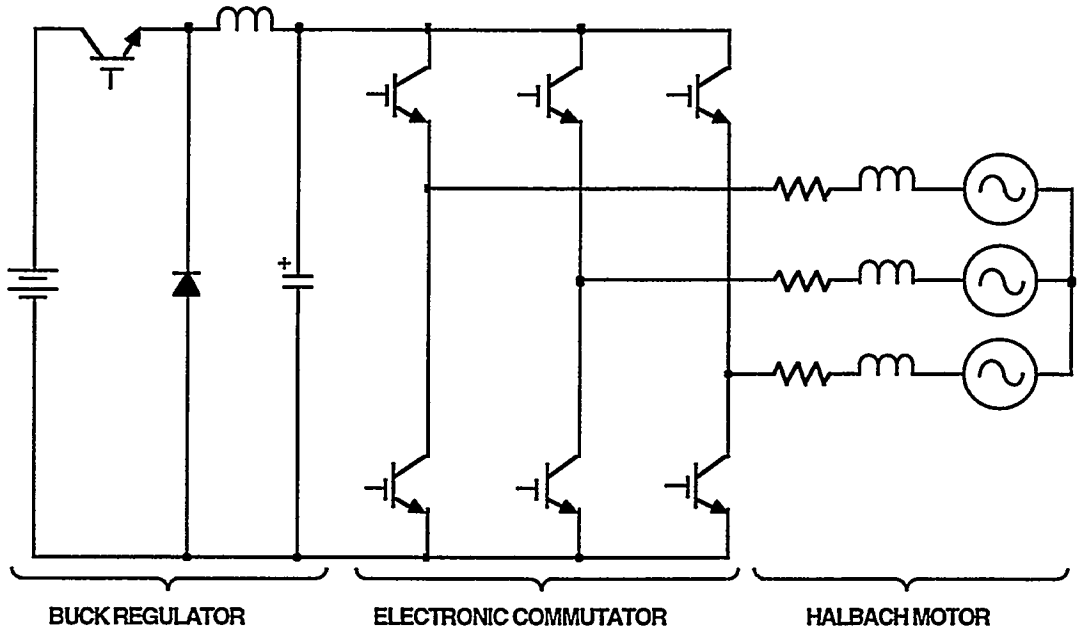

Figure 6. Simplified Schematic of Spin-up Circuit

A schematic for extraction of power from the flywheel is given in Figure 7. The three phases of the windings are connected to a six pulse diode bridge to convert the ac waveforms to dc. Since the speed changes a factor of two while energy is being extracted the dc voltage will also decrease by a factor of two. To accommodate this change in dc bus voltage a "boost" regulator is added. The boost circuit provides for a constant output voltage by changing the IGBT duty cycle.

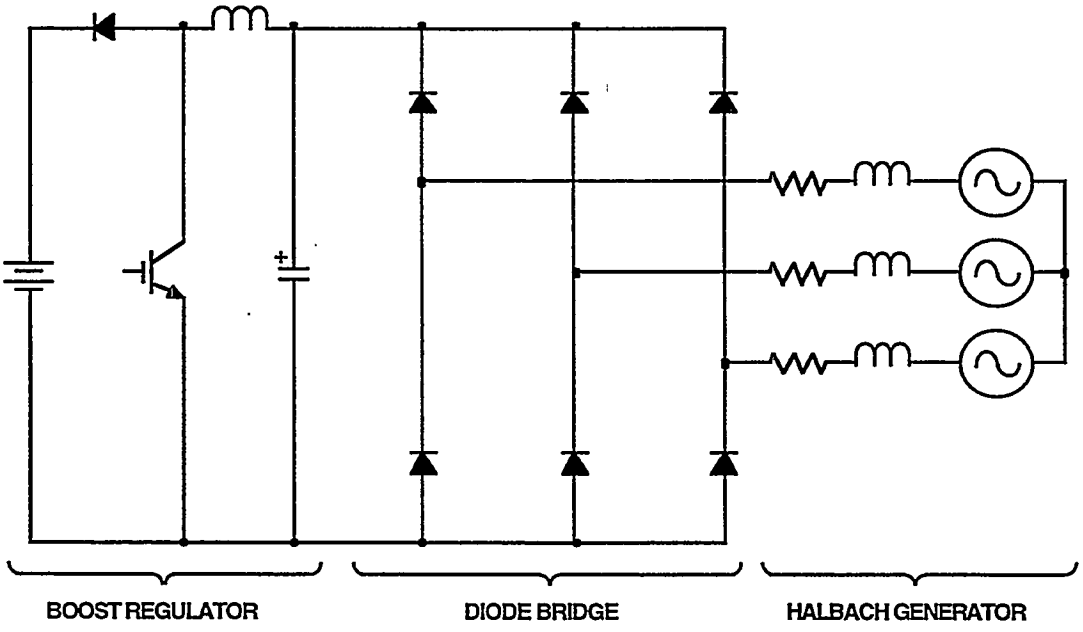

Figure 7. Simplified Schematic of Energy Extraction Circuit

Since IGBTs are normally packaged with an antiparallel diode, the spin-up and extraction circuit can be combined to one as shown in Figure 8. This circuit works best when the energy is added to the flywheel on the same time scale as it is extracted. Figure 8 is an example of circuit that creates a true electromechanical battery; the flywheel-power electronics system mimics a dc battery. For those applications where energy compression is important, that is, the energy is added/extracted on a much longer time scale than it is extracted/added, there is a cost advantage to separate the spin-up and extraction functions in order to minimize the cost of the power semiconductors.

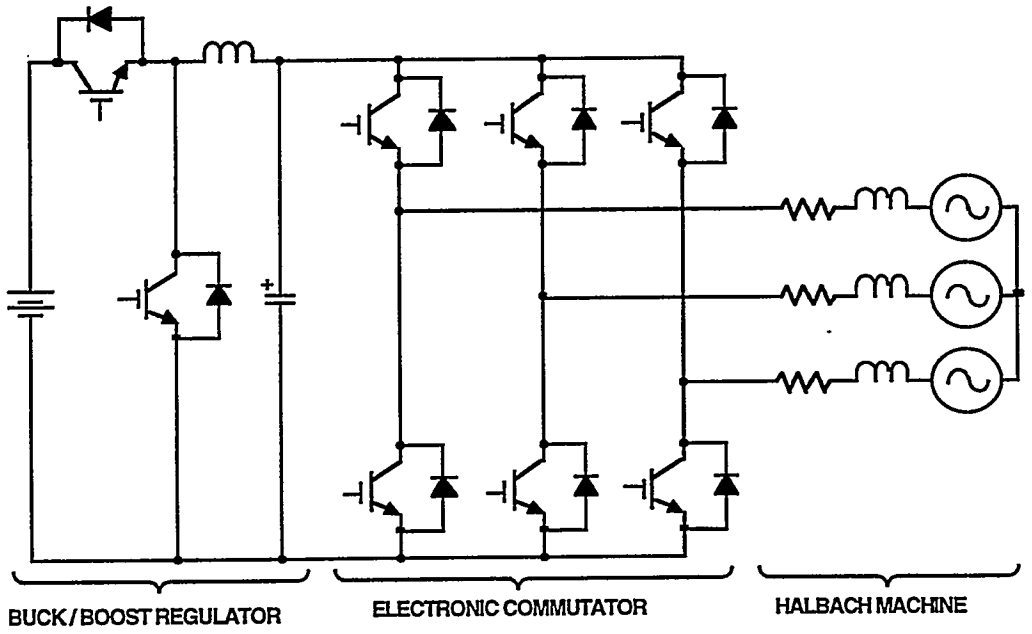

Figure 8. Simplified Schematic of Power Electronics for Electromechanical Battery

Performance

Although the flywheel system has not yet been operated at full speed, the fundamental characteristics of the Halbach array electric machine have been verified.

AC Operation

Figure 9a is a typical open circuit voltage waveform; the purity of the sinusoid is given in Figure 9b which shows that the highest amplitude harmonic is less than a factor of 300 than the fundamental (i.e., more than 50 decibels lower) .

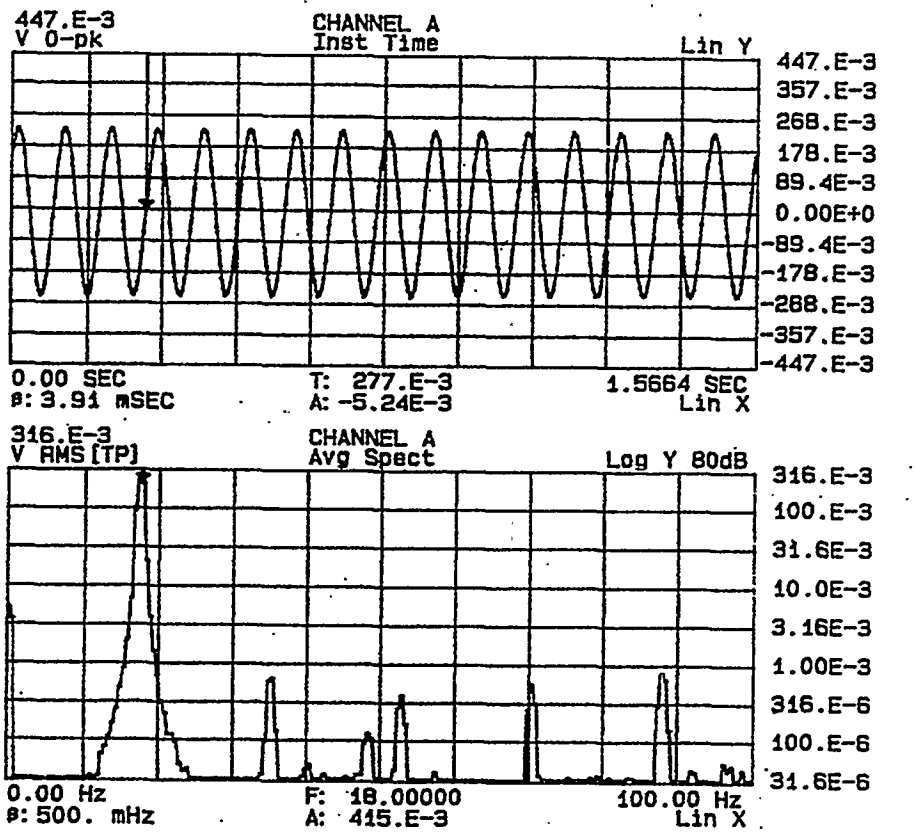

Figure 9. Open Circuit Voltage

Extraction of High Power

Using the flywheel with an integral Halbach array machine, over 50 kW of power (into a load that was not impedance-matched for maximum power) in about one second bursts have been successfully extracted. During this high peak power, the machine did not exhibit any indications of whirl instability. To perform this extraction, the windings were connected to a six pulse diode bridge that was then switched into a resistive load. Figure 10 shows typical bridge voltage and current during extraction. The peak power that has been extracted to date was 65 kW for about one second.

DC Operation

The flywheel with an integral Halbach array machine has been routinely operated at 40,000 RPM. During the spin-up, a single phase version of the power electronics as shown in Figure 6 was used. Figure 11 is a plot of speed versus dc bus voltage. The dc bus voltage is always slightly higher than the emf to ensure power flow into the motor during spin-up. This operation is typical of a dc motor with constant excitation.

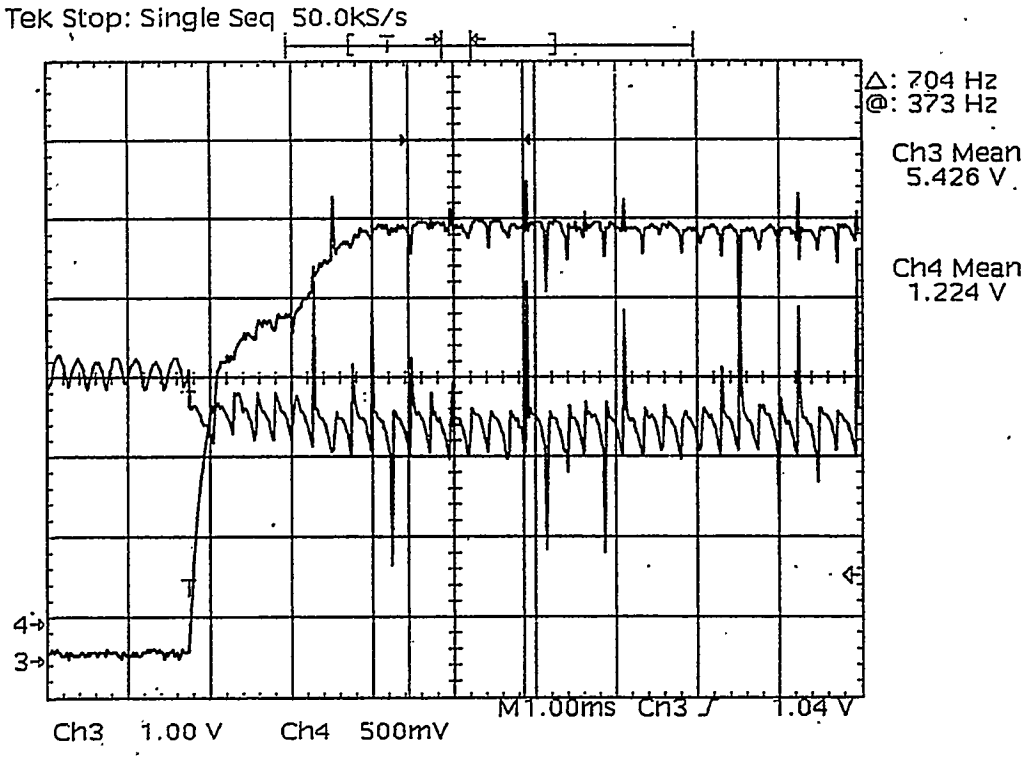

Figure 10. Bridge Current and Voltage During Extraction, upper trace - voltage, 50V/div, lower trace - current, 98A/div.

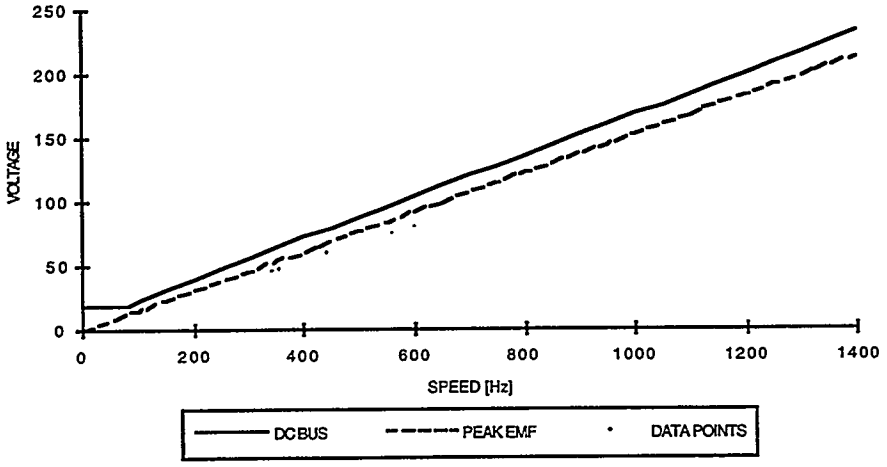

Figure 11. Graph of Flywheel Speed Versus DC Bus Voltage

Acknowledgment
This work was performed under the auspices of the U.S. Department of Energy by Lawrence Livermore National Laboratory under contract No. W-7405-ENG-48.

References

1. K. Halbach, "Design of Permanent Multipole Magnets with Oriented Rare Earth Cobalt Material", Nuclear Instruments and Methods, **169**, pp. 1-10, (1980).

2. K. Halbach, "Physical and Optical Properties of Rare Earth Cobalt Magnets," Nuclear Instruments and Methods, **187**, pp. 109-117, (1981).

3. K. Halbach, "Perturbation Effects in Segmented Rare Earth Cobalt Multipole Magnets," Nuclear Instruments and Methods, **198**, pp. 213-215, (1982).

4. K. Halbach, Specialty Magnets, Lawrence Berkeley Laboratory, LBL - 21945, (1986).

5. R. F. Post, T. K. Fowler, and S. F. Post, A High Efficiency Electromechanical Battery, Lawrence Livermore National Laboratory, UCRL-JC-110861, (1992).

6. R. F. Post, D. E. Baldwin, D. A. Bender and T. K. Fowler, Electromechanical Battery Research and Development ant the Lawrence Livermore National Laboratory, Lawrence Livermore National Laboratory, UCRL-JC-113905, (1993).

7. R F. Post, D. A. Bender and B. T. Merritt, "Electromechanical Battery Program at the Lawrence Livermore National Laboratory," IECEC, Monterey, CA, August 1994.

Bernie Merritt

Dick Post

Gary Dreifuerst

Harmonic Generation with Multiple Wiggler Schemes

R. Bonifacio, L. De Salvo and P. Pierini
INFN Sezione di Milano and Università degli Studi
Via Celoria, 16, 20133 Milano, Italy

In this paper we give a simple theoretical description of the basic physics of the single pass high gain free electron laser (FEL), describing in some detail the FEL bunching properties and the harmonic generation technique with a multiple-wiggler scheme or a high gain optical klystron configuration.

1. INTRODUCTION

Theoretical analysis [1,2] of the Free Electron Laser in the single pass configuration have shown the existence of a collective instability which leads to electron self-bunching and coherent emission. This regime, experimentally observed at Lawrence Livermore National Laboratory [3,4], is based on the unstable process of self-bunching of the electrons in the beam [1,5]: the electrons, subject to the ponderomotive potential created from the combination of the electromagnetic and the wiggler fields, bunch on the scale of the radiation wavelength and radiate coherently, increasing efficiently the radiation intensity.

The high gain FEL is interesting not only for the high radiation power that it can provide, but also for the effects that the process has on the electron beam. A FEL can be used also as a buncher for high current beams [6]. In fact, just before the saturation of the radiation power, the maximum spatial modulation of the electron beam on a scale shorter than the radiation wavelength is produced, modulating the beam current in a series of periodic spikes [7,8]. This technique is of great interest in the physics of future electron beam accelerators.

One of the most intense efforts in the FEL research is the production of powerful radiation in the region of the electromagnetic spectrum where conventional sources do not exist, as the UV and XUV regions (see e.g. [9]). It is well known that harmonic radiation is produced in a planar wiggler, however, its gain is usually considerably lower than the fundamental gain [10] and the process is limited by tight constraints on the necessary beam quality.

In this paper we review the scheme for the production of coherent spontaneous emission on higher harmonics using a multiple-sections wiggler and/or a dispersive section. In this device the electron beam is strongly prebunched on the fundamental and all the higher order harmonics in the first wiggler section (the modulator), as a consequence of the high gain amplification at the fundamental [11]. Then, the bunched beam emits coherently passing through the second section (the radiator), tuned on a harmonic of the first wiggler section. This technique provides an up frequency converter and amplifier. For a small initial energy spread a dispersive section can be inserted between the two sections, in order to enhance the bunching after the modulator.

2. THE FREE ELECTRON LASER BASICS

The high gain free electron laser amplifier is a device in which an electron beam is coupled to a co-propagating radiation field by a spatially alternating magnetostatic field produced by a wiggler [12,13,14]. Under proper conditions, the electron beam looses energy to the radiation field, which experiences an exponential amplification along the wiggler [1].

From the relativistic equation describing the energy variation of an electron interacting with an e.m. wave we have the well known resonance condition:

$$\gamma_r^2 = \frac{\lambda_w(1+a_w^2)}{2\lambda_r}, \tag{1}$$

where $a_w = eB^{rms}_w/(k_w mc^2)$, is the wiggler parameter.

In the steady state regime, i.e. neglecting the slippage between the electrons and the radiation field, the system of equations that describe the FEL reduces to an ordinary differential equations system, and can be easily exploited both analytically and numerically. In this case the 1-D model equations read:

$$\frac{d\theta_j}{d\bar{z}} = p_j \tag{2.a}$$

$$\frac{dp_j}{d\bar{z}} = -(Ae^{i\theta_j} + cc) \tag{2.b}$$

$$\frac{dA}{d\bar{z}} = \left\langle e^{-i\theta_j} \right\rangle + i\delta A \tag{2.c}$$

where we have introduced the detuning parameter $\delta = \left(\langle\gamma\rangle_0 - \gamma_r\right)/\rho\gamma_r$, in which $\langle\gamma\rangle_0$ is the average initial electron energy and ρ is the fundamental FEL parameter [1], and the bunching parameter $b = \left\langle e^{-i\theta_j} \right\rangle$ which describes the electron bunching on the scale of a radiation wavelength, λ_r.

In the 1D theory, ρ is the (only) parameter which gives the constraints on the FEL operation. In particular, to obtain the maximum gain the energy spread and detuning parameter must satisfy the following conditions:

$$\sigma \equiv \frac{\Delta\gamma}{\gamma_r} \le \rho \qquad \delta \le \rho. \tag{3}$$

3. EXPONENTIAL AMPLIFICATION AND SATURATION LENGTH

The linear analysis predicts an exponential instability of the emitted radiation field; nonlinear effects determine the saturation of this growth. The linear solution of the exponentially growing mode fits well the solution of the full non linear system up to the saturation of the radiated power. In the case of an initial radiation signal of intensity $|A_0|^2$, the asymptotic behavior of the linear solution for the radiated power $|A|^2$, in the cold beam, resonant case (δ=0) is:

$$|A|^2 \approx \frac{|A_0|^2}{9}\exp\left[\sqrt{3}z/l_g\right], \tag{4}$$

where $l_g=\lambda_w/4\pi\rho$. Since saturation occurs at a value close to one, we can write the saturation length with the following formula:

$$z_{sat}=\frac{l_g}{\sqrt{3}}\ln\frac{9}{|A_0|^2}. \tag{5}$$

We note from this relation that the dependence of the saturation length from the initial seed power is a slow, logarithmic dependence. The bunching parameter, the driving term of the radiation evolution, exhibits in the linear regime the same kind of exponential growth of the radiation field along the wiggler up to saturation. The saturation of the bunching parameter occurs nearly at the saturation of the radiated field, and its value is almost equal to one ($b_{sat}\approx$ 0.8), indicating that nearly all the electrons have been grouped in a spatial region much smaller that λ_r. As a consequence, at saturation, the electrons are tightly bunched on a scale λ_r, and there will be also an appreciable bunching on all the Fourier components of b [15].

4. HARMONIC BUNCHING DUE TO NON LINEAR COUPLING

In a linear wiggler, in the case of on-axis propagation, the electrons can couple to all the odd harmonics of the fundamental wavelength determined by the resonance condition eq.(1), with different coupling coefficients. It is possible to extend easily the 1D model to take into account a field composed by a superposition of several harmonics. However, in the linear regime the system reduces to a set of decoupled equations for the field harmonics, with different growth rates. This analysis predicts that the growth rate for the high order harmonics is usually lower than the growth rate for the fundamental and that, for a case of a pure excitation of the fundamental field, no harmonic emission is observed. However, a more detailed analysis, extended to the non linear regime, shows that the nonlinear behavior of the coupled system of equations differs strongly from the results obtained from the previously mentioned linear analysis, even well before saturation.

The simplest extension to the system (2.a-c) can be written as:

$$\frac{d^2\theta_j}{d\bar{z}^2}=-\sum_{hodd}F_h(\xi)|A_h|\cos(h\theta_j+\phi_h) \tag{6.a}$$

$$\frac{d}{d\bar{z}}(|A_h|\exp[i\phi_h])=F_h(\xi)\langle\exp[-ih\theta]\rangle \tag{6.b}$$

We have introduced the harmonics of the radiation vector potential (A_h, h odd) and the coupling coefficients $F_h(\xi)=(-1)^{(h-1)/2}\left[J_{(h-1)/2}(h\xi)-J_{(h+1)/2}(h\xi)\right]$ with $\xi=a_w^2/\left[2(1+a_w^2)\right]$. In Fig. 1 we show the numerical integration of the above system considering the fundamental wavelength and the first two harmonics, h=3,5. We can see that, even if the harmonic radiation reaches a power level substantially smaller than the fundamental, the bunching parameter saturates to

almost identical values, of the order of the unity. From this figure we can clearly see that, when the fundamental radiation starts experiencing an exponential growth, the two higher order bunching parameters exhibit a much faster growth rate than the fundamental, contrary to the results obtained by the linear analysis of the system, even if in the linear regime the fundamental mode is dominant.

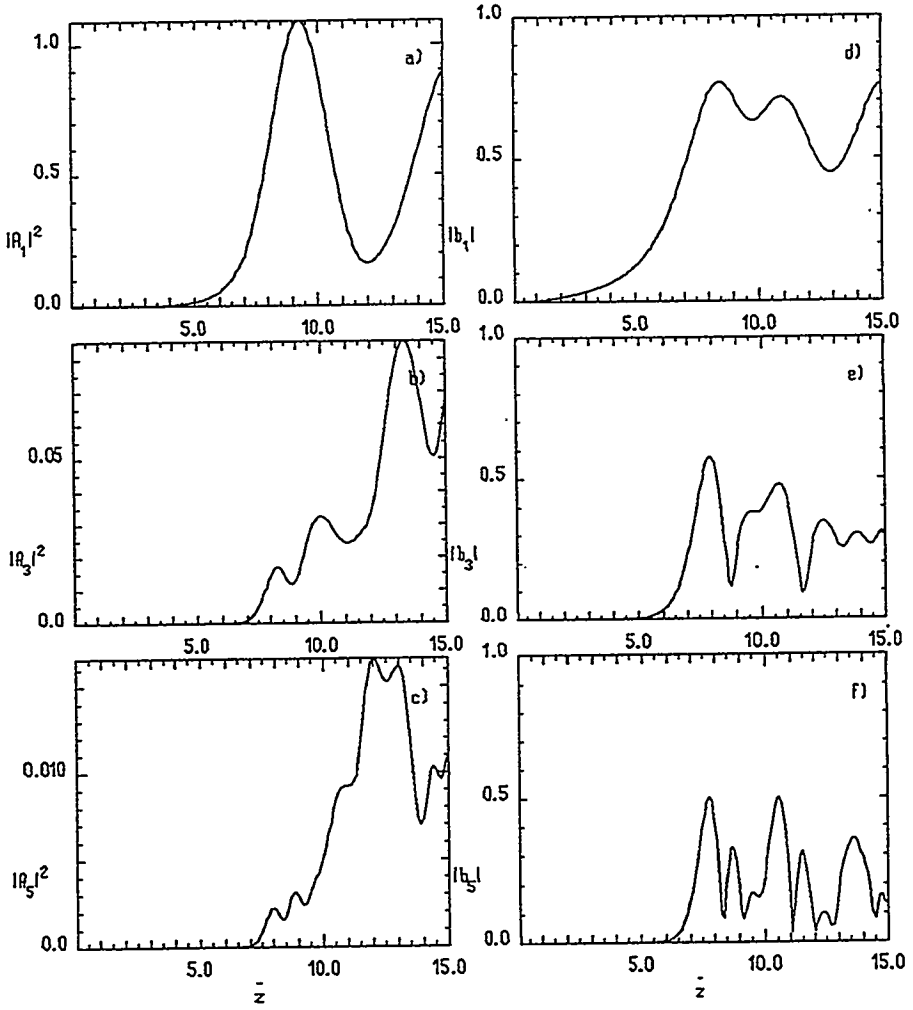

Fig. 1 Numerical integration of equations (6). a) to c) show the first three dimensionless emitted harmonics of the field (fundamental, h=3,5). d) to f) show the harmonic bunching components. Here we used an input field tuned on the fundamental component.

This fact can be easily explained analytically neglecting the effect of the high order harmonics on the evolution of the fundamental radiations (the power in the harmonics is much lower than the power radiated on the fundamental), and evaluating the effect of the exponentially diverging fundamental mode on the harmonics. In this way one can clearly see that the exponential growth of the

fundamental wavelength *drives* the instability of the higher order modes, at a rate h times greater than the fundamental, where h is the harmonic number. In fact, this non linear analysis, in the case of h=1 and h=3 allows us to write a closed equation for the evolution of the third harmonic bunching coefficient:

$$\frac{d^3 b_3}{d\bar{z}^3} - 3iF_3^2 b_3 = -\frac{9}{2} F_1 A_0^3 \exp[3i\lambda_1 \bar{z}], \tag{7}$$

where λ_1 is the growth rate of the fundamental unperturbed wavelength, solution of the cubic equation [1]

$$\lambda^3 - \delta\lambda^2 + 1 = 0. \tag{8}$$

The left hand side of this relation leads to the standard cubic dispersion relation for b_3 (and hence A_3), in the linear, decoupled limit where the right hand side can be neglected. The term appearing in the right hand side is due to the exponentially unstable fundamental mode. Due to this inhomogeneous term the asymptotic solution for b_3 turns out to be proportional to $\exp(3i\lambda_1 \bar{z})$, i.e. it has a growth rate *three times larger* than that of the fundamental. More generally, the solution for the third harmonic bunching is a linear combination of two exponentials with different growth rates: one is determined by the cubic relation derived by the linear homogeneous equation associated with eq.(7), the other is driven by the inhomogeneous term of the same equation at a rate $3\lambda_1$.This theoretical analysis can be easily confirmed in the non linear regime by means of simulations. In Fig. 2 we show the same case of Fig. 1, plotting on the same picture $|b_3|$ and $|b_1|^3$ as a function of the distance in the wiggler. As we can see, a definite proportionality between the two curves exist, up to saturation, confirming our results. This analysis can be performed on any harmonic of the bunching parameter, resulting in the fact that the h-th harmonic is driven by the fundamental at a rate h times the growth rate of the fundamental.

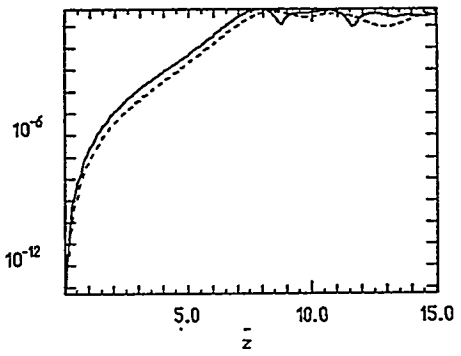

Fig. 2 Same case of Fig.1. Here we plot $|b_3|$ and $|b_1|^3$ on the same semilog picture.

5. THE OPTICAL KLYSTRON CONFIGURATION

An Optical Klystron [16] is composed by two wigglers, separated by a dispersive section, that can either be a free space section or a proper magnetic device. In the first wiggler (the modulator) an electron beam, interacting with a radiation field (that can be provided either by an external laser or by the spontaneous radiation emitted by the electron beam itself), receive an energy modulation that is then transformed into a spatial modulation (bunching) in the dispersive section. The bunching provided by the dispersive section enhances the coherent emission of radiation in the second wiggler.

This scheme has, in principle, two distinct advantages over the bunching produced by the conventional high gain FEL amplifier scheme [15]: first, the total length of the device can be considerably reduced, second, the electron bunching in the dispersive section is gained with no additional growth of the FEL induced energy spread. However, in an Optical Klystron the bunching efficiency is very sensitive to the initial energy spread of the electron beam, which needs to be sensibly smaller than the one required for the normal high gain FEL operation [1].

Fc small initial field intensities and short modulators the interaction between the electrons and the radiation field in the first wiggler can be described (as in the small gain theory of a FEL) assuming a constant field and an induced sinusoidal modulation of the electron beam [17,18]. This is the typical situation of the operation of an Optical Klystron in a storage ring [19]. It can be shown that there exists an optimum value both for the modulator length and the dispersive section strength, given the initial field amplitude and beam energy spread.

The inclusion of the energy spread in such an analysis introduces a strong damping term for the bunching obtained in the dispersive section [18]; such energy spread effects can be partially reduced by increasing the electron modulation amplitude, i.e. the initial field intensity or the length of the first wiggler. This can lead to a situation where the constant field approximation no longer holds, and the modulator operates in the high gain regime. This kind of operation has been recently proposed by several authors [20,21].

A complete analytical model has been proposed in Ref. [22], useful to describe the bunching process in both the small and high gain regimes and incorporating in a natural way energy spread effects. We have shown that strong energy spread limitations still hold in the high gain regime and, furthermore, we have described the optimization and evaluated the bunching on the fundamental and h-th harmonic for both regimes. The model presented in [22] can describe the bunching process also in a conventional FEL, and even in this case its validity holds deep in the exponential regime.

The behavior of the dispersive section in an Optical Klystron configuration can then be approximated by a simple point like region that imposes the following transformation on the electron phase and energy variables ($p \equiv \dot{\theta}$):

$$\theta(\bar{z}_{out}) = \theta(\bar{z}_{in}) + Dp(\bar{z}_{in}) \tag{9.a}$$

$$p(\bar{z}_{out}) = p(\bar{z}_{in}) \tag{9.b}$$

where D is the dispersive section strength, that, in the case of a magnetic device, can be evaluated, given a sufficiently large magnetic field $B(\bar{z})$, by the formula:

$$D = \rho k\left(\frac{e}{\gamma mc^2}\right)\int_{\bar{z}_{in}}^{\bar{z}_{out}} d\xi\left(\int_{\bar{z}_{in}}^{\xi} d\eta B(\eta)\right)^2 \tag{10}$$

For instance, a dispersive section made out of three dipoles of length $s/4$, $s/2$ and $s/4$ and field values $-B_0$, B_0 and $-B_0$, respectively, has a strength $D=(1/48)\rho k(eB_0/mc^2\gamma)^2 s^3$.

To evaluate the effect of the dispersive section in a optical klystron, we have integrated in the first wiggler the linearized equation of motion for the electron variables θ and p, using the self-consistent field as solved by the linear analysis for the driving term of the electron evolution. At the end of the first wiggler the dispersive section acts with the transformation rules given in eq.(9.a)-(9.b). Using the new values of the electron phases the harmonic bunching parameter at the beginning of the second wiggler can be easily calculated from

$$b_h^{in} = \left\langle \exp[-ih\theta(\bar{z}_{out})]\right\rangle = \left\langle \exp[-ih(\theta(\bar{z}_{in}) + Dp(\bar{z}_{in}))]\right\rangle \tag{11}$$

Here $\theta(\bar{z}_{in})$ and $p(\bar{z}_{in})$ are the phases and energies at the end of the first wiggler.

Carrying out explicitly the calculation as outlined in Ref. [22], with the proper initial conditions and electron initial distribution we can derive the bunching at the beginning of the second wiggler as a function of the initial beam energy spread σ, the dispersion section coefficient D, the initial field A_0 and the length of the first section, $\bar{z}$.

From the results obtained we can derive the expression:

$$|b_h(\bar{z})| = \exp[-h^2D^2\sigma^2/2]\left|J_h(2h\psi(\bar{z}, A_0, \delta, D))\right| \tag{12}$$

where J_h is the Bessel function of first kind of h-th order and ψ is a given function of the dispersive section strength D, of the detuning δ, of the initial field A_0 and monotonically increasing with $\bar{z}$. Since J_h is always smaller than one, the above expression shows the strong damping effect of the energy spread, and that the requirement $D\sigma \approx 1/h$, already referenced in the low-gain regime [18], holds also when the first wiggler operates in the high gain exponential regime. The above requirement, in the interesting case $D>>1$, leads to $\sigma \leq 1/hD$, which is much more restrictive than the condition $\sigma \leq 1$, necessary for the high gain operation of a FEL amplifier.

From the final expression for the harmonic bunching we can derive the optimizing criteria for D, given the buncher length, $\bar{z}$, and the initial energy spread, σ, provided that the energy spread constraint is satisfied ($hD\sigma \leq 1$)[22]. We can maximize the bunching at the beginning of the second wiggler either as

a function of the dispersive section strength D or as a function of the first wiggler length, given the initial beam distribution. In the limit of a very short modulator, $\bar{z}<<1$, the expression found for the bunching reduces to the usual expression of the bunching in a small gain Optical Klystron [17,18].

To perform a simultaneous optimization of D and $\bar{z}$, it is useful to look at the level curves of $|b(\bar{z})|$, obtained by plotting the analytical expressions for the bunching, and reported in Fig.3 and Fig.4, respectively in the case of σ=0.01 and σ=0.1. From these plots it can be seen easily that, increasing σ, the advantage of the Optical Klystron scheme in the overall length reduction becomes irrelevant. As can be seen in Figs.3 and 4, for σ=0.01 the value $|b|$=0.55 is reached at $\bar{z}$=2.5 (and D≈30), for σ=0.1 the modulator has to be increased to $\bar{z}$≈4.8 (and D≈4). The normal FEL instability (D=0) generates the same bunching at $\bar{z}$≈6. There is clearly an advantage in the decrease of the modulator length with a dispersive section in the first case, where the energy spread is small, but this advantage is nearly vanished in the second case, where the energy spread is larger.

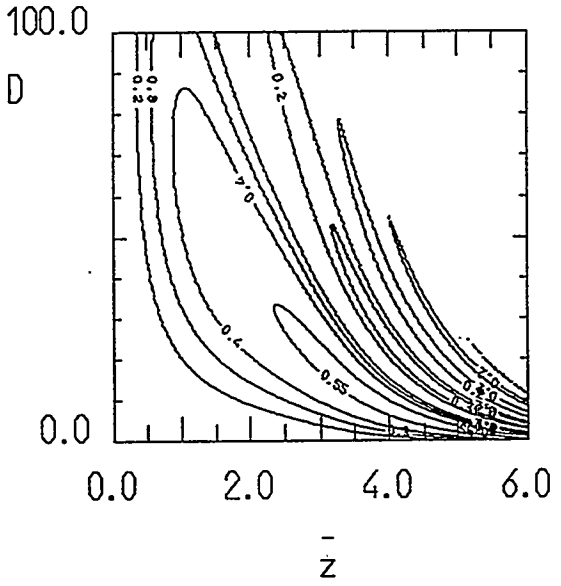

Fig. 3 Contour plot of the bunching factor (for h=1) given by expression (12) versus $\bar{z}$ (horizontal axis) and the dispersive section strength parameter D (vertical axis). Here σ=0.01 and A_0=0.01.

For even higher values of energy spread the advantage of the dispersive section over the normal FEL bunching process is considerably reduced with respect to the previous case, and its use is questionable. In fact, in order to satisfy the condition $D\sigma \leq 1$, smaller values of the dispersive section parameter D have to be chosen, so that the use of a dispersive section becomes a disadvantage, if not useless.

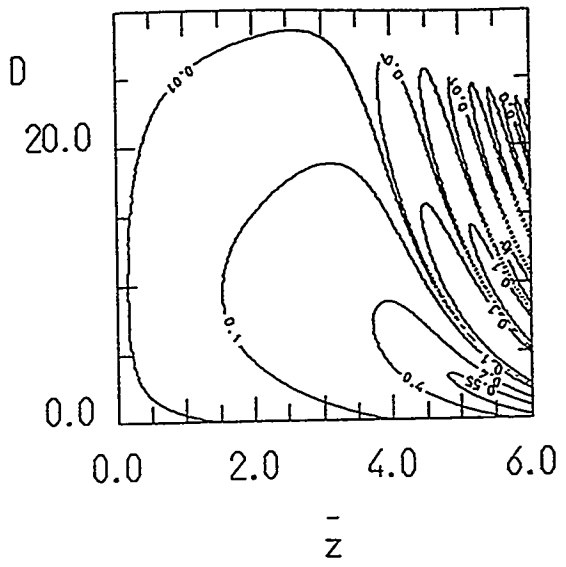

Fig.4 As Fig.3, for the parameters σ=0.1 and A_0=0.01.

As a last point we can note that the analytical results for the hth harmonic bunching at the end of the first wiggler section (obtained by taking D=0) show, using a different method, the result obtained by the non linear driving model outlined in a previous subsection. In this case eq.(12) reduces to

$$|b_h(\bar{z})| = \left| J_h\left(\frac{2}{3} h A_0 \exp(\sqrt{3}\bar{z}/2)\right)\right| \qquad (13)$$

From the above expression, since $J_h(x)$ behaves as x^h for small values of its argument, we recover the result that the growth rate of the h-th harmonic in a conventional FEL is h times larger than the growth rate of the fundamental [15]. Again, since the maximum value of J_h decreases very slowly with h, we have the analytical evidence that the harmonic bunching near saturation is very large even if the harmonic field is very small [15]. In conclusion the Optical Klystron configuration is convenient only for very small values of σ, and practically is not anymore convenient as $\sigma \approx 0.1$ (see Fig.4) whereas in a conventional high gain FEL high values of the bunching ($|b| \approx 0.8$) are reached until $\sigma \leq 1$.

6. HARMONIC GENERATION: FREQUENCY DOUBLING AND TRIPLING

It has been previously shown that the high-gain operation in a FEL amplifier generates bunching at the fundamental wavelength and its harmonics. This has suggested [11,15] the possibility to use a FEL amplifier as a resonant-frequency doubling or tripling device, generating strong bunching at the second or third harmonics of a conventional input source in an initial wiggler section, then using a second wiggler section resonant at the double or tripled frequency to emit strong bursts of radiation. This offers a new method to generate radiation in a

spectral range where conventional input sources are not available, as in the XUV range. Moreover, although the oscillator configuration has the advantage that does not require an input source, it has the disadvantage of requiring mirrors with adequate reflectivity to permit lasing, and appropriate mirrors at short wavelengths become harder to find.

The technique of using a FEL amplifier as a frequency converter is based on the fact that the spatial bunching in the high gain regime can be very strong and that in a linear wiggler electrons couple strongly to odd harmonics. Close to saturation, a large harmonic bunching is generated; by that point the energy spread induced in the beam by the amplification of the fundamental reaches a maximum. At some stage before saturation of the exponential gain regime, it is possible to change the wiggler field, in order to bring the second or the third harmonics radiation into resonance with the wiggler. The fundamental radiation in the first part of the wiggler is non resonant in the second, hence it does not interact with the electrons, while the second or third harmonic becomes the fundamental.

Since the beam has a large component of bunching at the selected harmonic, it will start to emit coherent spontaneous radiation, with a n_e^2 scaling due to the prebunching process performed by the first section of the wiggler. It can be shown that the harmonic radiation produced in the first section of the wiggler is inessential to the process, and can be neglected, because the main mechanism of emission in the second part of the wiggler is the strong bunching of the electron beam. In other words, the equivalent input noise of the electron beam in the second part of the wiggler is much greater than the small harmonic component of radiation generated in the first part.

In Fig.5 we present a case, showing the fundamental, the second and third harmonics of the radiated field and of the bunching, but with a wiggler length chosen so to be well into the exponential regime, but before saturation, to avoid a big induced energy spread in the electron beam. In this figure we have intentionally shown the second harmonic of the radiation field, which has no evolution along the wiggler, to stress the important point that, *even in the absence of second harmonic radiation the second harmonic bunching reaches a value close to the fundamental.*

We then change the wiggler, reducing the magnetic field, to bring the third harmonic into resonance at the fundamental with the same electron energy. The radiation intensity at the fundamental in the second section of the wiggler, as shown in Fig. 6, reaches the saturation value of 0.7 in dimensionless units (we recall that in these units the steady state saturation is about 1). The saturation value is less than the maximum value of nearly 1 because of the energy spread induced in the first section of the wiggler by the growth of the fundamental.

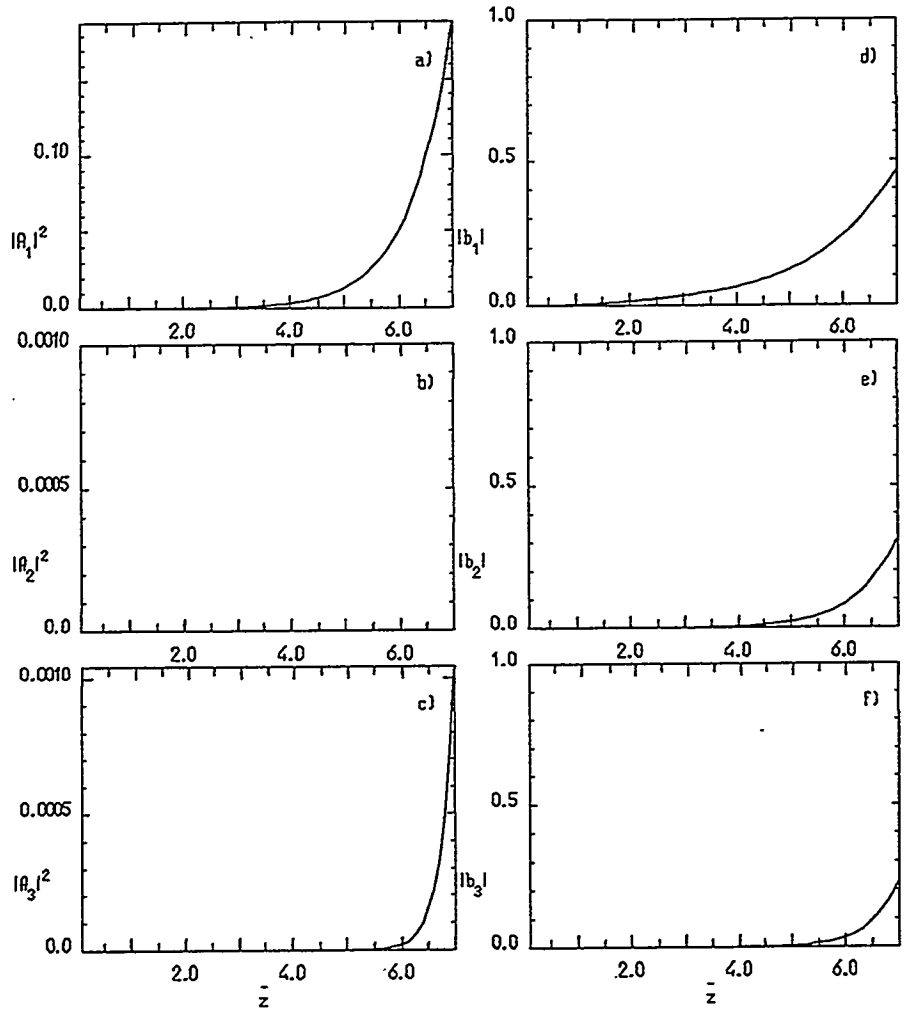

Fig.5 Emitted field on the fundamental (a), second (b) and third (c) harmonic as a function of the position along the wiggler. Harmonic bunching parameter b_n, for n=1 (d), n=2 (e) and n=3 (f).

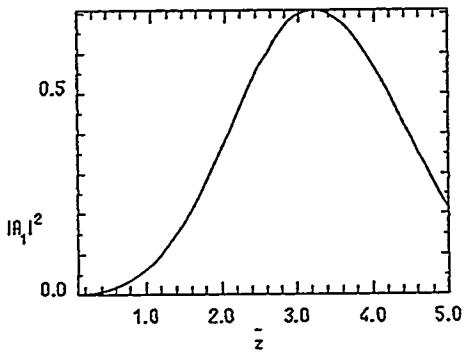

Fig. 6 Intensity of the emitted radiation in the second wiggler.

7. PRODUCTION OF XUV LIGHT BY RESONANT FREQUENCY HARMONIC GENERATION WITH A DOUBLE WIGGLER

For the generation of very short wavelength light, the oscillator configuration of the FEL has the virtue of being tunable and not to require an input source, but has the disadvantage of requiring mirrors with adequate reflectivity to permit lasing. As the signal wavelength becomes shorter, appropriate mirrors become harder to find. A single pass FEL requires no mirrors but usually requires an input signal which can be non available at short wavelength.

Single-pass FEL amplifiers can be excited by spontaneous emission in the wiggler, but a very long wiggler is necessary in this case and produces a broader-bandwidth output signal than obtainable from an FEL amplifier with a coherent input signal. In both the oscillator and amplifier configurations constrains on electron beam quality limit the wavelength that can be achieved.

The method proposed in Ref. [11] and described in the previous section, i.e. the coherent spontaneous emission on higher harmonics in a double wiggler amplifier configuration, requires no mirrors and the input signal frequency is lower than the output signal one. Also the requirements on the electron beam quality are relaxed and a higher power at shorter wavelength can be obtained than is possible in a amplifier excited by noise. This scheme can be used in the wavelength ranges hardly accessible to FEL. For instance this method allows the generation of high power radiation output at a wavelength of 80 nm, which can be used for the ion beam ionization in the scheme proposed by Rubbia [23] for the inertial fusion. In effect, the range 300-70 nm can be useful to induce fragmentation and ionization of any atom or molecule, leading to exciting new scientific possibilities in photo-induced chemistry and physics.

An harmonic generation experiment has been proposed for the BNL accelerator test facility (ATF) [24].The parameters of the experiment have been selected to match the electron beam parameters which have been demonstrated at ATF. In this experiment it is planned to produce 100 nm radiation starting from noise and by utilizing two superconducting wigglers and a dispersive section.

The 3D simulations reported in Ref. [25] presents the results of a series of GINGER [26] simulations which show the exponential gain starting from a signal at 240 nm and producing harmonics at 120, 80 and 60 nm, both with a double wiggler and a triple wiggler cascade without the use of a dispersive section, using the SLAC linac parameters and the PALADIN wiggler (λ_w= 8 cm, peak B_w up to 0.4 T). The simulations assume no external focusing. We change the wiggler parameter by changing the magnetic field so to tune on the various harmonics on the different sections of the wiggler. The first wiggler is optimized in all cases so to create enough bunching on the harmonics with an induced energy spread small enough not to suppress the exponential gain in the second wiggler.

In the first case (case 1 in Table 1) we reached 3 GW of power on the second harmonic with 15 m (6+9) of total wiggler. No dispersive section has been used. Detuning optimization on the second wiggler has been tried in case 2, doubling the output power from 2.4 to 5 GW. Case 3 is the same as case 2, but with a better energy spread, which allows to use 1 kW instead of 1 MW of input power. A third harmonic production at 80 nm is shown in case 4 with 1 kW of input laser.

Case	1	2	3	4	5	
I (kA)	2	2.5	2.5	2.5	2	
ε_n (mm mrad)		3.5	4	4	4	3.5
E (MeV)	623	485	485	485	623	
$\Delta\gamma/\gamma$ (%)	0.06	0.13	0.03	0.03	0.06	
P_{in} (MW)	1	1	0.001	0.001	1	
L_{w1} (m)	6	6	11	11	6	
a_{w1}	3.98	2.97	2.97	2.97	3.98	
L_{w2} (m)	9	9	7	10	4	
a_{w2}	2.63	1.85	1.85	1.27	2.63	
L_{w3} (m)					8	
a_{w3}					1.57	
P_{out} (GW)	3	2.4	3	1.86	0.8	
λ_{out} (nm)	120	120	120	80	60	

Table 1 Parameters for the simulations

In case 5 we show the first 3D simulation of a three wiggler cascade, tuning the second section after 6 m to the second harmonic (120 nm) and then, after 4 m, tuning the wiggler on the second harmonic of the second section (i.e. the fourth harmonic of the 240 input radiation) and finally reaching, after 8 m of the third section, 800 MW of output power at 60 nm with a total wiggler length of 18 m. In all cases the remaining part of the 25 m PALADIN wiggler can be used for tapering or for a further harmonic cascade to shorter wavelengths.

This method can be extended to shorter wavelengths, allowing to avoid the possible drawbacks, like spiking and fluctuations, of the shot noise startup[27].

REFERENCES

1. R.Bonifacio, C.Pellegrini, L.Narducci, *Opt. Commun.*, 50 (1984), 313, and R.Bonifacio, F.Casagrande, G.Cerchioni, L.De Salvo Souza, P.Pierini, N.Piovella, *La Rivista del Nuovo Cimento*, Vol. 13, 9 (1990).
2. N.M.Kroll and W.A.McMullin, *Phys. Rev.A* **17**, (1978), 300; I.B.Bernstein and J.H.Hirschfield, *Phys. Rev. A* **20**, 1661 (1979); V.N.Baier and A.I.Mil'shtein, *Sov. Phys. Dokl* **25**, (1980), 112; A.Gover and P.Sprangle, *IEEE J. of Quantum*

Electron. **QE-17**, (1981), 1196; G.Dattoli, A.Marino, A.Renieri and F.Romanelli, *IEEE J. of Quantum Electron.* **QE-17**, (1981), 1371; C.C.Shih and A.Yariv, *IEEE J. of Quantum Electron.* **QE-17**, (1981), 1378

3. T.J.Orzechowski, B.R.Anderson, W.M.Fawley, A.C.Paul, D.Proznitz, E.T.Scharlemann, S.M.Yarema, D.B.Hopkins, A.M.Sessler and J.S.Wurtele, *Phys. Rev. Lett*, **54**, (1985), 889.
4. T.J.Orzechowski, B.R.Anderson, J.C.Clark, W.M.Fawley, A.C.Paul, D.Prosnitz, E.T.Scharlemann, S.M.Yarema, D.B.Hopkins, A.M.Sessler and J.S.Wurtele, *Phys. Rev. Lett.*, **57**, (1986), 2172.
5. N.M.Kroll, L.P.Morton and M.N.Rosenbluth, in Free Electron Generators of Coherent Radiation, *Physics of Quantum Electronics*, eds. S.Jacobs, H.Pilloff, M.Sargent, M.Scully and R.Spitzer (Addison-Wesley, Reading, MA, 1980), Vol.7, Chap.5, p.113.
6. H.D.Shay, R.A.Jong, R.D.Ryne, S.S.Yu and E.T.Scharlemann, *Nucl. Instrum. and Meth.*, **A 304** (1991), 262.
7. W.A.Barletta and R.Bonifacio, *Rapporto Interno INFN*, **INFN/TC-91/15**, (1991).
8. W.A.Barletta, G.Bellomo, R.Bonifacio, R.Corsini, L.DeSalvo, P.Pierini and M.Pullia, *Nucl. Instrum. and Meth.* **A329**, (1993), 348
9. *Proceedings of the Workshop on Fourth Generation Light Sources*, Eds. M.Cornacchia and H.Winick, Stanford, February 24-27, 1992.
10. W.B.Colson, *IEEE Journ. of Quant. Electr.*, **QE-17** (1981), 1417.
11. R.Bonifacio, L.DeSalvo, P.Pierini, E.T.Scharlemann, *Nucl. Instrum. and Meth.*, **A 296** (1990), 787.
12. J.B.Murphy, C.Pellegrini: *Proc. of joint US-CERN Particle Accelerator School*, Lecture Notes in Physics, eds.M.Month, S.Turner, Springer Berlin (1988).
13. *Laser Handbook*, edited by W.B.Colson, C.Pellegrini and A.Renieri, (North-Holland, Amsterdam, 1990), Vol. 6, p. 195.
14. R.Bonifacio, F.Casagrande, G.Cerchioni, L.DeSalvo, P.Pierini, and N.Piovella, in *Proceedings of the INFN International School on Electromagnetic Radiation and Particle Beams Acceleration*, eds. R.Bonifacio, L.D.Salvo, C.Pellegrini, (Varenna, 1988), North-Holland, 1989.
15. R.Bonifacio, L.DeSalvo, P.Pierini, *Nucl. Instrum. and Meth.*, **A 293** (1990), 627.
16. P.L. Csonka, *Part. Accel.*, 8, 225 (1978); N.A. Vinokurov and A.N. Skrinsky, *Novosibirsk Institute of Nuclear Physics Report* No. **INP 78-88**, 1978.
17. DeMartini, in *Laser Handbook*, edited by W.B.Colson, C.Pellegrini and A.Renieri, (North-Holland, Amsterdam, 1990), Vol. 6, p. 195.
18. S. Baccaro, F. De Martini and A. Ghigo, *Opt. Lett.* 7, 174 (1982); J.M. Ortega, Y. Lapierre, B.Girard, M. Billardon, P. Elleaume, C. Bazin, M. Bergher, M. Velghe and Y. Petrof, *IEEE J. Quantum Electron.*, **QE-2**, (1985), 909.

19. B.Girard, Y.Lapierre, J.M.Ortega, C.Bazin, M.Billardon, P.Elleaume, M.Bergher, M.Velghe and Y.Petroff, *Phys. Rev. Lett*, **53**, (1984), 2405.
20. J.Gallardo, C.Pellegrini, *Nucl. Instrum. Methods*, A **296**, (1990), 448.
21. I. Ben-Zvi, L.F. Di Mauro, S. Krinsky, M.G. White and L.H. Yu, *Nucl. Instrum. Methods*, **A 304**, (1991), 181.
22. R.Bonifacio, R.Corsini and P.Pierini, *Phys. Rev. A*, **45**, (1992), 4091.
23. C.Rubbia, *Nucl. Instrum. and Meth.* A 278, (1989), 253, C.Rubbia, CERN-PPE/92-61 (1992), Third European Particle Accelerator Conference, Berlin, Germany, March 24-28, 1992.
24 I.Ben-Zvi, L.F.Di Mauro, S.Krinsky, M.G.White, L.H.Yu, Nucl. Instr. Meth, A304, (1991) 181, and I.Ben-Zvi, A.Friedman, C.M.Hung, G.Ingold, S.Krinsky, K.M.Yang, L.H.Yu, I.Lehrman and D.Weissenburger, *Nucl. Instrum. and Meth.* **A 318**, (1992), 208.
25. P.Pierini, L.De Salvo, R.Bonifacio, *Nucl. Instrum. and Meth.* **A 341** (1994) ABS 79.
26. R.A.Jong, W.M.Fawley and E.T.Scharlemann, SPIE Vol. **1045** *Modeling and Simulation of Laser Systems*, (1989), 18; and E.T.Scharlemann and W.M.Fawley, SPIE Vol. **642** *Modeling and Simulation of Optoelectronic Systems*, (1986), 2.
27. R. Bonifacio, L. De Salvo, P. Pierini and N. Piovella, *Phys. Rev. Lett.*, **73**, (1994), 70.

Rodolfo and Lucia Bonifacio with Klaus at his cabin in the mountains.

In Appreciation of Klaus Halbach

Jay Marx

This occasion honors one of this laboratory's heroes. My own appreciation of Klaus Halbach's contributions runs deep and it is only the occasion of my mother's 80th birthday that has kept me from attending the Halbach Symposium. In my absence, I hope these few words can communicate my respect and thanks for Klaus' many contributions, especially to the Advanced Light Source.

My years with the Advanced Light Source were among the most intellectually rewarding of my career, and much of this was due to Klaus Halbach. I joined the ALS after the basic concept was in place and the conceptual design in an advanced state. It became rapidly clear to me that the essential and driving technology behind the ALS was the possibility of high precision, high field, tunable undulators that could be integrated into a low emittance electron storage ring. These undulators were based on Klaus' pioneering concept of using permanent magnets in wigglers and undulators and on the developments of this concept that Klaus, Egon Hoyer, and others contributed in the years preceding the ALS. The bottom line for the ALS was—no Halbach, no undulators, no ALS. It was as simple as that.

You might think that this essential contribution of Klaus' would have saturated the possibilities for the ALS, but it was only the beginning. Klaus was an essential part of the ALS team in many ways, some that were recognized publicly and others that were essential and behind the scenes. I'd like to take a moment to mention just a few.

Klaus was our technical guru. There were many difficult decisions and design challenges along they way and, for the most critical and subtle, we insisted that they pass the "Klaus test." Having Klaus working with us to help evaluate technical solutions was an important part of our process of design reviews and problem solving. An important example was the resolution of one of our most difficult problems. Rather late in the design of the storage ring, at a review of the dipole magnets, Klaus raised a concern that there might be some saturation of the magnet steel that could lead to poor performance at the highest energies planned for the ALS electron beam. Solving this problem was non-trivial (translation--maybe impossible) because the space available for these magnets was fixed and could not be changed. The challenge was to redesign the magnets so that they gave the same field integral in the same space with a lower peak field. Klaus, Jack Tanabe, and others got to work and managed to solve this problem in an elegant way. The result was a dipole that worked and that allowed the ALS to operate up to 1.9 GeV. In fact, operation at 1.9 GeV in now one of the most important modes of operation for the facility.

Klaus' contributions to the ALS went way beyond just the technical and scientific. Klaus trained many of the best engineers who made the ALS possible...Jack Tanabe, Ron Yourd, Egon Hoyer... and many others. Without these graduates of the "Halbach Institute of Technology," the ALS would probably have been beyond LBL's capability.

Then there is the other of Klaus' non-technical contributions to the ALS. One day Klaus came into my office and told me in the most direct terms that he knew of a guy that I had to bring to the ALS or else I was missing a golden opportunity. That was Brian Kincaid. Given my deep respect for Klaus' judgment, I arranged to meet Brian. We hit it off right away (especially after I learned that Brian had, as a student, worked for a time in high energy physics with my undergraduate advisor) and the rest is history. Without Klaus' strong endorsement, we wouldn't have Brian at the ALS today.

Klaus also was a great help to me behind the scenes. When I first joined ALS, he spent time with me and gave me a crash course in the physics of undulators. I often sought out his wise counsel about important decisions, technical and otherwise, and always appreciated his willingness to hold my hand and encourage me when things looked bleak. A long construction project like the ALS is a difficult marathon and having the support of people you respect deeply is essential. Klaus provided important encouragement for me at the difficult moments.

To conclude, I want to thank the organizers of this Symposium. This is a fitting honor to a great scientist and a valued member of the LBL community. And I want especially to thank Klaus for his help, encouragement, many contributions, and for making LBL a unique place to make impossible dreams reality. Thank you Klaus and happy birthday!!

An Informal Note to Klaus

Max Cornacchia

I am happy to join the many physicists and engineers who have had the privilege to collaborate with, and to learn from, Klaus Halbach. I first met Klaus in 1984, when I became involved in the study and design of synchrotron radiation sources. Over the last 10 years I have admired and enjoyed his creativity, mathematical skill and rigor, but above all his contagious enthusiasm and appreciation of the beauty that underlines the mathematical representation of the physical world. Equally important to me and my wife was that the scientific collaboration led to a friendship with Klaus and Ruth that we both cherish.

In the course of the conceptual design of the Advanced Light Source, Klaus explained to us the subtleties of magnetic effects and how the tight magnetic field tolerances of accelerator magnets and insertion devices could be achieved. It was fascinating to follow the apparent simplicity and impeccable logic with which he could manipulate the elusive behavior of magnetic fields. Klaus' fundamental contributions to the theory and design of insertion devices are well known. Because of my particular professional interest, I often read his beautiful study on the description of beam position monitor signals with harmonic functions and their Taylor series expansions. In it, Klaus shows that the integral in the axial dimension of the 3-dimensional potential satisfies the 2-dimensional Laplace equation. This led to an enormous simplification of the problem of determining the optimal geometry for the pick up electrodes. His method was applied to the design of the ALS monitors and, more recently, to the new position monitors of SPEAR.

I was only an observer of the above research, and thus did not have the opportunity to interact closely with Klaus. I was fortunate, however, to collaborate with him on an interesting project. For some time I had been pursuing an idea that, by appropriately shaping the magnetic field of the chromaticity sextupoles, one could increase the magnetic aperture and correct the chromaticity. I had no idea how this magnetic field shape could be realized in practice, and I turned for help to Klaus.

We proposed a new type of chromaticity correction magnets ("modified sextupoles"), having the property of behaving like sextupoles near the magnetic axis, but where the field increases less rapidly at larger distances. The study showed that, if certain particle optics conditions are satisfied, the dynamic aperture increases with respect to the case with conventional sextupoles. Following a suggestion by Albert Hoffman, Klaus, Jeff Corbett and I extended the method to octupole fields. I now believe the latter to be a more promising application of modified magnets for low emittance storage rings. Modified octupoles behave like octupoles near the magnetic axis, but the field increases less rapidly as one moves away, in the transverse plane, from the axis. An amplitude dependent tune shift can be obtained even in a beam of very small emittance without destroying the dynamic aperture. This tune shift gives a tune spread in an ensemble of particles of different amplitudes, and may be used to Landau damp collective instabilities.

As he started studying the problem, Klaus became fascinated and, I think, amused, in finding solutions and designing iron shapes for unusual fields like: $B=B_0 z^2 \exp(-k z^2)$, $B=B_0 z^2/\cosh(z)$, and many others. He introduced me to the power and beauty of conformal transformations, and showed me how one can depart from the conventional expansion of the field in terms of magnetic multipoles. As is typical of his research, he derived a general theorem that gives a deep insight: the theorem expresses quantitatively the fact that if the absolute value of the magnetic field is smaller that the sextupole field strength at one location (for instance on the horizontal axis), it has to be larger than the sextupole strength someplace else.

I am thankful to Klaus for the time we spent together and his friendship, advice and support.

Insertion Device Calculations with Mathematica

Roger Carr
Stanford Synchrotron Radiation Laboratory
P.O. Box 4349, Bin 69, Stanford, CA 94309

Steve Lidia
Physics Department
University of California
Davis, CA 95616

Abstract

The design of accelerator insertion devices such as wigglers and undulators has usually been aided by numerical modeling on digital computers, using code in high level languages like Fortran. In the present era, there are higher level programming environments like IDL®, MatLab®, and Mathematica® in which these calculations may be performed by writing much less code, and in which standard mathematical techniques are very easily used. We present here a suite of standard insertion device modeling routines in Mathematica to illustrate the new techniques. These routines include a simple way to generate magnetic fields using blocks of CSEM materials, trajectory solutions from the Lorentz force equations for given magnetic fields, Bessel function calculations of radiation for wigglers and undulators and general radiation calculations for undulators.

Introduction

Among the most valuable and well known contributions made by Klaus Halbach to the field of magnet physics and technology were his work on the Poisson/Superfish suite of computer codes. [1] These codes have been used by hundreds of designers to model magnetic fields in accelerator devices and in other branches of magnet technology. If he chose to start these projects in the present time, he might be tempted not to write in Fortran, but in a higher level programming environment like IDL, MatLab, or Mathematica. These environments allow the programmer to write in single lines what might take pages in Fortran, they have easy access to powerful mathematical routines, and they have superior graphics interfaces. They generally do not execute as fast as Fortran codes, but on a modern RISC processor, they run reasonably quickly. IDL and MatLab are general calculational tools, but do not offer symbolic manipulation capability. A suite of undulator and wiggler modeling codes has been implemented in IDL [2] Mathematica is more

general, in that it has symbolic manipulation in addition to numerical capacity. In terms of programmer time, programs are much easier to learn, to write, and to debug.

This article comprises a suite of sample calculations used in wiggler and undulator modeling. It is designed as a Mathematica tutorial, a usable program with documentation, and as the basis of a package of modeling codes for the MathSource library. This is a world-wide on-line library of Mathematica codes maintained by Wolfram Research, the corporate source of Mathematica. The contents are available to anyone, and it is intended that designers who have generated additional codes will be able to add their contributions to the package. We will limit the present discussion to pure permanent magnet designs based on concepts initiated by Klaus Halbach [3]. The essential things one wishes to model about an insertion device are the magnetic fields, the trajectories of charged particles (electrons) in the devices, and the radiation produced by particles that pass through them. We illustrate the magnetic field calculations with a typical Halbach CSEM model. The trajectories are solutions to the Lorentz force equations. The radiation may be calculated for sinusoidal trajectories by analytical Bessel function solutions of the radiation integrals, or by numerical calculations for non-sinusoidal trajectories. We show how Mathematica can be used to generate the analytical solutions, and to calculate numerical solutions.

Analytical Approximations

For both wigglers and undulators, there are analytical approximations that employ Bessel functions and give spectra for ideal sine wave magnetic fields. [4] These approximations will serve here as an introduction to Mathematica calculational techniques. Throughout this paper, Mathematica code will be written in boldface. One typically breaks up code into 'cells', which are separately executed units. We will give examples of whole cells, and make text comments between cells. A Mathematica comment is delimited by (* and *). Mathematica considers variable names to be global, unless purposely localized, and is case, but not font sensitive, so $\omega = w \neq W$ The **'Clear'** command should be used freely to prevent confusion. First we declare a set of constants and parameters that will be used in our examples throughout this paper.

```
<<Graphics`Graphics`                    (* an 'include' for LogLogPlot *)
α = 7.29735308 10^-3;                   (* Fine structure constant *)
e = 1.60217733 10^-19;                  (* Coulombs *)
m = 9.1093897 10^-31;                   (* Kg *)
GeV = 9                                 (* Electron energy in GeV *)
```

```
ElectronEnergy = GeV*10^9                                   (* eV *)
ElectronCurrent = 0.100;                                    (* Amps *)
BandWidth = 0.001;                                          (* ΔE/E  = Δω/ω *)
γ = e*ElectronEnergy/(m*c^2);                               (* 1957*E (GeV) *)
ElectronsPerSecond = ElectronCurrent/e;
Normalization = BandWidth*ElectronsPerSecond/MilliradiansPerRadian^2
```

For the NdFeB/iron hybrid wiggler case, we use the following additional definitions. In Mathematica, one may define a function with an '=' sign, for immediate execution, or with an ':=' sign, for delayed execution.

```
Θopen = 0.0005;                                             (* opening angle - radians *)
λ = 0.250;                                                  (*  period length - meters *)
gap = 0.020;                                                (* meters *)
poles = 20;
Bo = 3.44Exp[-gap/λ(5.08 - 1.54gap/λ)];                     (* Halbach formula for NdFeB *)
CriticalEnergy = 0.665ElectronEnergy^2*Bo;                  (* keV - Bo in Tesla *)
K = 93.4*Bo*λ;                                              (* K parameter  *)
δ = K/γ;                                                    (* angular deflection - radians *)
Const = Poles*Sqrt[3]*α*γ*BandWidth*ElectronsPerSecond/(2*Pi);
Energy[Θ_] := CriticalEnergy*Sqrt[1 - Θ^2/δ^2]              (* energy of x-rays - keV *)
ysq[Θ_,Eγ_] := (Eγ/Energy[Θ])^2                             (* convenience definition *)
```

Wiggler radiation may be considered to be just a simple addition of bending magnet radiation, which has an angular flux distribution: [3]

$$\frac{dF}{d\theta} = \frac{\sqrt{3}}{2\pi}\,\alpha\,\gamma\frac{\Delta\omega\, I}{\omega\, e}\int_y^{\infty} K_{5/3}(y')\,dy' \qquad [1]$$

Mathematica has the impressive capacity to perform a symbolic evaluation of this integral; the result is G1, given below. (try this in Fortran!)

```
G1[Θ_,Eγ_] := (ysq[Θ,Eγ]*((-4*Pi*ysq[Θ,Eγ]^(1/2))/(3^(1/2)*ysq[Θ,Eγ]) +
(3*2^(5/3)*ysq[Θ,Eγ]^(1/6)*Gamma[5/3]*
HypergeometricPFQ[{-1/3}, {-2/3, 2/3}, ysq[Θ,Eγ]/4])/ysq[Θ,Eγ] -
(3*ysq[Θ,Eγ]^(5/6)*Gamma[-5/3]*
HypergeometricPFQ[{4/3}, {7/3, 8/3}, ysq[Θ,Eγ]/4])/2^(11/3)))/4
```

The flux integrated over an opening angle and properly normalized is:

```
F[Eγ_] := Const*NIntegrate[G1[Θ,Eγ],{Θ,-Θopen, Θopen}]
LogLogPlot[Evaluate[F[Eγ]],{Eγ,.1,25}, Frame -> True, PlotRange -> All]
```

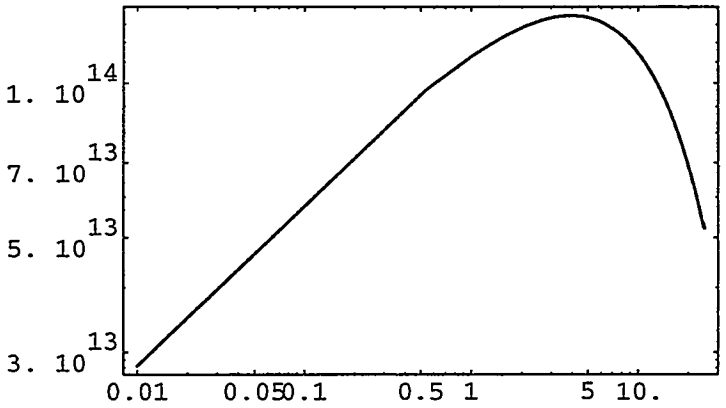

Figure 1: Wiggler angular flux density (photons/(sec•0.1A•0.001BW•mr^2)) integrated over a ± 0.5 mrad opening angle with the other parameters given above. The critical energy is 13.8 keV, the K parameter is 54, and the magnetic field has maximum value of 2.3 Tesla.

A wiggler has larger deflection parameter (K >> 1) and emits radiation like a searchlight sweeping periodically past the observer. [4] An undulator has smaller deflection parameter (K ≤ 1) and the observer is always illuminated by the 'searchlight'. This allows the radiation from consecutive emission events to interfere, so the spectrum is peaked. The Bessel function analytical approximation for sinusoidal field undulators is give by the code:

```
periods = 10;
λ = 0.04;                                   (* Meters *)
K = 2.0;                                    (* K parameter *)
ξ  = K^2/(4*(λ + K^2/2));                   (* Bessel function argument *)
Ef = 9.50*Ee^2/(λ*(1 + K^2/2));             (* Energy of fundamental  - eV*)
Const = Normalization*α*periods^2*γ^2**K^2/(1+K^2/2)^2;
nmax = 6;                                   (* calculate first nmax harmonics *)
Besselsum[n_] := (BesselJ[(n-1)/2, n*ξ] - BesselJ[(n+1)/2,n*ξ])^2;
Sincfun[E_ , n_] := (Sin[Np*Pi*(n - E/Ef )] / (Np*Pi*(n - E/Ef)))^2;
Spectrum[E_] := Sum[n^2*Const*Besselsum[n]*Sincfun[E,n], {n,1,nmax,2}];
Plot[Evaluate[Spectrum[E]],{E,0, 12Ef}, Frame -> True,
PlotRange -> All, PlotPoints -> 20nmax]
```

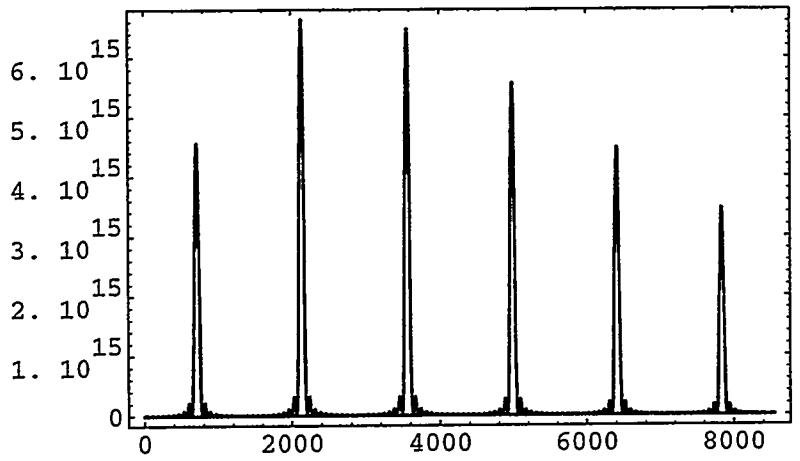

Figure 2: Undulator angular flux density (photons/(sec•0.1A•0.001BW•mr^2)) for 10 periods, K = 2, λ_u = 4 cm, and electron energy = 3 GeV.

We will now turn to a suite of calculations for the undulator case, which may be used for the case of non-ideal sine waves. The wiggler case is similar, but requires much more calculation, because one effectively calculates the undulator case for very large numbers of harmonics; very wide bandwidth Fourier transforms are required to satisfy the Nyquist criterion.

Undulator Magnetic Fields

Pure permanent magnet insertion devices are assemblies of blocks of magnetic materials, with no permeable materials around to concentrate or conduct magnetic fields. The permeability of modern SmCo or NdFeB materials is generally considered to be unity in calculations, though it is really slightly greater. Considering the permeability to be unity makes our simple calculations possible, because then all fields superpose linearly. The CSEM model refers to Charge Sheet Equivalent Magnets or Current Sheet Equivalent Magnets [5]. In this model, magnets may be thought of as sheets of charge or current on the faces of the block of material. For this paper, we will be interested in rectangular blocks whose easy axis of magnetization is normal to two opposite faces. Our CSEM model is two-dimensional; it is assumed that the transverse width of the magnet rows is great enough that the field is constant in the x direction.

The Halbach pure CSEM insertion device generates a periodic magnetic field using an assembly of magnet blocks as shown below, representing the simplest, but most common case [3].

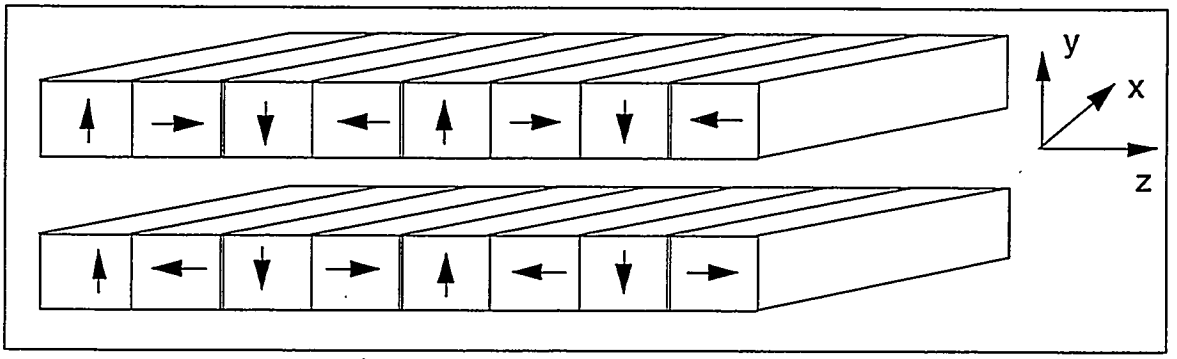

Figure 3: Two periods of a Halbach undulator, seen from the side. Each block is shown with an arrow indicating the easy axis direction of magnetization.

There are two rows of magnets, in this case each has 4 blocks of CSEM per period, and a typical wiggler or undulator may have tens of periods or more. We shall begin by showing how the CSEM fields may be calculated in Mathematica. First, initialize everything, and define global constants; the gap value is chosen so that we will have K = 2.

```
λ = 0.04; bh = λ/4; bw = λ/4; gap = 0.0147527;          (* distances in meters *)
periods = 12; blocks = periods*8 + 2; extra = 3;
```

There are a total of **periods*8 + 2** magnet blocks and we calculate fields for a distance of several (**extra**) periods on each end. Use the cell below if you are reading in measurement data from an ASCII file, such as a WORD 'text only' file. The file must have two columns, separated by spaces, and **blocks** entries in each column. The first entry is the easy axis B field measurement, and the second entry is the error field measurement, taken normal to the easy axis and the long axis of the block.

```
Magnetudes = ReadList["magfile.dat",Number,RecordLists -> True];
```

Or use the following cell instead if you just want an ideal case data set of 1.2 T along the easy axis, and 0 error fields; we use this case in what follows:

```
Magnetudes = Table[{1.2, 0.0}, {n,1,blocks}];
```

The next cell makes the end blocks have half strength, so that the trajectory has no net displacement, and normalizes the strength to physical values. It then calculates the CSEM fields, based on the fields of blocks that are arrayed in upper and lower rows, and rotated to have the Halbach sinusoidal arrangement. The field of the end half blocks points downward. The CSEM physics is in the **BlockField** which is a sum of the fields of two current sheets, flowing in opposite directions, that are equivalent to a block of CSEM with dimensions **bh** (block height) x **bw** (block width).

The **BlockStrength** function makes the end blocks half the strength of the center blocks. **Bo** is complex (I ≡ i), and **BlockField** is the field (B* ≡ By - iBz) of a block at (y + iz) observed at the origin. **By** is a spline fit interpolation that yields the field as a interpolating function that is much faster to evaluate than **TopJawField** and **BotJawField.**

```
BlockStrength[n_] := If[(n==1)||(n==blocks/2)||(n==blocks/2+1)||(n==blocks), 0.5, 1]

Bo[n_] := BlockStrength[n]*Magnetudes[[n]].{1,I}/(2*Pi)

BlockField[y_, z_] := Log[((y+I*z)^2-(bh/2-I*bw/2)^2)/((y+I*z)^2-(bh/2+I*bw/2)^2)]

TopJawField[y_, z_] :=

Sum[I^n*Bo[n]*BlockField[gap/2 + bh/2 - y, n*bw - z], {n,1,blocks/2}]

BotJawField[y_, z_] :=

Sum[I^(2-n)*Bo[n + blocks/2]*BlockField[-gap/2 - bh/2 - y, n*bw - z], {n,1,blocks/2}]

ByField[z_] = Re[TopJawField[0,z] + BotJawField[0,z]];

By = Interpolation[Table[{z,ByField[z]}, {z, -extra*λ, (periods + extra)*λ, λ/10}]];
```

We may now plot out the results. The real part of the field is in the vertical or 'y' direction, and the imaginary part is in the longitudinal or 'z' direction.

```
Plot[Evaluate[By[z]],{z, -extra*λ, (periods + extra)*λ},
Frame -> True, PlotPoints -> 200]
```

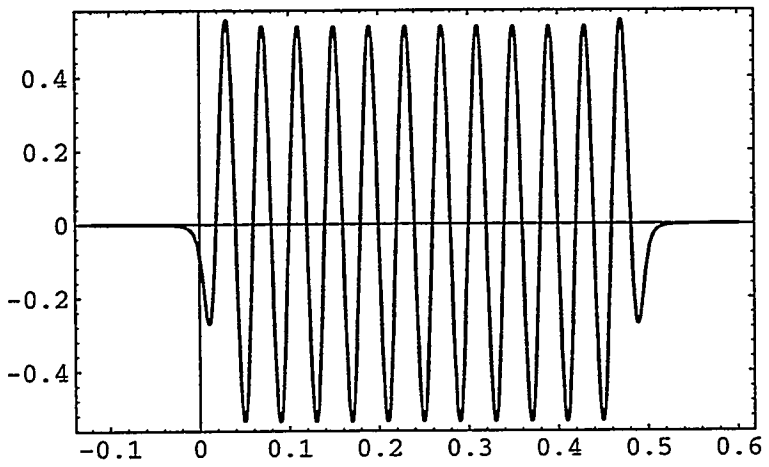

Figure 4: The By field strength (Tesla) as a function of axial distance (meters) for the parameters given above.

Tapered Undulator

And now for a little digression; we will show how a variable tapered undulator may be designed without any taper of the gap. Consider an undulator whose jaws have slightly different periodicity, and which may be moved longitudinally with respect to each other. The different periodicity creates the taper, and the longitudinal or phase motion varies the amount of taper. We model the situation quickly in Mathematica with a sum of two sine functions representing the fields from the upper and lower jaws.

```
λ = 0.04;  a = λ/1000;

SinSum[z_] := (Sin[2*Pi*z/(λ+a) - ϕ/2] + Sin[2*Pi*z/(λ-a) + ϕ/2])

Plot[Evaluate[SinSum[z]], {z,0,1}, Frame -> True,  PlotPoints ->200]
```

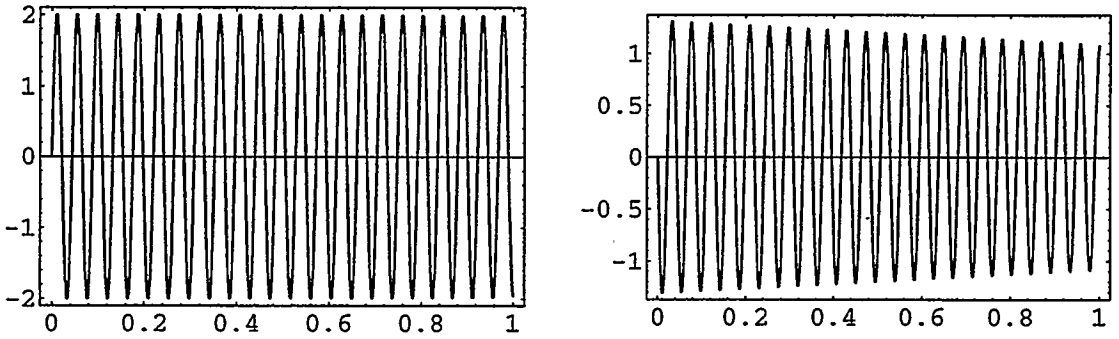

Figure 5: Sum of sine waves with slight differences of period length with no phase shift (left) and with slight phase shift (right).

The plot on the left shows the sum of the two sine wave fields with a difference of period length of $a = \pm \lambda/1000$ and $\phi = 0$. There is a very slight taper of about 1%. But when ϕ is increased to 0.5π, the taper becomes 20%. There is an overall decrease of field strength, but this can be compensated by decreasing the gap. There is also an overall cosine envelope over the taper, but with $a = \pm \lambda/1000$, the deviation from a linear taper is very slight. It may be more convenient to build an adjustable phase tapered undulator than one with a tapered gap, so this concept may be worth considering in free electron laser designs.

Undulator Trajectories

Now back to the central task of a numerical calculation of the undulator fields, trajectories, and spectra. From the fields, we calculate the trajectories of electrons using the Lorentz force equation: $\mathbf{F} = d(m\gamma\beta)/dt = e\,\beta\,\hat{}\,\mathbf{B}$. After a few definitions, Mathematica can integrate these equations in a single instruction.

```
η = c^2/ElectronEnergy;                          (* = e/(m*γ)  *)
βz0 = Sqrt[γ^2-1.0]/γ;                           (*  initial velocity /c *)
Const = Normalization* α*e*hbar/(4*Pi^2*c^2);
```

The Lorentz force equations are solved using NDSolve. The **AccuracyGoal** is the number of decimal units the solution is supposed to be accurate to; if it is set much lower than 40, broken trajectory solutions may occur. After finding the solutions, we employ the /. operator to generate callable interpolating functions from them.

```
trajectory = NDSolve[{                           (* NDSolve is a numerical DE solver *)
D[βx[t],t] == -η*βz[t]*N[By[rz[t]]],              (* N is the numerical evaluation function *)
D[βz[t],t] == η*βx[t]*N[By[rz[t]]],
D[rx[t],t] == c*βx[t],                           (* rx and rz are coordinates *)
D[rz[t],t] == c*βz[t],                           (* βx and βz are velocities/c *)
βx[0] == 0, βz[0] == βz0, rz[0] == -extra*λ, rx[0] == 0},
{rz,rx,βx,βz},{t,0,(periods + 2*extra)*λ/c}, AccuracyGoal -> 40, MaxSteps -> 1000*periods];
x = rx /. First[trajectory];                     (* convert rx table to x function *)
z = rz /. First[trajectory];                     (* convert rz table to z function *)
```

The trajectory is both displaced (because of the use of half blocks at the ends) and deflected angularly (because we did not use enough 'extra' length to include all the magnetic field, or because there is a dipole error). When using real magnets, corrector fields are used to null the deflection. For purposes of Fourier analysis, we truncate a period at each of the ends, straighten the deflection, and null the displacement. The code below is used for these purposes:

```
tptotal = (periods + 2*extra)*λ/c;                    (* total t' emitter time *)
xmin = FindMinimum[x[tp] - x[tptotal]*tp/tptotal, {tp,(extra + periods/2-1)*λ/c,
(extra + periods/2+1)*λ/c}][[1]];                     (* minimum displacement *)
xmax = FindMinimum[-x[tp] + x[tptotal]*tp/tptotal, {tp,(extra + periods/2-1)*λ/c,
(extra + periods/2+1)*λ/c}][[1]];                     (* maximum displacement *)
```

```
xmean = (xmin - xmax)/2;                    (* mean displacement *)
slope = (x[tptotal] - x[0])/tptotal          (* overall deflection *)
```

The horizontal trajectory, before and after surgery, is shown below:

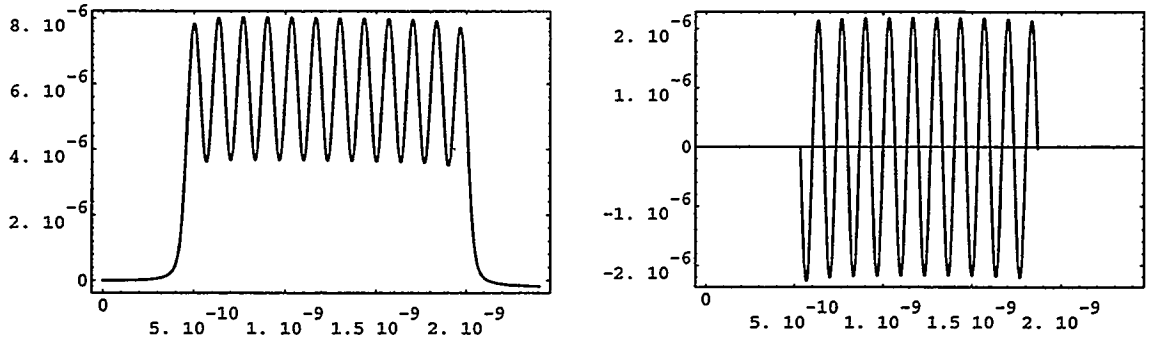

Figure 6: The horizontal displacement (meters) versus emitter time (seconds). The plot on the left is the raw calculation; the one on the right has been leveled, displaced to zero, and truncated by one period at each end.

Undulator Radiation

The flux per steradian per unit frequency interval is given by the expression [6]:

$$\frac{d^2I}{d\omega\, d\Omega} \cong \frac{e^2\omega^2}{4\pi^2 c}\left|\int_{-\infty}^{\infty} \mathbf{n}(t')\wedge[\mathbf{n}(t')\wedge\beta(t')]\, e^{i\omega(t' - \mathbf{n}(t')\cdot\mathbf{r}(t')/c}dt'\right|^2 \qquad [2]$$

where t' refers to the time coordinate of a radiating electron; it is traditionally called the 'retarded' time. It requires a time delay $t = t' + R(t')/c$ for the radiation to reach the observer at a distance R from the emitter. The electron is moving at nearly the speed of light, so two radiation events (like two poles of a wiggler) that are separated in space are squeezed very closely in time, because the photon emitted in the first event is accompanied closely by the electron. Events are squeezed together by approximately $1/2\gamma^2$. One must distinguish here between the concept of the 'observer' in discussions of special relativity where it refers to the laboratory coordinate system, and the radiation observer. Both the observer and the emitter time are in the laboratory system; when one solves for the trajectory, the coordinates are those of the emitter (t').

The radiation expression may also be written using a Fourier transform [7]:

$$\frac{d^2I}{d\omega\, dA} \cong \frac{e^2\omega^4}{4\pi^2c^2}\left|\int_{-\infty}^{\infty} \mathbf{n}(t')\; e^{i\omega t}\, dt\right|^2 \cong \frac{e^2\omega^4}{4\pi^2c^2}\left|\int_{-\infty}^{\infty} \frac{\dot{x}(t')}{R}\; e^{i\omega t}\, dt\right|^2 \cong \frac{1}{R^2}\,\frac{d^2I}{d\omega\, d\Omega} \quad [3]$$

$dA = R^2 d\Omega$ is the element of area subtended by the solid angle Ω for an observer a distance R from the source. In formulas [2] and [3], implementations require attention to boundary conditions, but for high frequencies and for an observer located far from the source, these formulas are good approximations [8]. The advantage of the Fourier transform is that it may be done very quickly by computer; the direct formula has a very rapidly oscillating phase that is difficult for numerical algorithms to handle; it calls for the use of very time consuming computation or the principle of stationary phase [9]. The integrand $\mathbf{n}_x \equiv \mathbf{x}$ generates the horizontally polarized component of the x-rays, which is dominant in this example.

Here we perform the inversion of the argument of the t' argument in the integrand, because it must be written in observer time as t'(t). In this calculation, all the "**tp**" symbols refer to t', the emitter (retarded) time. The "**t**' symbols refer to the observer (squeezed) time. The function **Tprime** gives t' in terms of t. We are using the trick of running **Interpolation** function backwards, by reversing dependent and independent variables to generate t' at evenly spaced intervals of t.

```
tpstart = (extra+1)*λ/c;                    (* truncated start of emitter time *)
tpend = (extra+periods-1)*λ/c;              (* truncated end of emitter time *)
dtp = (tpend - tpstart)/(50*periods);       (* increment of t' time *)
T[tp_] := tp - z[tp]/c;                     (* definition of observer time *)
Tprime = Interpolation[Table[{T[tp],tp},{tp,tpstart,tpend,dtp}]];
```

The time squeezing effect sharpens the peaks of the trajectory when plotted as x(t), which is nearly sinusoidal when plotted as x(t'). The generally triangular shape of the curve leads to an odd-harmonic Fourier series. The abcissa is the index of the data in the Table. We must pad the data set with a generous number of zeros in order to avoid the low frequency background caused by a small sized rectangular window. Mathematica performs a fast Fourier transform so it needs a data set with a power-of-two number of members; here we use 2^{11} data points plus 15×2^{11} zeros. We are now able to perform the Fourier transform on **fdata**, a table of the massaged x component of the integrand.

```
fpts = 2^11;                                    (* points in Fourier transform *)
tend = T[tpend];                                (* end of observer time *)
tstart = T[tpstart];                            (* start of observer time *)
dt = (tend - tstart)/(fpts-1);                  (* increment of observer time *)
fdata = Table[(x[Tprime[t]]- xmean - slope*Tprime[t]), {t,tstart,tend,dt}];
zdata = Table[0, {n,1,15*fpts}];                (* zero padding *)
ftrans = Fourier[Join[fdata,zdata]]/Sqrt[16^3*fpts]; (* scaled Fourier transform*)
xxEfun = 9.50*GeV^2/(l*(1 + K^2/2));            (* Energy of fundamental in eV *)
Ef = N[hbar*2*Pi/(fpts*dt)];                    (* Energy conversion factor  *)
nf = Efun/Ef;                                   (* index of fundamental peak *)
ω[n_] = 2*Pi*n/(fpts*dt);                       (* angular frequency of x-rays *)
AngularFluxDensity = Table[{ω[n-1]/(16*ω[nf]),  (* angular flux density *)
Const*w[n]^4*Abs[ftrans[[n]]]^2 },{n,1,fpts}];
```

The horizontally polarized component of the spectrum is shown below, normalized for comparison to the Bessel function result in Figure 2.

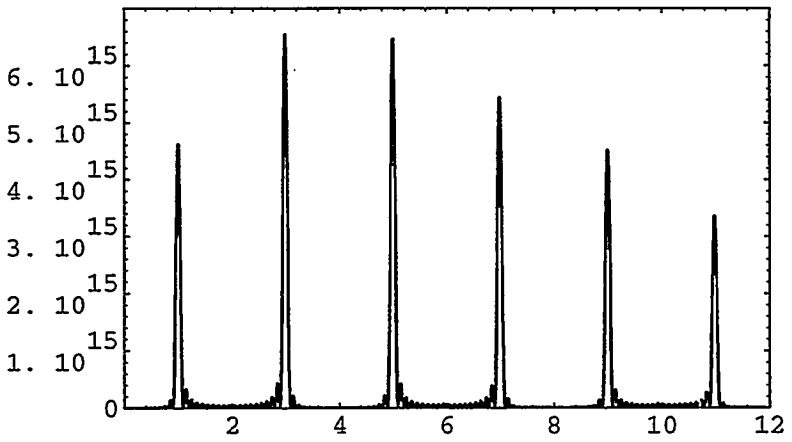

Figure 7: The on-axis, zero-emittance undulator angular flux density (photons/(sec•0.1A•0.001BW•mr^2)) versus harmonic number, for 10 periods, K = 2, l_u = 4 cm, and electron energy = 3 GeV.

Summary

We have presented above the basic suite of routines necessary to calculate the radiation from CSEM undulators. The exercise was done in order to show how a higher level programming language may be used to generate a

simple code set, where the mathematics is not obscured by programming conventions.

These are the most elementary calculations one might wish to perform in insertion device design; beyond this one wishes to calculate off axis and emittance effects. The effects of magnet imperfections are easily taken into account by preparing an imperfect data set at the beginning of the code above. These examples were implemented on an Apple MacII-fx using version 2.0 of Mathematica and 16 MBytes of memory. They are quite time consuming (most of a minute/period for B-field or trajectory calculations, but the Fourier transform is very fast). Mathematica can be used as a front end on a personal computer with a kernel running on a fast machine; these times will go down by an order of magnitude when running on a kernel on a RISC processor.

Acknowledgments

The authors thank Roger Dejus of the Advanced Photon Source for several very helpful discussions. IDL is a trademark of Research Systems, Inc., MatLab is a trademark of MathWorks, Inc., and Mathematica is a trademark of Wolfram Research, Inc. This work was supported by the US Department of Energy, Office of Basic Energy Sciences.

References

[1] Poisson/Superfish Reference Manual, LANL Publication LA-UR-87-126 (1987).
[2] R. Dejus, Nucl. Inst. & Methods A347 p. 56-60, (1994) and R. Dejus and A. Luccio, Nucl. Inst. & Methods A347 p. 60-66, (1994).
[3] K. Halbach Nucl. Inst. & Methods 187 p. 109-117 (1981).
[4] ALS Handbook LBL Publication 643, Rev 2 (1989).
[5] K. Halbach J. Appl. Phys 57, p. 3605 (1985).
[6] J. D. Jackson Classical Electrodynamics 2nd ed. p. 671 (1975).
[7] C. Wang, Phys. Rev E47, p. 47 (1993).
[8] R. Walker, Rev. Sci. Instrum. 60, p. 1816 (1989).
[9] C. Wang and D. Xian, Nucl. Inst. & Methods A288 p. 649 (1990).

Roger Carr

Steve Lidia

Letter To Klaus

Karl Brown

Dear Klaus

As I recall we first met at a conference in the late 50's or early 60's when I was presenting a review paper on the development of TRANSPORT theory for charged particle optics. After my talk you came up to me and said: "Karl, I think you should write a book on this!". I agreed and countered that you should write a book on your magnetic design principles. Since then we have become good friends and have observed the contributions and development of each other in the world of science and engineering but neither of us has yet published THAT book.

I have thought of many things that I might say to you in a letter for your Festschrift, or a scientific paper that I might present, that would remind both of us of the extensive interaction that we have had over the past years. But I must confess that none of the ideas that have come to mind seemed adequate to express how I really feel about our friendship or sufficient to cover the numerous scientific and technical accomplishments that we have experienced together over more than thirty years of our productive lives. Both of us, but especially you, have had the unique opportunity to interact with, and have a profound influence on, the scientific development of many Laboratories, Universities, and Business establishments. I plead guilty of getting you involved in many of these activities by introducing you to people who have had a need for your particular expertise. Just to name a few of these activities: There is Los Alamos, SSRL, Varian Associates, KFA, CERN, Saskatoon, and of course the many needs for your talents here at SLAC. So I hope you will forgive me for getting you involved in all of these activities and do not feel that it has been a waste of your time.

We now both find ourselves at what some would say is "the retirement age" but I don't believe that either of us think in such terms. I would rather say it is an age where we change the pattern of activity a little and can sit back and appreciate some of the results of important things that we initiated in an earlier phase of our careers.

Both of us find ourselves faced with a 'health' problem but I am optimistic that, with the knowledge and life styles that we have, we will be fortunate enough to end up on the positive tail of the distribution curve for such problems. I wish you good luck and want to express my sincere appreciation of having you for such a good friend over the many years that we have known each other.

May it continue...

Karl

Karl Brown

Low-Field Permanent Magnet Quadrupoles in a New Relativistic-Klystron Two-Beam Accelerator Design

Simon Yu and Andrew Sessler*
Lawrence Berkeley Laboratory
University of California,
Berkeley, CA 94720

Abstract.
Permanent magnets play a central role in the new relativistic klystron two-beam-accelerator design. The two key goals of this new design, low cost and the suppression of beam break-up instability are both intimately tied to the permanent magnet quadrupole focusing system. A recently completed systems study by a joint LBL-LLNL team concludes that a power source for a 1 TeV center-of-mass Next Linear Collider based on the new TBA design can be as low as $1 billion, and the efficiency (wall plug to rf) is estimated to be 36%. End-to-end simulations of longitudinal and transverse beam dynamics show that the drive beam is stable over the entire TBA unit.

INTRODUCTION

Two-beam-accelerators[1] (TBA) were first conceived as potentially very efficient power sources for future linear colliders. For example, the relativistic-klystron version[2] (RK-TBA) can be viewed simply as a klystron with energy recovery by the recycling of the 'spent' beam, which would otherwise have been 'wasted' in a final collector. Earlier experiments have demonstrated the extraction of very high rf powers from high current electron beams in induction linacs[3,4]. Recently, reacceleration of bunched beams was demonstrated in a system with three rf extraction cavities and two intervening reacceleration induction cells[5]. The rf power extracted shows amplitude and phase stability over a significant fraction of the beam pulse, in good agreement with code predictions.

In order for the TBA concept to be realizable as a practical power source for future colliders, a case must be made for the technical feasibility of a high current drive beam propagating stably over long distances as well as for the overall economical attractiveness of an induction-linac based TBA system. To this end, we have recently constructed a new design for an RK-TBA based power source for a 1 TeV Next Linear Collider (NLC)[6] and have performed a physics, engineering and costing study. A detailed report on the findings of this systems study is presented elsewhere[7].

A novel feature of this new RK-TBA design is the quadrupole focusing system based on low-field permanent magnets. In this paper, we show the central role played by this focusing system in the overall physics as well as the engineering design.

RK-TBA ARCHITECTURE

The power source requirement is based on the SLAC design of the "NLC Upgrade" with 1 TeV c.m. energy[6]. To generate an unloaded gradient of 100 MV/m in the high-gradient structures, the TBA must supply 360 MW of rf power at 11.4 GHz every 2 meters. The output rf field is specified to have a 100 ns linear rise followed by 200 ns flat-top. The repetition rate is 120 Hz.

To power a 15 km long collider (7.5 km for each arm), we propose an architecture with 50 RK-TBA units, each 300 m long, operating at an average drive beam energy of 10 MeV, with an average current of 600 amps over the duration of the pulse, and a reacceleration gradient of 300 kV/m.

The front end of each RK-TBA unit consists of a 1.5 kA injector, followed by an rf chopper at 2.5 MeV, and an 'adiabatic capture' unit in which the chopped beam (average current 600 A) is accelerated to 10 MeV and further bunched with idler cavities in preparation for injection into the main TBA. To enhance the efficiency of the TBA system, an 'afterburner' at the end of the main TBA continues to extract rf power through 12 successive output cavities before depositing the spent beam (average beam energy < 3 MeV) at the beam dump. The overall efficiency (drive-beam to rf) of each RK-TBA unit is 90%. The 10% loss is shared among the beam loss on the chopper (3.7%), beam dump (2.8%), and rf into induction cells (3.5%).

The new RK-TBA design is based on the technology of long-pulse (~ microseconds) induction machines that have been studied over the last 15 years for heavy ion fusion applications[8,9]. The magnetic material used in this design is Metglas™, which can accommodate a large flux swing of nearly 3 T before saturation. The induction cores can therefore be made quite compact. Commercial applications of this material over the last few years have led to dramatic reductions in the cost of Metglas.

In short-pulse induction machines with large pipes, such as ATA and ETA, it is not possible to use Metglas because of the excessively large core losses. However, the introduction of compact permanent magnet quadrupoles with small bore now permit us to make small Metglas cores with acceptable core losses. The resulting induction cell design has a transverse diameter of about 34 cm—much smaller than any of the previously known induction cells. Hence, the permanent magnet system affects not only the focusing system, but also, indirectly, the accelerating system, and is a cornerstone of the whole design.

The pulse power for the induction cells is a low voltage system. The induction cores consist of small 20 kV units, powered by pulse forming networks (PFN's) switched by ceramic thyratrons. Power is fed into the PFN's via DC power supplies and command-resonant-charging systems. The low voltage design bypasses step-up transformers with associated losses. The main losses in this system are associated with core currents in the induction cells. The efficiency of the pulse power system (wall plug to drive-beam) is estimated to be 40%. The overall efficiency of the entire system (wall plug to rf) is 36%.

The rf extraction cavities are located every 2 meters. Present designs center around traveling-wave structures with 3 inductively detuned rf cells, with an inner radius of 8 mm. A pair of iris-waveguide structures in the last cell are matched for power extraction.

QUADRUPOLE FOCUSING WITH PERMANENT MAGNETS

In the design of induction accelerators, the size of the beam tube is usually determined by BBU considerations, since the transverse impedance from the acceleration gap is inversely proportional to the square of the pipe radius. In our TBA design, the low frequency BBU arising from the induction gaps is ameliorated by the low beam current of 600 A, and the Landau damping associated with the large energy spread inherent in the rf buckets. Hence, with proper attention to the gap geometry, we are able to design a narrow tube with a radius of 2.5 cm, and predict acceptable low frequency BBU growth.

The small pipe radius allows us to take full advantage of permanent magnets, which have significant cost advantages when the focusing systems are small. Another major reason for the use of permanent magnets is the associated efficiency, as they eliminate the need for power supplies.

Several basic considerations govern the design of the FODO lattice. The foremost requirement is associated with a "trick" concocted to minimize the high frequency BBU growth arising from the HEM11 mode in the rf extraction cavities. To suppress the instability growth, we demand that the betatron period be equal to the distance between adjacent extraction cavities, i.e. 2 meters. In addition, the phase advance per lattice period must be less than 90 degrees to ensure beam stability.

In our design, we use a phase advance of 60 degrees. There are 12 half- lattice-periods in 2 meters. The physical occupancy factor is 0.48. A modified thin lens formula then gives a B-field at pole tip of 800 Gauss for 10 MeV electrons. This estimate is within a few percent of the actual B field required to give a 2 m betatron period, when we include realistic spatial profile of the magnetic field, as well as the energy variations of the drive beam as it is accelerated over the 2 m module.

A basic requirement of the transport channel is that the focusing strength must be sufficiently strong to keep the beam from hitting the beam tube. With a normalized edge emittance of 600 mm-mr, (which is achievable with a good gun design), we obtain an edge radius of slightly over 2 mm for the beam.

A very simple and elegant design of the permanent quadrupole magnets was proposed by Klaus Halbach[10]. Because of the low magnetic field required for this application, it is possible to use ferrites (with B_r of 3.2 kG), which is much less expensive than rare earth magnets. A preliminary quadrupole design consists of 4 rectangular blocks, each dimension is 1.1 cm by 3.32 cm by 8 cm. The first nonzero harmonic (n=10) has a strength which is 8.6% of the quadrupole field at aperture radius.

ERRORS AND CORRECTIONS

Since the beam apertures are small, particularly around the extraction cavities, beam centroid displacements must be kept to a minimum. Quad misalignments, when combined with energy variations from head to tail, can lead to beam offsets that change over the length of the pulse, i.e. the "corkscrew" phenomenon. Our strategy for minimizing beam displacements and associated corkscrew is to impose misalignment tolerances that are not

excessively tight, design for energy flatness of < 1%, and to correct alignment errors with closely spaced dipole steerers.

A key ingredient for the suppression of high frequency BBU is that the betatron period be equal to the distance between adjacent cavities. To ensure that this requirement is obeyed, a feedback system with 2 correction quadrupoles per betatron period is incorporated into the design. A possible monitor for the betatron motion is to use the rf output from the extraction cavities at the dipole frequency.

Steering and focusing corrections are achieved in the present design by means of low-field (~10 Gauss) DC coils located in the region immediately outside of the permanent magnets, at radial positions of about 4 cm from axis. These correction coils can be manufactured inexpensively on printed circuit boards.

RK-TBA BEAM DYNAMICS

End-to-end modeling of the longitudinal as well as transverse beam dynamics for bunched beams through 300 m long RK-TBA units were conducted as part of our systems studies. Longitudinal dynamics is simulated with the RKS codes (1-D and 2-D)[11]. We have shown stable beam propagation and rf generation over 150 inductively detuned traveling wave extraction structures[12]. These code calculations include the front end chopper and adiabatic capture section. The high frequency BBU instability associated with the HEM11 mode in the traveling wave structures was simulated with the OMICE code[13] constructed by Tim Houck, and BBU suppression over 300 meters with the betatron node scheme is explicitly demonstrated[12]. Sensitivity of the scheme to errors in magnetic field and beam energy was also explored, and it was concluded that without feedback, the required accuracy is a fraction of 1%. A separate low frequency BBU mode associated with the induction gaps was also simulated. It was shown that the Landau damping associated with the energy spread in the rf bucket was sufficiently strong to suppress this mode to tolerable levels over the entire RK-TBA unit. Design of the rf extraction cavities were made with MAFIA and URMEL, while the induction gaps were designed with the LLNL code AMOS.

RK-TBA COSTING

A first engineering and costing exercise for the full TBA system has been performed. The electrical design includes all components starting from the AC power distribution system, to the DC power supplies, the command resonant charging system, the pulse forming networks, and the induction cores. Racks and installation, as well as instrumentation and control, were included in this exercise. The mechanical design and costing includes details of the induction cells, rf structures, vacuum, alignment, and utilities. Costs were estimated with a 'bottom-up' approach, assuming mass production procedures for fabrication and assembly. ED&I costs are also included. Conventional facilities and any institutional overhead are considered as part of the main accelerator project, and are not included in the present power source costing exercise. Our preliminary cost estimate for the TBA-based power source for a 1 TeV c.m. NLC is $954 M. The overall efficiency of the system (wall plug to rf) is estimated to be 36%.

ACKNOWLEDGMENT

We are indebted to our collaborators in this study, namely; F. Deadrick, N. Goffeney, E. Henestroza, T. Houck, H. Li, C. Peters, L. Reginato, D. Vanecek, and G. Westenskow.

REFERENCES

* Work supported by the Director, Office of Energy Research, Office of High Energy and Nuclear Physics, Division of High Energy Physics of the U.S. Department of Energy, under Contract No. DE-AC03-76SF00098.

1. Sessler, A.M., "The Free-Electron-Laser as a Power Source for a High Gradient Accelerating Structure", Workshop on Laser Acceleration of Particles, NY, AIP Conference Proceedings 91, 154 (1982).
2. Sessler, A.M. and Yu, S.S., "Relativistic-Klystron Two-Beam Accelerator", Phys. Rev. Lett. 58, 2439 (1987).
3. Orzechowski, T.J., et al., "Microwave Radiation from a High-Gain Free-Electron-Laser Amplifier", Phys. Rev. Lett., 54, 889 (1985).
4. Allen, M.A., et al., "Relativistic Klystrons", SLAC-PUB-4861, LLNL Report UCRL-100634 (1989).
5. Westenskow, G.A. and Houck, T.L., "Results of the Reacceleration Experiment: Experimental Study of the Relativistic-Klystron Two-Beam-Accelerator Concept", Proceedings of the 10th International Conference on High Power Particle Beams, San Diego, Ca. (1994).
6. Siemann, R.H., "Overview of Linear Collider Designs", Proceedings of the 1993 Particle Accelerator Conference, Washington D.C., 532 (1993).
7. Yu, S.S. et al., "Relativistic-Klystron Two-Beam-Accelerator as a Power Source for a 1 TeV Next Linear Collider - A Systems Study", LBL Report, Nov. 1994.
8. Hogan, W.J., Bangerter, R., Kulcinski, "Energy from Inertial Fusion", Physics Today 42, #9, 42 (1992).
9. Fessenden, T., and Fong, C., editors, "Induction Linac Systems Experiments - Conceptual Design Report", LBL document PUB-5324 (1992).
10. Halbach, K., private communication (1994).
11. Ryne, R.D. and Yu, S.S., "Relativistic Klystron Simulations Using RKTW2D", Proceedings of the 1990 Linear Accelerator Conference, Albuquerque, New Mexico, September 10-14, 177 (1990).
12. Li, H. et al, "Design Study of Beam Dynamics Issues for 1 TeV Next Linear Collider Based on Relativistic-Klystron Two-Beam Accelerators", LBL Report, Oct (1994).
13. Houck, T.L., Westenskow, G.A. and Yu, S.S., "BBU Code Development for High-Power Microwave Generators", Proceedings of the 1992 Linear Accelerator Conference, 495 (1992).

On the Smoothness of Electric Fields Near Plane Gratings of Cylindrical Conductors

David L. Judd
Department of Physics and Lawrence Berkeley Laboratory
University of California
Berkeley, CA 94720

ABSTRACT

The electric field near an infinite plane grating of equally spaced round rods at the same potential, forming the boundary of a uniform field, is determined analytically to good accuracy by conformal transformations and evaluated numerically. This contribution, which has a frankly pedagogical flavor, to the Klaus Halbach Festschrift is offered to honor his displayed mastery of conformal techniques. Although the numerical work and the form of its presentation are new, the transformation used is not original. However, to locate its antecedents in an archival journal it was necessary to seek out a paper published in 1923 (close to the year of his birth, and of mine), in a place obscure to modern physicists, so my efforts cannot be said to replicate recent published work. A new insight is obtained in the form of a simple estimate of departures from field uniformity at all distances from rods of any size.

I. INTRODUCTION

The acceleration, transport, handling and focusing of intense beams of heavy ions is being studied in a research and development project whose ultimate goal is the production of useful power by inertial-confinement fusion reactions ignited by such beams. One problem receiving attention is the combining of four such beams with minimal increase in emittance (i.e., occupied phase area). The converging beam axes must be bent so as to become parallel, while along its path each beam must continue to experience a succession of alternating-gradient quadrupole fields that constitute its "focusing lattice" structure. The final element is the most difficult to design, because of diminishing space between adjacent beams. Generation of these combined dipole and quadrupole electric fields in regions which are separated transversely by only a very few millimeters may perhaps be accomplished by arrays of small cylindrical rods arranged parallel to the beams along lines near their expected boundaries, each maintained at the electrostatic potential appropriate to its location. When contemplating such a design it is desirable to know how small the rods should be. If they are large and few, unwanted field components near them will be too large and will extend too far into the beam region, but they will be rugged, easier to fabricate and assemble, and simpler to energize. On the other hand if they comprise a fine-mesh grid they will be hard to produce, assemble, and install, mechanically delicate or unstable, and

complex to energize. Because emittance growth during the combining operation depends sensitively on the final separations among the beams, it is important not to make the rods larger than necessary.

It seemed possible that useful guidance might be obtained from solutions of the prototype two-dimensional electrostatic problem of a uniform electric field bounded by an infinite plane grating of equally spaced round rods at the same constant potential. The important parameter defining such an array is the occupancy fraction μ, defined as the ratio of rod diameter to rod spacing, also the ratio of c, the rod radius, to b, half the rod spacing, shown on the figure. Because of reflection symmetry [V(y) = V(-y)] and periodicity [V(y) = V(y + 2b)], only the region $-\infty < x < +\infty$, $0 < y/b < 1$ need be considered.

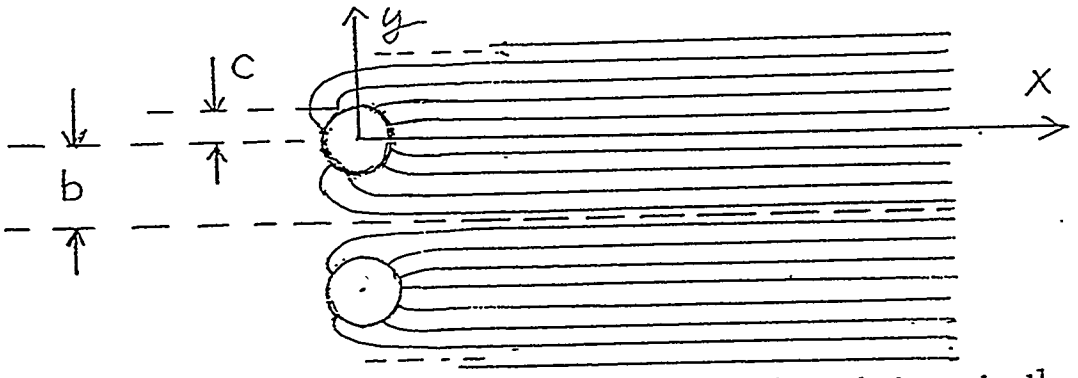

It is possible to solve this electrostatic problem by a simple analytic method[1] with adequate accuracy if $\mu = c/b$ is less than a few percent; another more complex analytic method[1,2] with adequate accuracy for μ up to and beyond 50 % is also available. The purpose of this paper is to display these methods, to evaluate numerically the departures from field uniformity as a function of distance away from the plane of the rod axes, and to interpret and summarize the results.

II. RESULTS AND CONCLUSIONS

Before describing Figure 1, which shows the most interesting and useful results of our calculations, we define the two relative field discrepancies D_X and D_y, and the two maximum relative field discrepancies $D_X(max)$ and $D_y(max)$. At large positive x, far from the rods, the electric field approaches $E_O = E_O e_X$; on approaching the plane of the rods the differences, $E_X - E_O$ and E_y, increase. These differences, divided by E_O, are the relative field discrepancies

$$D_X(x,y) = [E_X(x,y) - E_O]/E_O = E_X(x,y)/E_O - 1 ;$$

$$D_y(x,y) = E_y(x,y)/E_O .$$

We call the maximum values of these at fixed x over all values of y within the field the maximum relative field discrepancies. They depend only on x and on the occupancy fraction μ.

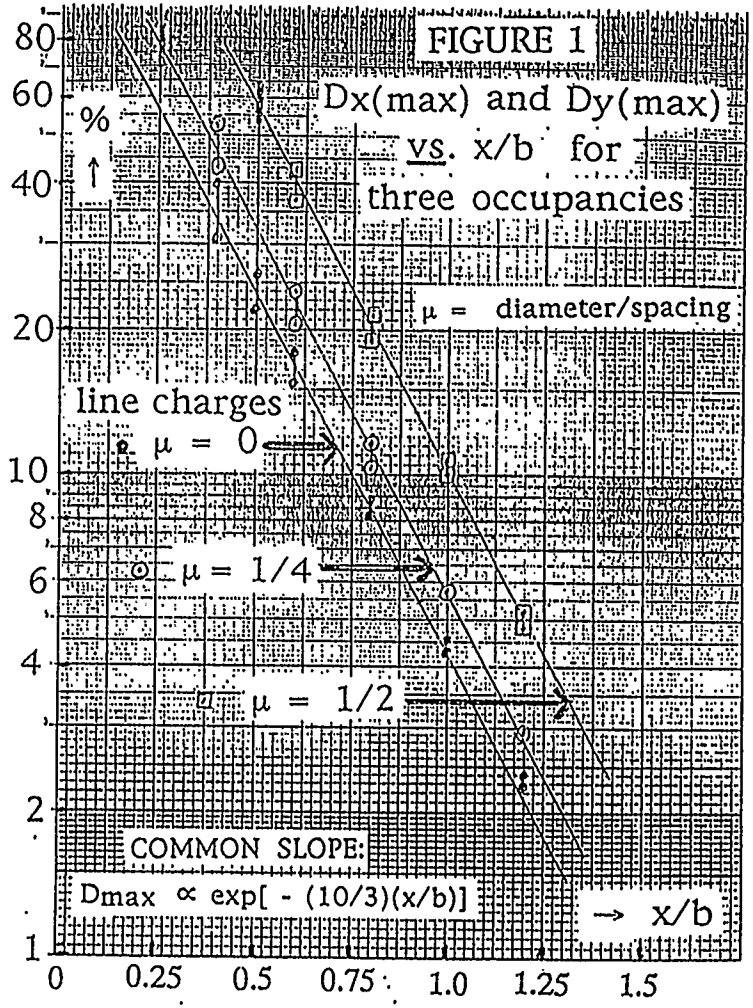
FIGURE 1
Dx(max) and Dy(max)
vs. x/b for
three occupancies
%
μ = diameter/spacing
line charges
μ = 0
μ = 1/4
μ = 1/2
COMMON SLOPE:
Dmax ∝ exp[- (10/3)(x/b)]
→ x/b
80
60
40
20
10
8
6
4
2
1
0
0.25
0.5
0.75
1.0
1.25
1.5

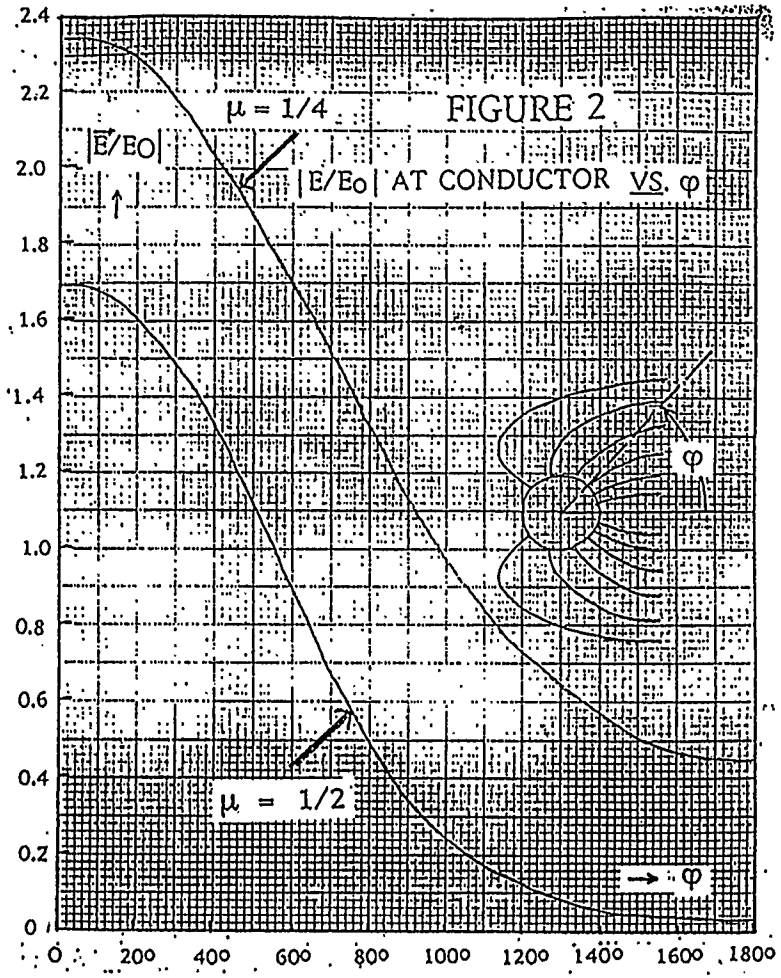
FIGURE 2
|E/EO|
|E/Eo| AT CONDUCTOR vs. φ
μ = 1/4
μ = 1/2
φ
→ φ
2.4
2.2
2.0
1.8
1.6
1.4
1.2
1.0
0.8
0.6
0.4
0.2
0
0
200
400
600
800
1000
1200
1400
1600
1800

We have calculated many numerical values (not presented here) of D_X and D_Y vs. the dimensionless lengths x/b and y/b at several appropriate values of x/b and well-spaced values of y/b throughout the physical region, for $\mu = 0$, 1/4, and 1/2 . [Values for y inside a rod are of course excluded.] From them we have found the values of the $D(max)$'s , and plotted all of them (for all three values of μ) on the same semilog graph vs. x/b , in Figure 1. Values for $\mu = 0$ are denoted by solid circles, for $\mu = 1/4$ by open circles, and for $\mu = 1/2$ by squares. The points for the two values $D_X(max)$ and $D_Y(max)$ for each pair (x, μ) are very close, and are connected by short solid vertical lines, D_X being slightly larger. [At two points for $\mu = 1/4$ their difference is too small to plot, and only a single open circle appears.] For each occupancy fraction μ , a straight line is drawn connecting these points at the different distances x . These lines fit the numerical data remarkably well. At the upper ends of the two lines for rods of finite radius, short heavy bars indicate the values of x corresponding to the rod radius.

From this graph we draw our principal conclusions:

I. Field discrepancies fall off exponentially with distance from the plane of the grating. [This conclusion is not unexpected.]

II. The decay-rate constant appears to be exactly the same for each of the occupancy fractions! It is not obvious that this could have been predicted without the benefit of calculations.

III. The exponential form remains valid surprisingly close to the rod surfaces.

The three straight lines with the same slope are well represented, in dimensionless form, by

$$\Delta E/E = C\, e^{-(10/3)(x/b)}$$

with $C = 133$ for $\mu = 0$, 170 for $\mu = 1/4$, and 300 for $\mu = 1/2$.

From Figure 1 one may read off answers to practical questions; for example, how far away from the plane of a grid with occupancy fraction 1/2 must one remain to avoid all field discrepancies greater than 5 %? The answer, from the graph, is that x must exceed 1.2 times the rod half-spacing b. Or one might want to know the largest field discrepancies encountered at $x = (3/4)b$ for rods with occupancy fraction 1/4 ; the answer is 15 %.

Rather than including extensive tables of field component values, the magnitudes of the field discrepancies D_X and D_Y for each of the three occupancy fractions are graphed in Figures 3, 4, and 5, which are labeled to make them self-explanatory.

Another useful result is contained in Figure 2, which shows the relative field strength vs. azimuth at the surface of a rod for $\mu = 1/4$ and 1/2. [Round rods are shown below to be badly approximated by equipotentials around a grid of line charges unless μ is rather small; they are out of round by about $\pm$ 10 % if μ is 0.06 , which is too small to be of interest for the application in view here. Further,

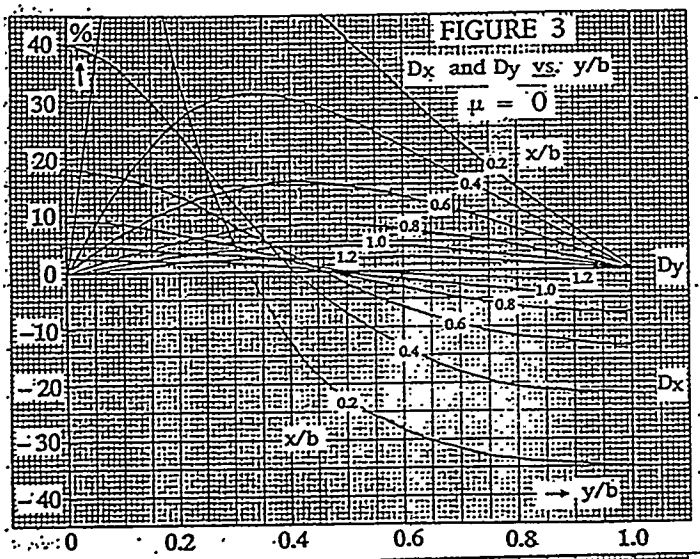
FIGURE 3
Dx and Dy vs. y/b
μ = 0
%
40
30
20
10
0
-10
-20
-30
-40
x/b
0.2
0.4
0.6
0.8
1.0
1.2
Dy
Dx
y/b
0
0.2
0.4
0.6
0.8
1.0

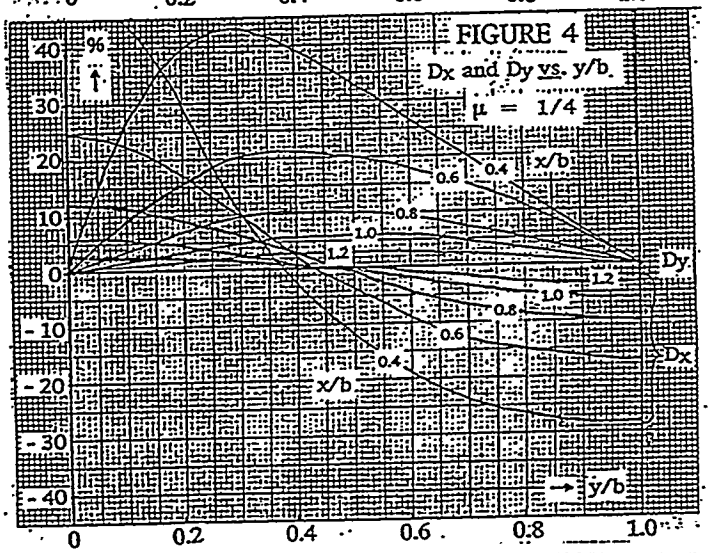
FIGURE 4
Dx and Dy vs. y/b.
μ = 1/4
%
40
30
20
10
0
- 10
- 20
- 30
- 40
x/b
0.4
0.6
0.8
1.0
1.2
Dy
Dx
y/b
0
0.2
0.4
0.6
0.8
1.0

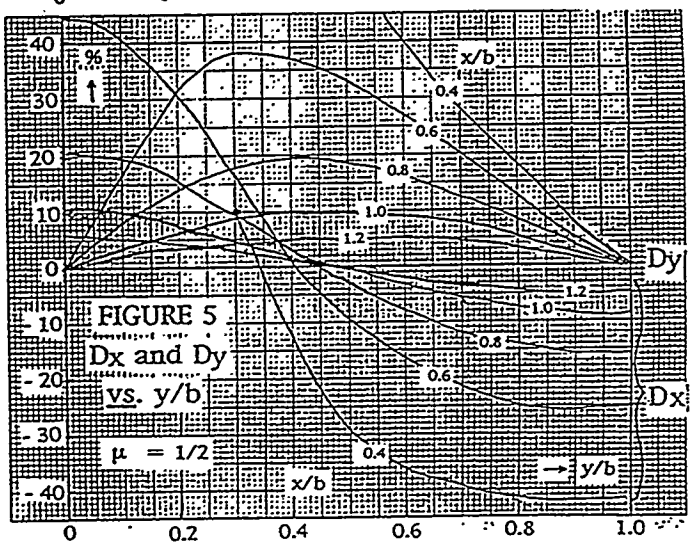
FIGURE 5
Dx and Dy
vs. y/b
μ = 1/2
%
40
30
20
10
0
- 10
- 20
- 30
- 40
x/b
0.4
0.6
0.8
1.0
1.2
Dy
Dx
y/b
0
0.2
0.4
0.6
0.8
1.0

the field strength on such small rods is more than five times the distant field.] As expected, the back sides of the larger rods are more shielded, and the maximum field on the smaller rods is significantly greater (2.35 rather than 1.7 times the distant field) because a smaller fraction of the space is filled with conductor to receive the field lines.

Another result obtained below is that even for the larger rods ($\mu = 1/2$) the mathematical model (which does not produce exactly round rods) departs from perfect roundness by less than $\pm$ 1 % of their mean radius; for the smaller rods ($\mu = 1/4$) the departure is less than 0.04 %.

III. SOLUTION FOR SMALL μ

For $\mu = c/b << 1$ the rods may be approximated by the quasi-cylindrical equipotential surfaces surrounding an array of line charges. We start with two equal line charges, having charge per unit length λ, in the complex z_1 plane at $z_1 = 0 \pm i$; their field lines are sketched below.

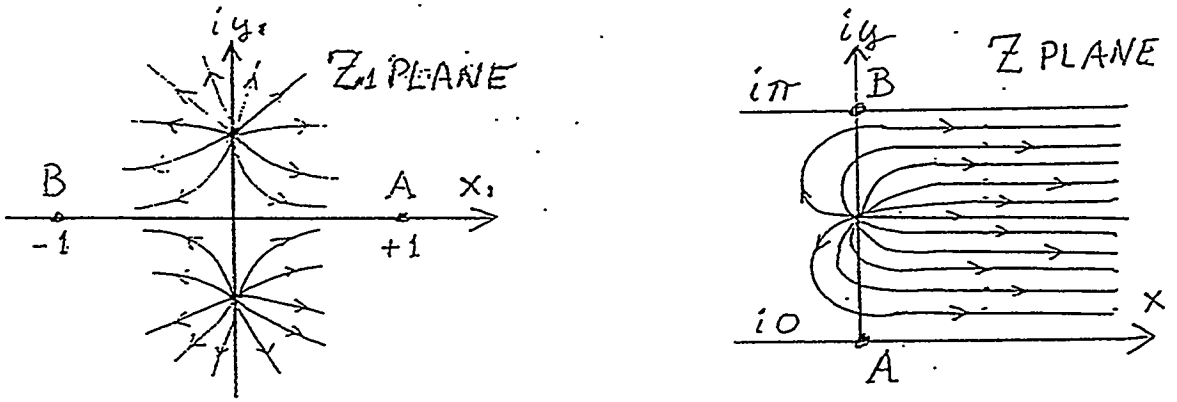

We apply to the complex z plane the conformal transformation defined by

$$z = \ln z_1 ;$$

the positive real axis $0 < x_1 < \infty$, $y_1 = 0$ is transformed into the entire real axis $y = 0$, and the negative real axis $-\infty < x_1 < 0$, $y_1 = 0$ is transformed into the parallel line $iy = i\pi$. The origin $z_1 = 0$ is transformed into the point at $x = -\infty$, $iy = i\pi/2$, thus producing the desired field configuration. This problem is so well known as to be almost a prototype of the method, so only the results will be quoted here. The complex potential is

$$W(z) = U(x,y) + iV(x,y) = -2\lambda \ln [e^{2z} + 1] ,$$

and the real potential is

$$U(x,y) = -\lambda \ln [e^{4x} + 2e^{2x} \cos 2y + 1] = -\lambda \ln F(x,y) ,$$

which defines F; $E = -\nabla U$. Before evaluating the field discrepancies we replace x by $\pi x/b$ and y by $(\pi/b)(y + b/2)$ to give a rod separation $2b$ with y measured from the center of a rod. Then

$$D_X = F^{-1} [\exp (\pi x/b) \cos (\pi y/b) - 1] ,$$

$$Dy = F^{-1} \exp (\pi x/b) \sin (\pi y/b) ,$$

$$F = \exp (2\pi x/b) - 2 \exp (\pi x/b) \cos (\pi y/b) + 1 .$$

Curves of D_X and D_Y vs. y/b (from zero to unity) for several values of x/b are plotted in Figure 3. [By symmetry, D_Y must vanish at $y = 0$ and b.] From them one sees, for example, that to encounter only discrepancies less than 5 % one must stay away from the plane of the rod axes by a distance b. See also Figure 1, on which are shown the distances required to avoid other discrepancies.

The equipotential curves are given by

$$e^{2\pi x/b} - 2 e^{\pi x/b} \cos \pi y/b + 1 = \text{constant} = K.$$

They are not circles; very near the line charge at $x = 0$, $y = 0$ they have the approximate form

$$(x^2 + y^2)(1 + 2x) + \text{4th and higher order} = \text{constant}.$$

For small K, approximate relations are

$$\mu \approx K^{1/2}/\pi , \quad \Delta R/R \approx \pm K^{1/2}/2 .$$

From these relations, and the exact equipotential, we find:

K	approximate		exact	
	μ	$\pm \Delta R/R$ %	μ	$\Delta R/R$ %
0.01	0.032	5		
0.04	0.064	10		
0.095			0.10	- 14 to +18
0.15			0.126	- 17 to + 23

The equipotentials are out of round by about ±10 % if about 6 % of the grating space is filled with rods, and are very non-circular for 10 % filling.

Smaller occupancies have the disadvantage of increasing the field strength on the rod surfaces. Because all the flux leaving a rod goes into a strip of width 2b at

large x, Gauss's theorem shows that for very small rods the ratio of field strengths is

$$E_{rod}/E_o = 2b/2\pi c = 1/(\pi\mu) .$$

The largest equipotentials that are within ± 5 % of being round have $\mu = 0.032$; the fields on these "rod" surfaces are ten times as great as the distant uniform field. A calculation with round-rod equipotentials that fill much larger fractions of the space, at least up to $\mu = 0.5$, is needed.

IV. SOLUTION FOR LARGE μ

Fortunately, an analytical solution of this problem, with adequate accuracy, can also be given[2]. To explain it we start with the portion of the complex z plane shown below.

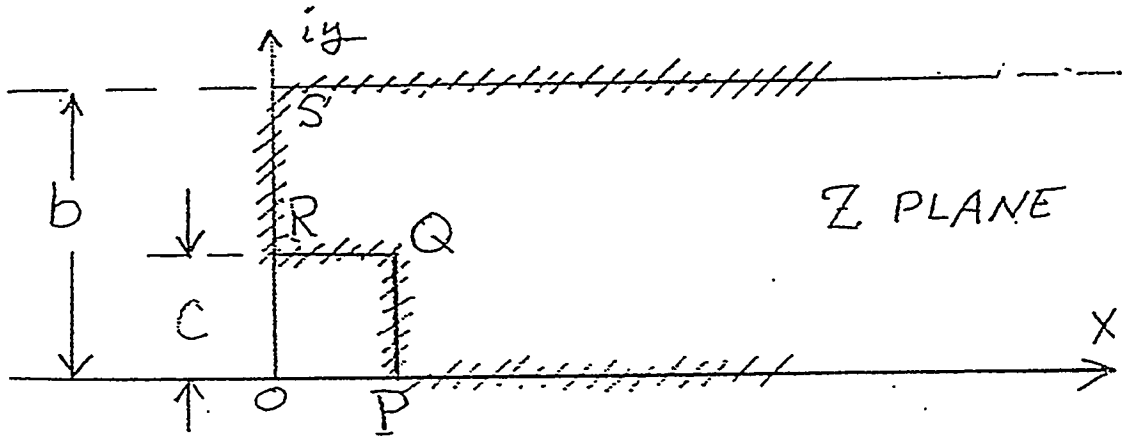

The accented contour consists of these segments:

$c < x < \infty$, $y = 0$;	P to ∞
$x = c$, $0 < y < c$;	P to Q
$y = c$, $0 < x < c$;	Q to R
$x = 0$, $c < y < b$;	R to S
$x = b$, $0 < y < \infty$;	S to ∞ .

The real axis of the z_1 plane may be transformed into this contour by means of a Schwartz transformation generating bends of $\pi/2$ at P, R, and S and a bend of $3\pi/2$ at Q:

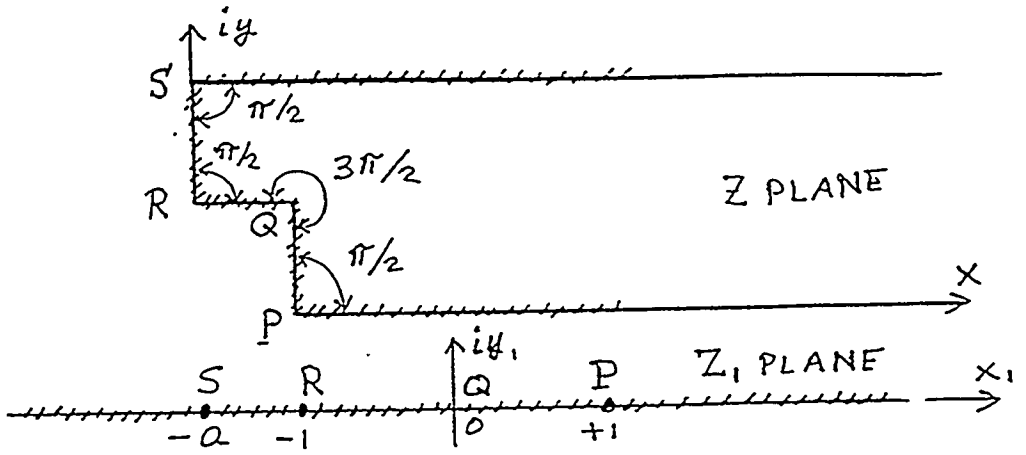

$$dz/dz_1 = C z_1^{1/2} (z_1 - 1)^{-1/2} (z_1 + 1)^{-1/2} (z_1 + a)^{-1/2} ,$$

in which each exponent is "angle/π - 1" at the position of its bend. The unwanted square corner at point Q may now be rounded by replacing the factor $z_1^{1/2}$ by a kind of average over points R and P, given by

$$(z_1 + 1)^{1/2} + k (z_1 - 1)^{1/2} .$$

This substitution not only converts the straight segments PQ and QR into a smooth arc but also alters the form of the derivative dz/dz_1 so that it may be integrated:

$$dz/dz_1 = C_1 \{[(z_1 - 1)(z_1 + a)]^{-1/2} + k [(z_1 + 1)(z_1 + a)]^{-1/2}\} .$$

By adjusting the real constant k a variety of shapes of the smooth arc may be realized[2], including ones like ellipses and (in appropriate limits) rectangular boxes and thin-strip shapes, with major axes along x or along y. Integrating, and imposing the condition that z shall increase by ib as z_1 traverses a semicircle of very large radius from $z_1 \approx (\infty) e^{i0}$ to $z_1 \approx (\infty) e^{i\pi}$, we find

$$C_1 = b/[\pi (1 + k)] ;$$

$$C_1^{-1} z = \ln \{1 + [(z_1-1)/(z_1+a)]^{1/2}\} - \ln \{1 - [(z_1-1)/(z_1+a)]^{1/2}\}$$

$$+ k \ln \{1 + [(z_1+1)/(z_1+a)]^{1/2}\} - k \ln \{1 - [(z_1+1)/(z_1+a)]^{1/2}\} + C_2 .$$

Next we impose the requirements that $z_1 = 1 + i0$ at $z = c + i0$ and that $z_1 = -1 + i0$ at $z = 0 + ic$, so as to get close to a circular arc ; these imply that $C_2 = 0$, and are equivalent to the two relations

$$(a+1)/2 = \coth^2 [\pi \mu (1+k)/2k] \ ,$$

$$(a-1)/2 = \cot^2 [\pi \mu (1+k)/2] \ .$$

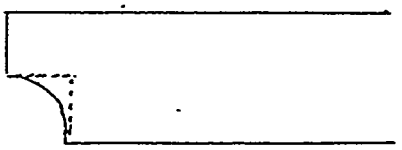

Subtracting, the following equation is obtained which may be solved numerically for k as a function of $\mu = c/b$;

$$\sin [\pi \mu ((1+k)/2] \ = \ \tanh [\pi \mu (1+k)/(2k)] \ .$$

Having found k , adding instead of subtracting provides the evaluation of a:

$$a \ = \ \coth^2 [\pi \mu (1+k)/(2k)] \ + \ \cot^2 [\pi \mu (1+k)/2] \ .$$

We have chosen to make numerical evaluations for $\mu = 1/4$ (grid one quarter filled with rods) and $1/2$ (grid half filled). For $\mu = 1/4$, $k = 0.90210$ and $a = 3.3328$; for $\mu = 1/2$, $k = 0.65326$ and $a = 1.15598$. The empirical fit $k = \exp[- 1.7 \mu^2]$ has error less than 3 % in the range $0 < \mu < 0.6$. The empirical fit $a = 1 + \exp[3.8 - 11.9 \mu]$ has a similar error in $0.15 < \mu < 0.7$.

Now we are ready to describe the physical situations in the two planes. To produce the desired configuration of conductors, field lines, and equipotentials in the z plane we must superpose the corresponding configurations of two different situations in the z_1 plane. The first of these, called Geometry I, is that of a flat charged conducting strip extending along the real z_1 axis (accented below) from $x_1 = - 1$ (point R) to $x_1 = + 1$ (point P).

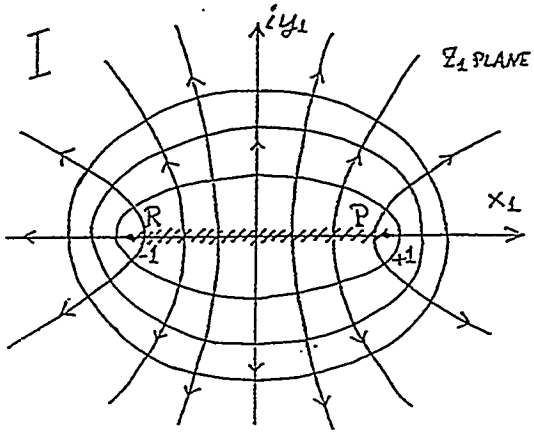

The equipotentials (drawn in the 2-D space) are a set of confocal ellipses, and the field lines are the orthogonal set of confocal hyperbolas. Their equations follow from

$$W_I(z_1) \ = \ U_I(x_1,y_1) \ + i \ V_I(x_1,y_1) \ = \ C_I \sin^{-1} z_1 \ .$$

Here we choose the potential function to be V , not U , so the electric field is given by $E = -$ grad V . To exhibit the forms of U and V we temporarily set the scaling potential equal to unity, and write

$$x_1 + i\,y_1 = \sin W = \sin (U + i\,V) = \sin U \cosh V + i \cos U \sinh V ,$$

from which $x_1 = \sin U \cosh V$, $y = \cos U \sinh V$, so that

$$\sin^2 U + \cos^2 U = (x_1/\cosh V)^2 + (y_1/\sinh V)^2 = 1 ,$$

showing the ellipses for constant values of V, and

$$\cosh^2 V - \sinh^2 V = (x_1/\sin U)^2 - (y_1/\cos U)^2 = 1 ,$$

displaying the hyperbolas for constant values of U.

By choosing the ends of the conducting strip to be at $x_1 = \pm 1$, $y_1 = 0$, we assure that the transformed portion of this segment of the real axis (accented below) will also be a conductor at constant potential.

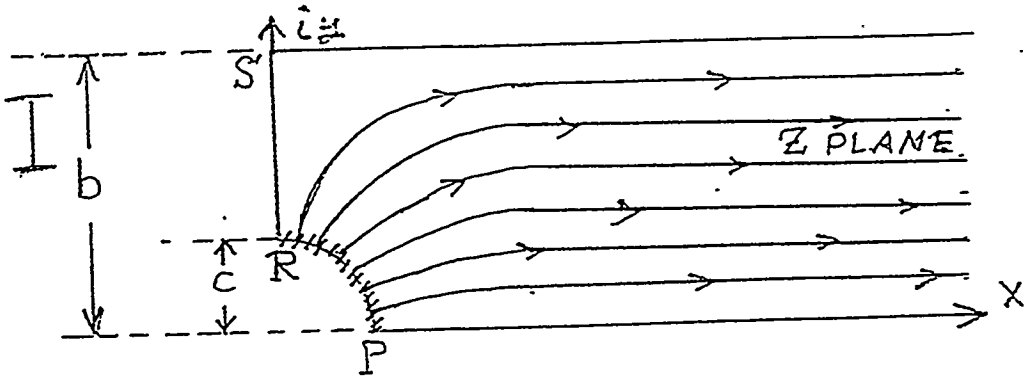

The field generated in the strip $0 < x < \infty$ may be defined to be reflection-symmetric about the x and y axes, so that in the z plane the field in Geometry I may be regarded as shown here:

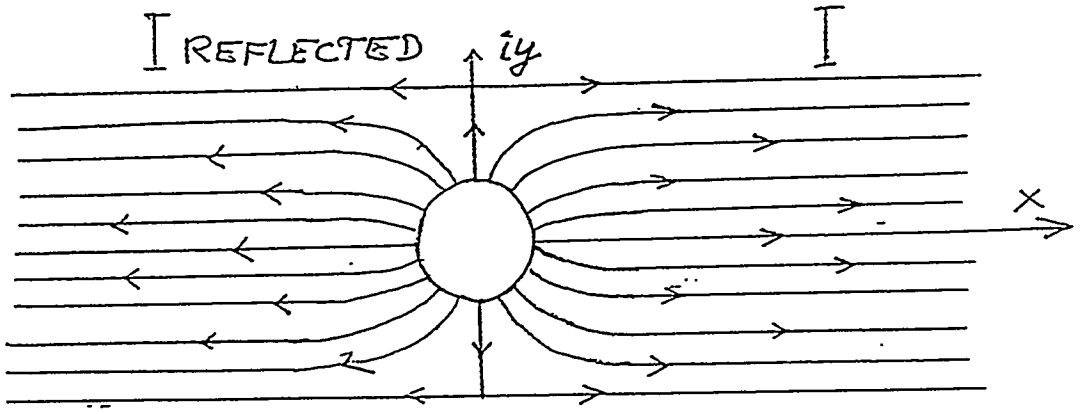

For Geometry II we seek a configuration in the z plane that will cancel the field of Geometry I near $x = -\infty$ and double it near $x = +\infty$. For positive x this configuration can be seen to be:

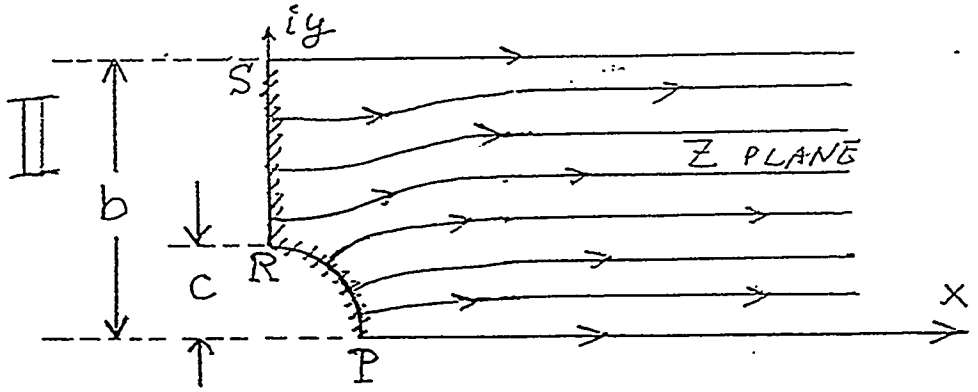

in which the accented contour is the conductor, an equipotential. This region is mapped from the z_1 plane provided the flat charged conducting strip there lies along the real z_1 axis between $x_1 = -a$ (point S) and $x_1 = +1$ (point P). Therefore the portion of the real axis x_1 representing the conductor must be adjusted. The strip ends are located where the arguments of the $\sin^{-1}$ function are ± 1. For Geometry I the argument is z_1, but for Geometry II the ends must be at $z_1 = -a$ and $z_1 = +1$, so the argument must be $cz_1 + d$, with $-ac + d = -1$ and $c + d = +1$. These conditions are satisfied by $c = 2/(a+1)$, $d = (a-1)/(a+1)$, giving

$$W_{II}(z_1) = C_{II} \sin^{-1} [(2z_1 + a - 1)/(a+1)] .$$

An examination of the field of Geometry II in $0 < x < \infty$, $0 < y < b$ shows that the desired reflected field as shown below in $-\infty < x < 0$, $0 < y < b$ is produced if E_y changes sign under $x \rightarrow -x$.

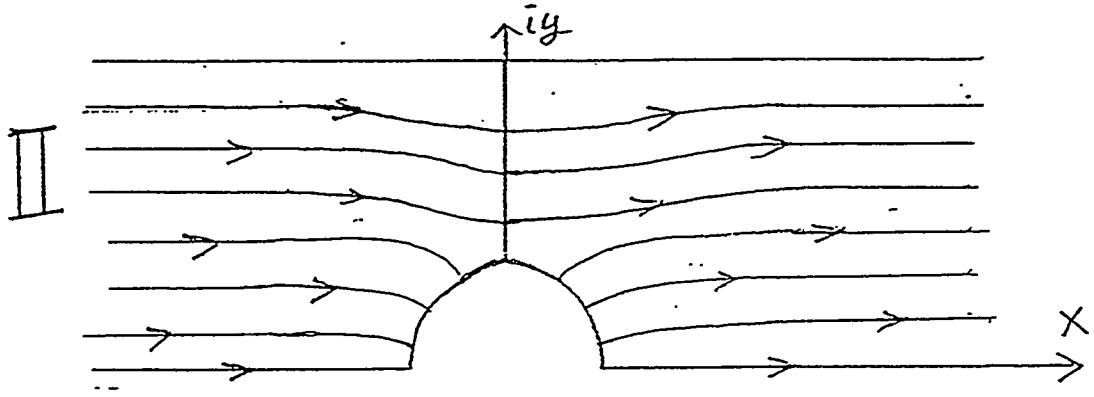

If then fields I and II as shown in $-\infty < x < +\infty$ are superposed we have the desired configuration:

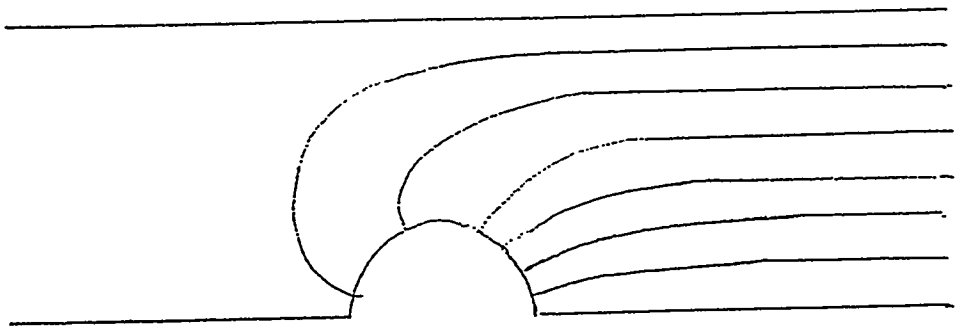

In this way we arrive at

$$W(z_1) = C_1\{\sin^{-1} z_1 + \sin^{-1}[(2z_1+a-1)/(a+1)]\}$$

with the same constant for each term to provide cancellation at $x = -\infty$. If we consider only the first of these terms in W,

$$z_1 = \sin(W/C_1) = \sin[(U + iV)/C_1 = \sin(U/C_1)\cosh(V/C_1) + i\cos(U/C_1)\sinh(V/C_1),$$

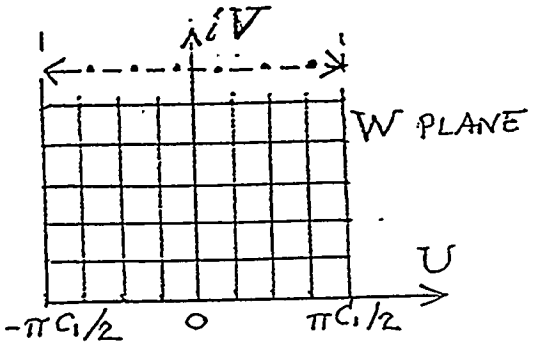

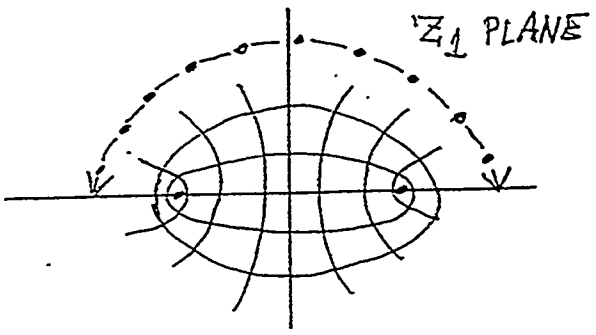

with V the potential, we see that the flux emanating from the strip into the upper half plane is equal to the increase in U from the value $-\pi C_1/2$ to $+\pi C_1/2$; $\Delta\Phi = \pi C_1$. After transforming to the z plane this flux should be that of a field $E_0/2$ at $x = \infty$ over a width b. [The other half of E_0 is generated by the second term in W.]-Equating, $\pi C_1 = E_0 b/2$, or $C_1 = E_0 b/(2\pi)$.

It is of interest to determine how near to round our nearly-round rods are for the selected value of μ. This is accomplished by evaluating $z = x + iy$ as a function of

z_1 along the real axis $y_1 = 0$ at a number of points in the range $-1 < x_1 < +1$, and calculating $r = (x^2 + y^2)^{1/2}$. Some results are tabulated here for $\mu = 0.5$:

x_1	x/b	y/b	r/b	% from <r>/b
- 1	0	0.5	0.5	- 0.96
- 0.5	0.33853	0.37958	0.5088	+ 0.84
0	0.41734	0.28849	0.5073	+ 0.44
+ 0.5	0.46535	0.19348	0.5040	- 0.16
+ 1	0.5	0	0.5	- 0.96

The maximum excursions from the central value 0.5046 b of rod radius are less than ± 1 %; such a rod would be called round by almost anyone! For $\mu = 1/4$ the largest excursions are only about 0.03 %.

Now we turn to evaluation of the field components. The complex derivative of the complex potential is

$$dW/dz = (dU + i\,dV)/(dx + i\,dy)$$

and for analytic functions $\partial U/\partial x = \partial V/\partial y$ and $\partial U/\partial y = -\partial V/\partial x$, so that dW/dz may be written as $\partial U/\partial x - i\,\partial U/\partial y$ or as $\partial V/\partial y + i\,\partial V/\partial x$. Because we have chosen V to be the potential function, $E = -\text{grad } V$, leading to

$$i\,E_x + E_y = -dW/dz\,.$$

In the pages above we have derived the desired forms for $W(z_1)$ and $z(z_1)$, but the field components are wanted in the z plane, where we evaluate them by finding the gradient as the quotient

$$dW/dz = (dW/dz_1)/(dz/dz_1)\,.$$

$$dW/dz_1 = (E_0 b/2\pi)(\partial/\partial z_1)\{\sin^{-1} z_1 + \sin^{-1}[(2z_1+a-1)/(a+1)]\}$$

$$= (E_0 b/2\pi)(1-z_1)^{-1/2}[(z_1+1)^{-1/2} + (z_1+a)^{-1/2}]\,.$$

$$dz/dz_1 = [b/\pi(1+k)](z_1+a)^{-1/2}[(z_1-1)^{-1/2} + k\,(z_1+1)^{-1/2}]\,.$$

$$dW/dz = [E_0(1+k)/2][(z_1+1)/(1-z_1]^{1/2}\ f(z_1)\,,\ \text{with}$$

$$f(z_1) = [(z_1+a)^{1/2} + (z_1+1)^{1/2}]/[(z_1+1)^{1/2} + k\,(z_1-1)^{1/2}]\,.$$

Note that $[(z_1-1)/(1-z_1]^{1/2} = \pm i$; this leads to $-E_y - i\,E_x = \pm [iE_0(1+k)/2]\,f(z_1) = \pm [iE_0(1+k)/2]\,[f_{re} + i\,f_{im}]$, with f_{re} and f_{im} the real and imaginary parts of f:

$$E_x/E_0 = (-/+)\,[(1+k)/2]\,f_{re}(x_1,y_1)\ ;\quad E_y/E_0 = \pm\,[(1+k)/2]\,f_{im}(x_1,y_1)\,.$$

We choose the lower signs so that the field directions will be those indicated by the arrowheads on the various drawings above.

It is still not enough to evaluate the real and imaginary parts of $f(z_1)$ without knowing the position (x,y) in z space that corresponds to each point (x_1,y_1) in z_1 space. This correspondence may be established numerically in various ways. Here it has been made as follows:

> First select x, a certain fixed value, defining a line along which y varies from zero (or from the conductor, for $x/b < \mu$) to b. Then select a specific value for x_1, and calculate $x(x_1, y_1)$ for a sequence of values of y_1 chosen iteratively so as to converge to a value of y_1 leading to the selected value of x; for this "converged pair" (x_1,y_1) calculate y. Then select another value of x_1 and repeat, until a set of values of y spanning the range of y has been obtained; each y along the selected line x = constant is then a known function of the pair (x_1,y_1), i.e., of z_1. [Alternatively, the roles just described for x_1 and y_1 may be interchanged during the iteration.] Then repeat the entire process after selecting a new fixed value of x. In the numerical work here we have evaluated $y(z_1)$ along lines x/b = constant, spaced at intervals of 0.2.

The results of these evaluations are presented graphically in Figures 4 and 5, in a manner similar to that in Figure 3; D_x and D_y are plotted as functions of y/b over the relevant range for each of several values of x/b. As in Figure 3, the curves for D_y must go to zero, by symmetry, at $y = b$, and at $y = 0$ for all values of $x > \mu b$ ($= b/4$ or $b/2$ for our evaluations here); for smaller x, the smallest value of y/b in the field region is $\approx [\mu^2 - (x/b)^2]^{1/2}$. However, D_y in these regions is off the scale, which extends only to $\pm$ 45 %.

The conclusions to be drawn from Figures 4 and 5, as for those from Figure 3, are very simple, but numerically different in each case. They are stated in Section II; as noted there, the variation of the largest discrepancies with distance from the plane of the grid is shown in Figure 1, summarizing the most useful result of this work.

Other properties of the field become accessible from the development described above. Because the imaginary component y_1 is zero on the conductor, the electric field strength on the surface of a rod, as a fraction of its value E_0 at large x, is easily evaluated as a function of the azimuthal angle $\emptyset$, which is zero along $x > 0$ and 180° along $x < 0$. This field ratio, $|E_{surf}|/E_0$, is shown vs. $\emptyset$ in Figure 2, for $\mu = 1/4$ and for $\mu = 1/2$. For the forward and back points on the surfaces ($\emptyset = 0^\circ$ and $\emptyset = 180^\circ$, respectively) the ratio is given by the two simple equations

$$|E_{surf}|/E_0 = [(1+k)/2]\{[(1+a)/2)]^{1/2} \pm 1\}$$

which give the values 2.35 and 0.448 for $\mu = 1/4$, and the values 1.68 and 0.032 for $\mu = 1/2$, as shown on Figure 2.

Free-hand sketches of some field lines for $\mu = 1/4$ and $1/2$ are shown in Figures

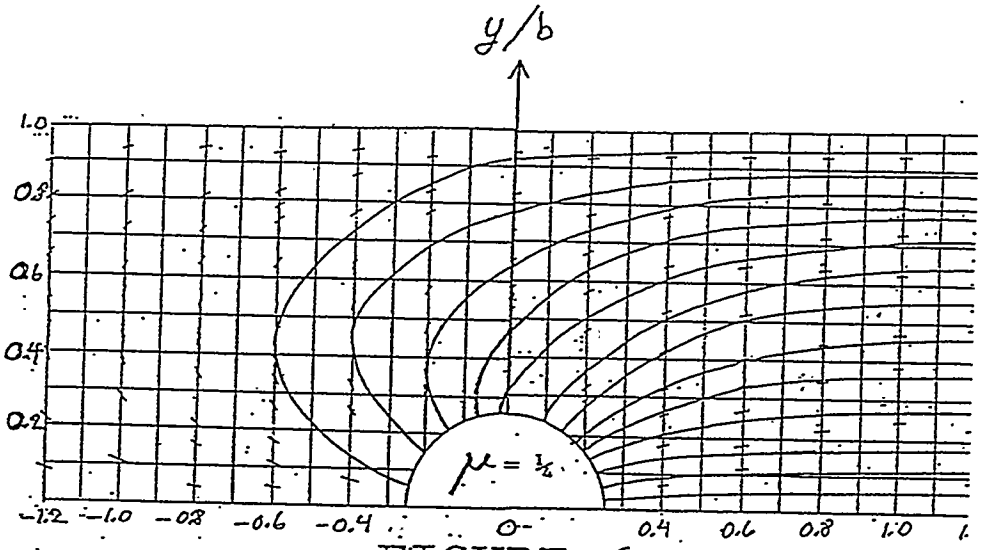

FIGURE 6

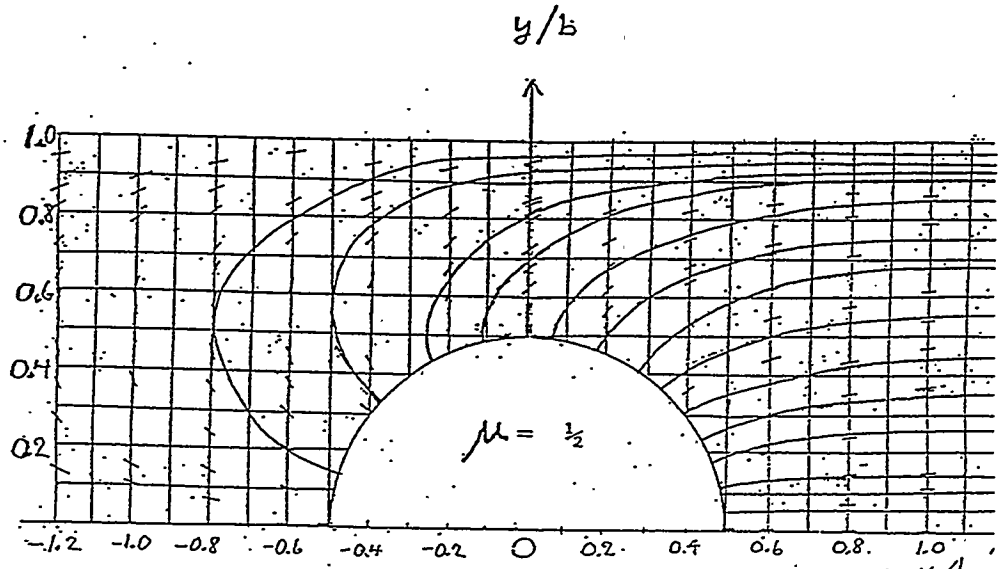

FIGURE 7

6 and 7, respectively. Because the field strengths near these rods vary by such large factors, the field line spacing as drawn is greatly altered from the true spacing, particularly for the larger rod; the line density leaving its forward side is actually about ten times greater than drawn, relative to that leaving its back side. All the numerical work for this report was carried out on a HP-32S programmable calculator. The two principal programs, for finding z vs. z_1 and dW/dz vs. z_1 (all complex numbers), each contained approximately a hundred instructions. The HP-32S has the capability to carry out a dozen different operations on complex numbers, without which the work could not have been done using a hand calculator.

REFERENCES

1. Smythe, W. R. , *Static and Dynamic Electricity,* 1st or 2nd ed., McGraw-Hill, N.Y., 1939, 1950 ; Ch 4.
2. Richmond, H. W., *Proc. London Math. Soc., Series 2, Vol. 22,* 1923; pp. 389-403.

Operation of a Small-Gap Undulator on the NSLS X-Ray Ring

P.M. Stefan, S. Krinsky, G. Rakowsky, and L. Solomon
National Synchrotron Light Source
Brookhaven National Laboratory
Upton, New York 11973

Abstract

We report results of an on-going experiment being carried out in the X13 straight section of the NSLS X-ray Ring which explores the limits of the operation of small-gap undulators. In particular, we discuss the operation of a 16 mm period small-gap undulator. At an electron beam current of 300 mA the variable gap vacuum chamber has been closed to an inner aperture of 3.8 mm with no effect on the electron beam lifetime. Measurements of the output radiation spectrum at a magnet gap of 7.5 mm are described.

I. Introduction

The development of high-brightness synchrotron radiation sources has been advanced by the utilization of permanent magnet insertion devices, pioneered by Klaus Halbach [1]. Such permanent magnet devices provide high field strength, excellent field quality, and impressive reliability in a very economical manner. Here, our interest is in the implementation of short-period, small-gap undulators situated in low-beta insertions of a storage ring. In particular, we report results of an on-going experiment being carried out in the X13 straight section of the NSLS X-ray Ring, which explores the limits of the operation of small-gap devices.

The vertical magnetic field B_y in a pure-permanent-magnet undulator has an approximately sinusoidal dependence on the axial coordinate z,

$$B_y = B_u \sin 2\pi z/\lambda_u ,$$

where λ_u is the undulator period length. The peak field B_u depends exponentially on the full magnet gap G,

$$B_u \propto \exp\left(-\pi G/\lambda_u\right) .$$

From this it is clear that to achieve high magnetic field strength at short periods

*Work perfromed under the auspices of U.S. Department of Energy, under contract DE-AC02-76CH00016.

requires small magnet gap and hence small electron beam aperture. Placing the undulator at a location with small vertical betatron function permits long electron beam lifetimes with small vertical aperture. In the X-ray Ring the vertical beta function has a value of β_v=0.33m at the insertion center.

The motivation for desiring short-period undulators is also clear. The fundamental radiated wavelength λ_1 from an undulator is

$$\lambda_1 = \frac{\lambda_u}{2\gamma^2}\left(1 + \frac{K^2}{2}\right),$$

where the field strength parameter K is given by

$$K = 0.93\ B_u(T)\ \lambda_u(cm),$$

and γ is the electron energy in units of electron rest mass. One usually wants K to be of order unity to have high flux and reasonable tuning range. For a given electron energy, in order to obtain shorter radiated wavelength in the fundamental, the period length λ_u must be decreased. To maintain K near unity, it is then necessary to reduce the gap G.

Some potential limitations on the electron beam aperture, and hence the undulator gap, are Coulomb scattering lifetime, transverse impedance of the vacuum chamber, vacuum pressure in the low-conductance region of the small aperture chamber, and possible ion trapping in this region. We have successfully operated the X-ray Ring with a vertical beam aperture of only 3.8mm in the prototype small-gap undulator chamber, and obtained a high-brightness output radiation beam at 3 KeV in the fundamental from a pure-permanent-magnet undulator having a 16mm period length, operating at a full gap of 7.5 mm.

In what follows, a brief description of the small-gap undulator system is presented, followed by results from studies of the stored beam lifetime as a function of electron beam aperture. Finally, a measurement of the output radiation spectrum is described and presented.

II. Description of Small-Gap Undulator System

The NSLS Prototype Small-Gap Undulator (PSGU) is comprised of three major components: a variable-aperture vacuum chamber with drive system, a

pure-permanent-magnet small-period undulator with an independent drive system, and an elevator base stage, upon which all of the above components are supported. The design concept of the variable-aperture chamber has been described elsewhere [2], but is summarized using Fig. 1.

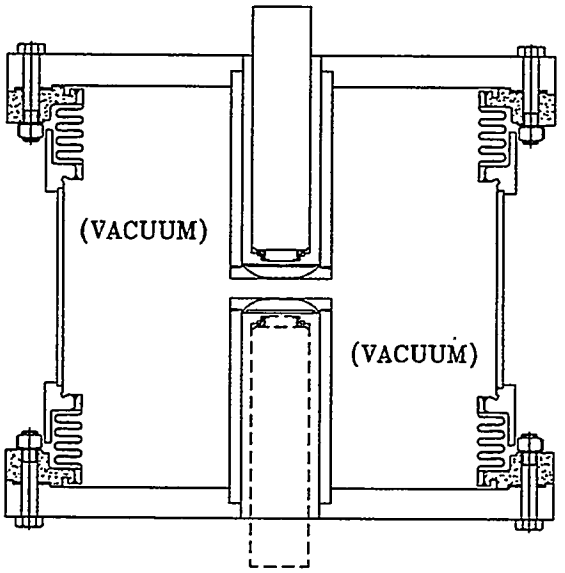

Figure 1 Cross section of the Prototype Small-Gap Undulator (PSGU) vacuum chamber, as seen along the stored beam direction. Deep wells from the top and bottom flanges extend toward the electron beam. Bellows permit the wells to be moved closer together, or apart. The regions of the wells nearest the electron beam are thinned to 1 mm and the undulator magnet arrays are inserted into the wells, up to the thinned region. The chamber is about 460 mm in diameter.

The figure presents a cross section of the vacuum chamber, as seen along the stored beam direction. Deep wells, from the top and bottom flanges, extend towards the stored beam and can be moved closer together or apart by means of top and bottom bellows. The central section of the chamber, between the bellows, is fastened through legs to the elevator base stage below, while actuators attached between the two flanges control the electron beam aperture. The portions of the wells near the stored beam are thinned to 1 mm, and the magnet arrays of the undulator are inserted into the wells, up near the thinned region. The chamber is cylindrical, about 460 mm in diameter, with its axis oriented vertically. At present, the electron beam aperture is variable between

14 mm and 3.8 mm, and the small-aperture region is 104 mm wide and 390 mm long.

The PSGU undulator magnet is 320 mm long, with a 16 mm period. It uses NdFeB magnets in a high-performance 6 block/period version of the Halbach pure-permanent-magnet design (see Fig. 2).

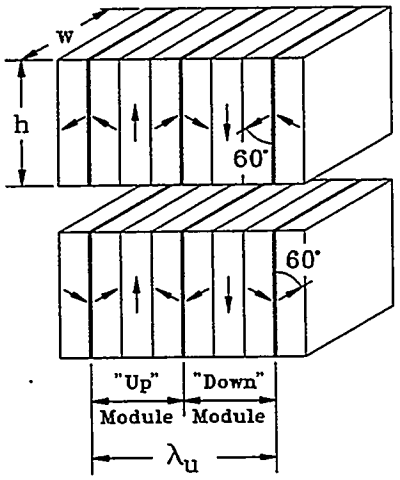

Figure 2 Schematic of the six block/period pure-permanent-magnet structure used in the PSGU undulator.

Its construction and magnetic field mapping are presented in detail elsewhere [3], but the mapping results are summarized in Table 1 and Fig. 3.

Table 1. PSGU Integrated Multipoles

Multipole	Goals	Measured	Units
Dipole	100	7	G•cm
Skew Dipole	100	-20	G•cm
Quadrupole	10	-5	gauss
Skew Quadrupole	100	-18‡‡	gauss
Sextupole	50	-37	G/cm
Skew Sextupole	50	-30‡‡	G/cm

‡‡Values determined using $\Delta x = \pm 2$ mm. All others: ±4 mm.

The magnet gap was fixed at 6 mm for these measurements, which is the design goal for actual use of the undulator. At this gap, a peak field of 0.623 Tesla was obtained.

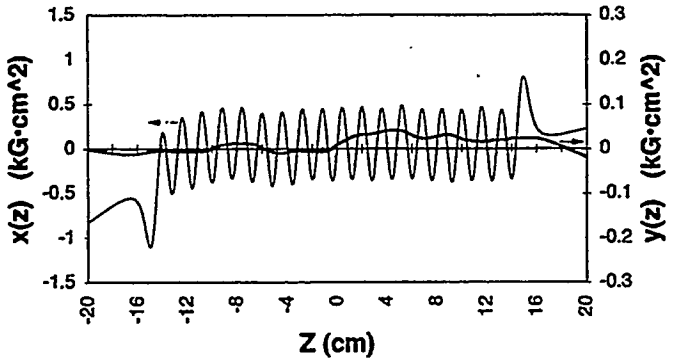

Figure 3 The x and y trajectories in the completed PSGU undulator, at a magnet gap of 6 mm. Note the different scales for x and y.

The undulator magnet beams are mounted to an independent drive system which presently enables magnet gaps between 7.35 mm and 26 mm within the wells of the PSGU vacuum chamber.

Using these parameters, the predicted performance of the undulator is summarized in Fig. 4 using a "tuning curve". This is a plot of the central-cone photon flux vs. photon energy for the whole range of possible magnet gaps. First, second, and third harmonics are illustrated as separate curves. Any single magnet gap corresponds to only three points, one on each curve. For example, the prediction for the 7.35 mm gap is indicated where the curves change from solid to dashed. The second harmonic curve is only roughly estimated, by doubling the flux expected in the third harmonic . The solid portion of the curve illustrates the capabilities of PSGU at the present time. However, we plan to re-work the vacuum chamber and the magnet drive in the near future to permit a minimum operational aperture of about 2mm and perhaps a magnet gap of as small as 5 mm. If the 5 mm magnet gap can be achieved, the dashed extension of the tuning curve results.

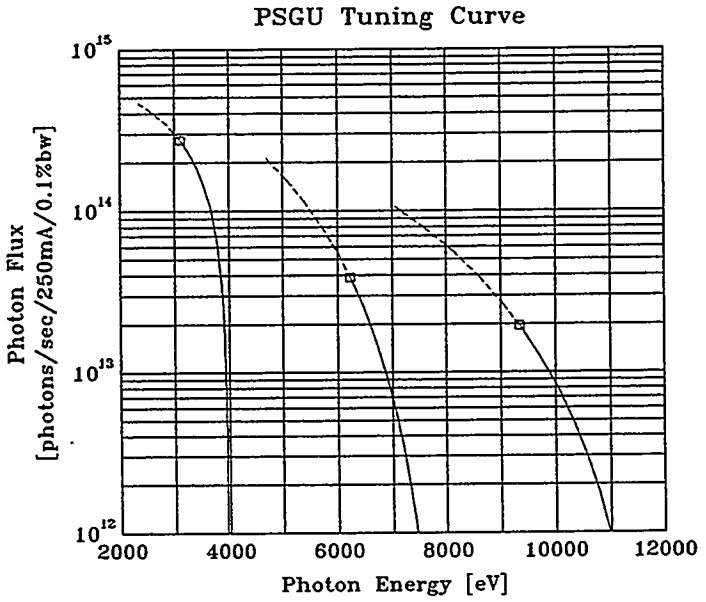

Figure 4 PSGU theoretical tuning curve, illustrating the first, second and third harmonics. The second harmonic curve is only a rough estimate, obtained by doubling the values for the third harmonic. The solid curves illustrate the present range of PSGU, to a minimum magnet gap of 7.35mm. If the minimum gap can be decreased to 5 mm, the dashed extension of the curves results.

The elevator base-stage provides mounting fixtures for the chamber and its drive, and the undulator magnet and its drive. In addition, it provides a ± 3 mm vertical translation of the chamber and magnet assemblies about nominal beam height.

III. Studies of Beam Lifetime vs. Electron Beam Aperture:

A. 4-jaw Scraper:

While design and fabrication of PSGU components were still on-going, an existing 4-jaw scraper assembly was refurbished and installed in the X-ray Ring, near the location intended for PSGU.

By measuring beam lifetime as a function of the electron beam aperture (determined by the scraper blades), we hoped to verify our estimates of the

existing storage ring limiting aperture and thereby obtain a preview of the best-case operational aperture for PSGU. The vertical blades of the scraper were located about 150 mm upstream of the X13 straight section centerline (β_v=0.4m), while the extreme ends of the small-aperture region in PSGU are about 200 mm from the straight centerline, upstream and downstream. The 4 scraper blades were uncooled copper, 5 mm thick, two horizontal and two vertical, each on individually-controlled actuators. Only a single blade was used at a time.

Data were taken by moving one blade of the scraper in small steps and measuring the beam lifetime which resulted. The DC current transformer is usually used to measure lifetimes during normal operations shifts, but for these studies its time-response was too slow, and sometimes became oscillatory. Instead, lifetimes were calculated by the change in amplitude of a stripline sum signal over time, which was monitored at 53 MHZ using a spectrum analyzer.

Fig. 5 presents one set of results.

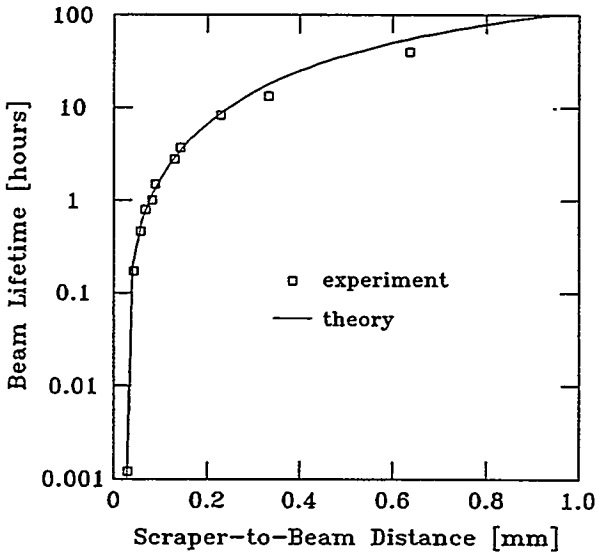

Figure 5 Vertical scraper results: initial stored beam of 21 mA at 2.584 GeV, 25 bunches, small-vertical-beam-size optics. These results suggest that a full electron beam aperture of about 2 mm might be imposed at this location without degradation of beam lifetime.

The initial stored beam was 21 mA at 2.584 GeV, in 25 bunches and used a small-vertical-beam-size optics [4]. (These optics have since become the normal-operation condition.) The theory curve [5] contains four contributions: the

quantum lifetime, the nuclear Coulomb scattering lifetime for both horizontal and vertical apertures, and the nuclear bremsstrahlung lifetime. Of these, only the quantum and the Coulomb components depend on the vertical beam aperture. By decomposing the total lifetime into its components, one finds that Coulomb scattering dominates for lifetimes above 0.1 hour, but below this the quantum lifetime dominates. The theoretical curve is fit to the data using a number of adjustable parameters. The experimental points are offset along the abscissa by a constant (185 μm), which reflects the lack of absolute position calibration of the scraper blade. The storage ring pressure is adjusted in the formulas for best fit in the 10-to-0.1-hour region (0.15 n torr), and the vertical beam size is similarly adjusted for best fit around 0.1 hour and below (σ_y=7μm). Of these adjustable parameters, the resulting ring pressure seems somewhat too low, but the other parameters seem reasonable. The observed ring lifetime with all scraper blades fully withdrawn (≥ 19 mm from the beam) was 100 hours or more. This suggests that the full ring lifetime is attained at a half aperture of about 1 mm, as seen in Fig.5 or full aperture of about 2 mm. Such a result is about half the minimum aperture expected from scaling the aperture at the β-max by the square-root of the beta function, and implies that PSGU might operate down to a 2.5mm aperture without lifetime degradation.

B. PSGU Vacuum Chamber

The implications of the 4-jaw scraper results held true for the operation of the PSGU variable-gap vacuum chamber. When centered on the electron beam and closed to the minimum aperture of 3.8 mm, no change in the storage ring lifetime was observed. This was true not only for low beam currents, but also for 300 mA at 2.584 GeV, which is above the limits for present normal operations. No instabiity from vacuum chamber impedance was observed, confirming expectations from theory [6] and impedance measurements [7]. When the undulator magnet was then closed to a gap of 7.5 mm, with both local and global feedback systems disengaged, no change in the electron beam orbit was observed, which is consistent with the integrated multipole field goals listed in Table 1.

To reduce the electron beam aperture below 3.8 mm, the small-aperture region was offset from its initial position (centered on the electron beam) by use of the elevator base stage. The results appear in Fig. 6. The stored beam conditions were essentially the same as for the scraper results presented in Fig. 5. The theory curve was generated as in the previous case, but offset to match the data, and reflected about the 0 mm position. The adjustable parameters required

were 0.3 ntorr for the pressure and σ_y=8.5μm, similar to the values obtained from the scraper measurements. As before, the quantum lifetime dominates the theory curve for lifetimes below 0.1 hours; otherwise, the Coulomb scattering lifetime is dominant. The lifetime with the aperture centered on the electron beam was about 61 hours, as can be seen from Fig. 6. Interpretation of these results takes a little more care. It seems clear that an offset of the aperture is possible before any lifetime degradation is seen; offsets between 0.5 mm and 1.0 mm seem reasonable. If we use 0.5 mm as an example, this means that the

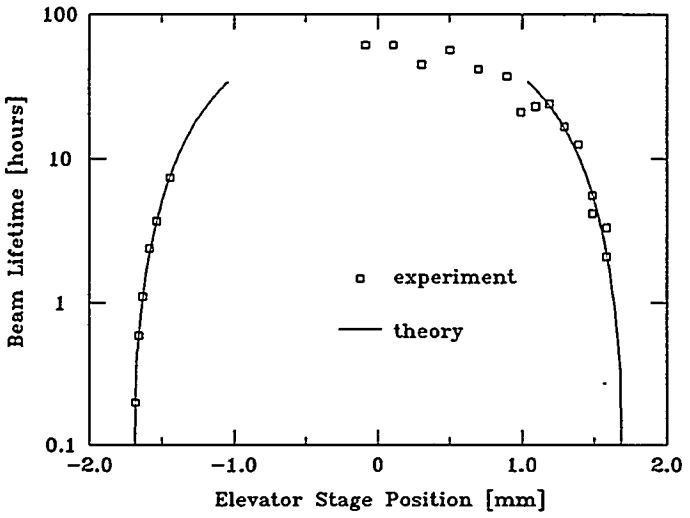

Figure 6 Results of vertical translation of the PSGU minimum aperture (3.8mm). Initial stored beam of 30 mA at 2.584 GeV, 25 bunches, small-vertical-beam-size optics. These results suggest that a minimum aperture 1 to 2 mm still smaller might be used without lifetime degradation.

minimum half aperture may be decreased by 0.5 mm, or a full aperture reduction of 1.0 mm, from 3.8 mm to 2.8 mm. While this neglects the effects of possible ion trapping or other instabilities which may not be well represented in this offset geometry, it suggests that a full aperture of between 2.7 mm and 1.7 mm may be plausible. This strongly motivates a re-work of the vacuum chamber to achieve such apertures while centered on the electron beam.

IV. Measurement of Undulator Radiation:

Following installation of the PSGU magnet and drive system, the X13

beamline was modified and a simple single-crystal x-ray spectrometer was installed to measure the radiation spectrum. The result appears in Fig. 7. The ultrahigh vacuum portion of the beamline was terminated with a 127 μm thick Be window, about 17 m from the undulator. The spectrometer was attached downstream of this window and consists of a 330 mm long flight path and a 450 mm diameter tank containing an entrance slit and a small θ/2θ goniometer system. A Si(lll) crystal was mounted on the θ axis, while a small, windowless ion chamber was attached to the 2θ arm. The slit was set to 1 mm vertical, which limited the radiation passed to a fraction of the central cone of the undulator output. The tank and flight path were filled either with He or N_2.

When He filled the spectrometer, the undulator fundamental radiation could reach the crystal and be diffracted into the ion chamber, where sufficient photon absorption in the He produced a measurable signal. For the higher harmonics, however, the He absorption was so low, that the ion chamber response was very weak. A different result occurred when the spectrometer was filled with N_2. Here, the *fundamental* was adsorbed in N_2 before reaching the crystal, while the *harmonics*, reached the crystal and produced sufficient photon absorption in the ion chamber to obtain a measurable signal. Therefore, combining the two spectra obtained with He or N_2 in the spectrometer permitted both the fundamental and harmonics to be measured.

To obtain an absolute energy calibration, a thin Ni foil was attached over the end of the flight path, where it joined the spectrometer tank. A short spectrum was taken which included the Ni K absorption feature, at (8.333 KeV) and was used to correct the other spectra.

The experimental data presented in Fig. 7 were taken at 26 mA at 2.584 GeV, with PSGU set to an inner aperture of 3.8 mm and a magnet gap of 7.5 mm (K=0.716). The current was kept low to prevent overheating of the Be window. The theory curve was obtained from the URGENT code [8], by specifying the basic undulator and storage ring parameters, the undulator K-parameter, and the location and size of the spectrometer slit. The processing of the experimental data involved almost no adjustable parameters. The absorption of the Be window and of the spectrometer gas (either He or N_2) was removed, and the absolute efficiency of the ion chamber was calculated using absorption coefficients and the chamber dimensions. Finally, the bandwidth of the Si(lll) analyzer was included. There was a significant scattered background from the analyzer crystal in the detected signal, especially in the case with He gas. Only in the He data, a constant background was subtracted to bring the lowest part of

the curve back to zero. In Fig. 7, the short vertical line in the experiment curve at about 4.6 KeV is the splice point between the data taken with He gas (to lower energies) and that taken with N_2 gas (higher energies). The departure of the

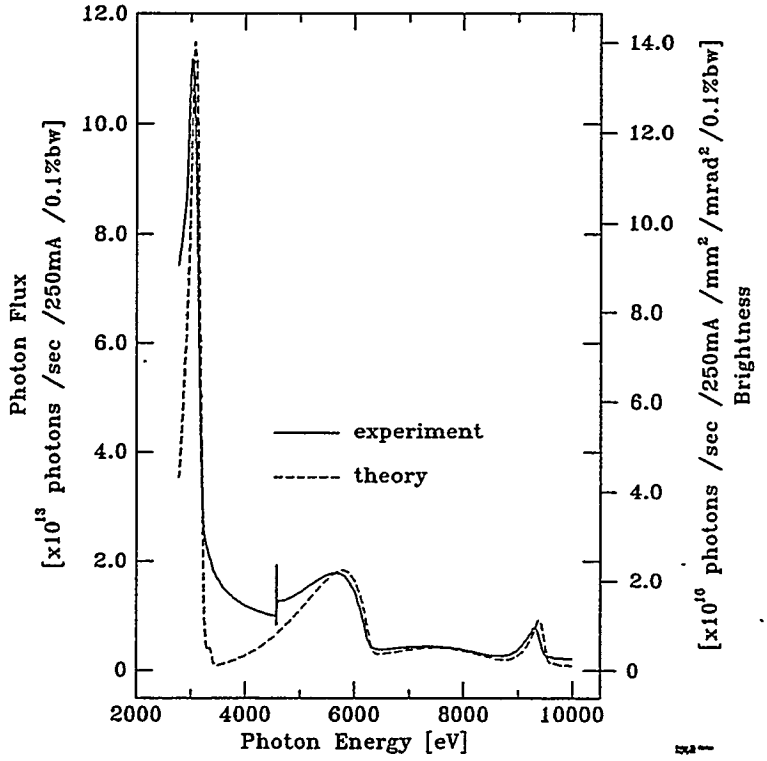

Figure 7 Spectrum measured for the PSGU undulator for a magnet gap of 7.5 mm, K=0.716, at 2.584 GeV, 26 mA, with an inner aperture of 3.8 mm. The theory curve was obtained using the URGENT [8] code.

experiment from the theory in this region may well be due to the scattered background, in the case of the He data, and to the influence of the Si(333) reflection, which produces a peak in the apparent position of the fundamental from the third harmonic. This peak is erroneously blown up to gigantic proportions when the absorption correction is applied, and its tail is still influencing the rising edge of the second harmonic. Despite these complications, the agreement with the theory is rather good. The data may suggest that the K parameter is somewhat greater than 0.716, since the peaks of first, second, and third harmonics all seem to be at slightly lower photon energies than predicted

by the theory.

V. Concluding Remarks

We have successfully operated a small-gap undulator with a full vertical electron beam aperture of only 3.8mm, with no degradation of beam lifetime. Measurements carried out using the elevator stage strongly suggest that successful operation will be possible for a vertical beam aperture less than 3mm. In order to verify this, we plan to rework the PSGU vacuum chamber in December, 1994 to permit a minimum-attainable aperture of 2mm. Also, consideration will be given to reducing the present clearance between the magnet and chamber. In this manner we believe we will be able to achieve the design goal of a 6mm magnet gap.

In the longer term there is the very exciting opportunity to build a device utilizing an in-vacuum undulator magnet, along the lines of the work at KEK [9]. This would permit the operation of an undulator having first harmonic radiation at 5 KeV, with a period length of 10mm and a field strength parameter K. 0.7. Alternatively, a device with the present 16 mm period but 1 m long could be operated at a 5 mm gap for a K of nearly 1.2.

Acknowledgement

We have benefited from discussions with E. Hoyer, J. Hastings, J. Galayda, H.C. Hseuh, G. Decker and E. Blum, and the contributions of D. Lynch, S. Hanna, J. Aloia, C. Stelmach, M. Radulescu, R. Freudenberg, D. Klein, C. Nielson, J. Dabrowski, L.E. Berman and D.P. Siddons. Also, we wish to express our appreciation to K. Halbach whose pioneering development of permanent magnet undulators laid the foundation for this work.

References

[1] K. Halbach, *Nucl. Instrum. Meth.*, **169**, 1, (1980); and *Nucl. Instrum. Meth.*, **187**, 109, (1981).

[2] P.M. Stefan, L. Solomon, S. Krinsky and G. Rakowsky, Proc. 1991 IEEE Part. Accel. Conf., San Francisco, CA, (1991) p. 1096.

[3] G. Rakowsky, R. Cover and L. Solomon, Proc. 1993 IEEE Part. Accel. Conf., Washington, DC, (1993), p. 1605.

[4] J. Safranek and S. Krinsky, ibid., p. 1491.

[5] Our analysis benefits from earlier work of G. Decker, unpublished, who used the scraper when it was located at a position where β_v=7m.

[6] K. Bane and S. Krinsky, Proc. 1993 IEEE Part. Accel. Conf., Washington, DC., (1993), p. 3375.

[7] S. Hanna and P. Stefan, unpublished.

[8] R.P. Walker and B. Diviacco, *Rev. Sci. Istrum.*, **63(1)**, 392, (1992).

[9] S. Yamamoto, T. Shioya, M. Hara, H. Kitamura, X.W. Zhang, T. Mochizuki, H. Sugiyama, and M. Ando, *Rev. Sci. Instrum*, **63**, 400, (1992).

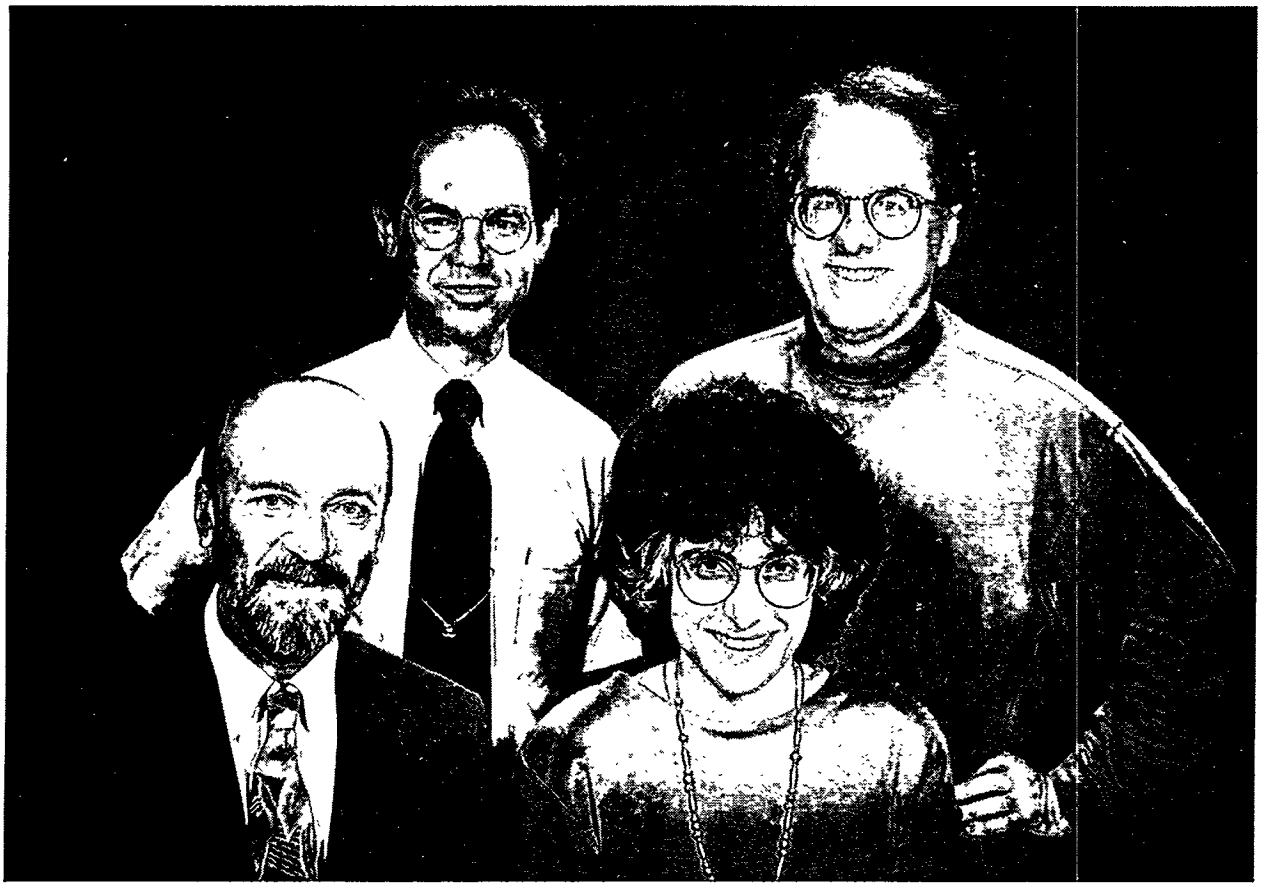

From left: George Rakowsky, Peter Stefan, Lorraine Solomon, and Sam Krinsky

Optimum Coil Shape for a Given Volume of Conductor to Obtain Maximum Central Field in an Air Core Solenoid

Paul Hernandez
Lawrence Berkeley Laboratory
University of California
Berkeley, CA 94720

Thank you Klaus for the recognition and strong scientific leadership you brought to the Lawrence Berkeley Laboratory Mechanical Engineering Department. My apologies, Klaus, for not completing the integration. It is beyond my expertise and an example of why we needed you.

These pages are a modification of an engineering note written in 1961 when superconducting coil wire was scarce - so scarce that at one time in 1961, I returned from a wire maker with the worlds supply of Niobium Zirconium wire in my overcoat pocket. At that time it was very important for the LBL Superconducting Group to make the best use of the wire we had. Given a length of wire we wanted to know the best shape to wind small test coils so that the highest magnetic flux density was obtained. Field uniformity was not important. In general the highest flux density is obtained at the midpoint of the coil on the axial centerline and when the coil inside radius is the smallest.

From this exercise it was found that the best use of the wire is made when a circular coil is wound having a cross-section that approximates a Toroid. We never made any Toroid shaped coils, but this exercise provided a guide for early test coil length-to-radius aspect ratios.

Coil cross sections for optimum shaped coils are shown on Figure 1. Each coil has a constant parameter, or shape factor, K. Figure 1 is shown as a function of coil radius, R, and Axial distance (coil length), z. Constant current density in the coil is assumed. The work in this note is in cgs units, as was the custom at LBL in 1961.

The constant parameter, K, is proportional to $\frac{dB_{z_o}}{dV}$, and

$$K = \frac{R}{(z^2 + R^2)^{3/2}} \qquad (1)$$

The derivative, $\frac{dB_{z_o}}{dV}$, represents the increase in the magnetic field per unit volume of conductor. As $\frac{dB_{z_o}}{dV}$ is a constant, a unit volume of conductor

applied anywhere on a constant K line will give the same increase in magnetic field at the center of the coil.

The magnetic field, B_{z_o}, of Toroid-like shaped coils wound to the K^{th} ring is:

$$B_{z_o,\ gauss,} = \frac{4\pi i}{10} \int_{R_1}^{R_2} \sqrt{1 - K^{2/3} R^{4/3}}\ dR \qquad (2)$$

where:
i is the current density, amperes/sq cm,
R is the coil radius, cm, on any K ring,
R_2 is the coil larger radius,
R_1 is the coil smaller radius, and
z is the + or - axial distance, cm, on any K ring.

The volume, V, of coil conductor wound to the K^{th} ring is:

$$V,\ cu\ cm,\ = 4\pi \int_{R_1}^{R_2} R \sqrt{\left\{\frac{R}{K}\right\}^{2/3} - R^2}\ dR \qquad (3)$$

Development of Optimum Shape and Expressions for Magnetic Field, (2) and Coil volume, (3).

From Ampere's Law the magnet field of a current segment, where I = total current in amperes, is:

$$dB = \frac{Id\ell}{10r^2} \qquad (4)$$

From Figure 1, the field derivative along the central z axis is:

$$dB_{z_O} = dB \cos\beta, \qquad (5)$$

$$\cos\beta = \frac{R}{(z^2 + R^2)^{1/2}}, \qquad (6)$$

Obtain (7) and (8) from Figure 1;

$$r2 = z^2 + R^2 \qquad (7)$$

$$d\ell = Rd\theta \qquad (8)$$

Substitute (7) and (8) in (4) to obtain, (9), dB, normal to r at z_0, R_0.

$$dB = \frac{IRd\theta}{10\,(z^2 + R^2)} \tag{9}$$

Substitute (6) and (9) in (5), to obtain, (10), dB_{z_O}, the field derivative parallel to z at the coil center, z_0, R_0.

$$dB_{z_O} = \frac{IR^2d\theta}{10\,(z^2 + R^2)^{3/2}} \tag{10}$$

From Figure 1;

$$da = dzdR, \text{ sq cm,} \tag{11}$$

$$I = i\,da = idzdR, \text{ and} \tag{12}$$

$$dV = Rd\theta dzdR \tag{13}$$

Substitute (12) in (10) to obtain (14), dB_{z_O} in terms of the volume element,

$$dB_{z_O} = \frac{iR^2d\theta dzdR}{10\,(z^2 + R^2)^{3/2}} \tag{14}$$

1. Optimum Coil Shape for a Given Volume of Conductor.

The Optimum Coil Shape for a Given Volume of Conductor is defined here when $\frac{dB_{z_O}}{dV}$ equals a constant. When a given amount of conductor is added anywhere on the outside of the coil, the central field changes the same amount.

Substitute (13) in (14), rearrange, and let K equal a constant,

$$\frac{dB_{z_O}}{dV} = \frac{iR}{10\,(z^2 + R^2)^{3/2}} = \frac{iK}{10} \tag{15}$$

with, $K = \frac{R}{(z^2 + R^2)^{3/2}}$, (1) on the first page. (1)

Rearrange (1) and solve for z, to obtain the Optimum Coil Shapes shown on Figure 1 for various values of K.

$$z = \sqrt{\left\{\frac{R}{K}\right\}^{2/3} - R^2} \tag{16}$$

For example, the largest coil cross section shown on Figure 1 was obtained from (16) by letting K = 0.01 then,

$$z = \sqrt{\left\{\frac{R}{0.01}\right\}^{2/3} - R^2}$$

Determine the Coordinates on the Coil Boundary for the Maximum Radius and Length.

a. Coil Radius, R, has a maximum and minimum when, z = 0.

By inspection of Figure 1, the Coil Radius on any K line is a maximum and a minimum when z = 0. Substitute, z = 0, in (16) and solve for R,

$$R_{max} = \frac{1}{\sqrt{K}} \tag{17}$$

also from (16), R = 0, when z = 0.

b. Find R when z is maximum.

Coil length, z, is a maximum when, $\frac{dz}{dR} = 0$

Rearrange (16)

$$z^2 + R^2 - \left\{\frac{R}{K}\right\}^{2/3} = 0 \tag{18}$$

Differentiate (18)

$$\frac{dz^2}{dR} + \frac{R^2}{dR} - \left\{\frac{R}{K}\right\}^{2/3} \frac{1}{dR} = 0$$

and

$$\frac{dz}{dR} + \frac{R}{z} - \frac{R^{-1/3}}{z\,K^{2/3}} = 0 \qquad (19)$$

Solve (19) for R,

$$R = \frac{R^{-1/3}}{3K^{2/3}}$$

and continue to obtain (20),

$$R_{\text{at z max}} = \frac{1}{3^{3/4}\sqrt{K}} = \frac{1}{2.2795\sqrt{K}} \qquad (20)$$

c. Find the Axial Maximum Half Distance, z_{max}.

To find the maximum coil half length, z_{max}, substitute (20) in (16),

$$z = \sqrt{\left\{\frac{R}{K}\right\}^{2/3} - R^2} \qquad (16)$$

$$= \sqrt{\frac{1}{\sqrt{3}K} - \frac{1}{3\sqrt{3}K}} \quad \text{and,}$$

$$z_{max} = \frac{\sqrt{2}}{3^{3/4}\sqrt{K}} \qquad (21)$$

or, by substituting (20) in (21),

$$z_{max} = \sqrt{2}\ R \qquad (22)$$

2. Expression for Magnetic Field, (2).

The Magnetic Field, B_{z_O}, of a coil wound to the K^{th} ring is developed by integrating (14) with respect to θ, from 0 to 2π, and with respect to z from +z to −z to obtain (2). The axial distance, z, is defined by (16).

3. Expression for Coil Volume, (3).

The Volume, V, of a coil wound to the K^{th} ring is developed by integrating (13) with respect to θ, from 0 to 2π, and z from -z to +z, to obtain (3). The axial distance, z, is defined by (16); and radius, R, from R_1 to R_{max} is defined by (17).

Optimum Coil Shape for a Given Volume of Conductor to obtain Maximum Central Field, B_{z_o} in an Air Core Solenoid.

$$\text{Shape factor, } K = \frac{R}{(z^2 + R^2)^{3/2}}$$

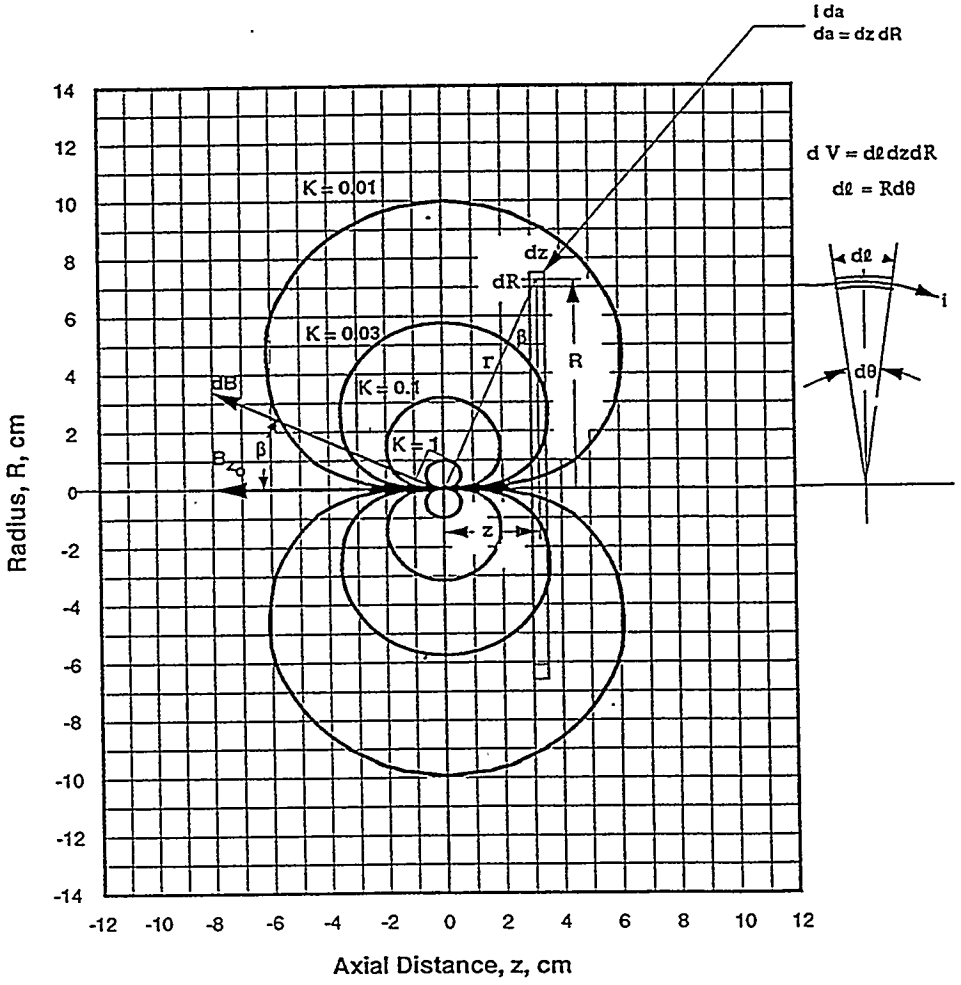

Figure 1

Lawrence Berkeley Laboratory
University of California Berkeley, California 94720
(510) 486-4000 • FTS (510) 486-4000

31 October 1994

Dear Klaus,

The Mechanical Engineering Department was very honored when you joined us. We all feel very proud of your success, your international reputation, and the recognition you brought to our department. In particular, your leadership in permanent magnet wigglers brought world wide recognition to you and LBL. Your physics background, your strong analytical abilities, and your broad interests make you a real renaissance man.

You always had a clear and firm idea of what you wanted to accomplish. No one ever led you (except perhaps Mrs. Halbach). When I was Department Head, I tried to create the illusion of directing you by finding out which way you were going then hoping to get out in front of you in time.

You are always generous with your help to all of us, teaching us individually or with your lectures and notes. Many thanks Klaus, and Happy Birthday.

Sincerely,

Paul Hernandez

Powerful Electrostatic FEL: Regime of Operation, Recovery of the Spent Electron Beam and High Voltage Generator

I. Boscolo
University and INFN
Milan, Italy

J. Gong
Southwest Jiaotong University
Chengdu, P.R. China

Abstract.
FEL, driven by a Cockcroft-Walton electrostatic accelerator with the recovery of the spent electron beam, is proposed as powerful radiation source for plasma heating. The low gain and high gain regimes are compared in view of the recovery problem and the high gain regime is shown to be much more favourable. A new design of the onion Cockcroft-Walton is presented.

1- Introduction

The problem of building a powerful millimetre radiation source for toroidal plasma start-up, plasma current profile control and plasma heating had received a partial solution with the gyrotron device [1].Nevertheless, it is worth to pursue the path of FEL driven by electrostatic accelerators (FELTRON) [2] because it has the advantage over the gyrotron of having a relatively simple set-up for the FEL interaction (the gyrotron has the heavy magnet for the strong axial magnetic field), and of providing high frequency and tuneable radiation. The disadvantage is that the recovery of the spent electron beam must be done with high efficiency, around 99%.

In this paper we discuss the design of the FEL, that is its regime and electron beam energy distribution after the interaction, in relation to the problem of the recovery. We will see that the high gain+tapered regime with an efficiency ε=5% is the most favourable, because the electron distribution after the interaction allows for a rather simple collector design. The possibility of exploiting a very efficient FEL, $\varepsilon \approx 50\%$, although very appealing, is not viable because a high voltage generator of the needed level of power does not exist.

The Cockcroft-Walton proposed for this FELTRON has the new design with nested shells (onion Cockcroft-Walton [3], see fig 1). The design is reviewed after the first test [4].

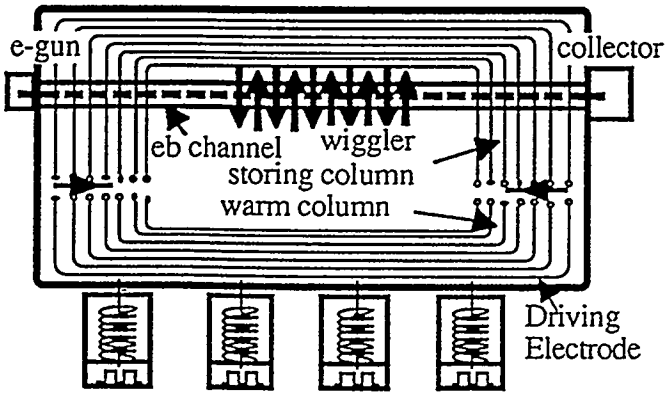

Fig. 1 Mechanical scheme of the Cockcroft-Walton: the onionskin disposal of the capacitor plates.

We will fix our goal to 1MW continuos power at 300 GHz, be-cause this is the set of parameters that Fusion Community is talking about for toroidal plasma heating [5].

2- Scheme of the machine and relevant physical and technological problems.

For the general discussion and philosophy of a CW powerful FEL we refer to the two papers in ref. [2]. Here we make a short summary for easy reference. CW operation means straightforwardly static accelerating field, thus an electrostatic accelerator. The FEL interaction requires a relativistic eb (electron beam), hence a high voltage electrostatic accelerator. Since the high voltage is a very difficult achievement (unless a Van De Graaf is used but the Van De Graaf has too low power), we must get along with the lowest voltage compatible with the operation of the FEL at that frequency and power. A reference value for a powerful high voltage generator is 2MV. The most powerful generators providing that voltage level, can deliver 300 kW power only [6]. This power level is not compatible with the 1MW required, even considering 100% efficiency. Hence the system must have a second generator. The electrostatic accelerator for this kind of FEL must have a recovery system for the spent eb (so the overall efficiency is rather enhanced) and a second generator must be inserted into the system. The scheme of an electrostatic FEL is then the one shown in fig.2.

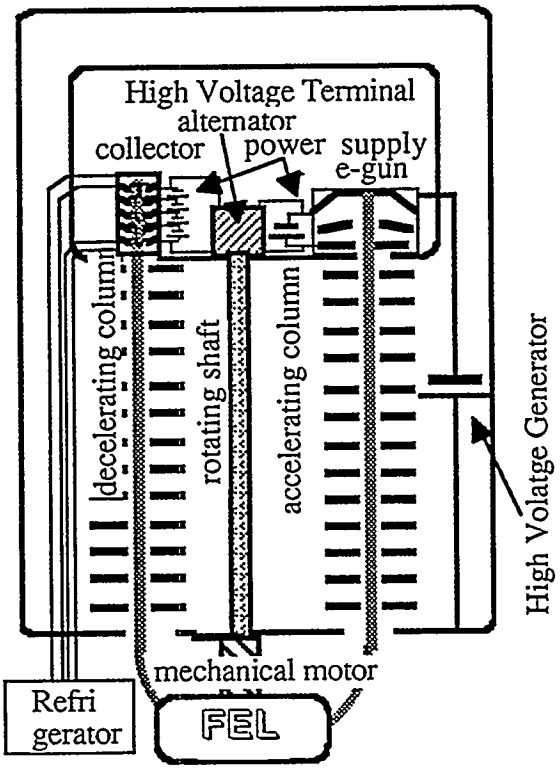

Fig.2. Scheme of an electrostatic FEL: the spent eb must be recovered and a powerful low voltage generator supplies to the eb the power that it has lost within the FEL.

The spent eb is recovered and the second power supply is set between the collector and the high voltage terminal for replenishing to electrons the energy they have lost within the FEL and to provide for losses. The low voltage generator feeding the collector (see fig.2) must be very powerful because it has to provide both the 1MW power that the eb transfers to the radiation field and the power lost by electrons in hitting the walls of the collector (the electrons cannot arrive with zero energy onto the collector wall), which is again around 1 MW. Because of this power loss the collector must be equipped also with a cooling system (see fig.2). It is clear that such amount of power and heat cannot be handled with the collector set at the high voltage terminal. The scheme of the machine must then have the collector at ground potential, so the system becomes the one shown in fig. 3. The FEL action onto the eb, more specifically, the energy spread induced by the FEL interaction on the eb, must comply with the possibility of a simple and good recovery of the eb at the collector. At this point we must look at the maximum allowed voltage for the collector generator, because it decides the accepted energy spread of the eb due to the FEL interaction. A reference number might be 100-150 kV, as

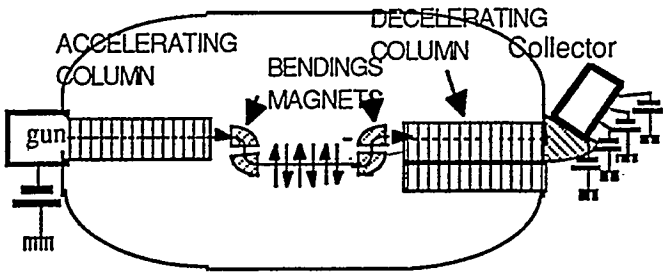

Fig.3: scheme of the electro-static FEL with the collector at ground potential.

can be figured out from power supplies of powerful klystrons and gyrotrons and from the power of the high voltage oscillator in refs [3,7]. This problem of the collector voltage is related also to the relatively small number of stages of an efficient collector.

Once the limiting technological conditions on the initial energy and final energy spread of the eb are established, the basic relation which guides the FEL design is the relation between the efficiency and the energy spread induced on the eb by the FEL interaction. That relation depends on the FEL physics: in LGR-Low Gain Regime [8,9] (Madey experiment regime and all experiments except for the Livermore experiment [10]) the relation reads

$$\Delta E \approx 2\,\varepsilon\,E_{initial}\ ; \qquad \varepsilon \approx 1/2N \tag{1}$$

where N is the number of wiggler periods; in HGR-High Gain Regime [9,11], the eb is splitted into two parts with respectively 20% and 80% of the particles and both have an energy spread which is approximately the FEL parameter ρ, that is

$$\frac{\Delta E}{E} \approx \rho\ ; \qquad \rho = \frac{1}{\gamma}\left(\frac{a_0}{4}\,\frac{\omega_p}{\omega_0}\right) \tag{2}$$

but the 80% beam has an energy reduction with respect to the initial one which is

$$\Delta E_{80\%} = E_{initial} - \langle E_{final} \rangle \approx \frac{\varepsilon}{0.8}\,E_i \tag{3}$$

In eq (2), a_0 is the wiggler parameter $a_0 = (e\,B_0\,\lambda_0)/(\sqrt{2}\,2\,\pi\,m\,c)$ (λ_0, B_0 are the undulator period and magnetic field strength respectively), ω_p is the plasma frequency and ω_0 is the undulator frequency. The value of the parameter ρ for the FEL under discussion is typically less than 1%. We remark that in HGR the induced energy spread is roughly a factor two less than in LGR. This occurs because in the former regime 80% of the electrons, that is almost the whole eb, are bunched and then the bunch is slowed down in energy, while in the latter regime the electrons at different positions are differently depressed in energy (the gain is due to the shift of the electrons average energy).

In LGR the efficiency can be as high as 2%, so the number of wiggler periods is N = 20 and the induced energy spread results in about 100 KeV (initial energy E_i = 2 MeV). In fig. 4 the results of the simulation are reported; the energy spread comes out to be 140 KeV. We notice that the wiggler and so the FEL length is well acceptable being less than one meter ($L = N\,\lambda_0 \cong N\,2\,\gamma^2\,\lambda$).This regime of operation leads to a very high current, $I \approx 20$ A, in order to obtain the wanted power. The circulating current lowers proportionally to the increase of the efficiency. Exploiting the HGR operation the FEL efficiency can be doubled because the energy spread is reduced of about a factor two with respect to the low gain regime. Therefore, an efficiency of about 5% can be chosen. The evolution of the eb, in crossing the wiggler, calculated for the FEM

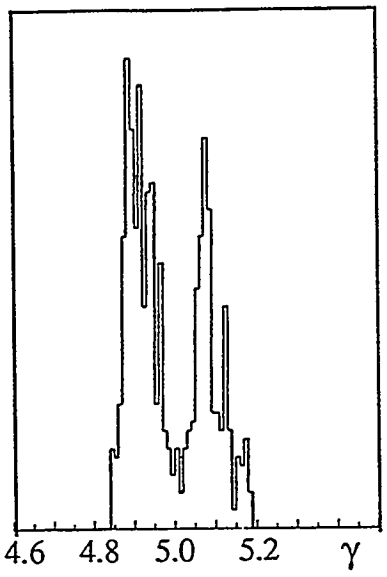

Fig.4.Diagram of the energy dispersion after the FEL interaction for 1 MW output power for E = 2.5 MeV, I = 20 A.

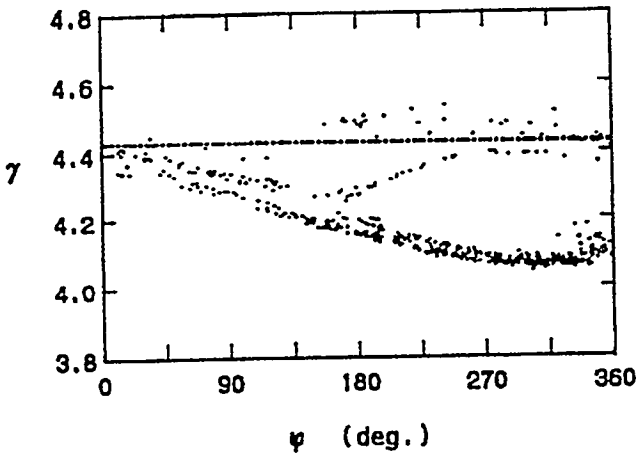

Fig.5. Phase energy diagram of the eb at the exit of the undulator for E = 1.75 MeV and I = 12 A. The straight line indicates the initial particle distribution [After fef.13]. We note that the energy spread is comparable with the one of fig. 4, but the more than 80% of the beam is accumulated around γ = 4.1 level of energy.

experiment at FOM Institute Nieuwegein-Nederlands [12] is reported in fig.5. The energy dispersion results more or lessthe same as the previous FEL operating in LGR. With this efficiency the 1 MW power requires a current of 16 A only (in the project of fig.5 the output foreseen power is a bit less). In order to elucidate better the difference between the two cases we make some simple calculations. In Table 1 we list the parameters referring to the FEL operating in LGR and HGR regimes. With the energy spread indicated in the table we can assume in LGR a five stages collector separated by 28 kV one another (as sketched in fig.6) and 4 A current arriving at each stage (we have assumed a flat distribution of the electrons versus the energy). The total power of the generators feeding the collector results in

$$P_{coll} = V_1 \cdot \Delta I + V_2 \cdot \Delta I + V_3 \cdot \Delta I + V_4 \cdot \Delta I = (140 + 112 + 84 + 56 + 28)\,\text{kV} \times 4\,\text{A} = 2.1\,\text{MW}$$

Here the Losses amount to 1.1 MW. The estimates losses at the collector are $P_{losses} \approx [(28/2)\,\text{kV} \cdot 4\,\text{A}] \cdot 5\ \text{steps} = 280\,\text{kW}$. The others 800 kW are due to FEL process. In HGR there are only two generators whose total power is

$$P_{collector} = V_1 \cdot 4\Delta I + V_2 \cdot \Delta I = 140\,\text{kV} \times 12.8\,\text{A} + 28\,\text{kV} \times 3.2 \approx 1.9\,\text{MW}$$

There is a reduction of 200 kW, i.e. 20%, of losses. Of these the losses are $P_{losses} \approx [\Delta E\ \Delta I_1 + \Delta E\ \Delta I_2] = 280\,\text{kW}$. What is very important is the great reduction in the complexity of the collector design. In order to understand the great benefit gained with HGR with respect LGR operation, we point out that the multistage collector required in LGR (left scheme in fig. 6) must be a good spectrometer in order to separate

TABLE 1

PARAMETERS	LGR	HGR
Output FEL Power	1 MW	the same
FEL Efficiency	2 %	5 %
Charge Recovery	99.5 %	the same
Energy	2.5 MeV	1.75 MeV
Current	20 A	16 A
Electron Beam Power	50 MW	20
Induced Energy Spread	140 KeV	140 KeV
Losses	1100 MW	0.9 MW
nº stages of the collector	5	2

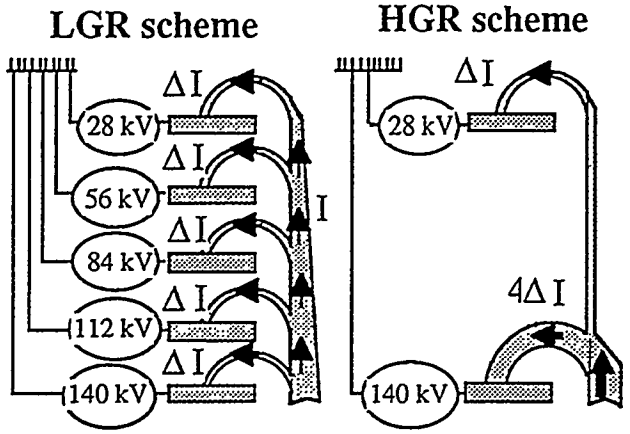

Fig.6. Conceptual scheme of the collector in the two regimes: In LGR the collector has five stages because the energy spread is almost uniform, in HGR it has only two stages because the eb is divided into two streams.

the electron streams with different energies [15], while in HGR the collector could be ultimately a simple Faraday cup, that is a plate.

The length of the wiggler in this high gain+tapered regime with 5% efficiency, being $L \approx 1.6$ m is still acceptable from the point of view of the machine dimension. An higher efficiency would lead to a too big machine[+] . For completeness, we cite the idea of the eb cooling of ref.[16]. If technologically viable, that is if it would not require a too long interaction section, it would lead to an increase of the collector efficiency and, because of this, to a reduction of cooling problems at the collector.

3- The new Cockcroft-Walton

The powerful high voltage generator proposed for this FELTRON is the onion Cockcroft-Walton. The name comes from the fact that the capacitors of the two warm and storing columns (see fig.1) are made up by nesting half ellipsoid foils one within the other. This multi-shells design brings-about a uniform field distribution and a multi-shielding of the high voltage terminal from ground. The plates of the capacitors make the natural voltage divider for the accelerating column in an electrostatic accelerator configuration. Those features of the onion Cockcroft-Walton increase the reliability of an electrostatic accelerator. We point out that in this design, the accelerating column forms a unique block with the multiplying voltage system. This intrinsic unity leads to a natural control of current leaks and voltage distribution.

The drawback of the design is that the capacitances of the stages are relatively small, a value less or equal to 2 nF can be reasonable, because they are air volume capacitors. In

[+] By the way, we add that it would be worth to investigate the possibility of substituting the wiggler tapering with the waveguide tapering [14] in order to simplify the FEL design.

order to get high capacitance, a very large machine should be built. The small value of the stage capacitance requires consequently a very small value of the shunt capacitances between the Cockcroft-Walton stages. In fact, the Cockcroft-Walton is a high-pass lumped transmission line (see fig.7). Solving the equations of this system, it comes out that the output voltage V_0 depends on the number of the multiplying stages N and on the ratio of the column capacitance C over the shunt capacitance C_p [see ref.7]

$$V_O = \sqrt{\frac{C}{C_P}} V \tanh 2N \sqrt{\frac{C_P}{C}} \qquad (4)$$

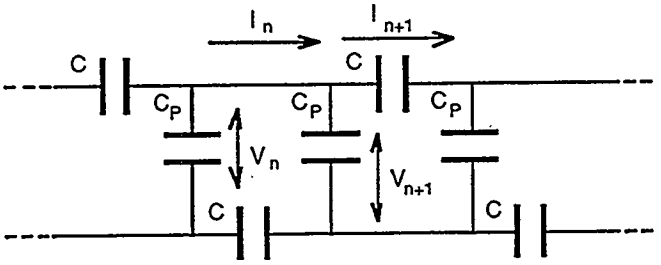

Fig.7. Scheme of the Cockcroft-Walton as a lumped transmission line.

The shunt capacitance C_p must be nearby or less 1 pF (C_p = 1/1000 C) in order to avoid the saturation of the voltage at already a relatively small number of stages. In fig.8 we have considered the typical case of an interstage capacitance C = 1 nF and two values

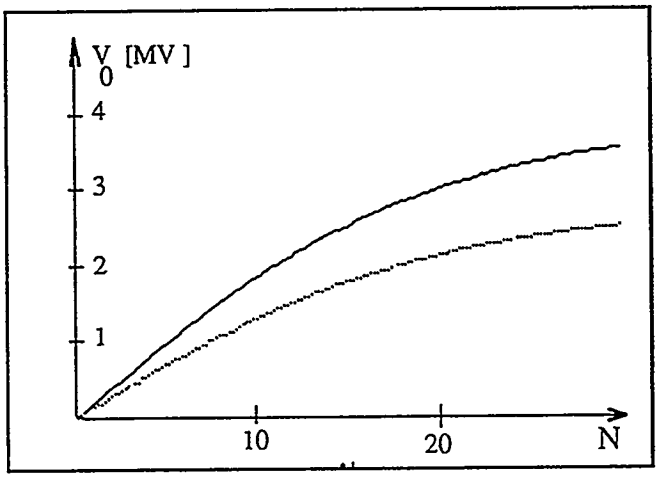

Fig.8. Output voltage versus the number of the stages with C =1 nF and C_p = 1 pF continuous line, C_p = 2 pF dotted line; the oscillator voltage has been assumed 100 kV.

of shunt capacitance: $C_{p,1}$ = 1 pF and $C_{p,2}$ = 2 pF. Assuming the voltage of the driving oscillator V= 100 kV and the total number of stages N = 20, the output voltage reaches respectively 3 MV and 2.1 MV. In view of this, we understand that it prejudicial to the usefulness of this design that the only contribution to the shunt capacitance comes from the rectifying diodes. From fig.1 we observe that the rims of the shells of the capacitors face each other, but we see also that each shell is sandwiched by two other foils. From general arguments, we can guess that the two nearer plates would attract all the field lines coming from the inner plate if the interdistance in the sandwich is enough less (more or equal to one third) than the distance between the two half onion. Using the image charge argument, since the force felt by a charge depends on the inverse square of the distance, we may conclude that the ratio between the two distances ought to be higher than three. The experiment [4] has proven that the two columns are electrically separated, except for the last inner plates. However , we have also found that because of this coupling the slope of the output voltage with the number of stages is notably reduced. The complete decoupling is accomplished with the generator design of fig.9. In fact, the last plates result completely sandwitched as all others.

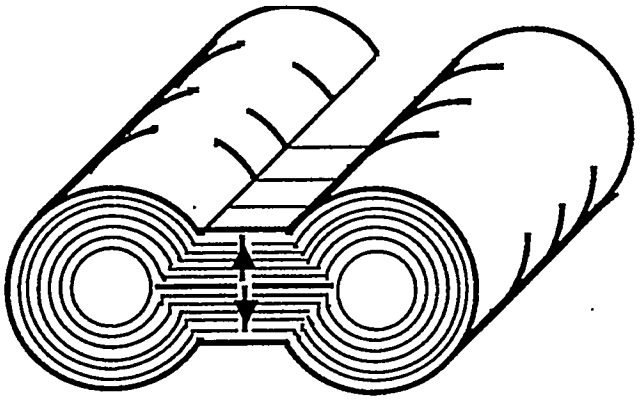

Fig.9. Design of the onion Cockcroft-Walton with no shunt capacitance between the two last plates of the two columns.

4- Conclusions

The electrostatic FEL with electron beam recovery seems feasible and competitive with gyrotron as high frequency radiation source for plasma heating. The FEL must operate in the High Gain Regime with 5% efficiency. In fact, in this regime the electron beam current is minimized, the energy recovery efficiency is maximized and, more important, the collector is a simple Faraday cup, instead of a set of Faraday cups arranged as a spectrometer. The multi-layers Cockcroft-Walton (i.e. onion type Cockcroft-Walton) must have the design with the two stack of metallic layers geometrically separated, so the shunt capacitance between the two last stages is dropped out.

REFERENCES

[1] V. L. Bratman et al, Talk and Paper presented at Intern. Conf. on Plasma Science and Technology, June 1994, Chengdu-China.

[2] I. Boscolo, V. Stagno, V. Variale NIM Phys. Res. A279, 646, 1989; I. Boscolo, F.Giuliani, M. Valentini, "A 1-MW, 1-mm Continuous-Wave FELTRON for Toroidal Plasma Heating", IEEE Trans. on Plasma Science Vol 20, 256-262, 1992

[3] I.Boscolo, F.Giuliani, M.Roche,'Powerful high-voltage generators for FELTRON, the electro-static-accelerator FEL amplifier for TeV Colliders", NIM Phys. Res. Vol A 318, 465-471,1992.

[4] I. Boscolo " The electronic test of the onion Cockcroft-Walton" NIM Phys. Res. Vol A 342, 309-313,1994.

[5] M. Shiho et al. NIM Phys. Res A 304, 141, 1991; S. W. Bidwell et al. ibidem pag. 187.

[6] This number comes from the brochures of the companies and direct information.

[7] I. Boscolo, F.Giuliani, M. Valentini, M. Roche, 'A Cockroft-Walton for FELTRON, the new m-wave source for TeV-Colliders', IEEE Nucl. Sci. 39, 308-314, 1992; J. Moret-Bailly and M. Roche, Project SIRIUS Report, 1992 Bourgogne Tecnologies 9 avenue de la Découverte BP 258- F21007 DIJON.

[8] W. B. Colson, Novel Sources of Coherent Radiation, Physics of quantum El. Vol 5, pag. 192, Eds. S.F. Jacobs, M. Sargent, M. Scully, Addison Wesley Phys. Conf. 1978.

[9] R. Bonifacio, F.Casagrande, G.Cerchioni, L.De Salvo Souza, P.Pierini and N. Piovella "Physics of the High Gain FEL and Superradiance" Rivista del Nuovo Cimento 1990,Vol 13, nº 9.

[10] T.J. Orzechowski et al., Phys. Rev. Lett. 54,889,1985; T.J. Orzechowski et al., Phys. Rev. Lett. 57,2172,1986.

[11] E. T. Sharlemann " High Gain, High Power Free Electron Laser: Physics and Application to TeV Particle Acceleration", Proc. INFN Int. School on Electromagnetic Radiation and Particle Beams Acceleration, Varenna,Italy; Ed. R. Bonifacio, L. De Salvo, C. Pellegrini, North Holland Delta Series,1989, pag. 95.

[12] W.H.Urbanus, et al. "Design of the 1 MW, 200 GHz, FOM fusion FEM" NIM Phys. Res.A 331, 235,1993; M. Caplan et al. "Predicted performance of a dc beam driven FEM oscillator designed for fusion applications at 200-250 GHz.

[13] W.H.Urbanus, et al. "Engineering Design of the FOM fusion FEM" FOM-92.2213/1, pag.19.

[14] I. Boscolo, A. Dipace, E. Sabia "A Microwave FEL Design with Waveguide and Wiggler Tapering" report ISSN / 1120-558X ENEA Frascati, Italy, to appear on IEEE QE

[15] I. Boscolo, V. Stagno, V. Variale and M. Bianconi, "Physics and Simulations of a New Design Multistage Collector Inserted in an Immersed Flow Configuration Electrostatic Accelerator", Nucl. Instrum. Meth. Phys. Res. A 311 (1992) 386-394

[16] V. A. Bazylev, A. V. Tupulov "Cooling of relativistic electron beams" NIM Phys. Res. Vol A 331, 332-334,1993.

Klaus having dinner at the home of Ilario Boscolo, Bussero-Milan, in 1991.

Radiation and Gas Conduction Heat Transport Across a Helium Dewar Multilayer Insulation System

Michael A. Green
Lawrence Berkeley Laboratory
University of California
Berkeley, CA 94720

This report describes a method for calculating mixed heat transfer through the multilayer insulation used to insulate a 4 K liquid helium cryostat. The method described here permits one to estimate the insulation potential for a multilayer insulation system from first principles. The heat transfer regimes included are: radiation, conduction by free molecule gas conduction, and conduction through continuum gas conduction. Heat transfer in the transition region between the two gas conduction regimes is also included.

The cryogenic multilayer insulation system is modeled as a stack of flat plates. The following assumptions apply: 1) The spacing between the plates is much smaller than the smallest surface dimension of the plate. As a result the form factor F for radiation and free molecular heat transfer is one. 2) The spacing between the plates is larger than 0.6 times the predominant wave length of the emitted heat, so there is no radiation tunneling between the plates. At the lowest temperature (say 4 K), the plate spacing must be greater than 0.42 mm. On the room temperature side (300 K), the plate spacing has to be greater than 0.006 mm. 3) The plates shall be metallic or coated with a metal so that they are opaque to the wavelengths of infrared on the plates. At 300 K, mylar with 300 angstroms of aluminum on it is opaque to thermal radiation. At low temperatures, the aluminum thickness has to increase (to 0.03 mm at 4 K). 4) Since the multilayer insulation operates over a temperature range from 4 K on up, the medium between the plates is assumed to be helium gas at pressures that vary from good vacuum ($<10^{-5}$ Pa) to atmospheric (10^5 Pa). 5) The medium between the plates is non-participating. This means that the gas between the plates does not absorb nor emit thermal radiation. 6) The spacing between the plates is small enough to prevent convection cells from forming during continuum gas conduction.

RADIATION HEAT TRANSFER BETWEEN PLATES

The radiation heat transfer per unit area Q_R between plate N and plate N–1 can be calculated using the following expression:

$$Q_R = E(T_{N,N-1})\,\sigma\,[T_N^4 - T_{N-1}^4] \qquad (1)$$

where Q_R is the radiation heat transfer between plate N and N–1; $E(T_{N,N-1})$ is form and emissivity factor for the heat transfer; σ is the Stefan–Bolzman constant ($\sigma = 5.67 \times 10^{-8}$ W m^{-2} K^{-4}); T_N is the temperature of plate N; and T_{N-1} is the temperature of plate N–1. The form and emissivity factor for diffuse reflection is defined as follows:

$$E(T_{N,N-1}) = F\,\varepsilon_{N,N-1} = F\frac{\varepsilon_N\,\varepsilon_{N-1}}{\varepsilon_N+(1-\varepsilon_N)\,\varepsilon_{N-1}} \qquad (1a)$$

where F is the form factor. In our case, we assume F = 1. As long as F is one, Equation 1a applies for specular reflection as well as diffuse reflection. Another implication of F being one is that radiation heat transfer is independent of plate separation (as long as the plate separation is more than 0.6 times the peak heat wave length). ε_N is the emissivity of plate N; and ε_{N-1} is the emissivity of plate N–1. When the plates have the same emissivity ε and the plate emissivity is small, $E(T_{N,N-1})$ is approximately $\varepsilon/2$.

The emissivity of a metal plate is temperature dependent. For metallic plates, the Hagen–Rubens approximation can be used to estimate the plate emissivity as long as the radiation wave length is longer than 5 microns. (Thermal radiation at 300 K has a peak wave length of 9.7 microns; thermal radiation at 4 K has a peak wave length of 725 microns.) When the Hagen–Rubens relationship is integrated over all wave lengths the following temperature dependent form for the emissivity $\varepsilon(T_s)$ can be developed[1]:

$$\varepsilon(T_s) = 5.76\,[\rho(T_s)\,T_s]^{0.5} + 12.4\,\rho(T_s)\,T_s \qquad (2)$$

where $\rho(T_s)$ is the temperature dependent electrical resistivity of the metal in the plate that is at a temperature T_s.

From Equation 2, one can say: 1) The lowest emitters are the best electrical conductors. 2) The emissivity of the plate increases with temperature. 3) Alloying a good reflecting metal increases its emissivity 4) Mechanical polishing that results in work hardening increases emissivity. At 300 K, the theoretical emissivity of 1100 aluminum is 0.0166; at 4 K the emissivity goes down to 0.00034 (provided the oxide layer does not increase the emissivity)[2]. In practical terms, the average emissivity of a stack of multilayer insulation with aluminum should be about 0.02 provided the aluminum layer on each plate is thick enough. If there is a heavy aluminum oxide coating on the aluminum, the emissivity can go up as high as 0.1. Gold coated mylar can have a lower emissivity than aluminized mylar because there is no oxide layer. It should be noted that it does not matter how low the plate emissivity is, if that plate is not opaque to thermal radiation.

GAS CONDUCTION HEAT TRANSFER BETWEEN PLATES

Gas conduction between the plates falls in two general regimes: 1) The free molecule regime is where gas molecules carrying heat travel from plate to plate without colliding with each other. The spacing between the plates is much less than a mean free path for gas molecule collisions 2) The continuum gas conduction regime is where the gas molecules carrying the heat from plate to plate collide with each other in the process of traveling from one plate to the other. The spacing between the plates is much greater than a mean free path for gas molecule collisions There is a transition regime between the free molecular gas conduction regime and the continuum gas conduction regime.

The mean free path for collisions between gas molecules can be determined from the viscosity of the gas. The mean free path is defined as follows[3]:

$$\lambda(T_g) = 1.23 \frac{\mu(T_g)}{P} \left[\frac{R\,T}{M}\right]^{0.5} \tag{3}$$

where $\lambda(T_g)$ is the mean free path for gas molecule collisions for gas at a temperature T_g; $\mu(T_g)$ is the gas viscosity at a temperature T_g; T_g is the average temperature of the gas between plate N and plate N–1; R is the universal gas constant (R = 8314 J K^{-1} $mole^{-1}$); M is the molecular weight of the gas (for helium M = 4 kg $mole^{-1}$); P is the pressure measured by a vacuum gauge looking at a space with a temperature T. Note: the equations here are all given in SI units. (A vacuum of 1 torr is 133.29 Pa.) The viscosity of helium gas can be calculated using the following analytic expression (valid from 5 K to 500 K)[4]:

$$\mu(T_g) = 5.03 \times 10^{-7}\, T_g^{0.65} \tag{3a}$$

In order to determine the gas heat conduction regime one can define a dimensionless number called the Knudsen number[3] Kn;

$$Kn = \frac{\lambda(T_g)}{S} \tag{4}$$

where S is the spacing between the plate N and plate N–1. The free molecular heat transfer equations can be applied precisely when Kn > 10. In many cases, the free molecule equation can be used as Kn approaches 1, but the accuracy is reduced. The ordinary conductive heat transfer equation can be applied when Kn < 0.003. The region from 0.003 < Kn < 10 is a transition region. Heat transfer in this region can be looked at from either the free molecular or the continuum gas

point of view. Neither method is completely accurate over the whole transition region, but the accuracy of a given method can be surprisingly good.

Free Molecule Gas Conduction

When the vacuum pressure is relatively low, heat conduction between plates will be by free molecule gas conduction. Free molecule gas conduction occurs when the Kn > 10. The upper limit pressure P_u for free molecular conduction (defined as Kn = 10) can be estimated using the following expression:

$$P_u = 0.123 \frac{\mu(T_g)}{S} \left[\frac{R\,T}{M}\right]^{0.5} \tag{5}$$

where S is the spacing between plates. μ, R, T, and M are previously defined.

In the free molecular conduction regime, conduction heat transfer is a function of pressure (or number density). Heat flow per unit area $Q_{N,N-1}$ by free molecular conduction between plate N and plate N–1 can be calculated using the following expression:

$$Q_{N,N-1} = D(T_{N,N-1},P)\,[T_N - T_{N-1}] \tag{6}$$

where the transfer function $D(T_{N,N-1},P)$ takes the form:

$$D(T_{N,N-1},P) = F \frac{\alpha_{N-1}\,\alpha_N}{\alpha_N + \alpha_{N-1}(1-\alpha_N)} \frac{k+1}{k-1} \left[\frac{R}{2\pi M T}\right]^{0.5} P \tag{6a}$$

where F is the form factor (F = 1); α_N is the accommodation coefficient of plate N; α_{N-1} is the accommodation coefficient of plate N–1, k is the ratio of specific heats for the gas (Use k = 1.67 for helium.); R is the universal gas constant ; M is the molecular weight of the gas; P is the pressure. When the accommodation coefficient α is the same for both plates and it is relatively small,

$$D(T_{N,N-1}) = F \frac{\alpha}{2} \frac{k+1}{k-1} \left[\frac{R}{2\pi M T}\right]^{0.5} P \tag{6b}$$

where F, k, R, M, P and T have been previously defined.

At low temperatures (less than 60 K), the accommodation coefficient is temperature dependent; the helium between the plates collides with molecules of air gasses that stick to the plates. The accommodation coefficient approaches one at 4 K. As the temperature rises, the accommodation coefficient decreases until it drops to about 0.1 between 60 and 120 K. Then the accommodation coefficient

increases to 0.25 at 300 K. The following approximate expression can be used to estimate the temperature dependent accommodation coefficient $\alpha(T)$ of helium to an aluminum plate:

$$\alpha(T) = 1.23\, e^{-T/20} + 8.34 \times 10^{-4}\, T \tag{7}$$

where T is the temperature of the plate. Equation 7b applies over a range of temperatures from 5 K to 500 K. The average accommodation coefficient between 4 K and 300 K is between 0.13 and 0.17 (the higher accommodation coefficient applies when radiation heat transfer dominates); the average accommodation coefficient between 4 K and 80 K is around 0.1.

Ordinary Continuum Gas Conduction

Heat is transferred by ordinary continuum gas conduction when $Kn < 0.01$. Gas conduction heat transfer per unit area $Q_{N,N-1}$ from plate N to plate N–1 can be estimated using the following expression:

$$Q_{N,N-1} = k(T) \frac{dT}{dx} \tag{8}$$

$$Q_{N,N-1} = k(T) \frac{T_N - T_{N-1}}{S_N} \tag{8a}$$

where k(T) is the thermal conductivity of the gas at temperature T; S_N is the plate separation distance between plate N and plate N–1.

The distance between the high temperature wall and the low temperature wall S_N is the governing factor for continuum conductive heat transfer. The role of the plates in continuum conduction is to keep convection cells from forming.

The temperature dependent thermal conductivity k(T) for helium gas can be estimated using the following analytical expression[4]:

$$k(T) = 3.83 \times 10^{-3}\, T^{0.65} \tag{9}$$

Equation 9 is useful between 5 K and 500 K, from 100 Pa to 10 MPa. For a vacuum space filled with helium gas above 100 Pa, continuum conductive heat transfer per unit area $Q_{N,N-1}$ from plate N to plate N–1 can be calculated using the following equation that comes from integrating Equation 9 from T_{N-1} to T_N:

$$Q_{N,N-1} = 2.32 \times 10^{-3} \frac{[T_N^{1.65} - T_{N-1}^{1.65}]}{S_N} \tag{10}$$

where S_N is the distance from the plate N at a temperature T_N to plate N–1 at a temperature T_{N-1}.

Gas Conduction in the Transition Region

Heat conduction through gas in the transition region may be obtained by extrapolation from either the continuum region or free molecular region. Lees' linearized four moment Maxwell molecule model[5] approaches the problem from the free molecular end (Kn > 10). Experimental measurements taken by Teagan and Springer were found to agree favorably with the Lees' four moment model[6]. The ratio of transition region heat flow to free molecular heat flow Q_T/Q_{FM} using the Lees' four moment model can be stated as follows:

$$\frac{Q_T}{Q_{FM}} = \frac{\Xi\ Kn\,(2/\alpha - 1)}{1 + \Xi\ Kn\,(2/\alpha - 1)} \tag{11}$$

where Q_T is the heat flow per unit area between the plates in the transition region; Q_{FM} is the heat transfer per unit area between the plates if the heat flow is assumed to be in the free molecule region; Ξ is a fitting parameter. Lees in his paper proposed that $\Xi = 3.166$, but Ξ may have another value that makes the solution fit better at both ends. (In our case $\Xi = 1.8$ makes the fit much better.) One can make a strong case for Ξ being temperature dependent. Kn is the Knudsen number; and α is the average accommodation coefficient between the plates. It is interesting to note that if the fitting parameter Ξ is properly chosen, Q_T will equal $Q_{N,N-1}$ given by Equation 10 when the Knudsen number is small. Regardless of the value of Ξ, the value of Q_T calculated using Equation 11 will equal $Q_{N,N-1}$ calculated using Equation 6 when the Knudsen number is large.

COMBINED RADIATION AND CONDUCTION HEAT TRANSFER

Combined Heat Transfer in the Free Molecule and Transition Regimes

The heat flow through a stack of multilayer insulation can be approximated using a radiation heat transfer term plus a free molecular gas heat transfer term provided Kn >10. Heat transfer through a stack of multilayer insulation can be approximated as follows:

$$Q_{RF} = \frac{H(T_m) - H(T_o)}{m} \tag{12}$$

where Q_{RF} is the combined heat transfer through multilayer insulation that has an upper stack temperature of T_m and a lower stack temperature of T_o. There are m

layers of multilayer insulation in the stack. The values of $H(T_m)$ and $H(T_o)$ are defined as follows:

$$H(T_m) = E(T_m)\,T_m^4 + G(T_m,P)\,T_m \tag{13a}$$

and

$$H(T_o) = E(T_o)\,T_o^4 + G(T_o,P)\,T_o \tag{13b}$$

where E is the radiation heat transfer function and G is the free molecular heat transfer function.

One can make the simplifying assumption for E and G that neither is very temperature dependent. If one assumes that E and G are temperature independent, the following expressions for E and G result:

$$E = E(T_m) = E(T_o) = \frac{\varepsilon\sigma}{2} \tag{14}$$

where ε is the emissivity of the multilayer insulation (use $\varepsilon = 0.02$); and σ is the Stefan–Bolzman constant ($\sigma = 5.67\text{x}10^{-8}$ W m^{-2} K^{-4}).

$$G(P) = G(T_m,P) = G(T_o,P) = \frac{\alpha}{2}\frac{k+1}{k-1}\left[\frac{R}{2\pi M T}\right]^{0.5} P\,\frac{Q_T}{Q_{FM}} \tag{15}$$

where α is an overall accommodation coefficient (use $\alpha = 0.14$); k is the ratio of specific heats for the gas ; R is the universal gas constant; M is the molecular weight of the gas; P is the pressure measured by a vacuum gauge looking at a plate at a temperature T. The ratio Q_T/Q_{FM} is defined by Equation 11. (The fitting parameter Ξ in Equation 11 should be about 1.8.)

When the high temperature plate is at 300 K (outside an 80 K shield), the radiation heat transfer term and the free molecular gas conduction term are of the same order when the pressure is about 0.055 Pa ($4\text{x}10^{-4}$ torr). When the high temperature plate is at 80 K and the low temperature is at 4 K (inside an 80 K shield), the radiation heat transfer term and the free molecular gas conduction term are of the same order when the pressure is about $5.5\text{x}10^{-4}$ Pa ($4\text{x}10^{-6}$ torr). Since the free molecule heat flow and radiation heat flow equal each other at a relatively low pressure inside an 80 K shield, it is clear that it is very useful to put several layers of multilayer insulation between the shield and the helium vessel to reduce the heat leak in the event that there is a small helium leak into the vacuum space between the plates.

Combined Heat Transfer in the Continuum Regime

The heat flow through a stack of multilayer insulation can be approximated using a radiation heat transfer term plus a continuum gas conduction heat transfer term provided Kn < 0.01. Heat transfer through a stack of multilayer insulation with helium in the vacuum space can be approximated as follows:

$$Q_{RC} = \frac{E(T_m)\,T_m^4 - E(T_o)\,T_o^4}{m} + 2.32 \times 10^{-3}\,\frac{[T_m^{1.65} - T_o^{1.65}]}{S_{mo}} \qquad (16)$$

where Q_{RC} is the combined heat transfer through a stack of multilayer insulation that has an upper stack temperature of T_m and a lower stack temperature of T_o. There are m layers of multilayer insulation in the stack. S_{mo} is the distance between plate at temperature T_o and the plate at temperature T_m. The values of $E(T_m)$ and $E(T_o)$ are defined by Equation 14.

The heat transfer through a stack of plates in the continuum regime is dominated strongly by the continuum gas conduction heat transfer unless the number of plates is small, the plate emissivity is large, and/or T_m is substantially above room temperature (300 K). In practical multilayer insulation systems with Kn < 0.01, the radiation term can be neglected.

A CALCULATION OF COMBINED HEAT FLOW THROUGH A STACK OF ALUMINUM PLATES

Figure 1 shows the calculated heat flow from 300 K to 4 K through 25 aluminum plates with a spacing of 1 millimeter. The heat flow calculations were made over a range of helium gas pressures from 10^{-3} Pa (7.5×10^{-6} torr) to 10^5 Pa (0.987 atm). The following constants were used to make the heat flow calculations that are shown in Figure 1: $\varepsilon = 0.02$; $\Xi = 1.8$; $T_g = 160$ K; and $\alpha = 0.14$.

From Figure 1, one can see that radiation heat transfer dominates the heat flow through the plates at pressures less than 0.01 Pa. From 0.3 Pa to 100 Pa, heat flow through the stack of plates is dominated by free molecular gas conduction. In this region the heat flow through the stack of plates is proportional to the gas pressure between the plates. Above 3000 Pa, ordinary continuum gas conduction dominates. Continuum gas conduction is independent of the pressure between the plates. The four moment transition region solution smoothly connects the free molecular gas conduction region and the continuum gas conduction region. The accuracy of the heat transfer calculation is probably at its worst in the transition region between free molecule gas conduction and continuum gas conduction (at pressures between 100 and 3000 Pa).

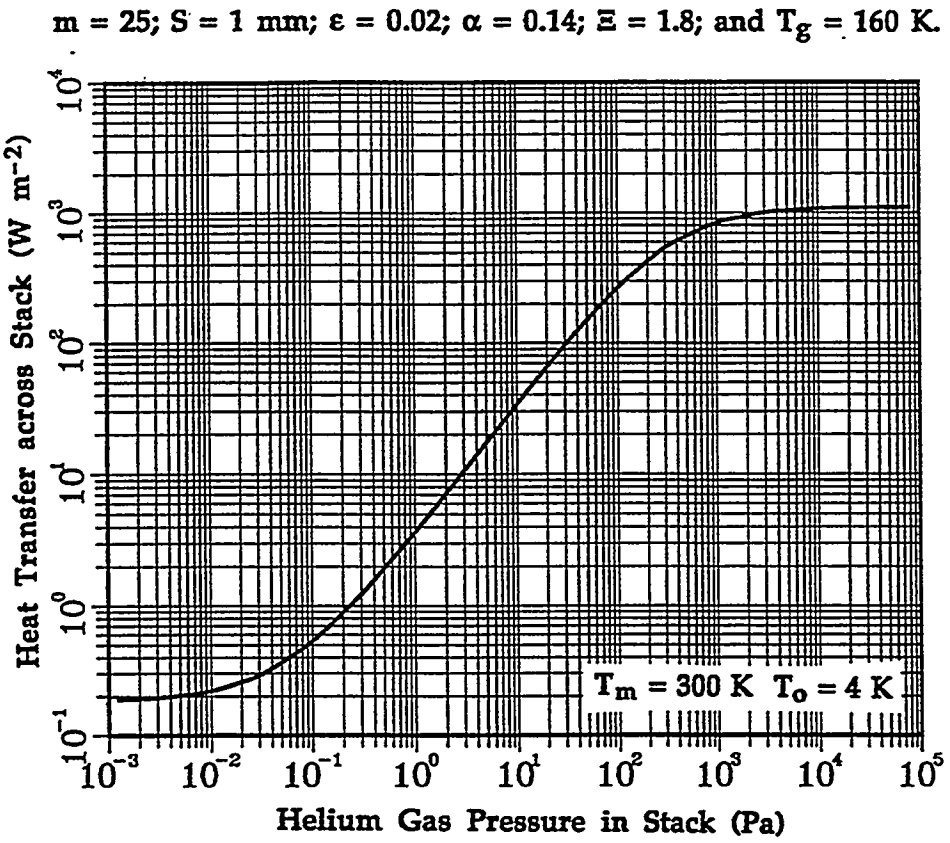

Fig. 1 The Heat Transfer Rate Across a Stack of 25 plates 1 mm Apart as a Function of the Gas Pressure Between the Plates

CONCLUSION

Heat transfer through a stack of plates in a vacuum is combination of radiation and gas conduction heat transfer. Radiation heat transfer across the stack of plates is proportional to the plate emissivity and inversely proportional to the number of plates in the stack. At pressures below 10 Pa, the gas conduction through the stack of plates is by free molecular gas conduction. Free molecular gas conduction is proportional to the gas pressure and the accommodation coefficient of the gas to the plate material. Like radiation heat transfer, the gas conductive heat transfer through the stack of plates in the free molecular regime is inversely proportional to the number of plates. In both the radiation and free molecular gas conduction regimes, more plates in the stack mean less heat is transferred. In the transition and continuum regimes, the number of plates in the stack is of less concern. In the these regimes, conduction heat transfer is controlled by the

distance between the highest temperature plate and the lowest temperature plate. A smooth transition from the free molecular region and the continuum region can occur if the fitting parameter Ξ is correctly chosen.

ACKNOWLEDGMENTS

This work is dedicated to Klaus Halbach, a mentor, a colleague, and a friend. The problem that is presented here is one that is usually solved the wrong way. This is the kind of problem that Klaus Halbach would take great delight in solving correctly. Much of the thinking and the methodology that has gone into this work comes from the way that Klaus Halbach would approach a problem of this nature. It is fitting that this paper be dedicated to Klaus Halbach on the occasion of his birthday. Happy Birthday Klaus and may there be many more opportunities for this author to learn from you.

This work was supported by the Director of the Office of Basic Energy Science, High Energy Physics Division, United States Department of Energy under contract number DE-AC03-76SF00098.

REFERENCES

1. E. M. Sparrow and R. D. Cess, Radiation Heat Transfer, p 63-74, Brooks/Cole Publishing Company, Belmont CA, (1966)

2. Handbook on Materials for Superconducting Machinery, Metals and Ceramic Center, Battelle Columbus Laboratories Data Book MCIC-HB-04, NIST Boulder, CO. 80302, Jan. 1977

3. James Jeans, An Introduction to the Kinetic Theory of Gases, Cambridge Press, (1962)

4. V. D. Arp and R. D. McCarty, "Thermophysical Properties of Helium-4 from 0.8 K to 1500 K with Pressures to 1000 MPa," NIST Tech Note 1334, November 1989

5. C. Y. Lin and L. Lees, Rarefied Gas Dynamics, p 391, Edited by L. Talbot, Academic Press, New York (1961)

6. W. P. Teagan and G. S. Springer, "Heat Transfer and Density Distribution Measurements between Parallel Plates in the Transition Regime," MIT Fluid Mechanics Laboratory Report 67-5, September 1967

REFERENCES

1. E. M. Sparrow and R. D. Cess, Radiation Heat Transfer, p 63-74, Brooks/Cole Publishing Company, Belmont CA, (1966).

2. Handbook on Materials for Superconducting Machinery, Metals and Ceramic Center, Battelle Columbus Laboratories Data Book MCIC-HB-04, NIST Boulder, CO. 80302, Jan. 1977.

3. James Jeans, An Introduction to the Kinetic Theory of Gases, Cambridge Press, (1962).

4. V. D. Arp and R. D. McCarty, "Thermophysical Properties of Helium-4 from 0.8 K to 1500 K with Pressures to 1000 MPa," NIST Tech Note 1334, November 1989.

5. C. Y. Lin and L. Lees, Rarefied Gas Dynamics, p 391, Edited by L. Talbot, Academic Press, New York (1961).

6. W. P. Teagan and G. S. Springer, "Heat Transfer and Density Distribution Measurements between Parallel Plates in the Transition Regime," MIT Fluid Mechanics Laboratory Report 67-5, September 1967.

Simple Surface Structure Determination from Fourier Transforms of Angle-Resolved Photoemission Extended Fine Structure

Yu Zheng[1,2] and D. A. Shirley[1]
[1] Departments of Chemistry and Physics, Pennsylvania State University, University Park, PA 16802
[2] Chemical Sciences Division, Lawrence Berkeley Laboratory, University of California, Berkeley, CA 94720

Abstract

We show by Fourier analyses of experimental data, with no further treatment, that the positions of *all* the strong peaks in Fourier transforms of angle-resolved photoemission extended fine structure (ARPEFS) from adsorbed surfaces can be *explicitly* predicted from a trial structure with an accuracy of about ±0.3 Å based on a single-scattering cluster model together with the concept of a strong backscattering cone, and *without any additional analysis*. This characteristic of ARPEFS Fourier transforms can be developed as a simple method for determining the structures of adsorbed surfaces to an accuracy of about ±0.1 Å.

Since its introduction by Hussain *et al.*,[1] the Fourier-transform (FT) analysis has been used as a qualitative first step in the atomic structural determination of adsorbed surfaces from angle-resolved photoemission extended fine structure (ARPEFS).[2-7] In these studies, ARPEFS-FTs were used to determine the adsorption site geometry directly. In this work we shall show how ARPEFS-FTs can be interpreted more quantitatively to determine local structures with fairly good accuracy from the transform spectra alone, with no additional data treatment.

Inspired by the work of Szöke,[8] the Fourier-transform analysis has recently been applied to obtain the real-space atomic images of adsorbed surfaces from two-dimensional fixed-energy photoelectron diffraction[9-11] data. This photoelectron holography method can determine the adsorption site geometry directly with fair accuracy.[12] More recently, two direct methods for adsorbed surface structure determinations, based on ARPEFS-FT spectra, have been proposed by Tong *et al.*[13] and Fritzsche and Woodruff,[14] and successfully tested with experimental data.[15-17] Both methods, which exploit the strong backscattering amplitude near 180°, have the attractive feature of locating a single backscattering atom in both direction and distance, through the combination of many ARPEFS-FT spectra taken from different emission directions. By extending either approach to FT peaks from other neighboring atoms, local structures could be determined to a comparable level of accuracy.

We shall discuss these methods, and compare them with similar approaches which have been considered in our laboratory, in a separate paper.

In the present work we describe another method for determining local structures simply from ARPEFS-FTs which appears to possess some advantages. We show that the positions of strong peaks in FTs of ARPEFS data from adsorbed surfaces can be predicted with an accuracy of about ±0.3 Å based on geometry alone, by using the single-scattering cluster (SSC) model together with the concept of strong backscattering from atoms located within a cone around 180° from the emission direction. This leads to a simple method for determining the adsorption sites of adsorbates, using *all* the strong peaks from a single ARPEFS-FT spectrum. The bond lengths to the nearby atoms around an adsorbate atom can be determined with an accuracy of about ±0.1 Å.

To test this simple FT method we selected ARPEFS data sets from six adsorbate systems studied earlier in this laboratory. All involved the (001) face of a bcc or fcc metal lattice, with the adsorbate atom in a fourfold hollow site and the photon polarization vector essentially collinear with the emission direction, which was chosen to be off-normal, near the [011] direction, to emphasize the surface-layer nearest atom as a backscatterer. The ARPEFS data were fast-Fourier-transformed based on the auto-regressive linear prediction (ARLP) methodology[18] to preserve, in the transform spectrum, the resolution that is inherent in ARPEFS data, but obscured by conventional fast-Fourier-transformation methods because of the finite data range. In the present work, a special ARLP method was used, with a window function that is flat over most of the ARLP-extended data range, and tapered at the ends to suppress side bands. Fig. 1 compares the ARPEFS-FTs obtained with and without the ARLP method for p(2x2)S/Cu(001), using an ARPEFS data set taken 40° off-normal toward the [011] direction and only 5° from the photon polarization direction.[7] The ARLP approach improves the apparent real-space resolution in the transform spectrum and helps distinguish real peaks. At the same time, the positions of all the strong peaks except the first one (which was resolved into two components) remained about the same to an accuracy of about ±0.1 Å. We have analyzed ARPEFS data sets from five other systems similarly. All were taken in directions 40°-45° off-normal toward [011] with the photon polarization vectors parallel or nearly parallel to the emission directions. Table 1 summaries the (strong) ARLP-FT peak positions up to 15.0 Å for the six adsorbed surfaces: c(2x2)S/Ni(001),[2] c(2x2)S/Cr(001),[3] c(2x2)S/Fe(001),[4] c(2x2)P/Fe(001),[5] c(2x2)Cl/Cu(001),[6] and p(2x2)S/Cu(001).[7]

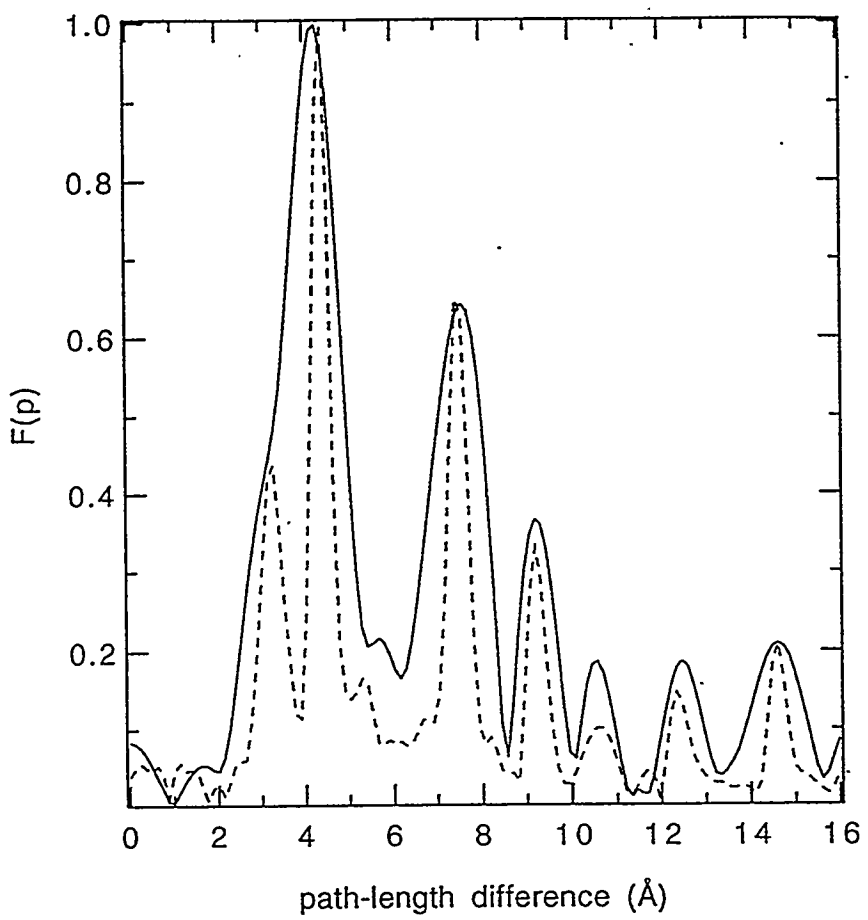

Fig. 1. Comparison of the ARPEFS Fourier transforms obtained using the conventional (solid line) and ARLP-based (dashed line) Fourier transformation methods for p(2x2)S/Cu(100).

Table 1. Summary of experimental and calculated path-length differences for six adsorbed surfaces.

surfaces		P_1(Å)	P_2(Å)	P_3(Å)	P_4(Å)	P_5(Å)	P_6(Å)	P_7(Å)
c(2x2)S/Ni(001)	Exp	3.4	4.4	7.2	9.4	12.2	14.4	
	Cal	3.1	4.4	7.5	9.4	12.2	14.4	
p(2x2)S/Cu(001)	Exp	3.2	4.4	7.5	9.2	10.5	12.4	14.5
	Cal	3.3	4.4	7.5	9.4	10.2	12.4	14.6
c(2x2)Cl/Cu(001)	Exp	2.8	4.9	7.7	10.2	12.7	14.8	
	Cal	3.6	4.8	8.0	9.9	12.9	15.1	
c(2x2)P/Fe(001)	Exp	3.8	7.5	12.0	15.5			
	Cal	4.0	7.6	11.8	15.7			
c(2x2)S/Fe(001)	Exp	4.0	7.8	12.1	15.7			
	Cal	4.1	7.6	11.8	15.7			
c(2x2)S/Cr(001)	Exp	3.9	7.7	12.1	15.5			
	Cal	4.2	7.5	11.9	15.8			

Earlier ARPEFS studies have shown[2-7] that strong peaks in ARPEFS-FTs arise from the nearest atoms and atoms almost directly "behind" the source atom, included within a "backscattering cone" around the direction opposite the emission direction. This backscattering cone is a consequence of the peaking of the electron-atom scattering amplitude around 180° in the intermediate energy range[19] and is enhanced by collinearity of the photon polarization vector and the emission direction as well as other effects.[20] Using this concept, the nearest atoms and atoms located within a backscattering cone were identified, and single-scattering path-length differences (SS-PLDs) up to 15.0 Å for each adsorbed surface were calculated according to the formula: P=r(1-cosq), where r is the bond length of a scattering atom and q is the scattering angle of the scattering atom, and listed in Table 1, using structural parameters obtained from previous ARPEFS studies.[2-7] Fig. 2 illustrates the results for p(2x2)S/Cu(001), in which the total opening angle of the backscattering cone was taken to be about 45° for Cu (the exact value selected is somewhat arbitrary: the results are fairly insensitive to the choice of the opening angle). Calculated SS-PLDs are compared to experimental values for the six adsorbed surfaces in Table 1.

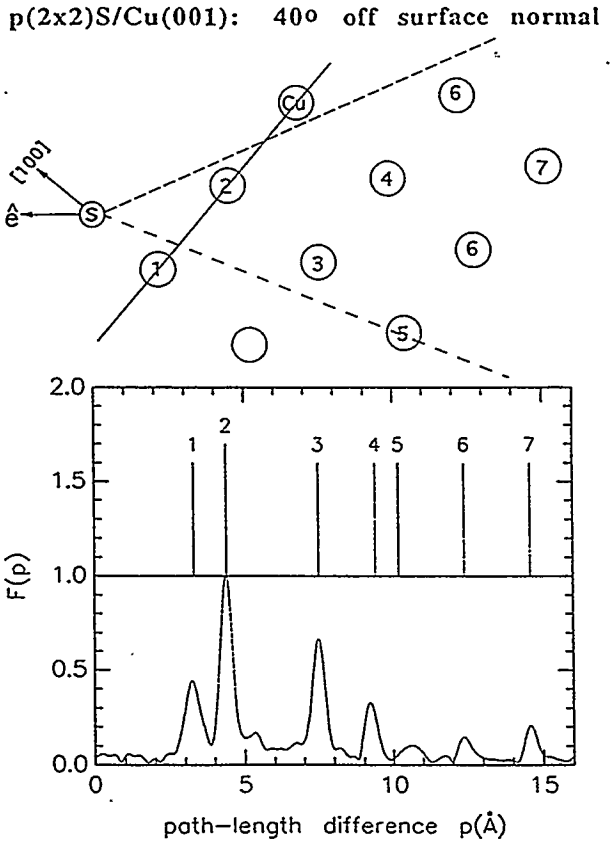

Fig. 2. Calculations of the single-scattering path-length differences for p(2x2)S/Cu(100). Note that the two dashed lines in the top panel make a backscattering cone.

The agreement is excellent: always within about ±0.3 Å, with an rms deviation of 0.2 Å for all the strong peaks except the 2.8 Å peak in c(2x2)Cl/Cu(001), which is known to be shifted by the Ramsauer-Townsend effect.[21] Thus the positions of *all* the strong peaks in all of these ARPEFS-FTs were predicted to an accuracy of about ±0.3 Å by a SSC model together with the concept of the backscattering cone. However, previous ARPEFS studies have shown[2-7] that multiple-scattering (MS) effects are important in ARPEFS. To reconcile this apparent conflict, we have examined the effects of MS on ARPEFS-FTs theoretically. We found that MS effects shift the positions of strong peaks in ARPEFS-FTs by typically less than ±0.3 Å, and do not produce additional strong peaks. In particular, MS effects basically do not shift the positions of peaks in ARPEFS-FTs in the case of exact (180°) backscattering.[22] We have also found theoretically that the positions of strong peaks in ARPEFS-FTs are more strongly affected by atomic scattering phase shifts than by MS per se. So how do we understand that MS effects are important in ARPEFS? Let us look at an example in a previous ARPEFS study,[20] in which single- and double-scattering calculated ARPEFS Chi curves were compared for a two-atom cluster. The comparison showed[20] that MS effects changed the phase and amplitude of the ARPEFS Chi curve, but basically not its frequency, which corresponds to the peak position in the ARPEFS-FT. If the single-scattering model is used to fit the double-scattering ARPEFS Chi curve, the structural parameters cannot be accurately determined due to the phase change.[23] Therefore, MS effects must be included to fit ARPEFS Chi curves in order to determine adsorbed surface structures with an accuracy of 0.01-0.02 Å.

In the above discussion the ARPEFS-FT spectra have been predicted using known adsorbate-surface structures. Several approaches could be taken to reverse this process and determine local structures simply from the ARPEFS-FT spectra. For brevity, we discuss only one method here, chosen for its simplicity. We first assume that the adsorbate-induced substrate relaxation is small, and calculate SS-PLDs for the nearest atoms and atoms located within a backscattering cone aligned along the emission direction for all the plausible adsorption sites on the unreconstructed substrate, if necessary varying the parameters through plausible ranges of adsorbate-substrate interlayer spacings. Typically only one site will give ARPEFS-FT peak positions that agree even qualitatively with experiment. If two or more are close, a second ARPEFS-FT spectrum in another direction may be needed. If none fit, reconstructed surfaces should next be considered, and the algorithm is repeated. After the adsorption site is thus qualitatively determined, the local structure around the adsorbate can then be refined by adjusting the interlayer spacing between the adsorbate layer and the first substrate layer to achieve good agreement between calculated and experimental positions of strong peaks in the ARPEFS-FT spectrum. The agreement can be described, for example, using an R-factor: $R=\Sigma(P_t-P_e)^2$, where P_t and P_e denote respectively calculated and experimental positions of strong peaks in the ARPEFS-FT

spectrum. This approach should yield a reasonably accurate structure quickly. A full multiple-scattering spherical-wave fit of the ARPEFS Chi curve or its Fourier transform is still required to obtain a very high accuracy fit, including subtle lattice reconstruction, etc.

To illustrate this method, we take p(2x2)S/Cu(001) as an example. Fig.1 shows that there are seven strong peaks, at 3.4 Å, 4.4 Å, 7.2 Å, 9.4 Å, 10.5 Å, 12.2 Å, and 14.4 Å in the ARPEFS-FT spectrum of p(2x2)S/Cu(001). There are *a priori* three plausible adsorption sites for the S adsorbate atom on the Cu(001) surface: an atop site, a bridge site, and a fourfold hollow site. Adjusting the S-Cu interlayer spacings for all the three sites to produce a dominant peak at the observed position of 4.4 Å, SS-PLDs for the nearest atoms and atoms located within the backscattering cone aligned along the emission direction were then calculated up to 15.0 Å, for the three hypothetical sites. There are six strong peaks at 4.4 Å, 6.6 Å, 8.6 Å, 9.1 Å, 11.5 Å, and 14.2 Å for the atop site, seven strong peaks at 3.2 Å, 4.4 Å, 6.7 Å, 7.4 Å, 9.3 Å, 11.7 Å, and 14.4 Å for the bridge site, and seven strong peaks at 3.2 Å, 4.4 Å, 7.6 Å, 9.5 Å, 10.2 Å, 12.5 Å, and 14.6 Å for the fourfold hollow site. It is obvious by visual inspection that only the fourfold hollow site gives acceptable agreement, but in the interest of establishing one criterion for possibly automating the selection process in the future, we note that the three sites give R-factors of 2.7, 5.3, and 0.31, respectively. This provides a strong quantitative criterion for selection, which can be readily automated.

To refine the local structure further, the R-factor was calculated for different S-Cu interlayer spacings d_{01} for the unreconstructed fourfold hollow adsorption geometry, yielding R=2.34, 1.31, 0.61, 0.40, 0.21, 0.34, 0.97, 1.91, and 3.16, respectively for d_{01}=0.9 Å, 1.0 Å, 1.1 Å, 1.2 Å, 1.3 Å, 1.4 Å, 1.5 Å, 1.6 Å, and 1.7 Å. We can infer that the S atom adsorbs at 1.3 Å above the first Cu substrate layer with the S-Cu bond length of 2.23 Å. These values agree very well with the S-Cu interlayer spacing of 1.32 Å and bond length of 2.26 Å obtained from the multiple-scattering spherical-wave data analysis[7] which includes surface reconstruction and relaxation. Similar analyses were also made for the other data sets in Table 1 and the accuracy of about ±0.1 Å has been generally obtained for the determination of the nearest adsorbate-substrate bond length.

The method described above makes very effective use of even a single ARPEFS-FT spectrum, deriving a fairly accurate local structure for simple cases such as the six examples cited here. It is, however, implicit rather than explicit in its algorithm, requiring trial structures. The extent to which it can be automated and thus turned into an explicit structural analysis remains to be determined. We are optimistic that this is feasible, especially if ARPEFS data from two or three directions are combined. Another promising approach

is to exploit the complementarity of this method with those of Tong *et al.*[13] and Fritzsche and Woodruff.[14]

In summary, we have shown that the positions of *all* the strong peaks in FTs of experimental ARPEFS data from adsorbed surfaces can be determined with an accuracy of about ±0.3 Å, using the SSC model based on the concept of the backscattering cone. This characteristic of ARPEFS-FTs can be used to develop a simple method for determining the local structures of adsorbed surfaces with an accuracy of about ±0.1 Å. This new method requires a very small amount of data and can yield reasonably accurate structural information.

YZ thanks the Pennsylvania State University for financial support, and DAS thanks the Alexander von Humboldt Foundation for support during 1989-90, when the early work on this method was carried out. This work was supported by the Director, Office of Energy Research, Office of Basic Energy Sciences, Chemical Sciences Division of the U. S. Department of Energy under Contract No. DE-AC03-76SF00098. The experiments were performed at the Stanford Synchrotron Radiation Laboratory and the Brookhaven National Light Source, which are supported by the U. S. Department of Energy's Office of Basic Energy Sciences.

References

1. Z. Hussain *et al.*, Proc. Natl. Acad. Sci. USA 78, 5293 (1981).
2. J. J. Barton *et al.*, Phys. Rev. B34, 3807 (1986).
3. L. J. Terminello *et al.*, Phys. Rev. B38, 3879 (1988).
4. X. S. Zhang *et al.*, J. Chem. Phys. 89, 6538 (1988).
5. X. S. Zhang *et al.*, unpublished.
6. L. Q. Wang *et al.*, Phys. Rev. B44, 1292 (1991).
7. A. E. Schach von Wittenau *et al.*, Phys. Rev. B45, 13614 (1992).
8. A. Szöke, in *Short Wavelength Coherent Radiation: Generation and Application*, edited by D. T. Attwood and J. Boker, AIP Conf. Proc. No. 147 (American Institute of Physics, New York, 1986).
9. J. J. Barton, Phys. Rev. Lett. 61, 1356 (1988).
10. C. M. Wei *et al.*, Phys. Rev. Lett 65, 2278 (1990).
11. G. R. Harp *et al.*, Phys. Rev. B42, 9199 (1990).
12. S. Thevuthasan *et al.*, Phys. Rev. Lett 70, 595 (1993).
13. Tong *et al.*, Phys. Rev. B46, 2452 (1992).
14. V. Fritzsche and D. P. Woodruff, Phys. Rev. B46, 16128 (1992).
15. J. G. Tobin *et al.*, Phys. Rev. Lett 70, 4150 (1993).
16. H. Wu *et al.*, Phys. Rev. Lett 71, 251 (1993).
17. K. M. Schindler *et al.*, Phys. Rev. Lett 71, 2054 (1993).

18. J. Barton, Ph.D. thesis, University of California, Berkeley, 1985.
19. P. J. Orders and C. S. Fadley, Phys. Rev. B27, 781 (1983).
20. J. Barton *et al.*, Phys. Rev. B34, 778 (1986).
21. J. Barton *et al.*, Phys. Rev. B35, 933 (1987).
22. Y. Zheng and D. A. Shirley, Chem. Phys. Lett. 203, 114 (1993).
23. Y. Zheng, Phys. Rev. B37, 9083 (1988).

Dave Shirley

Recollections of Klaus Halbach at LBL

David A. Shirley

My earliest encounters with the fruits of Klaus Halbach's ideas came in 1980, during my first year as Director of LBL. I had an abiding interest in synchrotron radiation, and had participated in the 1976 National Academy of Sciences report on the national need for dedicated synchrotron radiation facilities. The committee had struggled mightily to analyze and understand the best configuration for producing the brightest practical light sources based on electron storage rings. The principles of magnetic insertion devices such as wigglers and undulators were known, but no convincing technology was available for producing magnetic fields of the required homogeneity, combined with sufficient field strength, on a small enough length scale. The final report therefore recommended the construction of "second generation" storage rings (NSLS, Aladdin), designed to produce synchrotron radiation in bend magnets.

Klaus Halbach changed all this at the end of the 1970s, with his paradigm of permanent-magnet insertion devices. He showed that permanent magnets would outperform superconducting magnets or electromagnets in the short wavelength limit, and he also showed that structures based on materials such as $SmCo_5$ could be used as practical, high-performance undulators. By staying close to the design and manufacturing processes, Klaus was rewarded in 1980 with seeing a permanent-magnet undulator constructed at LBL for use at SSRL. My encounter referred to above occurred when this undulator went out the door at LBL, and I realized that a new technology had been born. To keep this process moving, we developed a collaboration with SSRL and Exxon which led to the famous 54-pole wiggler featured on the cover of Physics Today in July 1983. By that time Berkeley's Advanced Light Source, the prototype third-generation storage ring, was on the drawing board, to be followed by many more around the world.

So Klaus is the father of the permanent-magnet undulator, which in turn made third-generation rings feasible. But that's not all. Throughout the 1980s and beyond, he defined the frontier of this field with one good idea after another. Indeed, for a while a laboratory building its first such undulator did not feel comfortable going ahead until its design passed the "Halbach test," and indeed Klaus was able to point out design flaws in several cases.

Rarely does a single individual make such a distinctive, and clearly recognized contribution to a field that is so dependent on teamwork. That Klaus Halbach is so far ahead of the curve is reason enough for this Festschrift.

SOS and the Eternal Struggle for Human Rights

Andrew M. Sessler and Morris Pripstein

"How", you may ask, Klaus, "has an article on human rights gotten into this volume?" Clearly we could rather easily have written a technical article. (Just in the last ten years one of us [AMS] has been a co-author of 135 scientific papers; one more wouldn't have been that difficult.) But, instead, we thought it most appropriate, after all, you have long been interested in human rights, to tell about our experiences, which occurred during a decade of very active involvement, in the human rights struggle. We realize that the struggle for human rights is never ending, and we still are active to a certain degree, but our time of major activity was limited to a decade; you must recall that our principal profession is physics.

Perhaps both of us, and also the people we worked with, believed as Thomas Jefferson has said, "I have sworn upon the altar of God, eternal hostility against all forms of tyranny over the mind of man." When we saw what was being done by the Former Soviet Union (FSU) during those very dark years from (about) 1970 to 1986, we were so outraged that we became—we couldn't help becoming—active. Just how we did that, and how others joined us, and the ultimate success we had, is what we would like to chronicle here. Our story should be of interest to you—you lived through those times—and for younger people it may serve as an example, showing how active research physicists sacrificed a paper or two, but believed—still believe—that the time was more than well-spent; maybe, even, history will call it "their finest hour."

We formed, with others who were primarily at LBL, the international organization called Scientists for Sakharov, Orlov, Sharansky (SOS). Our focus was on these three, but our interest, and goal, was to improve the situation in the FSU for many more. Thus it was a tactical choice, and we think the right one, to focus on three, attempt to make widely known what was being done to them, to make their names "household words." Let us, then, to "set the stage," very briefly chronicle the harassment history of these three.

I. THE THREE

Surely the best known was Andrei Sakharov, an extraordinary physicist, "father of the Soviet hydrogen bomb" and one of the first to realize the dangers of atmospheric atomic tests. He spoke to Khruschev about this danger, starting in 1961, and therefore was instrumental in developing the Partial Test Ban Treaty, between Kennedy and Khruschev, in 1963. He was the author of the essay on Peaceful Co-existence in 1968, which brought him international recognition and Soviet wrath. He was awarded the Nobel Peace Prize in 1975, but wasn't allowed by the Soviet authorities to attend the ceremonies. In 1980 he protested the invasion of Afghanistan and was exiled to Gorky. While there he engaged in a 17 day

hunger strike to allow his daughter-in-law, Alisa Alexeyeva, to join her husband in the USA. He engaged in hunger strikes in 1984 and in 1985 to allow his second wife, Luisa (married in 1971) to go to Italy and the USA for various medical treatments. He was released, in December 1986 by Gorbachev, and allowed to return to Moscow.

Yuri Orlov, also a physicist, is in fact an accelerator physicist and known to AMS, for they had met, before his difficulties, on a number of occasions. He was noticed by the KGB (possibly for the first time) in 1973, when the first persecution of Sakharov began and Orlov supported Sakharov. In 1976 Orlov formed the first Helsinki Watch Group, this one in Moscow, but by the very next year there were groups in Poland and Czechoslovakia, and soon they existed in many countries. These Groups were designed to monitor the progress on human rights made by nations that had signed, in 1975, the Helsinki Accords in which they promised just that. The Soviets arrested Orlov in February 1977, interrogated him for more than a year, and brought him to trial in May 1978 at which he was sentenced to 7 + 5; i.e., 7 years of prison and 5 years of internal exile. After years of torture cells and prison life, in 1984 he was transferred to Sagar, Kolyai District (near the Arctic Circle). He was released in September 1986 and sent to USA.

Natan Sharansky, a computer expert, was little known before his problems, but he became the rallying cry for Jews through out the world. He was arrested in March 1977 at the age of 29. His wife, Avital, left the Soviet Union, one day after their marriage, in 1974. He was tried in July 1978 after extensive (16 months) of interrogation and sentenced to 13 years in jail. His wife worked ceaselessly, in the West, for his release, and he was released, in a prisoner exchange, in January 1986.

II. THE START OF SOS

Perhaps our first action was precipitated by Orlov's arrest. Within hours we had news of that event, transmitted by a physicist in Germany, and within a few days we had a petition, protesting this action, signed by more than 100 scientists throughout the world.

In the Spring of 1978 we, and Denis Keefe, who is no longer with us, in response to the ever-worsening situation in the Soviet Union, formed a group at LBL called Scientists for Orlov and Sharansky (SOS).* Later, in 1980, this group evolved into the international organization known as Scientists for Sakharov, Orlov and Sharansky, still keeping the acronym SOS.

Our first major public initiative occurred in July 1978 during the Sharansky trial in Moscow. We invited Avital Sharansky, then living in Israel, to come to the United States and meet with scientists from around the country so as to galvanize support for her husband. This was financially problematical, as we had no money, but we charged the expenses to our personal

* The "inner circle" consisted of Owen Chamberlain, Paul Flory (Stanford), George Gidal, Gerson Goldhaber, Kurt Gottfried (Cornell), J. David Jackson, Joseph Weizenbaum (MIT), and the three of us. Later we were joined by Michael Chanowitz and Robert Cahn.

credit cards, hoping to eventually be reimbursed by our colleagues, as in fact, turned out to be the case.

Locally, we organized a highly successful rally on the Berkeley Campus, which included the folk singer Joan Baez, as well as Avital Sharansky. There were 5,000 people in attendance, making it the largest rally there since the end of the Vietnam War. Even more remarkable was that this large turn-out occurred during the summer when most students are not in Berkeley. Our speeches in defense of human rights, and most importantly the elegant and poignant speech by Avital Sharansky, brought many a tear to the eyes in the audience and produced many volunteers for future efforts.

III. SOS

Spurred on by the enthusiastic response to our first venture we embarked, with much misgiving and much discussion, for it is so against the scientific tradition, on a moratorium on scientific exchange between individual American scientists and the Soviet Union. We viewed this as a protest of the blatant mistreatment of our Soviet colleagues by the Soviet authorities. In an action unprecedented during peacetime, more than 2,400 American scientists signed the moratorium pledges. Many of the signatories had previously been in the vanguard of promoting exchanges between the two scientific communities. Of course we made good play of this action, having a press conference in Washington in February, 1979.

We believed, as we said at that press conference, "that scientists and engineers—acting as individuals—can have considerable influence upon the Soviet Union. The direct action, as evidenced by the many who have signed the SOS petitions, will have an effect, for clearly the Soviets need international scientific cooperation to achieve and maintain first-rate science and technology. Thus by our activities, we expect to eventually achieve the release of Orlov and Sharansky and, more generally, modify the Soviet Government attitudes and actions against those Soviet citizens who are doing no more than exercising their God-given human rights."

Reaction from the Soviet Union was swift and strong. Within weeks, we received a smuggled letter from Andrei Sakharov and Naum Meiman, written on behalf of many dissidents, strongly praising our actions. At the same time we were denounced in the Soviet media, both on Moscow radio news and in a rather long article in Pravda.

Further repression of human rights within the Soviet Union accompanied their invasion of Afghanistan in 1980. It was at this time that Andrei Sakharov was exiled to Gorky. We, in SOS, escalated our activities and organized a worldwide moratorium of scientific exchange. This resulted in 7,900 scientists in 44 countries committing themselves, on behalf of their beleaguered Soviet colleagues, to this severe course of action.

During this period we worked actively to change the venue of international conferences scheduled for the Soviet Union. And we worked on American scientists, if they planned to attend conferences in the Soviet Union, by writing letters to each of them. (We had a mole within the Washington bureaucracy who sent us lists of such scientists.) We also adopted

the strategy of publicly protesting visits to the U.S. of prominent Soviet scientists who had led campaigns of vilification against Sakharov and other dissidents. On several occasions we established picket lines on the streets outside the meetings where the Soviet scientists were to appear. The media was generous in reporting our activities and we responded with appropriate statements like calling a Nobelist, "a great scientist, but a lousy human being." Remarks like that went all the way back to Moscow.

Still another action was taken by us in 1984. Elena Bonner desired to travel to the West for medical reasons, but the Soviet authorities would not let her go alleging that she would use this occasion to vilify and embarrass the Soviet Union. We decided to challenge the literal excuse of the Soviet authorities by organizing a hostage exchange program for the release of Mrs. Bonner. Our scheme was that Western scientists, of great repute, would go there two at a time, each for a week or two, while Mrs. Bonner was in the West. They would be "good-faith witnesses" to guarantee that Mrs. Bonner's trip would be solely for medical purposes. It wasn't hard to recruit 55 prominent scientists, despite the danger involved, and—as you can imagine— the media "ate it up." Probably the laughter did some good, for a year later Mrs. Bonner did travel to the West for medical purposes (and did not use the occasion to make propaganda).

One should note the persistence of SOS; it didn't just do one thing and then go away. It kept, and we know this was to the Soviet Government's surprise and distress, being ever-more active and, of course, maintaining—and attempting to extend—its moratorium. We believe this persistence was very important.

In January 1986, Sharansky was released, in September 1986 Orlov was released, and in December 1986 Sakharov was allowed to go back to Moscow. As everyone knows, within a brief time all the dissidents in the Soviet gulag were out. On a personal note, we had the pleasure of entertaining each of the S, O, and S in Berkeley. And with that, SOS "closed up shop."

IV. THE PRESENT

Human rights require, as we noted in our title, an eternal struggle. SOS did its job and now no longer exists, but unhappy actions goes on against people in many different parts of the world. Other organizations such as the AAAS Committee on Human Rights, the NAS Committee on Human Rights, the Committee of Concerned Scientists, the Campaigns for Human Rights, and the APS Committee on the International Freedom of Scientists, are groups within the scientific establishment, that carry on the struggle. And, of course, there are many organizations, not just consisting of scientists, such as Asia Watch, the Committee to End the Chinese Gulag, and Amnesty International, just to name a few, that work hard for human rights. We like to think that many physicists look up, on occasion, from their laboratory bench or computer screen, see that all is not well with this world, and devote some time, effort, and money to working with some of the above groups. The opportunities are there, and the need is there, for the struggle for human rights is an eternal one.

ACKNOWLEDGMENTS

It is impossible for us to thank all of whom contributed to SOS. Some signed—and honored—a pledge, some gave money, some gave time—and effort—and some did all three things. To all of them we owe our thanks, and that we do not list their names they will understand, for they didn't do what they did for glory, recognition, or fame, but rather because they could do nothing else.

Some Ideas on the Choice of Designs and Materials for Cooled Mirrors

M. R. Howells
Advanced Light Source, Lawrence Berkeley Laboratory,
University of California, Berkeley, CA 94720

1.0. Introduction

It is a pleasure to join in this celebration of the achievements of Klaus Halbach and to record my personal gratitude to him for the many insights I have gained both via his written and spoken presentations and through personal contacts. I am happy to contribute a section to this book which I believe will be a very unusual document. It offers some special opportunities to write in a more subjective and speculative way than do the conventional avenues of scientific publication and I plan to take advantage of that to express some of my views on how the fabrication of future synchrotron beam-line optics ought to be approached.

Many of the most interesting new ideas for beam-line mirrors, especially those with a promise of low costs, involve metals. Historically these materials had posed certain problems, but these have been overcome in recent times[1] to the extent that the initial complement of Advanced-Light-Source (ALS) beam-line optics were made of metal and have met their specifications. To go further along that road we need to get more interested in the metallurgical issues involved in making high-quality metal mirrors. I will recount the results of some of my investigations into these materials questions and will try to draw on some of the experiences and achievements of other communities which have hitherto had only limited contact with synchrotron radiation researchers.

Most of the directly cooled mirrors used in synchrotron beam lines have fairly simple designs based on cooling channels of *uniform* cross section. These are sufficient for many purposes as we shall see but for the most challenging heat loads a more sophisticated type of design, the cellular-pin-post system[2] employing a very complex coolant flow path, has been developed. We will return to the cellular-pin-post system later but first we consider the theoretical description and analysis of a simpler mirror with uniform cooling channels.

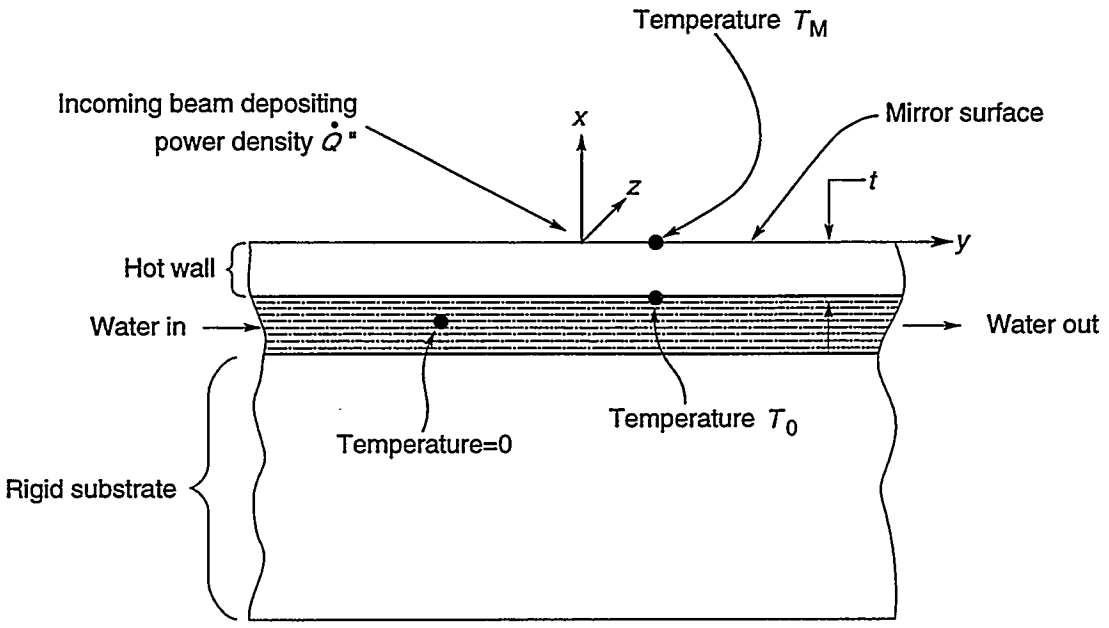
Temperature T_M
Incoming beam depositing
power density $\dot{Q}''$
x
z
Mirror surface
t
y
Hot wall
Water in
Water out
Temperature=0
Temperature T_0
Rigid substrate

Fig. 1.

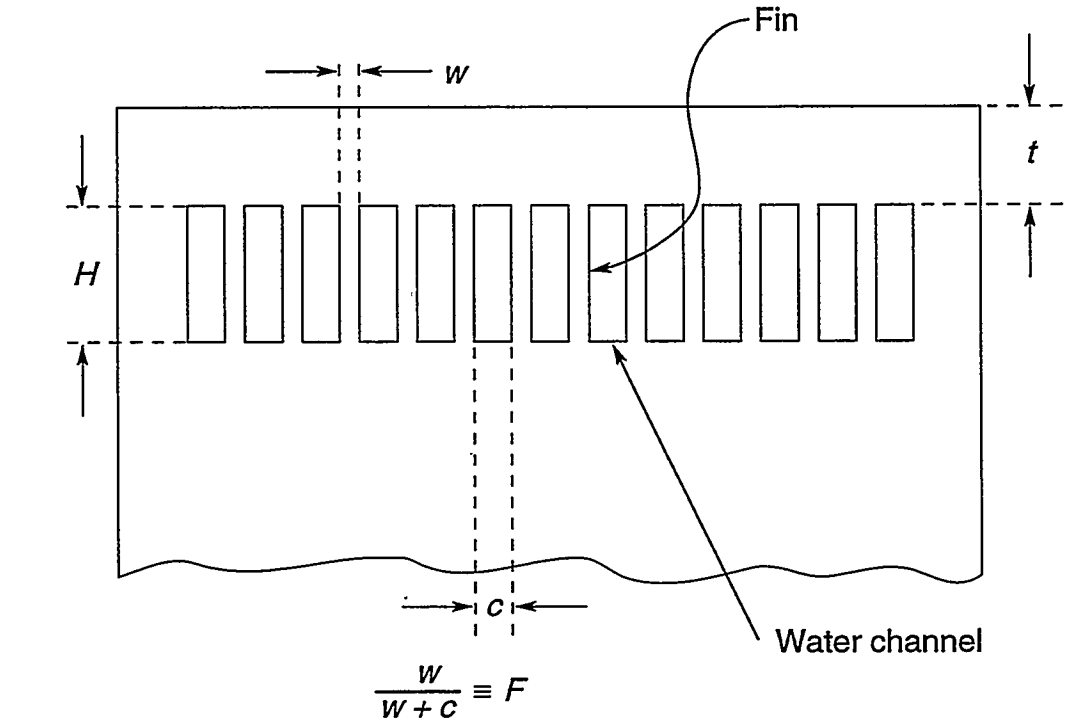
Fin
w
t
H
c
Water channel
$\frac{w}{w+c} \equiv F$

Fig. 2.

2.0. Theoretical analysis

The basic layout that we will consider for cooling a heated surface is a layer of identical side-by-side cooling channels below the surface as shown in Figs. 1 and 2. There is a thin, flexible layer of material above the water channels (the "hot wall") which has a temperature gradient across it. Underneath the water channels is a large thick block; the main mirror substrate, which has a much greater stiffness (thickness) than the hot wall. The principle of the design is to remove all the incoming heat via the water so that the whole lower substrate should be at a uniform temperature close to that of the water. With this type of design the gross bending can be reduced as much as desired by increasing the ratio of the thickness of the main substrate to that of the hot wall. The most important distortion is therefore the swelling of the mirror perpendicular to its surface which "maps" the shape of the incoming power distribution. This distortion has been calculated using simple heat-transfer theory by the present author and was reported in detail in an earlier paper[3]. Only the general trends and insights provided by that calculation will be presented here. Later we will try to use the understanding provided by the theoretical analysis as a guide in developing mirror designs and in choosing substrate materials.

Following the arrival of an absorbed power density $\dot{Q}''(y,z)$, heat will flow from the top surface of the mirror to the water with a conductive temperature drop across the hot wall and a convective temperature drop across the solid-water interface. These are determined by a conductivity, k, and a convective heat transfer coefficient, h (defined as the rate of heat flow per unit area per unit temperature drop). For a mirror made of a good conductor, the temperature drop across the coolant interface usually dominates and we speak of convection-limited heat flow. Conversely, for poor conductors, we expect conduction-limited heat flow.

To make a quantitative analysis we assume the coolant geometry shown in Fig. 2 which is easy to manufacture, close to optimum in performance and amenable to calculation. The hot-wall thickness should be enough to provide mechanical strength to resist the forces due to polishing and water pressure. We consider the rectangular segments of mirror material between the water channels to be "cooling fins" for the hot wall. The properties of such structures have long been analyzed in the engineering literature[4, 5]. For suitably good conductors, a fin can remove much more power per unit area per unit temperature difference (relative to the water) than can a direct solid-water interface.

We assume that the hot wall is restrained in two dimensions, the length and width directions of the mirror, and is unrestrained in the thickness direction while the fins are restrained in only one dimension, their length. This can be accounted for by defining two

new expansion coefficients $\alpha_1 = \alpha(1+\nu)$ for the fins and $\alpha_2 = \alpha(1+\nu)/(1-\nu)$ for the hot wall, where ν is Poisson's ratio. For a given water-flow rate one can calculate h and thence, via the standard analysis of fins[5], obtain the temperature distribution[3]

$$T_0 = \frac{\dot{Q}''}{h\left[\frac{2FH\eta_f}{w} + 1 - F\right]} \tag{1}$$

where we have used a fin efficiency factor $\eta_f = \tanh(mH)/mH$ with $m = \sqrt{2h/kw}$ and the rest of the notation is given in Figs. 1 and 2. The surface-height error is then

$$x(y,z) = \dot{Q}''(y,z)\left\{\frac{\frac{\alpha_1}{h}H\eta_f + \frac{\alpha_2}{h}t}{\frac{2FH\eta_f}{w} + 1 - F} + \frac{\alpha_2}{k}\frac{t^2}{2}\right\}. \tag{2}$$

Equation (2) represents our analysis of the "mapping" distortion of the mirror. We may summarize it as $x = A\dot{Q}''$ in which case the quantity A, the height error per unit power density is a measure of the goodness of the cooling and is known in some communities as the "worm factor". The first term in the brackets describes the growth in the length of the fins. The second term describes the growth in thickness of the hot wall due to the rise in the temperature of the fin-hot-wall interface resulting from the convective heat transfer. The third term describes the growth in thickness of the hot wall due to its conductive top-to-bottom temperature difference (ΔT_{0M}). The two h terms will dominate for convection-limited heat flow and the k term for conduction limited heat flow.

The significance of the so-called "distortion figure of merit" k/α becomes clearer. It determines (via the third term of equation (2)) the growth of the hot wall thickness due to its conductive temperature drop which is the main effect in conduction-limited heat flow. On the other hand the importance of α /h in determining the size of the first two terms which dominate in convection-limited heat flow is also evident. Thus k/α is not a true, simple figure of merit in this situation. In a mirror made of glidcop, for example, the last term, which contains k/α, is likely to account for only a few per cent of the total distortion.

In Ref. 3 the above theory was applied to an example glidcop mirror design with a 2-mm hot wall and both channels and fins having a 1×6 mm^2 cross section. The x-ray source was a ESRF wiggler which deposited a power density of 0.46 W/mm^2 at the mirror. The following conclusions could be made:

- Even in such a high powered beam, the slope errors were in the arc-second or sub-arc-second range for all the materials considered so that this type of design is useful.
- The slope errors were best for invar, silicon carbide and silicon. They were good for molybdenum and beryllium and only fair for glidcop, aluminum and stainless steel. Fused silica had to be ruled out because of excessively high surface temperatures.
- Both the temperature and height values obtained from equations (3) and (4) agreed with those from finite-element calculations using the RASNA code within less than 5 per cent.
- For stainless steel, invar and fused silica the heat flow was conduction-limited, for the other materials it was convection-limited.
- If the materials are placed in slope-error order of merit, they are with few exceptions in *inverse order* of ease of fabrication and general convenience.

We do not wish to concentrate on the details of these calculations which are covered fully in Ref. 3. Rather we wish to explore the consequences of the insights that the theory provides for mirror design and for materials choices.

3.0. Cooling channel design considerations

The optimum design of the fin structure depends on whether the heat flow is conduction- or convection-limited as indicated by the values of the thermal resistances $\theta_h = T_0 / \dot{Q}''$ and $\theta_k = t/k$. For conduction-limited cases it is less important to have good fin design, in fact the fin advantage tends to disappear in such cases, but it is very important to have a thin hot wall both for better slope errors and lower temperatures. To the extent that the lower conductivity materials are useful, this is the key to using them. To have a thin hot wall it is also necessary to keep the channel width small enough compared to the hot wall thickness to avoid "print through" of the underlying structures but for materials like steel it should be quite practical to use 0.5-1 mm walls with appropriate care. The thin hot wall is especially significant for invar because the reduction of the mirror surface temperature prevents a growth in the expansion coefficient in addition to the other effects. On the other hand for convection-limited cases the hot-wall thickness is less important than good fin design. This essentially means increasing the effective area of the solid/water interface which implies enlarging the *number* of fins which again means narrow fins and channels. A limit to this is set by the desire to maintain turbulent flow at the available water pressure. Some examples of parameters for reasonable design scenarios are given in Ref. 3.

We need to consider where the ultimate limits lie in the most challenging cases. They break down into two major categories: (i) extreme heat loads where there is a difficulty to keep the mirror surface at a safe temperature and the coolant interface below boiling temperature (an example is the first mirror of the ALS infrared beam line) and (ii) extreme surface tolerances (an example would be a projection x-ray lithography imaging mirror). For case (i) where distortion is secondary, the design will have the smallest possible grazing angle and the largest number of channels one can manufacture. The material choice will be based on high conductivity and perhaps microyield stress and glidcop would be a leading candidate. This then puts the onus on providing sufficient water pressure to achieve enough flow speed to get the required h value (h is proportional to $(\text{speed})^{0.8}$). The pressure drop needed for a given h is proportional to the flow distance through the mirror so that even after we have assigned the highest pressure drop we can, we still have one final recourse which is to make the flow distance through the fin system *short*. This was the strategy of Tuckerman[6] and for many synchrotron radiation mirrors the beam footprint is narrow in one direction so a flow distance of a centimeter or two is often possible. An even better approach to this kind of extreme heat load would probably be a cellular-pin-post design[2] (see section 4.3) in glidcop.

For case (ii), where distortion is the pre-eminent consideration, we need to minimize α/h for convection-limited and α/k for conduction-limited flow. Thus, considering only the thermal parameters α and α/k, we find that invar (carefully processed as described later), silicon and silicon carbide become the leading candidate materials.

4.0. Choice of mirror material

4.1. *General principles and overview*

The question of choosing a mirror (or grating) substrate material is one of the most difficult and controversial of all the steps involved in planning a beamline. The issues have to be evaluated in the context of the prevailing requirements and tolerances but they are roughly as follows:

- Polishing: can a good optical figure and finish be obtained?
- Cooling: can a good thermal design be made?
- Engineering: can one design and fabricate the mirror to suite beam-line constraints?

- Material quality: can the material be obtained in the required quality and size and will it hold its shape over long times?
- Cost: is it within budget?

We now discuss some candidate materials in the light of these questions.

4.2. *Silicon carbide*

Recognition of the x-ray-beam-power problem in the 1970's lead some members of the community to the notion of silicon carbide mirrors[7] which had originally been proposed in 1976 by Choyke[8]. In those days the prevailing material in use was glass, particularly fused silica, and it is certainly true, as we have seen, that the low thermal conductivity of glass is a fatal disadvantage for high-power applications. Once the idea of a silicon-carbide solution became known it gained momentum rapidly and has been favored in one way or another by most of the synchrotron-radiation laboratories. We will consider the trade-offs involved in using silicon carbide in some detail mainly to show that it has not provided and still does not promise a credible pathway to building the most challenging mirrors for the beam lines of the present day and the near future. What it has done, in essence, is to provide a way to extend the design style associated with glass optics from low power to medium power radiation beams. We believe that this is not an adequate return on the large integrated investment that the community has now made in silicon-carbide mirrors and that it is time to recognize that this approach to beam-line optics is being overtaken by events.

Most of the bulk silicon carbide available today is made by sintering and/or hot pressing powders of silicon carbide leading to the sintered-α and hot-pressed forms of the material which are less than 100% dense. Another type known as reaction-bonded silicon carbide is made by isostatically pressing fine mixtures of silicon carbide and graphite powders which are then siliconized in a furnace. Being 100% dense and fairly inexpensive, this material is of particular interest for ultrahigh vacuum components. It has been supplied to the synchrotron radiation community for example by British Nuclear Fuels[9] as Refel and Carborundum Company[10] as KT. The material has about a 10% excess of silicon which is non-uniformly distributed and this seems to have prevented the raw material from being used directly to make superpolished optical surfaces[11]. The type of silicon carbide with the best optical properties (high uniformity, 100% density, small grain size) is the chemical-vapor-deposited (CVD) material which can be coated on a suitable substrate by pyrolysis of methyltrichlorosilane in an excess of hydrogen in a low-pressure CVD reactor[12]. The rate of deposition is slow, generally less than 0.1 mm/hour, so thick coatings are difficult and expensive. They are also prone to excessive stresses. The group at Morton International[13]

have produced some of the largest pieces of optical-grade silicon carbide and have made extensive measurements to characterize the material[14, 15].

For making mirrors, the preferred approach is normally to coat a fairly thin CVD layer on a substrate of one of the other forms of silicon carbide or graphite[16]. The advantages of silicon carbide for beam-line mirrors are:

- good values of k and α,
- capability to be polished to a good finish,
- chemical inertness sufficient to allow acid cleaning in the event of hydrocarbon contamination,
- high specific stiffness.

Some of these advantages are lost if a graphite substrate is used. There are also a number of disadvantages to be concerned about. Optical-grade CVD silicon carbide is still a research and development material which is specially made for each application. Its physical properties are sensitive to many production parameters[15, 17] and are not yet repeatably measured[3]. Only a few laboratories can make optical CVD material and the number that can make large (hard-x-ray-mirror-sized) pieces in reliable quality is even smaller. The extreme hardness of silicon carbide (about Moh 9.5) which is advantageous for resisting handling damage is a major disadvantage in working the material which becomes limited to specialists. Even more serious is the fact that the use of internal cooling of CVD-coated-substrates is so difficult that it appears never to have been attempted for a synchrotron-radiation optic. This has had the effect of locking out the silicon-carbide technology from the most challenging thermal problems which are specifically the ones for which it was introduced. Even the polishing step, although capable of good results, is several times slower and thus more expensive than for competing materials.

The closest so far to the technology needed for a silicon-carbide beam-line mirror with intensive cooling was a high-power laser mirror reported in 1982 by the group at the TRW company[18-20]. This was a circular mirror with a layered structure composed of plates of pure CVD silicon carbide diffusion bonded together. The circular plates had machined cooling channels and fins similar to those in Fig. 2 and were separately fed with cooling water. The scheme appeared to be adaptable to the rectangular grazing-incidence geometry, but further study would have been needed to achieve a UHV technique for coolant connections. Altogether, the prospect for a reasonably-priced beam-line mirror by this route did not look very good and it was not pursued.

Another approach to cooling silicon-carbide mirrors which has often been used on beam lines is indirect cooling of the mirror sides via cooled pressure plates. Although such schemes can extend the usefulness of simple block-shaped mirrors toward higher heat

loads, we do not believe that they are the natural way to approach the cooling problem nor that they are the way of the future. Most engineers presented with the task of removing the heat arriving at a surface would put coolant below the surface. This is what the designers of high-power laser mirrors have been doing for years and it is what the military do for "directed energy" mirrors. Thus we must ask ourselves, "if internal cooling is really the natural way to approach the problem, why is it that indirect (side) cooling is so often used at synchrotrons"?

In the opinion of this author it is a matter of the evolution and the commercial availability of the technical capabilities for making high-power beam-line mirrors. There is an interesting parallel with the cooling of electronic circuits. For the earliest semiconductor devices, there was no need for any dedicated cooling system and heat was removed via the connecting pins. Later, cooling was applied to the board carrying the circuit and then, as the heat output increased, heat sinks and cooling clips were clamped to the devices and cooling-fin systems were added. In recent times more serious thermal engineering has been applied and for the highest-heat-flux devices (currently radio-frequency amplifiers and laser diodes) water-cooling channels have been integrated into the device package while the Pentium computer chip has internal air-cooling channels. It would appear that the synchrotron optics technology is in the middle of a similar sequence of developments where useful incremental improvements have been achieved by switching from glass to silicon carbide or (more recently) silicon and from cooling via the mirror mountings to cooling via clamp-on structures. However, as the heat loads and distortion specifications get tougher, there is an increasing necessity to apply cooling directly to the heated object (the mirror) and close to the applied heat load. This is not necessarily more expensive than the other approaches but it leads to different designs and materials (metals and silicon will be favored) and requires that the optical, mechanical and thermal aspects of the project be integrated into a single design process. Such an integrated process was behind the success of the ALS optics program[1] and a similar pattern will probably be reproduced in other places.

These changes in the way beam-line optics are built happen gradually. The industrial infrastructures and manufacturing skills that are needed to implement the evolving designs take time to get in place. At present only a few companies are able to build internally cooled synchrotron optics and indirect cooling continues to be a useful and available technique. However, it is certainly not the route to increasing ultimate performance levels and it is debatable whether it is a route to lower costs at moderate performance levels. Both of these R and D goals are best pursued in the view of this author via internal cooling schemes using less exotic materials than silicon carbide and with a

"whole-system" approach to the design. Among the ceramics, the one which is best suited to such an approach is silicon which is already replacing silicon carbide as the leading non-metallic candidate material and to this we now turn.

4.3. *Silicon*

Silicon has been a somewhat neglected material for beam-line optics in view of its excellent properties but that is now changing. Intrinsic single-crystal silicon has a thermal conductivity and expansion coefficient almost the same as silicon carbide and is readily obtained in large stress-free pieces of outstanding purity and uniformity made for the electronics industry. Moreover, there is a great deal of experience in the synchrotron-radiation community and elsewhere in cutting and shaping silicon for use in x-ray monochromators and interferometers including the use of designs with internal water cooling[21]. It is a matter of routine to fabricate internal cooling channels in silicon optics and most of the silicon mirror developments in recent years have involved much more elaborate structures. Nonetheless, published reports of the use of silicon for making mirrors are rather few[22], which is due in part to classification. It is known in the industry that first class figure and finish are obtainable in silicon but this is not yet well-documented in the open literature.

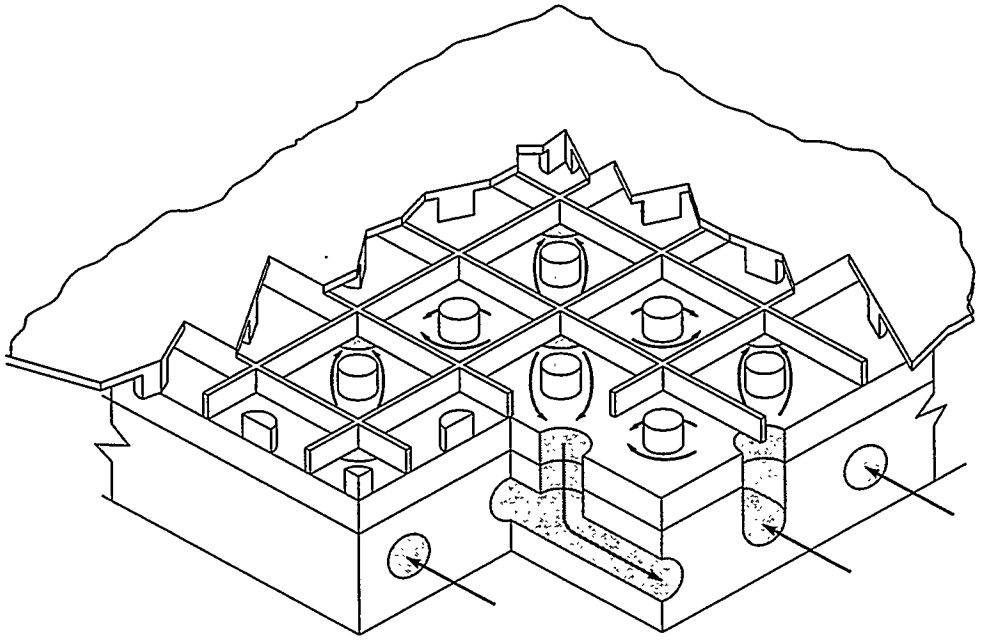

Fig. 3.

A number of major development programs for cooling high power laser mirrors were supported by the US government during the 1980's. These schemes were highly sophisticated and silicon was used in several of them. One, carried out by the group at Rockwell International [21], produced a series of silicon mirrors cooled by water in the so-called "cellular-pin-post" geometry which is explained in Fig. 3. This scheme has been adapted for use on both beamline mirrors[23] and crystals[24]. The construction consists of several silicon plates which are machined by conventional ultrasonic techniques and bonded together by means of melted glass ("frit" bonding). The design produces a rapid turbulent flow at the underside of the hot wall and heat transfer is by both the pin fins and the rectangular fins as well as directly to the underside of the wall. The key to the high performance is the flow geometry in which the water channels are narrow in the region where the coolant interacts with the hot wall and wider elsewhere. The effect is that for realistic pressures the coolant flow speed near the hot wall is as much as an order of magnitude higher than the values one can normally achieve with channels of uniform cross section. Since h varies roughly linearly with flow speed, one expects about an order of magnitude improvement in the heat transfer and this is indeed realized with overall heat transfer coefficients greater than 1 W/mm^2/°C having been achieved. These manufacturing techniques hold great promise for use with synchrotron radiation beam lines and several cellular-pin-post beam-line mirrors are at or near completion at the present time.

A different approach to cooling using silicon has been used by Tuckerman[6]. The work of this author on the cooling of silicon chips has shown that one can get very effective cooling with straight fins and channels on the order of 50 μm wide microfabricated in silicon. This moves the scheme into the laminar flow regime which has some attractions in mirror design because of "quietness" considerations. The Tuckerman designs gain an advantage in h value and maintain reasonable pressure drops by using sufficiently short flow distances. Overall heat transfer coefficients of the order of 0.1 W/mm^2/°C were achieved for nominal 1 cm flow paths. The same concept has been applied by Arthur and coworkers[21] to cooling monochromator crystals on synchrotron-radiation x-ray beam lines and a similar h value was achieved. Microchannels are less appropriate for cooling large objects like grazing-incidence mirrors although they could still be considered when the beam footprint is sufficiently narrow.

4.4. *Metals in general*

Metal optics have been used since the earliest days of reflecting telescopes. For example, in 1778, the astronomer W. Herschel polished a 16-cm-diameter telescope

objective mirror made from Molyneux's metal (71% copper, 29% tin). He used that telescope to discover Uranus and went on to try larger mirrors, some weighing hundreds of kilos, which were less successful. Nevertheless all telescope reflectors continued to be made of metal until around 1857 when an efficient process for silvering glass was discovered by Foucault[25]. In modern times, nickel-plated metal mirrors, both cooled and uncooled, adaptive and rigid, particularly of aluminum and beryllium, continue to be used for telescopes. Now they are in the form of sophisticated grazing-incidence x-ray reflectors as well as the huge objectives of modern optical telescopes (see later).

Water-cooled metal mirrors[26] have long been used for applications involving high absorbed power densities, particularly from infra-red lasers, and are available as catalog items from a number of vendors. Electroless-nickel-plated copper and molybdenum have been the most popular materials with tungsten and aluminum also used. The figure accuracy of these infra-red mirrors is often based on the needs of carbon dioxide lasers ($\lambda/4$ or $\lambda/10$ say at λ=10.6 μm) and the finish is determined by the need for a high laser damage threshold (10-30Å rms is common). Thus, although they have some of the characteristics needed for high-power synchrotron-radiation beam-lines, the surfaces of standard commercial metal mirrors have not been of sufficient quality for modern requirements. There is another level of high-power-laser-mirror technology which is much more sophisticated. Custom mirrors made by aerospace companies mostly for the military deliver very high performances. However, the high costs and the problems of classification have so far made this sector unattractive to synchrotron beamline builders.

During the period around 1980, opticians tried to achieve the higher quality figure and finish needed for beam lines using nickel-plated metal substrates. For some time these attempts were unsuccessful. Part of the reason was the low level of investment in optics by the synchrotron radiation community at that time. The technical problem, as pointed out by Becker[17], was that the electroless-nickel material, and therefore its removal rate during polishing, was not sufficiently uniform. When the best quality finishing was attempted, it was also found to have insufficiently fine grain.

This situation has been dramatically turned around by recent developments in both the production and polishing of nickel-plated surfaces. Figure accuracies in the 0.5-5 μradian range and finishes of 1-4 Å rms[1] (i. e. hardly any different than the best values for glass) are now being routinely achieved so that metal mirrors are now being made with both the accuracy and the cooling needed for the third generation light sources. Since these surfaces were worked in the plated nickel, the same success would apply to any substrate for which the nickel could be used. The properties of electroless nickel as an optical material have been reviewed by Killpatrick[27].

4.5. *Glidcop*™[28]

The Berkeley group have now made a number of glidcop optics for the Advanced Light Source beam lines which meet or exceed their optical specifications and are predicted by detailed ANSYS calculation to meet their thermal distortion specification. We regard the success of this program as well-established and well-documented. Apart from giving references, we do not consider it here since we are more interested in new possibilities. The key elements involved in making cooled optics of ALS quality are the thermal/mechanical engineering of the substrate[29, 30] electroless nickel plating[31], optical working[32, 33], ruling (in the case of gratings) [34], whole-surface metrology[35] and the integration of these into a real-world solution[1, 34, 36].

4.6. *Aluminum*

Aluminum is a convenient and inexpensive material and, with a nickel-plated layer for polishing, has been popular in varying degrees for making optics for high powered lasers, synchrotron beam lines and certain optical telescopes for the last thirty years or so. Generally, the optics have not been of the first quality figure and finish due to:

- Poor uniformity and grain of the nickel (as for other metal optics of the period),
- Thermal mismatch with the nickel and consequent bi-metallic bending,
- Dimensional instability of the gross figure of the substrate material of three possible types (i) metallurgical instability (ii) microcreep under load and (iii) stress relief.

Fortunately there has been considerable progress in recent years on most of these issues so that we can now consider aluminum for a much higher quality type of optic. Firstly, the problems of earlier times with nickel quality have been successfully addressed as described earlier. Secondly, two solutions to the bimetallic bending have appeared: the "metal-matrix composite" SXA (see later), which can be thermally matched to nickel, has become available and also the technique of nickel plating *all* surfaces has evolved which reduces the bimetallic bending. Use of a stiff mirror shape also helps. Finally, there has been considerable research and development aimed at finding the most stable alloys and learning how to use them[37].

A large part of the effort to rehabilitate aluminum has come from the visible astronomy community and is driven by three main considerations

- Telescopes have grown too large for the traditional glass-based technologies to be cost-effective.

- Aluminum has about a hundred times larger thermal diffusivity than glass representing an approach to thermal equilibrium in minutes rather than hours.
- Adaptive designs have become necessary to hold figure during scanning of the sky so dimensional instability is less of a concern than hitherto.

A portion of the experiences with aluminum telescope mirrors have been with castable alloys such as A356 and tenzalloy which would not be considered ultrahigh vacuum compatible and we discount these for beam-line applications. On the other hand there is also considerable experience with wrought alloys of which essentially three can be considered serious candidates: 6061-T6, the 5000 series (including 5083, 5086, 5456 and 5754) and SXA. The 5083 alloy is especially familiar to ALS engineers since it was used in making the giant ALS vacuum vessel.

The "optical grade" metal-matrix composite SXA[38, 39] has a matrix of 2124-T6 (copper-containing) aluminum alloy and 30% of added fine-grain silicon carbide which leads to about a factor two higher elastic modulus and a factor two lower thermal expansion coefficient compared to standard aluminum alloys. The composition is chosen to give a thermal match to electroless nickel. This family of materials, which was developed to compete with beryllium for weight-critical applications, is machinable by conventional and electric-discharge machines and has improved dimensional-stability, microyield and creep properties compared to conventional aluminum alloys. An independent measurement of the dimensional stability of four samples of SXA, heat treated according to the manufacturer's specification, was made by S. Jacobs at the University of Arizona. It showed an average shrinkage of 5.7±1.0 parts per million (ppm)/year. From an optical stability point of view, one should probably attach more significance to the ±1.0 spread rather than the actual value of the shrinkage since the latter would not, on its own, lead to shape distortions. The chief disadvantage in using SXA will be the difficulty of welding and brazing. One solution is apparently to plate the surfaces with something like nickel and join them using tin-based solder.

On theoretical grounds, one can object to both 6061 and SXA because they are heat-treatable (i. e. thermodynamically-unstable) alloys whose properties depend on "aging" treatments. However, such data as exist[40-42] on the shape stability of optics made from these three classes of alloy is not conclusive and good results have been achieved in certain cases with all three.

Table 1: Thermal cycling treatments for stabilization of aluminum alloy optics*

Author and material	Before finish machining	High temperature	Low temperature	Total # of cycles	Notes
[Vukobratovich 1993] [41] 6061-T6		191 for 3 hr	-40 for 0.5 hr	2	Rate <8°C/minute
[Vukobratovich 1993 [41] SXA	-59 for 1 hr	100 for 1 hr	-59 for 1 hr	5	Rate <3°C/minute
Average of several other sources	Anneal at 520**	185	Liquid nitrogen (-196°C)	5	Not specified
Manufacturer's treatment (SXA)	Anneal at 520**	177	Liquid nitrogen (-196°C)	several	Thought to be non-critical

* all temperatures in °C

**plus a quench and an aging treatment for 6061 and SXA or a slow cool for a 5000 series alloy

A major reason for the inconsistency of the published data on the dimensional stability of aluminum alloys is that there is no standard stabilizing heat treatment and some treatments are considered proprietary. In conventional engineering the recommended temperatures for heat treatment of the various aluminum alloys are 350-450°C for annealing and about 250°C for stress relief. On the other hand the literature of *optical* applications of such alloys shows a general practice of much more rigorous treatments including usually a solution anneal (at 520°C) after rough machining and then stabilization treatments consisting of thermal cycling between a moderately high temperature and liquid-nitrogen temperature. Such cycling is almost universally advocated[43] in spite of the effort involved and the fact that there seems to have been no systematic investigation of its effectiveness. One of the few authorities in this branch of engineering is D. Vukobratovich at the University of Arizona and we show in Table 1 his recommended treatments for alloys 6061-T6 and SXA[41]. We also show the manufacturer's recommendation for SXA and an average of the recommended treatments from several other sources which are generally described incompletely but are, in most cases, more rigorous than those of Vukobratovich. Some authors even recommend stabilization treatments at several stages during manufacture[44, 45].

Although only a few large telescope mirrors have been made of aluminum in the past (most of which were cast), aluminum alloys are now leading contenders for a number of important telescope projects. One is the 6 m diameter mirror which will be installed as the upgrade optic for the 30-year-old McMath-Pierce telescope at the Kitt Peak National

Observatory in Tucson, USA. Another is the Very Large Telescope (VLT) to be built at the European Southern Observatory (ESO) in Italy. In order to establish the best technical solutions for the VLT and other large telescopes, a project known as LAMA (Large Active Mirrors in Aluminum) was set up[46, 47]. Two phases of studies and demonstration projects have been completed involving the manufacture of several mirrors of 0.5 m diameter for the first phase[48] and 1.8 m for the second[47]. A great deal has been learned from which we may select the following items of interest for our application:

- Of the sixteen 0.5-m mirrors tested, seven showed good stability under thermal cycling (–20 to +50°C), of which four were castable alloys and three wrought. Two of the latter were 1000 series (>99.5% pure Al) and one was a 5000 series (3% Mg).
- The 0.5-m figure stability measurements refer to high-spatial-frequency distortions. Simple focal length changes were not interesting to the investigators and were not reported.
- There was no correlation between the method of 0.5-m blank preparation (sand cast, open-mold cast, forged or rolled) and the observed stability of the mirror.
- The nearly-pure aluminum mirrors were expected to show better stability due to lack of heat-treatability effects but they did not do so.
- Response to thermal cycling was tested after completion of both types of mirrors and it appeared that the dimensions were often more stable after four cycles. This is evidence for the validity of using a stabilization sequence between nickel coating and polishing.
- The best 1.8-m blank was cycled several times between the annealing temperature and liquid nitrogen temperature before commencement of manufacturing.
- The figure of the best 1.8 m mirror was within 34 nm rms of the required 6.0-m-radius sphere (100 nm rms was specified) and figure changes due to 32 thermal cycles (–20 to +40°C) were below 20 nm rms.

The evidence on choosing an aluminum alloy is by no means conclusive. The most-promising but least-known is SXA. A number of mirrors have been made from optical-grade SXA although none so far for synchrotron radiation. It should be competitive with glidcop for cooling of low to medium intensity and superior to it for large mirrors (especially toroids needing large waster plates) and benders where the specific stiffness and total weight are issues. This alloy appears to offer the best chance of bringing aluminum into the realm of first-quality synchrotron optics. For mirrors of lower cost it is still interesting to consider the question of 6061-T6 versus the 5000 series. The prevailing view in the literature favors the high-magnesium 5000 series, particularly 5083, for mirrors where a performance advance over and above the state of the art (of aluminum mirrors) is being sought. It is commonly available and has more favorable welding and diamond

turning characteristics than 6061. We may cite its use for both of the LAMA 1.8-m blanks[47, 49] and its advocacy by Taylor[45] and Franks[50]. For mirrors within the state of the art of aluminum optics the well-tried 6061-T6 has many supporters and will be hard to beat. It also brazes well which 5083 and most of the other 5000 series do not. 5050 is better for brazing and might be a compromise choice if brazing were high-priority. Whichever alloy is chosen, a critical ingredient of success will be careful application of the best stabilizing thermal treatments.

4.8. *Invar*

Invar has the best thermal-distortion performance in the temperature range 0-80°C of all the materials considered here plus wide availability and most of the engineering advantages of a steel-type alloy. Such advantages include the capability to be welded, brazed and machined without major deviations from the normal practices for dealing with steels [51, 52]. These are very significant advantages but they can only be exploited if the major issue of dimensional stability can be addressed. We consider this in more detail below. The importance of invar has lead to a great deal of study and its length-change behavior for both varying and constant temperature has an extensive literature. Saito and McCain-and-Maringer [53, 54] have summarized most of the work up to about twenty years ago while Jacobs, in whose laboratory many of the recent measurements have been made, has reviewed the more recent work[55].

The low expansion properties of the nickel-iron alloys were discovered by Charles Guillaume in 1886 [56, 57]. Invar (36%Ni+64%Fe) is the alloy with the lowest expansion coefficient in the neighborhood of room temperature. It is an austenitic (face-centered cubic) material which is ferromagnetic at room temperature with a Curie temperature of about 260°C. The low expansion property results from a balance between a decrease in atomic spacing associated with the loss of ferromagnetic ordering as the Curie temperature is approached and the normal increase in atomic spacing with temperature. For our purposes the practical range in which the expansion coefficient is low is about 0-80°C. At higher temperatures it rapidly reverts to a behavior similar to that of other steels. The invar property is compromised by certain impurities, particularly carbon, manganese and silicon. Expressed in ppm/°C/0.1% of impurity, the increase in the expansion coefficient is 0.4 for carbon and 0.15 for manganese. Impurity silicon does not affect α directly but reduces the useful temperature range of the invar property. The carbon content is thus of particular importance and should ideally be below about 0.01% but this is not normally achieved in commercial invars. Low values of α can also be produced by both heat treatment and cold

working, although cold working would not be indicated for optical applications because its effects are neither permanent nor isotropic.

The main difficulty in using invar as a material for making mirror substrates is the fact that, without careful countermeasures, it changes its dimensions with time. This property has long been known and was studied by Guillaume who measured one sample at constant temperature for almost 30 years. The result of this and other studies was that commercial invar does stabilize within a ppm/year or so after a sufficient time but at room temperature, it may take many years. The principal effect is an expansion (known as the γ expansion) which when complete, amounts to a growth of about 50 ppm. An understanding of the γ expansion and the development of countermeasures to it were first achieved in a landmark study by Lement, Averbach and Cohen[58]. These authors used x-ray analysis to show that the γ expansion is a true volume, i.e. lattice-parameter, change. They also found that there are three main effects to be concerned about in using invars (i) stress relief, (ii) the γ expansion and (iii) graphite formation. If the invar contains carbon above about 0.02%, as most commercial invars do, then its presence as graphite must be avoided or it will raise the coefficient of thermal expansion. Now the solubility of carbon in invar is 0.18% at 830°C and zero at room temperature. Thus the invar must be heated to 830°C to dissolve the carbon and then *quenched* in order to suppress the precipitation of graphite. The consequence of the quench is significant stress but this can be relieved, according to Lament et al., without precipitating graphite or raising the expansion coefficient provided the stress-relieving temperature is kept below about 315°C. After these procedures the material is still capable of undergoing the γ expansion, but results showed that it could be made to take place rapidly at an elevated temperature and could be fully completed in 48 hours at 95°C. An important related finding was that not only the graphite effect but also the γ expansion disappears for invars with carbon below about 0.02%.

The conclusion of the work of Lament et al. was thus the following three-step heat treatment for invar (the MIT triple treatment) that has received wide acceptance in the literature as providing the best combination of low α and good dimensional stability: after rough machining and high temperature procedures such as brazes

(i) heat to 830°C for 30 minutes, water quench,

(ii) heat to 315°C for 1 hour in air, air-cool,

(iii) heat to 95°C in air for 48 hours, air cool to room temperature.

It is clear from the arguments presented, that the triple treatment is essentially a way to deal with the presence of unwanted carbon and is thus applicable to commercial invars. With its help one can get expansion coefficients near zero (0.15-0.4 ppm/°C for temperatures 0-80°C[59]) and reasonable length stabilities.

The data on just how good the length stability can be after the triple treatment are sparse and somewhat contradictory. There is a general belief that the triple treatment favors good values of the expansion coefficient at the expense of dimensional stability and this has lead to a practice of replacing the quench in the first step with a slow cool or even of omitting the anneal altogether. Such procedures were used by Schwab and coworkers[60] who measured α values of 2-2.5 ppm/°C and an (isothermal) length change of 8-11 ppm/year with a standard invar at 38°C and an α value of 0.9-1.9 ppm/°C and a length change of 0.9-2.5 ppm/year with a low-carbon invar at 38°C. On the other hand Marschall and Maringer reported a length change of 1-2 ppm/year following a full triple treatment including a quench. Other results (Table 23 in McCain and Maringer) [53] suggest that the first step of the triple treatment is not severely prejudicial to stability and that an aging step of a month at 70°C after the triple treatment reduces the length change rate to less than 5 ppm/year (these results were only quoted to the nearest 5).

A recent study by Steel and coworkers[61] may resolve some of the apparent contradictions. These workers measured the length changes of high (0.06%) and low (0.02%) carbon invar after both the triple treatment and the triple treatment with the quench replaced by a slow cool. They found that the results could be represented by two exponential growth processes: a fast one of time constant 0.26 years with an initial rate of 10 ppm/ year and a slow one of time constant 3.0 years with an initial rate of 4.9 ppm/year. For the *slow* process, which is the most important one in practice, the length change rates were as shown in Table 2.

Table 2: Long-term length change rates of invar measured by Steel et al[61]

	Room temperature	Room temperature	38°C	38°C
	High carbon (ppm/year)	Low carbon (ppm/year)	High carbon (ppm/year)	Low carbon (ppm/year)
Full triple treatment	2.1-3.8	2	2.0-4.6	0.8
Triple treatment with a slow cool instead of a quench	2.3	0.7	2.9	0.5

Given that there is both a fast and a slow growth rate we at least have the possibility to reconcile all of the above results from the Schwab, McCain, Marschall and Steele references. The observed benefits of aging are confirmed and since the Schwab

measurements lasted 47 days and the Steele ones 258 days the broad picture becomes reasonably consistent. Furthermore, all studies agree on the benefits of low carbon for both the expansion coefficient and the stability. The tentative conclusion is that commercial invars without special reduction of carbon can give expansion coefficients in the range 0-0.5 ppm/°C and stabilities of 2-4 ppm/year provided the triple treatment and some degree of aging is used. If carbon is low 1-2 ppm/year may reasonably be expected.

So far we have concentrated on dealing with carbon-containing commercial invars, however, although invar alloys with carbon below 0.02% are not readily available, they can be obtained to special order. They should be free of both the γ expansion and graphite precipitation and thus offer another possible route to both low expansion and good stability. This has been the thrust of recent developments by the Jet Propulsion Laboratory (JPL) [62] for application of invar to thermal stabilization systems in spacecraft. The basic approach is to use powder metallurgy to achieve a highly controlled composition with carbon especially held below 0.01%. The triple treatment was again applied except that with such a low carbon level there is no longer a need for a quench following the initial high temperature anneal. The invars produced in this way have been tested by Jacobs' group and have shown expansion coefficients below 1 ppm/°C and stability better than 1 ppm/year using the triple treatment with the quench replaced by a slow cool. For comparison "standard" fused silica has α=0.6 ppm/°C and a length change rate of 0.2 ppm/year.

These expansion and stability figures of the JPL invar are certainly within the range needed for high quality optics. Moreover, the JPL material has already been made in large enough pieces for beam-line mirrors. It thus appears that both commercial and JPL-type invar offer very interesting possibilities for beam-line mirrors on condition that the operating temperature is kept below 80°C.

5.0. Conclusions and ideas for further research

For the most challenging combinations of heat load and distortion specification where there is a need for very intensive (and thus internal) cooling, the present practice in the synchrotron-radiation community seems to be to use nickel-plated glidcop or silicon . For less severe challenges the same materials or silicon carbide are employed and cooling may be direct or indirect. For the mildest heat loads, fused silica or ULE are naturally still the most popular.

We are interested in how we can improve both the performance and the price in the future. For the highest performance mirrors, where the emphasis is on dealing with an

extreme heat load we believe that the way forward is to continue the glidcop developments perhaps to cellular-pin-post systems. When the emphasis is on complying with extreme distortion specifications then it appears that silicon is indicated and that invar offers a promise of both improved performance and lower price. For less extreme challenges but still with cooling, it seems clear that nickel-plated metals have the cost advantage and that SXA and other aluminum alloys can be added to glidcop and invar as candidate materials. For mirrors with sufficiently mild cooling requirements, stainless steel would have many advantages including low cost and minimal technical risk. In the opinion of this author, once the internal cooling designs are established, they will be seen as more cost-effective and reliable than clamp-on schemes and the latter will gradually lose popularity. Continuing down the scale, there is a range of optics where no coolant is needed and radiation cooling can suffice. Silicon and silicon carbide are indicated here, in part due to emissivity considerations. Finally, for the range where no special cooling arrangements are to be made and the mirror is a simple rectangular block, the ceramics silicon, silicon carbide and the glasses have the advantage. From this analysis it appears that, although silicon carbide offers certain capabilities, it is almost never the simplest and most cost effective solution to beam-line mirror needs.

For future research we identify the following as interesting items to pursue:

- apply the cellular-pin-post design to glidcop,
- study the long-term dimensional stability of the materials we use now as well as new candidates,
- include the effect of electroless nickel layers on cooling designs (it is often neglected at present),
- develop a way to finish nickel that is compatible with multilayers, i. e. achieve low roughness at all spatial periods down to near-atomic dimensions implying surface measurement by atomic force microscope as well as the optical profiler (Wyco or equivalent).

Acknowledgments

The author is happy to acknowledge helpful conversations with R. Avery, C. Corradi, R. DiGennaro, D. Lunt, W. McKinney, H. Padmore, T. Swain and T. Tonneson. This work was supported by the United States Department of Energy under Contract Number DE-AC03-76SF00098.

References

1. W. McKinney, S. C. Irick, D. L. J. Lunt, "Water-cooled Metal Optics for the Advanced Light Source", *Nucl. Instrum. Meth.*, **A319**, 179-184 (1992).
2. T. W. Tonnessen, S. E. Fisher, "Design and Analysis of cooled optical components for synchrotron beamlines" in *Optics for High-Brightness Synchrotron Radiation Beamlines* J. Arthur, (Ed.) Proc. SPIE, vol. 1740, 18-23, (SPIE, Bellingham, 1992).
3. M. R. Howells, "Some fundamentals of cooled mirrors for synchrotron radiation beam lines", *Submitted to Opt. Eng.*, , preprint LBL-36082 (1994).
4. M. Jakob, *Heat Transfer*, , vol. I, (John Wiley, New York, 1949)
5. J. P. Holman, *Heat Transfer, 6th edition*, , (McGraw-Hill, New York, 1986)
6. D. B. Tuckerman, "Heat-Transfer Microstructures for Integrated Circuits", PhD thesis, Stanford (1984).
7. V. Rehn, V. O. Jones, "Vacuum Ultraviolet (VUV) and Soft X-ray Mirrors for Synchrotron Radiation", *Opt. Eng.*, **17**, 504-511 (1978).
8. J. R. Choyke, F. Farich, R. A. Hoffman, "SiC a New Material for Mirrors", *Appl. Opt.*, **15**, 2006-7 (1976).
9. British Nuclear Fuels,
10. Carborundum Co.,
11. M. M. Kelly, J. B. West, "Silicon Carbide Mirrors at the Daresbury SRS", Daresbury Laboratory, Technical Memorandum, (1983).
12. R. L. Gentilman, E. A. McGuire, "Chemical Vapor Deposition of Silicon Carbide for Large Area Mirrors" in *Reflecting Optics for Synchrotron Radiation* M. R. Howells, (Ed.) vol. 315, 131-4, (SPIE, Bellingham, Bellingham, 1981).
13. Morton International Inc.,
14. M. A. Pickering, R. L. Taylor, J. T. Keeley, G. A. Graves, "Chemically Vapor Deposited Silicon Carbide (SiC) for Optical Applications" in *Space Optical Materials and Space Qualification of Optics* R. R. Hale, (Ed.) Proc. SPIE, vol. 1118, 1-13, (SPIE, Bellingham, 1989).
15. S. G. Jitendra, M. A. Pickering, R. L. Taylor, B. W. Murray, A. Lompado, "Properties of Chemical-Vapor-Deposited Silicon Carbide for Optics in Severe Environments", *Appl. Opt.*, **30**, 3166-3175 (1991).
16. S. Sato, A. Iijima, S. Takeda, M. Yanagihara, T. Miyahara, A. Yagashita, T. Koide, H. Maezawa, "SiC Mirror Development at the Photon Factory", *Rev. Sci. Inst.*, **60**, 1479-1485 (1989).
17. K. B. Becker, "Synchrotron Radiation Mirrors for High Intensity Beamlines", *Rev. Sci. Inst.*, **63**, 1420-3 (1992).
18. J. R. Palmer, "Continuous wave laser damage on optical components", *Opt. Eng.*, **22**, 435-446 (1983).
19. P. Z. Takacs, "Evaluation of CVD Silicon Carbide for Synchrotron Radiation Mirrors", *Nucl. Instrum. Meth.*, **195**, 259-266 (1982).
20. TRW Space and Technology Group, Applied Technology Division, Redondo Beach, CA 90278, USA.
21. J. W. Arthur, H. Thompkins, C. Troxel, R. J. Contolini, E. Schmitt, D. H. Bilderback, C. Henderson, J. White, T. Settersten, "Microchannel Water Cooling of Silicon X-ray Monochromator Systems", *Rev. Sci. Inst.*, **63**, 433-7 (1992).
22. K. C. Sun, R. L. Wahl, F. M. Anthony, T. W. Tonnessen, Silicon mirrors for advanced free-electron lasers, Proceedings of the conference on High Power Laser Optical Components, J. L. Stanfords, (Ed.) (Naval Weapons Center, China Lake, Boulder, Colorado, 1989), pp. 124-135.
23. T. Tonnessen, S. Fisher, F. Anthony, D. Lunt, A. Khounsary, K. Randall, E. Gluskin, W. Yun, "High heat flux mirror design for an undulator beamline" in *High Heat Flux Engineering* A. M. Khounsary, (Ed.) Proc. SPIE, vol. 1739, 340-353, (SPIE, Bellingham, 1992).
24. T. W. Tonnessen, J. Arthur, "Cooled silicon crystal monochromator test results" in *High Heat Flux Engineering* A. Khounsary, (Ed.) Proc. SPIE, vol. 1739, 622-627, (SPIE, Bellingham, 1992).
25. L. Foucault, *C. R. Acad. Sci. Paris*, **441**, 339 (1857).
26. W. P. J. Barnes, (Ed.) Design Manufacture and Application of Metal Optics, Proc SPIE, vol. 65 (SPIE, Bellingham, 1975).
27. D. H. Killpatrick, Review of the Properties of Electroless Nickel, Proceedings of the conference on Aluminum, Beryllium and Silicon Carbide Optics, W. B. Snyders, (Ed.) (Oak Ridge National Laboratory, Oak Ridge, 1993),
28. SCM Metal Products Inc.,

29. R. DiGennaro, T. Swain, "Engineering for High Heat Loads on ALS Beamlines", *Nucl. Inst. Meth.*, **A291**, 313-6 (1990A).
30. R. T. S. DiGennaro, "A Directly Cooled Grating Substrate for ALS Undulator Beamlines", *Nucl. Instrum. Meth.*, **A291**, 305-312 (1990B).
31. Acteron Corp.,
32. Photon Sciences International Inc.,
33. Rockwell Power Systems,
34. W. R. McKinney, C. L. Shannon, E. Schults, "Water-Cooled Ion-Milled Diffraction Gratings for the Synchrotron Community", *Nucl. Instrum. Meth.*, **347**, 220-225 (1993).
35. P. Z. Takacs, S. K. Feng, E. L. Church, S. Qian, W. Liu, "Long Trace Profile Measurements on Cylindrical Aspheres" in *Advances in Fabrication and Metrology for Optics and Large Optics* J. B. Arnold, R. E. Parks, (Eds.), Proc. SPIE, vol. 966, 354-364, (SPIE, Bellingham, 1988).
36. W. R. McKInney, S. C. Irick, D. L. Lunt, "XUV synchrotron optical components for the advanced light source: summary of the requirements and the development program" in *Optics for high brightness synchrotron beam lines* J. Arthur, (Ed.) Proc. SPIE, vol. 1740, 154-160, (SPIE, Bellingham, 1992).
37. R. G. Bingham, D. D. Walker, (Eds.), Metal Mirrors, Proc. SPIE, vol. 1931 (SPIE, Bellingham, 1992).
38. W. R. Mohn, D. Vukobratovich, "Recent applications of metal matrix composites in precision instruments and optical systems", *Opt. Eng.*, **27**, 90-98 (1988).
39. Advanced Composite Materials Corp.,
40. A. A. Ogloza, D. L. Decker, P. C. Archibald, D. A. O'Connor, E. R. Bueltmann, "Optical properties and thermal stability of single-point diamond-machined aluminum alloys" in *Advances in Fabrication and Metrology for Optics and Large Optics* J. B. Arnold, R. E. Parks, (Eds.), Proc. SPIE, vol. 966, 228-251, (SPIE, Bellingham, 1988).
41. D. Vukobratovich, "Optomechanical Systems Design" in *Electro-Optical Systems Design, Analysis and testing* M. C. Dudzik, (Ed.) The Infrared and Electro-Optical Systems Handbook, vol. 4, 123-196, (SPIE, Bellingham, 1993).
42. D. Vukobratovich, Aluminum and aluminum/silicon carbide metal matrix composites for optical systems, Proceedings of the conference on Aluminum, Beryllium and Silicon Carbide Optics, W. B. Snyders, (Ed.) (Oak Ridge National Laboratory, Oak Ridge, 1993),
43. M. C. Gerchman, "Specifications and manufacturing considerations of diamond machined optical components" in *Optical Component Specifications for Laser-based Systems and Other Modern Optical Systems* R. E. Fischer, W. J. Smith, (Eds.), Proc. SPIE, vol. 607, 36-45, (SPIE, Bellingham, 1986).
44. J. B. C. Fuller, P. Forney, C. M. Klug, "Design and fabrication of aluminum mirrors for a large aperture precision collimator operating at cryogenic temperatures" Proc SPIE, vol. 288, 104, (SPIE, Bellingham, 1981).
45. H. D. Taylor, "Metal mirrors in the large", *Opt. Eng.*, **14**, 559-567 (1975).
46. J.-P. Rozelot, "Metallic alternative to glass mirrors (active mirrors in aluminum): a review" in *Space Astronomical Telescopes and Instruments* P. Y. Bely, J. B. Breckinridge, (Eds.), Proc. SPIE, vol. 1494, 481-490, (SPIE, Bellingham, 1991).
47. J.-P. Rozelot, "The "L. A. M. A." (Large Active Mirrors in Aluminum) programme" in *Metal Mirrors* R. G. Bingham, D. D. Walker, (Eds.), Proc. SPIE, vol. 1931, 33-42, (SPIE, Bellingham, 1992).
48. L. Noethe, P. Giordano, K. Mischung, F. Franza, R. Wilson, "Optical analysis of thermally cycled 515 mm metallic Al/Al-alloy mirrors", *Astron. Astrophys.*, **156**, 323-336 (1986).
49. M. Morette, M. Dupont, J.-P. Rozelot, "Interest in Aluminium alloy 5083 for telescope mirrors" in *Metal Mirrors* R. G. Bingham, D. D. Walker, (Eds.), Proc. SPIE, vol. 1931, 144-148, (SPIE, Bellingham, 1992).
50. A. Franks, "X-ray telescope mirrors-materials, manufacture, tolerances and metrology" in *Space Optics-Imaging X-ray Optics Workshop* M. Weisskopf, (Ed.) Proc. SPIE, vol. 184, 110-122, (SPIE, Bellingham, 1979).
51. MIL-SPEC, . Navy, (Ed.) (Naval Air Engineering Center, 1974),
52. F. Rosebury, *Handbook of Electron Tube and Vacuum Techniques*, , (Addison Wesley, Reading Mass, 1965)
53. W. S. McCain, R. E. Maringer, "Mechanical and physical properties of invar and invar-type alloys", Battelle Memorial Institute, Defense Metals Information Center, (1965).
54. H. Saito, (Ed.) Physics and applications of invar alloys, (Maruzen company, Tokyo, 1978).
55. S. F. Jacobs, "Dimensional stability of materials useful in optical engineering", *Optica Acta*, **33**, 1377-1388 (1986).

56. C. E. Guillaume, *Les Application des Aciers au Nickel*, , (Gauthiers-Villars, Paris, 1904)
57. C. E. Guillaume, "The Anomaly of the Nickel-Steels", *Proc. Phys. Soc.*, **32**, 374-404 (1920).
58. B. S. Lement, B. L. Averback, M. Cohen, "The dimensional behavior of Invar", *Trans. Am. Soc. Met.*, **43**, 1072-1097 (1951).
59. Y. S. Touloukian, R. K. Kirby, R. E. Taylor, P. D. Desai, *Thermal Expansion Metallic Elements and Alloys*, Thermophysical Properties of Matter, vol. 12, (IFI/Plenum, New York, 1976)
60. D. E. Schwab, S. F. Jacobs, S. C. Johnson, Isothermal dimensional instability of invar, Proceedings of the conference on National SAMPE Symposium, (Society for the Advancement of Materials and Process Engineering, Reno, 1984), vol. 29, pp. 169-184.
61. J. M. Steele, D. A. Thompson, S. F. Jacobs, D. L. Bass, "Temperature and age effects on the temporal stability of invar" in *Current Developments in Optical Design and Optical Engineering II* R. E. Fischer, W. J. Smith, (Eds.), Proc. SPIE, vol. 1752, 40-51, Bellingham, 1992).
62. W. Sokolowski, S. Jacobs, M. Lane, T. O'Donnell, C. Hsieh, "Dimensional stability of high purity invar 36" in *Quality and reliabilty for optical systems* J. W. Bilbro, R. E. Parks, (Eds.), Proc. SPIE, vol. 1993,, Bellingham, 1993).

Some Selected Recollections About My Fellow Student and Close Friend Klaus Halbach

Eugen Baumgartner

We both studied physics under the guidance of Prof. Paul Huber at the University of Basel. Both of us were impressed by the profound wisdom of Prof. M. Fierz (theoretical physics) and of Prof. E. Baldinger (electronics and engineering) at our department. There was a stimulating, lively atmosphere and both of us worked hard. Frequent outings with the Professors and our fellow students gave us much joy and contacts which lasted for a lifetime. (see photographs).

Klaus was married and had a daughter. He lived in Grenzach, which was at the time in a French zone of Germany. This meant, that he had to cross daily, with a complicated procedure, the border to Switzerland. Regardless of the weather, he had to use his bike. Sometimes Klaus and I spent a full night till sunrise discussing our open problems in physics. It may have sounded like: "You have a monochromatic beam of electrons. Naturally we can calculate the electromagnetic fields. But if you sit on an electron ...!" We were not satisfied with our partial solutions. A long time later, 1964, we found the correct quantitative answers in Feynman's "lectures on physics." I wonder where Richard Feynman got that question.

During those days Klaus had to do experimental physics with his own hands. For example, he had to invent and to build electronic circuits. At that time, all electronics were done with valves. Burns on the knuckles from the soldering iron and dense smoke were accepted with coolness. But if that thing oscillated, instead of producing what Klaus had calculated, you could hear him swearing in good German.

It happened once that we overestimated the possibilities of our constitutions, or perhaps our knowledge of the mountains. One day (summer 1950), we decided to go on a extended trip to the mountains. Ruthli, the wife of Klaus, and a fellow student Conrad Biber joined us. After three days of riding bicycles, we reached the region of the sources of the Rhine. There is not much to report from these lovely days, only that the chain on Klaus's bike broke. We then bought food for four days, stored it in our knapsacks, and hiked successfully to the first mountain cabin (Terrihütte). We were on our way to Piz

Medels (see photograph). The next day was a Sunday, but not for us. Unexpected things happened: A bridge over one of the cold, wild mountain streams was destroyed. We had to climb up until we found a bridge of snow to pass the torrent. The snowbridge was not thick. At the thinnest part Klaus decided to fall with the heavy load on his shoulders. God did save him and nothing happened, except that the weather turned cold and it grew foggy. We could not find the next cabin. We stumbled the full night all around in those steep mountains. In the early morning, we found the cabin of a shepherd. On the beautiful, warm open fire, he prepared coffee for us. Klaus received a coffee with goat milk. He hates coffee; ask him sometime to describe the smell of the mixture. A photograph of him showing our exhaustion from the night trip, his recovery and a picture of the cabin at Medels with Klaus and Ruthli shall terminate this short survey of my many invaluable recollections of Klaus.

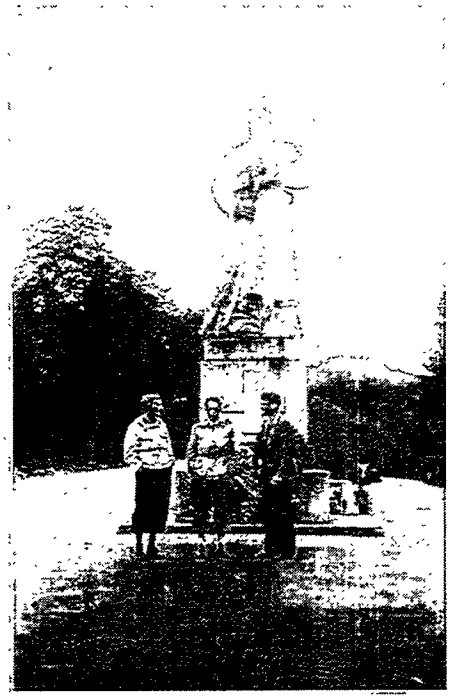

Klaus Halbach, E. Baldinger, and the author, Summer 1949.

Summer 1949 (left to right): Paul Huber, Beat Hahn, Frau M. Huber, Hans Bichsel, Jüng Seitz, Arnold Müller, Alfred Meier, E. Baldinger, Gerhard Backenstass, the author, Klaus Halbach, Reinhard Buddhe, Willi Haeberli.

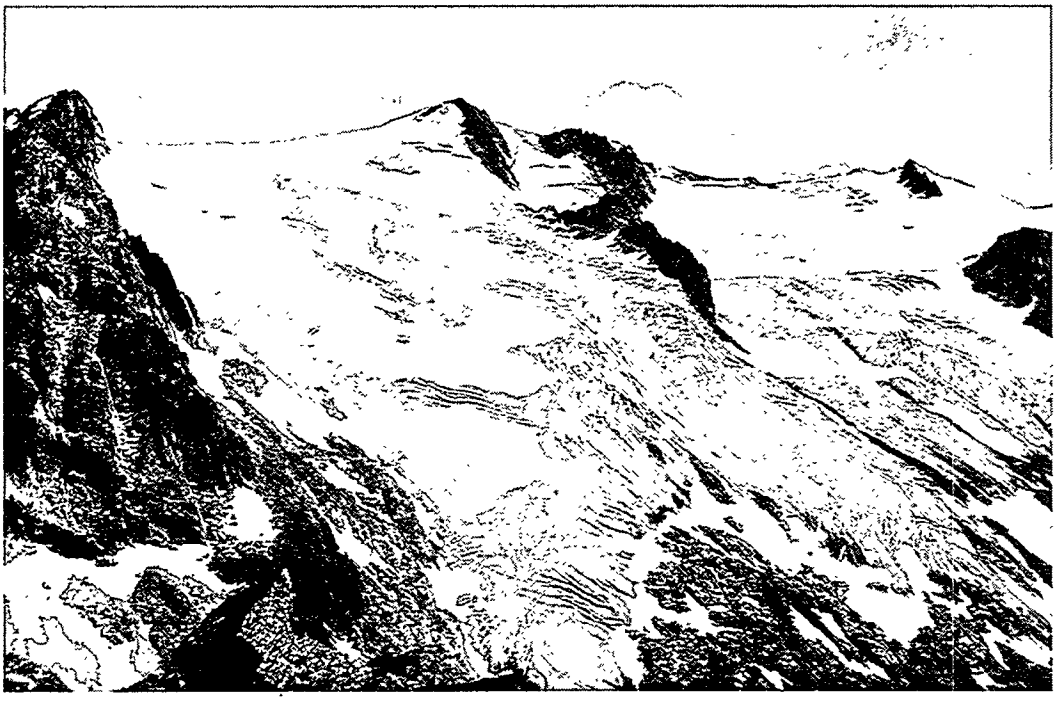

Piz Medels, the goal of a mountain tour, Summer 1950.

Klaus, exhausted after a disastrous day in the mountains.

Recovery afterwards.

Finally at the cabin at Medels.

The Effective Field Boundary in a Parallel-Plate Condenser of Different Electrode Width

B. Pfreundtner*, A. Tolmachev†, and H. Wollnik*

* II. Physikalisches Institut, Universität Giessen, 35392 Giessen, Germany.
† Russian Academy of Sciences, Institut of Energy Problems of Chemical Physics, 142432 Chernogolovka, Russia.

Abstract

The position and the curvature of the effective field boundary of a parallel–plate condenser of electrode separation $2g_0$ and electrode width $2b$ has been calculated. This investigation requires the solution of a three–dimensional Dirichlet problem which in the present paper has been achieved by the surface charge method. It is shown, that the description of the required charges at sharp edges can be improved by the use of singular functions.

1 Potential calculation

For potential calculations we like to use the integral equation method [1] combined with the method of surface charges [1,2], which has advantages as compared to the finite–difference method [3] and the finite–element method [4,5], i.e., the Laplace equation is always fulfilled, no knowledge of the potential far from the system is needed, and three–dimensional problems are reduced to two–dimensional ones. Most importantly the surface charge method determines to high accuracy the real potential distribution produced by electrodes that only approximate the designed electrode geometry while the three–dimensional grid methods use a stepwise exact electrode geometry to determine a potential distribution that fulfills Laplace's equation only approximately. To solve a boundary–value problem by the surface–charge method on the other hand, a charge density σ is assumed,

distributed along the electrode surfaces F from which one finds the spatial potential distribution as:

$$V(\vec{r}) = \int\int_F \frac{\sigma(\vec{r}')}{|\vec{r} - \vec{r}'|} d^2 f'.$$

The charge density σ is then varied such, that V on F reproduces the potentials on the electrode. In order to solve this problem, the surface of the system under investigation is dissected into a finite number of M elements. The potential at an arbitrary point then is the sum over the effects of all elements:

$$V(\vec{r}) = \sum_{j=1}^{M} \int\int_{F_j} \frac{\sigma(\vec{r}')}{|\vec{r} - \vec{r}'|} d^2 f', \tag{1}$$

where F_j denotes the surface of the j_{th} element. The surface–charge density σ within each element we describe by a two–dimensional interpolation:

$$\sigma(\vec{r}) = \sum_{i=1}^{N} \mathcal{L}_i(u, v)\sigma_i(\vec{r}_i). \tag{2}$$

where N is the number of control points for polynomial interpolation. The interpolation functions $\mathcal{L}_i$ are here chosen to be modified Lagrange–polynomials of third order, described by surface coordinates $u(\vec{r}), v(\vec{r})$. Considering, that the surface–charge density must increase to infinity at any edge or corner of an electrode, it is obvious that the description of the surface charge by a polynomial of limited power is inadequate. Thus, it is useful to add a singular function to the dependence (2), which behaves as the inverse square root of the distance to the singular edge. This function should be expressed in a form of linear combinations of K singular functions f_i multiplied by some scalable amplitudes $\sigma_i, i = N+1, ..., N+K$. In this way an additional set of functions can be defined:

$$\mathcal{L}_i(u, v) = f_i\left(\frac{1}{\sqrt{u - u^*}}, \frac{1}{\sqrt{v - v^*}}\right),\ i = N+1, ..., N^* \tag{3}$$

where u^*, v^* denote the points of singularity, $N^* = N + K$. The substitution of the eqs.(2) and (3) into eq.(1) leads to a system of linear equations

$$V_k(\vec{r}_k) = \sum_{i=1}^{N^*} M_{k,i}\sigma_i(\vec{r}_i),$$

from which one can determine the charge values σ_i at these points. Here the coefficients $M_{k,i}$ determined numerically from:

$$M_{k,i} = \sum_{j=1}^{M} \int\int_{F_j} \frac{\mathcal{L}_i(u,v)}{|\vec{r}_k - \vec{r}'|} d^2 f'.$$

2 The potential distribution in an ideal parallel–plate condenser

Using the described method, we calculated the potentials in an electrostatic condenser that consists of two rectangular, thin parallel plates of area $l * 2b$ separated by a distance $2g_0$. In detail we have calculated geometries in which $2b = 4g_0$,$6g_0$,$8g_0$,$10g_0$,$12g_0$,$14g_0$,$16g_0$ and $l = 6b$. Thanks to the symmetry, only 1/8 of the electrode surface must be dissected into elements. This was done using 49 rectangular elements. The obtained surface–charge densities for a region close to one corner of one of the electrodes are shown in fig.1. Obviously the singular functions lead to a fast increase at the edges as postulated by Laplace's equation. The surface charge distribution in the inner region on the other hand is smooth and nearly constant.

The field strength in and perpendicular to the midpotential surface of the condenser is shown in fig.2. The accuracy of the calculated values is about 10^{-5} in the main field region of the condenser and 10^{-3} to 10^{-4} near the edges. For condensers with different width $2b = 4g_0, 6g_0, 8g_0, 10g_0, 12g_0, 14g_0$ and $16g_0$ the distance v^*/g_0 between the effective field boundary and the electrode boundary is shown in fig.3 as well as the corresponding curvatures g_0/R^*.

3 Acknowledgement

For financial support we are thankful to the Deutsche Forschungsgemeinschaft and the German Bundesminister für Forschung und Technologie.

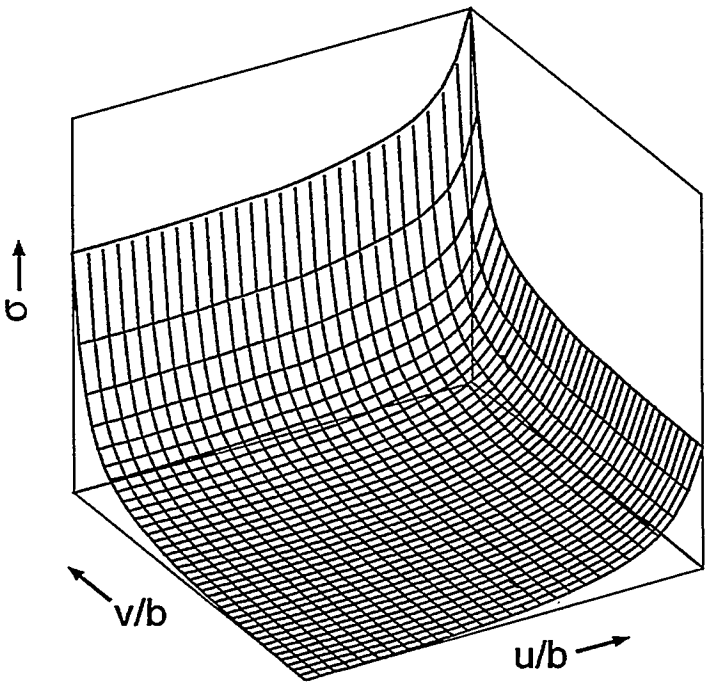

Figure 1. Calculated surface-charge density σ in the corner region of one condenser electrode. The charge density values are not plotted exactly up to the edge but rather stop at a short distance from the edge.

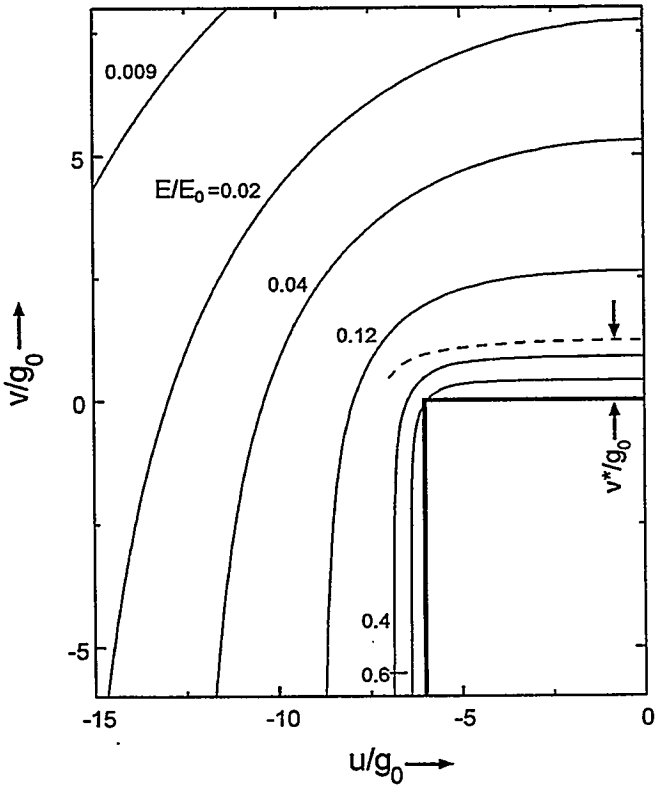

Figure 2. A contour plot of the field strength perpendicular to, and in the midpotential surface of, an electrostatic condenser of an electrode separation $2g_0$ is shown for electrodes of width $6g_0$. The dashed line denotes the effective field boundary. For the determination of the position v^*/g_0 and the curvature of the effective field boundary (see Figure 3), a much larger area had been used than shown in this figure.

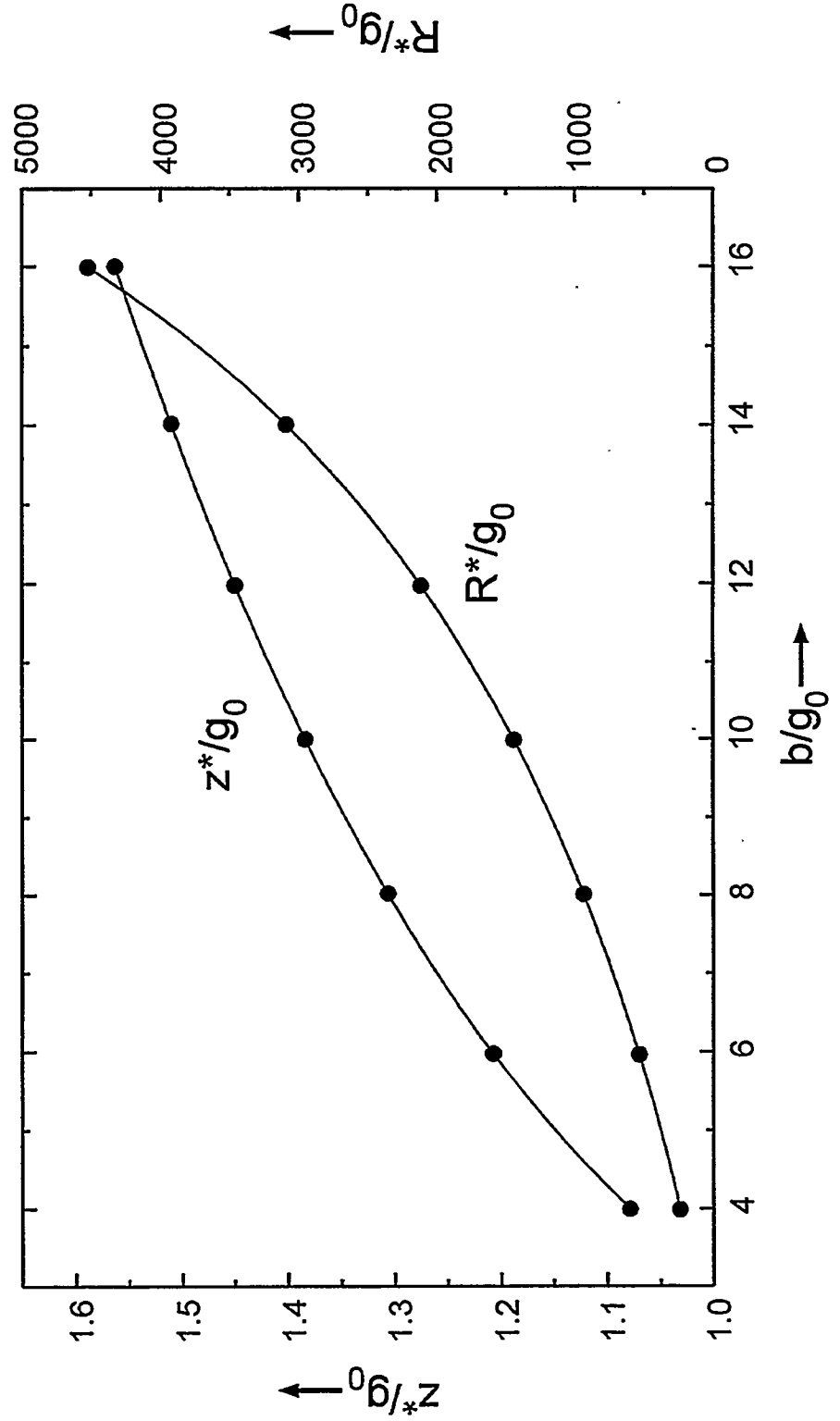

Figure 3. The position v^*/g_0 as well as the curavture g_0/R^* of the effective field boundary, i.e., in the middle of the electrostatic condenser, is shown for different electrode widths $2b = 4g_0$, $6g_0$, $8g_0$, $10g_0$, $12g_0$, $14g_0$, $16g_0$.

4 References

1. A. B. Birtles, B. J. Mayo and A. W. Bennet, Proc. IEE **120** (1973) 213.

2. E. Munro and H. C. Chu, Optik **61** (1982) 1.

3. C. Weber, Philips Res., Repts Suppl. No. 6 (1967).

4. R. Courant, Bull. Am. Math. Soc. **49** (1943) 1.

5. E. Munro, Computer–aided Design Methods in Electon Optics. Dissertation, Cambridge (1971).

The First Insertion Devices at SSRL
- Some Personal Recollections -

Herman Winick
Stanford Synchrotron Radiation Laboratory
Stanford Linear Accelerator Center

It is now about 15 years since insertion devices were first used as radiation sources at SSRL and at the Budker Institute of Nuclear Physics (BINP) in Novosibirsk. The increased photon flux and brightness delivered by the first wiggler and undulator insertion devices led to their widespread adoption in existing storage rings around the world and also to the new generation of third generation rings, designed specifically around insertion devices as the primary sources. Many thousands of scientists and engineers around the world are now actively involved in the design, construction and utilization of wigglers and undulators.

These developments are due in no small measure to the fact that very powerful wiggler and undulator insertion magnets can be made with permanent magnet material. Klaus Halbach understood the immense capability of this technology at a very early stage. During the past 15 years he has had many innovative ideas about the design of permanent magnet devices and has been a tireless and effective consultant and promoter of this technology around the world.

The first insertion devices used at SSRL were electromagnets. Now virtually all undulators and most wigglers are now made with permanent magnets. The origin of this transition at SSRL was rather fortuitous and humorous. It reflects some of the personality characteristics of Klaus Halbach.

SSRL experience with insertion devices started with a modest six pole, 1.2 meter long, 1.8 T electromagnet wiggler which was installed and tested in SPEAR in October, 1978 in a project led by J. Spencer [ref. 1]. Earlier wiggler magnets (called Robinson wigglers [ref. 2] after their inventor, Kenneth Robinson working at the Cambridge Electron Accelerator (CEA) at Harvard University) were used to redistribute damping to convert the CEA alternating gradient synchrotron at Harvard to a storage ring. The experience I gained in participating in that project before coming to Stanford made me enthusiastic about wigglers and led to the SSRL proposal for the first wiggler, an electromagnet as was the CEA damping wiggler.

The immediate success of the first SSRL wiggler led to a SLAC/SSRL collaboration to design and produce two longer (2 meters long) 8 pole, 1.9 T electromagnet wigglers which would be used for both enhancement of luminosity in colliding beam research and as the source for two beam lines at SSRL. The original 6 pole wiggler was loaned to Cornell University where it provided hard x-rays for CHESS users for many years and is now on its way back to SSRL where it may be used to jump-start a new beam line until we get funding for a permanent magnet wiggler. The 8 pole wigglers were installed in SPEAR in 1980 and are still major sources of intense hard x-rays at SSRL.

While electromagnet wigglers were being developed at SSRL, a superconducting undulator magnet [ref. 3] was being developed at Orsay as part of a free electron laser program using the ACO storage ring. Undulators, like wigglers, are periodic magnetic structures which deflect the electron beam in alternate directions while producing no net bending. In an undulator the deflection angle in each pole is small; of the order of the natural angle of emission of synchrotron radiation given by mc^2/E, or only 10^{-4} radians for

a 5 GeV electron. In a wiggler this angular spread is 5-100 times larger, resulting in wide beams.

The small angular spread of electrons traversing an undulator produces a very narrow beam, preserving the intrinsic high brightness of synchrotron radiation. In addition, in an undulator, interference effects in the radiation produced at the many collinear source points leads to enhancement of the radiation at certain wavelengths and suppression at other wavelengths; i.e., a quasi-monochromatic spectrum which further enhances the brightness at certain wavelengths. Although wiggler spectra exhibit interference peaks at very low photon energies, they are mostly used at high photon energies where the spectrum is a smooth, featureless continuum, similar to a bending magnet spectrum. For most purposes, a wiggler spectrum can be thought of as the superposition of the bending magnet spectra from each pole.

I followed the Orsay superconducting undulator development with interest and wished that we could follow up our success with electromagnet wigglers at SSRL by building a high brightness soft x-ray undulator. At the time I, along with most others, thought that the only way to reach high enough magnetic field in a short period undulator suitable for use in a storage ring was to use short superconducting coils for each pole, as was being done at Orsay. However, SSRL's 50% use of SPEAR for dedicated synchrotron radiation runs was just beginning and I felt that we should wait a few years before complicating this shared operation with a superconducting device in the SPEAR tunnel.

This all changed sometime in 1979 when Klaus Halbach and I were both at one of the parties given at SLAC to celebrate reaching a major milestone in the construction of the 15 GeV PEP colliding beam storage ring. PEP was a joint LBL/SLAC project and Klaus was a bona-fide member of the team, contributing his knowledge on the design of various electromagnets. I had no involvement with PEP, except to dream of its future use as a light source. However, I liked parties and the opportunity to socialize with many SLAC and LBL friends, so I was there also. Klaus had been working on the design of permanent magnet quadrupoles, primarily for use in proton linacs. His knew something about synchrotron radiation from his participation in a workshop that I ran in March of 1977 on wiggler and undulator magnets. In particular, he listened to Albert Hofmann and others describe the high brightness, quasi-monochromatic radiation that could be produced by short-period undulator magnets.

Klaus later told me that when he saw me in the distance at the party, he remembered about undulators and the proverbial light bulb lit up in his head. In an instant, he realized that the scaling laws and other properties of permanent magnets that made them suitable for quadrupoles could also be exploited in making short period, permanent magnet linear arrays; i.e., undulators. An undulator can, in fact, be thought of as a circular multipole magnet with many alternating polarity poles stretched out in a linear fashion. Much of the analytic work that he had been doing on permanent magnet quadrupoles could be readily adapted to the undulator geometry.

He ran up to me excitedly and pulled me away from the party into an adjacent empty conference room where he proceeded to tell me of his realization while filling the blackboard with equations. I was rather dismayed by this turn of events because I was really eager to stay at the party with my friends and could hardly follow Klaus' rapid fire and excited presentation of these new concepts, particularly after having had some beer.

At the time I hardly knew Klaus. To me he appeared to be a fanatic, making the (apparently) absurd assertion that simple blocks of permanent magnet material could be

assembled into short period structures which would produce magnetic field strength that matched or exceeded those produced by superconducting magnets. I found this difficult to believe because my previous experience with permanent magnets was primarily in their use in holding notes on refrigerator doors. However, I listened dutifully and nodded at appropriate intervals until Klaus released me to go back to the party which, by that time, was almost over.

About a week later, I received a call from Klaus. He said, "Hello Herman; what have you done with the ideas I gave you about permanent magnet undulators?" I cleared my throat a bit and mumbled some response. Klaus quickly realized that I had done nothing since our discussion at the party. I equally well remember his next statement. He said, "I think I have to come to speak to you again". And he did! Those who know Klaus at all know that he does not give up easily when he is convinced that something ought to be done. It took about three sessions to educate me about this new approach to undulator design.

Within a short time, we embarked on an LBL/SSRL collaboration to design and build a 2-meter long, pure samarium cobalt, permanent magnet undulator [ref. 4] which Klaus calculated should reach a field of almost 0.3 T with a 2.7 cm gap and 6.1 cm period. A photograph of the device is shown in figure 1. Each of the 60 poles of this device would produce a maximum angular deflection (or K-value) of about 1.5 (mc^2/E). This deflection angle could be lowered, and the peaks in the spectrum tuned, by lowering the field. This could be accomplished simply by opening the magnet gap mechanically. We could fit 30 periods in the 2 meter space available in SPEAR so that we could expect significant interference effects and an increase in brightness by about two orders of magnitude over a SPEAR bending magnet.

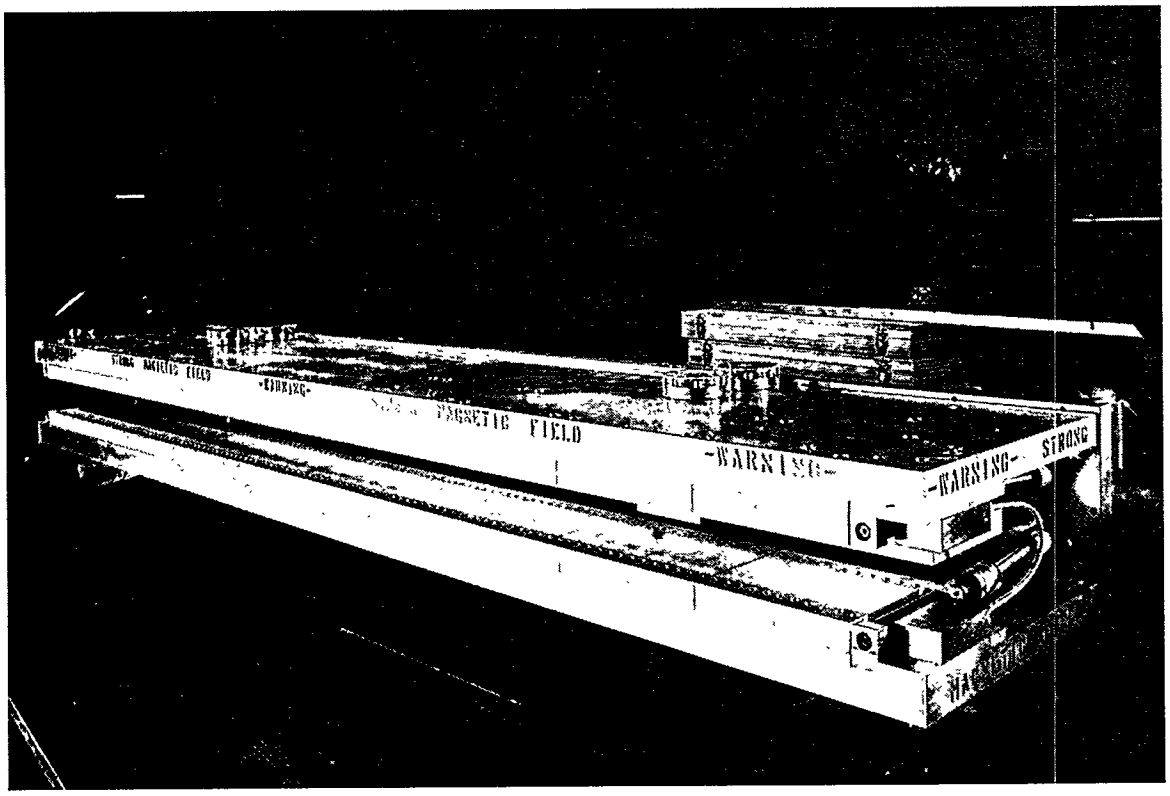

The first LBL/SSRL permanent magnet undulator.

The magnet was installed and tested in SPEAR in December of 1980. It met all expectations. It was used for the first experiments [ref. 5] in 1981. Since then Klaus has stayed closely involved with the design of many insertion devices at SSRL, including the first permanent magnet hybrid wiggler; the 54 pole wiggler for SSRL beam line 6 which used a variable gap vacuum chamber to achieve a magnetic field in excess of 1 Tesla.

The first undulator has since been removed from SPEAR and replaced by the beam line 5 multi-undulator array. It is now on loan to the Synchrotron Radiation Center in Wisconsin where it is installed in the ALADDIN ring and doing yeoman service as the source for the MAXIMUM project. With MAXIMUM scheduled to move to the ALS soon, this first undulator will again become available and may be used as a radiation source elsewhere.

In subsequent years of close association with Klaus, I have learned that his apparent "fanaticism" is due to his enthusiasm for a good idea (including ideas from others as well as his own ideas) and to a missionary zeal to make sure that all who might benefit from it are informed. The synchrotron community in general, and SSRL in particular, owe a great deal to these characteristics of Klaus Halbach.

Acknowledgment

SSRL is funded by the Department of Energy, Office of Basic Energy Sciences. The Biotechnology Program is supported by the NIH, Biomedical Research Technology Program, National Center for Research Resources. Further support is provided by the Department of Energy, Office of Health and Environmental Research.

References

1. M. Berndt, W. Brunk, R. Cronin, D. Jensen, A. King, J. Spencer, T. Taylor and H. Winick; IEEE Trans. Nucl. Sci. 26, 3812-15, (1979).

2. A. Hofmann, R. Little, J.M. Paterson, K.W. Robinson, G.-A. Voss and H. Winick; Proc. 6th Int. Conf. on High Energy Accel., CEAL-2000 (September, 1967), pp 123-9.

3. M. Billardon, P. Elleaume, J.M. Ortega, C. Bazin, M. Bergher, M. Velghe, Y. Petroff, D.A.G. Deacon, K.E. Robinson and J.M.J. Madey; Phys. Rev. Lett. 51, (1983) 1652.

4. K. Halbach, J. Chin, E. Hoyer, H. Winick, R. Cronin, J. Yang and Y. Zambre; IEEE Trans. Nucl. Sci NS-28, 1981.

5. H. Winick, R. Boyce, G. Brown, N. Hower, Z. Hussain, T. Pate and E. Umbach; Nuc. Instr. & Meth. 208 (1983) 127-137.

6. E. Hoyer, T. Chan, J.W.G. Chin, K. Halbach, K.-J. Kim, H. Winick, and J. Yang, IEEE Trans. Nucl. Sci. NS-30, No. 4, 3118-3120 (1983).

The "First" Problem

Ronald F. Holsinger
Aster Enterprises, Inc.

Introduction

This paper describes the first magnet design problem that Klaus and I worked on together. At the time, over 30 years ago, Klaus was working as a plasma physicist in the Controlled Thermonuclear Research (CTR) Group, and I was assigned from the Mechanical Engineering Department to help with the design of experimental equipment for various research projects. Klaus' primary research program was to develop a "plasma gun" for injecting plasma into "mirror machines." As described below, the magnet design aspect of this plasma gun was a challenging task, and led to some innovations that were quite advanced at that time.

The Problem

The magnetic field configuration that was required for this experiment is shown in Figure 1. This figure shows the axial field strength distribution that was needed for the experiment. The task was to conceive a design of co-axial cylindrical coils which would efficiently produce this field distribution with a high degree of accuracy, and at the same time be practical to build and energize.

The First Approach

This magnetic field design problem was very complicated to attempt to solve by analytical methods, i.e. "by hand." Therefore, we investigated the possibility of using a computer to aid in finding the solution. At this time neither Klaus nor I had any experience with digital computers, but the "Rad Lab" had just installed a state-of-the-art IBM 7094 digital computer[1]. We learned through colleagues in the CTR program and in the Computer Department at the Lab that a computer program, which would run on the IBM computer, had been written for evaluating the magnetic fields in axisymmetric systems[2]. This computer program was called COILS.

At the same time, soon after the IBM 7094 computer was installed, a course in FORTRAN II programming was offered at the Laboratory. I signed up for this course, and Klaus began formulating the magnet design problem as a mathematical system which could b solved by a suitable computer program, combined with the existing COILS program. Thus was launched a new direction for the analysis and synthesis of magnetic field and magnet design problems.

Over a period of several months, we worked diligently to bring together the components of theory, mathematics and computing to solve the specific problem. The first approach was to formulate the problem as a linear system of simultaneous equations relating the current in a number of coils to the total magnetic field distribution that they produced. The region which would be occupied by the coil system was divided up into 20 equal length solenoid coils, and the desired magnetic field distribution was specified at 20 points on the axis of the coil system. This is illustrated in Figure 1. Since the fields b_n are linear functions of the currents i_m, this system, $b = |A|\ i$, could be solved for the currents in the 20 coils, i.e. $i = |A|^{-1}\ b$.

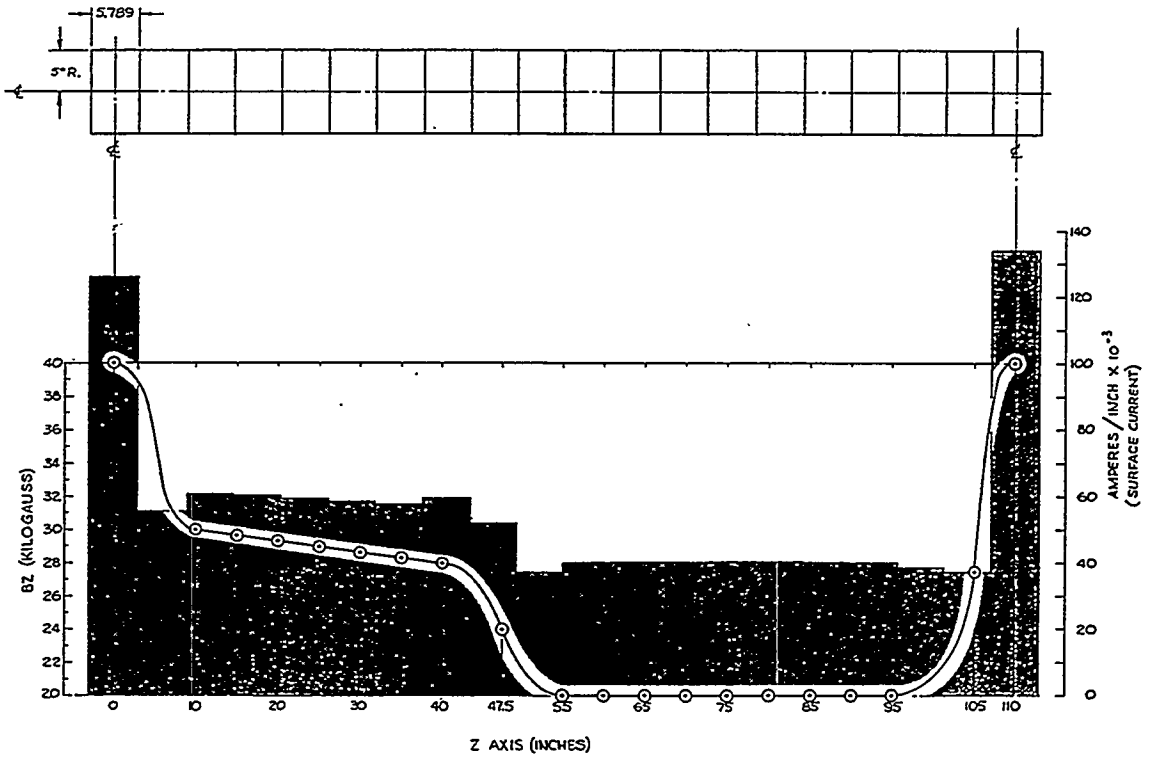

Figure 1

After initially getting some "wild" solutions with very large positive and negative currents, we learned our first lesson in appropriate parameter selection. This was soon recognized by Klaus as the "spacing and width of the influence function" problem, and the solution shown in Figure 1 was arrived at after many iterations to find the correct relationship between the number

of coils and the number of field points at which the simultaneous equations were determined. In recent times I have seen this understanding of appropriate parameter selection for similar problems replaced both literally and figuratively by the "Fuzzy Logic" approach.

The Solution

The solution for the current distribution in the 20 equal length coils suggested a logical way to design the coil system with a smaller number of coils. By grouping coils with similar currents into single coils, the number of different coils with different currents was reduced to 6, and the coils with the large currents at each end were made with an appropriately larger cross section. The final design and resulting field distribution is shown in Figure 2.

The optimization of this 6-coil system was greatly complicated by the fact that the parameters that were available to adjust the field distribution were, in addition to the currents, the lengths of and the gaps between the coils, and the magnetic fields are nonlinear functions of these geometry parameters. Thus, we launched the effort to develop and understand iterative nonlinear optimization procedures.

The problem now could be stated mathematically as $\Delta b = |M| \Delta v$, where the Δb_n field changes result from the Δv_m parameter changes in coil currents and positions. The COILS program did not allow the direct calculation of the $\partial b_n / \partial v_m$ $|M|$ matrix elements when v_m was a geometry parameter, so these derivatives were approximated by difference quotients. Also, since the equations relating the Δb_n and v_m are nonlinear, the optimization process was an iteration of successive approximations to the solution to minimized the Δb deviations from the desired values. This iterative solution method is shown in Figure 3, and can be described as "Newton's Method in Many Dimensions." A complete computer package was eventually developed for the optimization of these axisymmetric systems called "Coil SYstem Design (CSYD), which incorporated many of the features of the Program for the Inversion of System Analysis (PISA)[4].

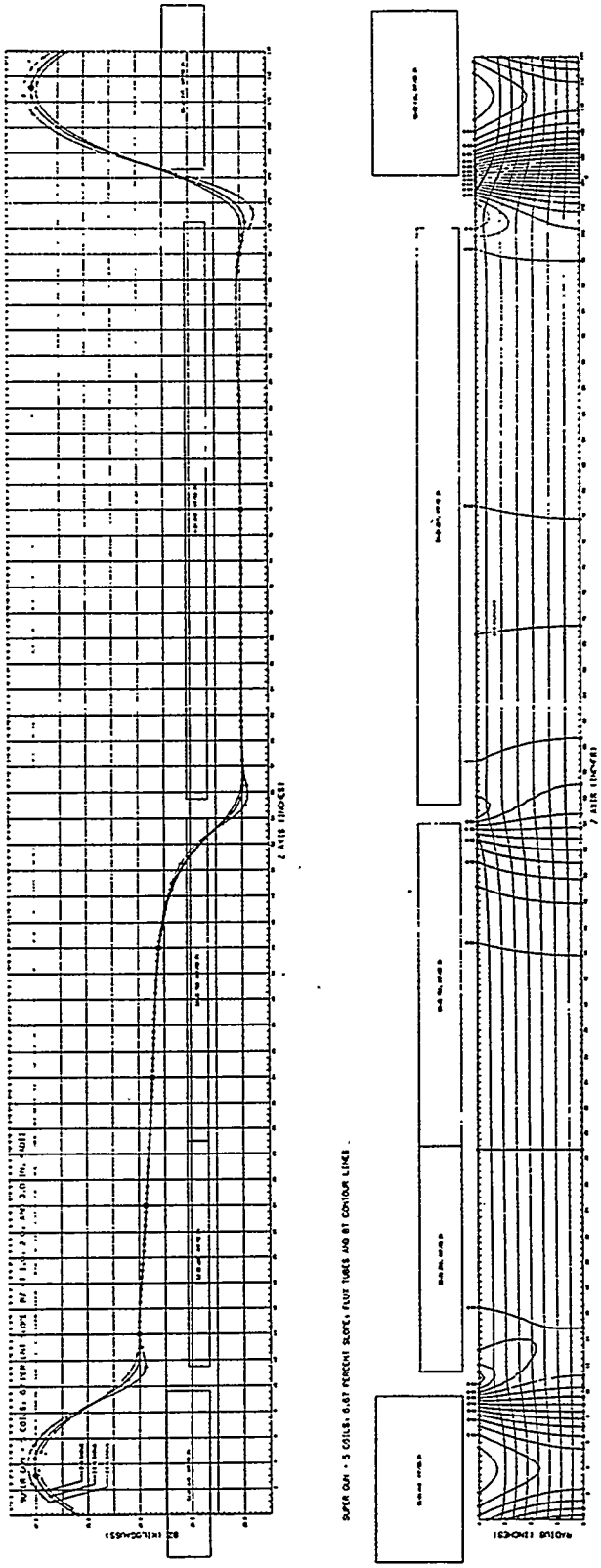

Figure 2

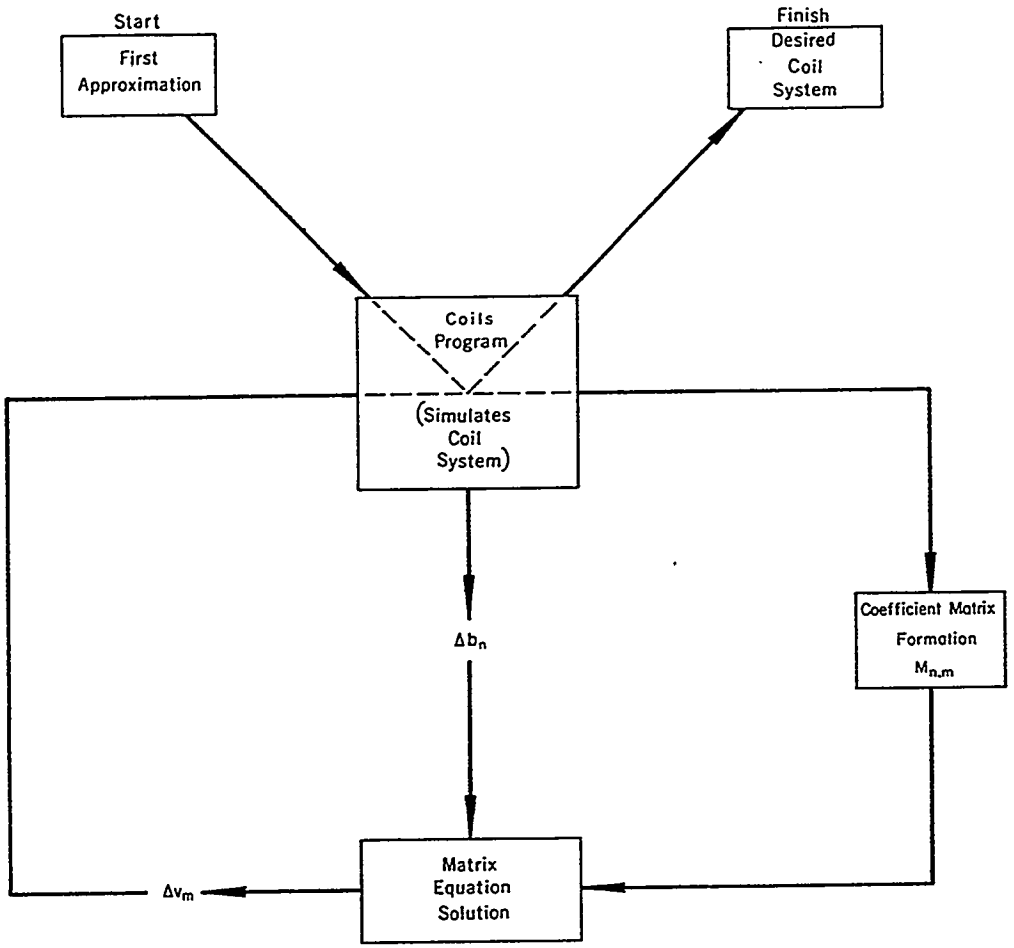

Figure 3

Conclusion

At the time this work was done in the early 1960s, this was a pioneering effort. To our knowledge, no other practical magnet design problems had been solved by such a digital computer-based synthesis method. It was my good fortune to have had the problem to work on, the tools to solve it available, and, most of all, to work with Klaus, who had the insight and imagination to formulate the problem and guide the work to a successful solution. And of course this was the beginning of a chain of developments in more complex iron core magnet design problems with POISSON, MIRT, etc., and the beginning of Klaus' interest in magnet design and theory.

References

1. Technical Specifications for the IBM 7094 Computer System. (this subject is still being researched at press time)

2. M.W. Garrett, "An Elliptic Integral Computer Package for Magnetic Fields, Forces, and Mutual Inductances of Axisymmetric Systems, and a Versatile Line-Tracing Routine, ORNL-3575, Oak Ridge, 1965.

3. K. Halbach, R.F. Holsinger; "A Method for Determining the Geometry and Current Configuration of a System of Cylindrically Symmetric Solenoid Coils from a Specified Magnetic Field Shape," Proceedings, Symposium on Engineering Problems of Controlled Thermonuclear Research, Livermore, 1965.

4. K. Halbach, A Program for the Inversion of System Analysis and its Application to the Design of Magnets," Proceedings Second International Conference on Magnet Technology, Oxford University, Oxford, 1967.

To Grosser Klaus

Klaus H. Berkner

Dear Grosser Klaus,

"Hello Klaus. This is Klaus.....the other Klaus."

My earliest Halbach recollections go back to the homopolar device days in Building 52--you and Bill Baker having lively discussions about the experiments: Bill with his superb intuition and lack of mathematical formality (he always talked of magnetic flux in "lines per"), and you with your "starting from first principles" approach were quite a combination. I could swear that in those days you made comments that the only people who used digital computers were those who were too lazy (or not smart enough) to obtain analytical solutions....but I probably mis-remember.

At last I will confess: I never was very successful at running the PISA code (in the days of punch cards, of course). I tried to use it to design the coil configuration for a plasma target I needed for a HILAC experiment.....and I always ended up with virtual coils in non-physical locations. Some years later I thought I should learn to use the WOLF code, but when I found out how tedious it was to generate the mesh just to get started, I decided to leave that to people with greater patience.

I'm glad that others, all over the world, persevered and mastered your techniques, for you have truly had a global impact--wherever there were magnetic challenges, there was input from you.

Without your insertion-device creations there would have been no third-generation light sources, and without an ALS, LBL would be quite different today.

Congratulations on a truly remarkable career.

Sincerely yours,

Kleiner Klaus

Klaus H. Berkner
Deputy Director for Operations

Transition Undulator Radiation as Bright Infrared Sources

Kwang-Je Kim
Lawrence Berkeley Laboratory
University of California
Berkeley, CA 94720

I thank Klaus Halbach for sharing his unique insights in physics, and for his support and encouragement from the very early days of our association.

ABSTRACT

Undulator radiation contains, in addition to the usual component with narrow spectral features, a broad-band component in the low frequency region emitted in the near forward direction, peaked at an angle $1/\gamma$, where γ is the relativistic factor. This component is referred to as the transition undulator radiation, as it is caused by the sudden change in the electron's longitudinal velocity as it enters and leaves the undulator. The characteristics of the transition undulator radiation are analyzed and compared with the infrared radiation from the usual undulator harmonics and from bending magnets.

1. INTRODUCTION

Undulators in modern synchrotron radiation facilities are normally optimized for bright soft x-ray and x-ray radiation in the forward direction. It is well known that the spectrum of the undulator radiation at a large angle, away from the forward direction, is red-shifted to a low frequency. It is probably less well known that low frequency radiation is also generated in the near forward direction, peaked at an angle $1/\gamma$, where γ is the relativistic factor. The origin of this radiation lies in the fact that when electrons enter or leave an undulator, their average longitudinal velocity changes suddenly. The situation here is similar to the case of the transition radiation [1,2] which is generated when a charged particle passes through an interface separating two optical media. Thus, the low frequency radiation in the near forward direction may be referred to as the transition undulator radiation (TUR). In this paper, we derive the characteristics of the transition undulator radiation in the infrared region, and compare with those of the bending magnet radiation and the red-shifted normal undulator radiation. It is shown that the TUR could be an intense, bright, infrared radiation source.

2. TRANSITION UNDULATOR RADIATION

The flux per unit solid angle into a frequency bandwidth $\Delta\omega$ due to a beam of relativistic electrons moving on a curved trajectory is given by (See, for example, Ref. [3])

$$\frac{d^2F}{d^2\Omega} = \alpha \frac{\Delta\omega}{\omega} \frac{I}{e} |A(\omega)|^2 \quad , \tag{1}$$

where $\alpha \approx 1/137$ is the fine structure constant, ω the radiation frequency, I the beam current, e the electron charge and $A(\omega)$, the electric field amplitude given by

$$A(\omega)=\frac{1}{2\pi}\int_{-T/2}^{T/2}dt\frac{d}{dt}\left(\frac{\mathbf{n}\times(\mathbf{n}\times\beta)}{\kappa}\right)\exp\, i\omega\int_{0}^{t}\kappa(t')dt' \quad . \tag{2}$$

Here T is the time interval during which the acceleration is non-zero, $\mathbf{n}$ is the observation direction, $\beta(t)$ the electron velocity divided by c (the speed of light) as a function of the emitter time t [3], and $\kappa(t)=1-\mathbf{n}\cdot\beta(t)$.

We apply the above formula for electrons passing through an undulator of length $L = N\lambda_u$ where N is the number of the periods and λ_u is the period length. We consider the case where the frequency ω is so small that

$$\omega\int_{0}^{T/2}\kappa(t')dt'=\omega\cdot\frac{T}{2}\cdot<\kappa>\approx\pi N\nu(\theta)<1 \quad . \tag{3}$$

In the above, $<\kappa>$ is the average of κ in one period, θ is the angle of observation with respect to the forward direction, and

$$\nu(\theta) \;=\; \frac{\lambda_1(\theta)}{\lambda}=\frac{\omega}{\omega_1(\theta)} \quad . \tag{4}$$

Here $\lambda_1(\theta)=\lambda_u<\kappa>$ is the fundamental wavelength of the undulator radiation as a function of θ, and λ is the radiation wavelength, and $\omega_1(\theta)=2\pi c/\lambda_1(\theta)$.

The integral in Eq. (2) can be evaluated by expanding the exponential function as

$$\exp\, i\omega\int_{o}^{t}\kappa(t')dt'=1+i\omega\int_{o}^{t}\kappa(t')dt'+... \tag{5}$$

Keeping to the second term in the above expansion, Eq. (2) becomes

$$A(\omega)=\frac{i\omega}{2\pi}\left[\frac{\mathbf{n}\times(\mathbf{n}\times\beta_0)}{\kappa}\int_{-T/2}^{T/2}dt\;\kappa(t)-\int_{-T/2}^{T/2}dt\mathbf{n}\times(\mathbf{n}\times\beta(t))\right] \tag{6}$$

Here $\beta_0=\beta(T/2)=\beta(-T/2)$ is the value of β before and after the undulator. Assuming that there is no angular deflection in the undulator, we have

$$\beta_0=\beta\mathbf{e}_z \tag{7}$$

where $\mathbf{e}_z$ is the forward direction and βc is the electron speed (which is a constant for a motion through a static magnetic field). Assuming further that there is also no net displacement in the transverse coordinates through the undulator, Eq. (2) can be evaluated as follows:

$$\mathbf{A}(\omega)=\frac{i\omega}{2\pi c}\mathbf{n}\times(\mathbf{n}\times\mathbf{e}_z)\frac{\beta cT-L}{1-\beta\ \cos\ \theta}\ . \tag{8}$$

In the above, βcT is the arc length of the curved trajectory in the undulator, while L is the straight distance between the undulator ends. Thus, we have, in terms of the transverse velocity $\beta_\perp$,

$$\beta cT\approx\left(1+\frac{1}{2}<\beta_\perp{}^2>\right)\cdot L\ . \tag{9}$$

Here $<\ >$ implies taking the average over an undulator period. Equation (8) becomes

$$\mathbf{A}(\omega)=\frac{i\omega}{4\pi c}\mathbf{n}\times(\mathbf{n}\times\mathbf{e}_z)\frac{L<\beta_\perp{}^2>}{1-\beta\ \cos\ \theta}\ . \tag{10}$$

Finally, we obtain, by inserting Eq. (10) into Eq. (1), and assuming $\theta<<1$,

$$\frac{d^2F}{d^2\Omega}=\alpha\frac{\Delta\omega}{\omega}\frac{I}{e}\left(\frac{L}{\lambda\gamma}\right)^2<\gamma^2\beta_\perp{}^2>^2\frac{\gamma^2\theta^2}{\left(1+\gamma^2\theta^2\right)^2}\ . \tag{11}$$

According to Eq. (11), the angular distribution of the low frequency radiation vanishes in the forward direction, peaked at angle $\theta=1/\gamma$, and decreases as $1/\theta^2$ for $\gamma^2\theta^2>>\ 1$ .According to Eq. (10), the polarization is radial, i.e., directed away from the forward direction. These properties are very similar to those of the transition radiation [1,2]. The similarity is due to the fact that the low frequency radiation from undulator analyzed here arises from the fact that the electron's average longitudinal velocity $\bar{v}_z$ within the undulator is slower than that outside of the undulator, $v=\beta c$. In fact, a factor occurring in Eq. (8) can be written as

$$T-\frac{L}{v}=\frac{L}{\bar{v}_z}-\frac{L}{v} \tag{12}$$

If $\bar{v}_z=v$, then Eq. (8) vanishes and hence it is necessary to consider higher order terms in the expansion (5). We are therefore justified to refer the low frequency radiation from undulator as given by Eq. (11) as the TUR.

By integrating Eq. (11) over the solid angle, one obtains the total flux. Since the angle integration is logarithmically divergent, one must specify the upper limit of θ. Assuming that photons in $\theta\leq\ 3/\gamma$ are collected, one obtains

$$F_{TUR}=1.4\pi\alpha\frac{\Delta\omega}{\omega}\frac{I}{e}\left[\frac{L}{\lambda\gamma^2}<\gamma^2\beta_\perp{}^2>\right]^2;\ \ \theta\leq\frac{3}{\gamma}\ . \tag{13}$$

When $\pi N\nu(\theta) > 1$, then the above formulae are not valid since the inequality (3) is not satisfied. However if

$$\pi\nu(\theta) < 1 \ , \tag{14}$$

then one can still obtain similar results by rewriting Eq. (2) as follows.

$$A(\omega) = \frac{1}{2\pi}\left[\frac{\sin N\pi\nu(\theta)}{\sin\pi\nu(\theta)}\right]\int_{-\lambda_u/2c}^{\lambda_u/2c} dt \ \ a(t)\exp\left(i\omega\int_0^t \kappa(t')dt'\right) . \tag{15}$$

The exponential function in the integral of the above can now be expanded in a Taylor series when the inequality (14) is satisfied. Keeping to the second term as before, the final result is that Eq. (11) becomes modified as follows:

$$\frac{d^2F}{d^2\Omega} = \alpha\frac{\Delta\omega}{\omega}\frac{I}{e}\left(\frac{\sin N\pi\nu(\theta)}{N\pi\nu(\theta)}\right)^2\left(\frac{L}{\lambda\gamma}\right)^2 <\gamma^2\beta_\perp{}^2>^2 \frac{\gamma^2\theta^2}{\left(1+\gamma^2\theta^2\right)^2} \ . \tag{11.a}$$

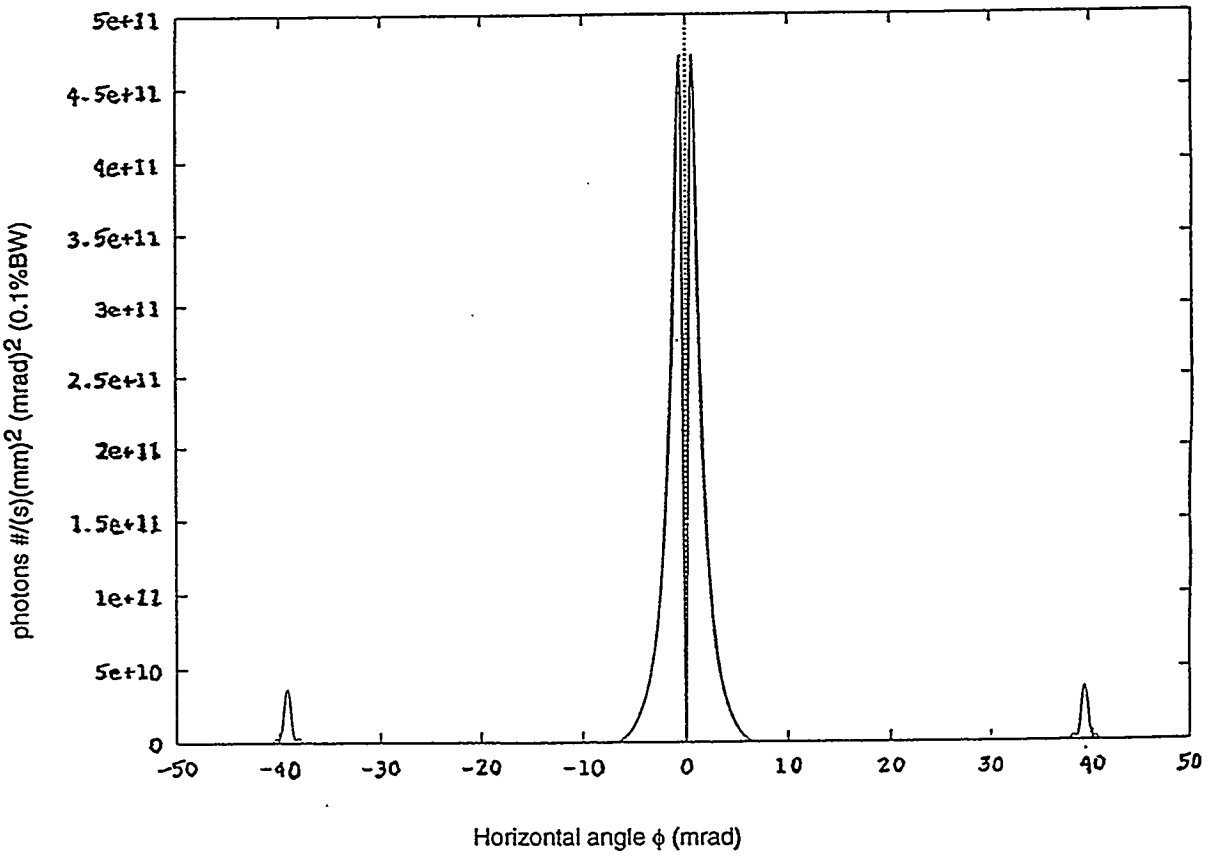

Figure 1—Angular density of the flux from Super Aco SU2 undulator at λ=100μ as a function of the longitudinal angle ϕ.

Figure 1 shows the angular distribution as a function of the horizontal angle ϕ at $\lambda = 100$ μ from the SU2 undulator $(\lambda_u = 0.129\text{m}, N = 24, K = 6.9)$ at Super Aco (beam current = 0.2A, electron energy = 0.8 GeV) calculated by C.X. Wang with his RADID code [4]. The double peaks near the center is due to the TUR. The curve in this region agrees very closely with Eq. (11.a). Note there is also a ring of radiation near $\phi \approx 40$ mrad. This is the red-shifted undulator radiation to be discussed in detail in Section 3.1.

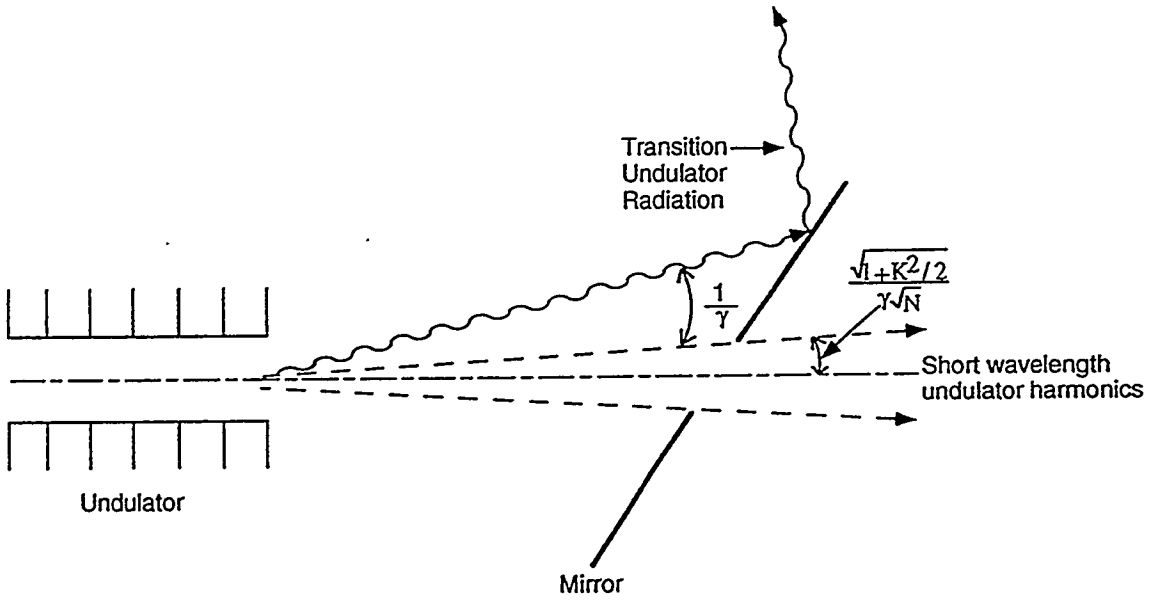

Figure 2—A schematic illustration of a beam line. The TUR is reflected by a mirror and the usual undulator radiation is transmitted through a narrow aperture in the mirror.

The TUR is bright because it has a small angular width less than a few times $1/\gamma$. It can be collected in an optical arrangement schematically shown in Fig. (2), where a mirror intercepts and reflects the TUR, while the short wavelength undulator radiation is transmitted through an aperture in the mirror with an angular opening $\sqrt{(1+K^2/2)}\ /\gamma\sqrt{N}$.

3. COMPARISON WITH OTHER INFRARED SOURCES: LARGE-ANGLE UNDULATOR HARMONICS AND BENDING MAGNET RADIATION.

3.1 Large-Angle Undulator Harmonics.

The nth harmonic undulator radiation at angle θ has the frequency

$$\omega = \omega_n(\theta) = \frac{2\pi nc}{\lambda_u \langle \kappa \rangle} \ . \tag{16}$$

We are interested in frequencies much lower than that of the undulator harmonic in the forward direction:

$$\frac{\omega}{\omega_1(0)} << 1 \ . \tag{17}$$

Since

$$<\kappa> = <\kappa>_{\theta=0} + \frac{\theta^2}{2} \ , \tag{18}$$

The undulator harmonics are red-shifted to very low frequencies at a large angle. An infrared radiation beam line collecting the large angle undulator harmonics was constructed at Super Aco [5].

The angular density of the undulator flux at a large angle can be calculated starting from Eq. (15). The argument in the exponential function is decomposed into two terms:

$$\omega \int_0^t \kappa \ dt \ = \ \omega <\kappa> t + \omega \int_0^t \Delta\kappa dt' \ , \tag{19}$$

Here $\Delta\kappa$ is the deviation of κ from its time average value $<\kappa>$. In the low frequency limit defined by the inequality (17), it can be shown that the second term in eq. (19) is negligible. Thus the integral appearing in Eq. (15) simplifies as

$$\int_{-\lambda_u/2c}^{\lambda_u/2c} dt \ \mathbf{a}(t) e^{i(2\pi nct/\lambda_u)} \ . \tag{20}$$

It can be shown that the acceleration **a** becomes, in the large angle limit,

$$\mathbf{a} = \left(a_x, a_y\right) \sim \frac{2}{\theta^2}\left(\dot{\beta}_x \cos 2\xi + \dot{\beta}_y \sin 2\xi, \ \dot{\beta}_x \sin 2\xi - \dot{\beta}_y \cos 2\xi\right) \ . \tag{21}$$

Here, we have decomposed the transverse direction into x and y components, ξ is such that $\theta\cos\xi$ and $\theta\sin\xi$ are respectively the x and y components of the observation direction, and the dot represents the derivative with respect to the time variable.

Inserting the resulting expression into Eq. (1), one obtains the angular density of flux. Integrating over the angular distribution, which is sharply peaked around θ determined by Eq. (16), and summing over the contributions from different harmonics n, it can be shown that the total flux in the undulator harmonics at frequency ω satisfying the condition (17) is given by

$$F_{UH} = \alpha\pi \frac{I}{e}\left[\frac{L}{\lambda\gamma^2} <\gamma^2 \beta_\perp{}^2>\right] \ . \tag{22}$$

Here the subscript UH refers to the undulator harmonics. Note the close resemblance of this expression to that of the undulator transition radiation Eq. (13). Both expressions contain the factor

$$f = \frac{L}{\lambda\gamma^2} < \gamma^2 \beta_\perp{}^2 > \ . \tag{23}$$

However, Eq. (13) is quadratic in f while eq. (22) is linear.

3.2 Bending Magnet Radiation

The spectrum of the bending magnet radiation extends to very low frequencies. This fact has been utilized by several infrared radiation beam lines [6] .

The flux of the bending magnet radiation per unit horizontal angle ϕ and integrated over the vertical angle is given by

$$\frac{dF_B}{d\phi} = \frac{\sqrt{3}}{2\pi} \alpha\gamma \frac{\Delta\omega}{\omega} \frac{I}{e} y \int_y^\infty K_{5/3}(y')dy' \ . \tag{24}$$

Here $y = \omega / \omega_c$, ω_c (the critical frequency) $= 3\gamma^3 c / 2\rho$, ρ = the bending radius, and $K_{5/3}$ is the modified Bessel function of the 2nd kind. In the limit $y \to 0$, $y\int_y^\infty K_{5/3}(y')dy' \to 2.15\ y^{1/3}$. The bending magnet flux with a horizontal collection angle $\Delta\phi$ in the infrared limit, then, becomes

$$F_B \sim 0.59\ \alpha\gamma\Delta\phi \frac{\Delta\omega}{\omega} \frac{I}{e} \cdot \left(\frac{\omega}{\omega_c}\right)^{1/3} ; \ \frac{\omega}{\omega_c} \to 0 \ . \tag{25}$$

3.3 Comparison of the Performances

In view of Eqs. (13), (22) and (25), we obtain the following ratios between the fluxes of the transition undulator radiation, the large angle undulator harmonics, and the bending magnet radiation:

$$\frac{F_{TUR}}{F_{UH}} = 1.4f \ . \tag{26}$$

$$\frac{F_B}{F_{UH}} = \frac{0.59\gamma\Delta\phi(\omega / \omega c)^{1/3}}{\pi f} \ . \tag{27}$$

The factor f was defined in Eq. (23).

Let us now consider an explicit example for 30 μm infrared radiation at ALS (1.5 GeV). The undulator parameters are those of U8, a hybrid design with $\lambda_u = 8$ cm. At the pole

gap of 2.4 cm, the deflection parameter K = 5.67. We will assume that the undulator field is sinusoidal. The fundamental wavelength in the direction θ is given by

$$\lambda_1(\theta) = \frac{\left(1 + K^2/2 + \gamma^2\theta^2\right)\lambda_u}{2\gamma^2} = \left(1 + \frac{\gamma^2\theta^2}{1 + K2/2}\right)(0.079\mu m) \ . \tag{28}$$

With N = 61, the inequality (3) is satisfied for $\gamma\theta \le 3$. The ratio $F_{TUR} / F_{UH} = f$ becomes

$$f = \frac{L}{\lambda\gamma^2}\frac{K^2}{2} = 0.31 \ . \tag{29}$$

The ALS bending magnet radiation $(\rho = 4.8m)$ has the critical wavelength $\lambda_c \approx 8\mathring{A}$. Assuming the collection angle $\Delta\phi = 100$ mrad , we have

$$\frac{F_B}{F_{UH}} = 5.5 \ . \tag{30}$$

From these results, we have $F_{TUR} : F_{UH} : F_B = 1 : 3.2 : 17.7$; Compared to the flux of the transition undulator radiation, the fluxes of the undulator harmonics and the bending magnet radiation are larger by a factor of 3.2 and 17.7, respectively.

However, it should be noted that the undulator harmonics and the bending magnet radiation require much larger collection angles; The transition undulator radiation is collected in an angular cone $\theta \le 3/\gamma$, which in the present case is about 1 mrad. The undulator harmonics is collected in a thin annular region centered at an angle θ such that $\lambda_1(\theta) = \lambda$. In the present case, this leads to $\theta \approx 78$ mrad. For the bending magnet, we have assumed the horizontal collection angle of 100 mrad.

The large collection angle places demanding requirements on the optical system. Even more important, it has implication on the transverse coherence. For the bending magnet radiation with the horizontal collection angle $\Delta\phi$, the rms phase space area is approximately $\rho(\Delta\phi/2)^3$. In the present case, this is about 6×10^{-4}m-rad, and is larger than the minimum coherent phase space area $(\lambda/4\pi)$ by a factor 250. This means that the radiation is incoherent transversely. The maximum horizontal collection angle $\Delta\phi$ that is transversely coherent is $\Delta\phi \approx 2(\lambda/4\pi\rho)^{1/3}$, which is about 16 mrad in the present case. The coherent flux is therefore smaller by a factor 6 compared to the 100 mrad collection.

For the undulator harmonics, the source size viewed at an angle 78 m-rad is large, about 20 cm. This large source size can, in principle, be compensated by the small width of the angular annulus. However, the angular divergence of the electron beam, the near field effect, etc., will rapidly destroy the transverse coherence.

ACKNOWLEDGMENTS

I thank Pascale Roy for inviting me to visit LURE, thus providing me an occasion to develop materials presented here. I thank Chun Xi Wang for carrying out numerical calculations confirming the analytical results.

REFERENCES

[1] V.L. Ginzburg and I.M. Frank, Zh. Eksp & Ther. Fiz. 16, 15 (1946).
[2] L.D. Landau and E. M. Lifshitz, "Electrodynamics of Continuous Media", Chapter XV (Pergamon Press, 1984).
[3] K.-J. Kim, "Characteristics of Synchrotron Radiation", AIP Conference Proceeding 184 "Physics of Particle Accelerators", M. Month & M. Dienes ed., AIP 1989.
[4] C.X. Wang and D. Xian, Nucl. Instr. and Meth., A288, 649 (1990).
[5] P. Roy, et.al., Nucl. Instr. Meth., A325, 568 (1993).
[6] G.P. Williams, Nucl. Instr. Meth., A291, 8 (1990).

Use of the Halbach Perturbation Theory for the Multipole Design of the ALS Storage Ring Sextupole

S. Marks
Lawrence Berkeley Laboratory
University of California
Berkeley, CA 94720

Abstract

The Advanced Light Source (ALS) storage ring sextupole is a unique multi-purpose magnet. It is designed to operate in the primary or sextupole mode and in three auxiliary trim modes: horizontal steering, vertical steering, and skew quadrupole. Klaus Halbach developed a perturbation theory for iron-dominated magnets which provides the basis for this design. Many magnet designers, certainly those who have been exposed to Klaus, are familiar with this theory and have used it for such things as evaluating the effect of assembly alignment errors. The ALS sextupole design process was somewhat novel in its use of the perturbation theory to design essential features of the magnet. In particular, the steering and skew quadrupole functions are produced by violating sextupole symmetry and are thus perturbations of the normal sextupole excitation. The magnet was designed such that all four modes are decoupled and can be excited independently. This paper discusses the use of Halbach's perturbation theory to design the trim functions and to evaluate the primary asymmetry in the sextupole mode, namely, a gap in the return yoke to accommodate the vacuum chamber.

Prototype testing verified all operating modes of the magnet and confirmed the expected performance from calculations based upon the Halbach perturbation theory. A total of 48 sextupole magnets of this design are now installed and operating successfully in the ALS storage ring.

1 Introduction

1.1 Halbach Perturbation Theory

The subject of this paper is the practical use of a theory of perturbations in iron core magnets developed by Klaus Halbach [1]. In this context, a perturbation is understood as any violation of a magnet's natural symmetry. The theory is therefore quite general. It can be used to evaluate unintentional violations of symmetry such as due to assembly errors, and in this way be used to establish appropriate design tolerances. It can also be used to design deliberate violations of symmetry to achieve excitations not consistent with normal symmetry, as was done for the magnet discussed in this paper.

I make no attempt at a general discussion of the theory itself, but illustrate its usefulness with a particular example: the design of the Advanced Light Source (ALS) storage ring sextupole. While the perturbation theory is only one of many important contributions Klaus has made to the theory and design of accelerator magnets and other sophisticated magnetic devices, its relevance, quality and generality are typical

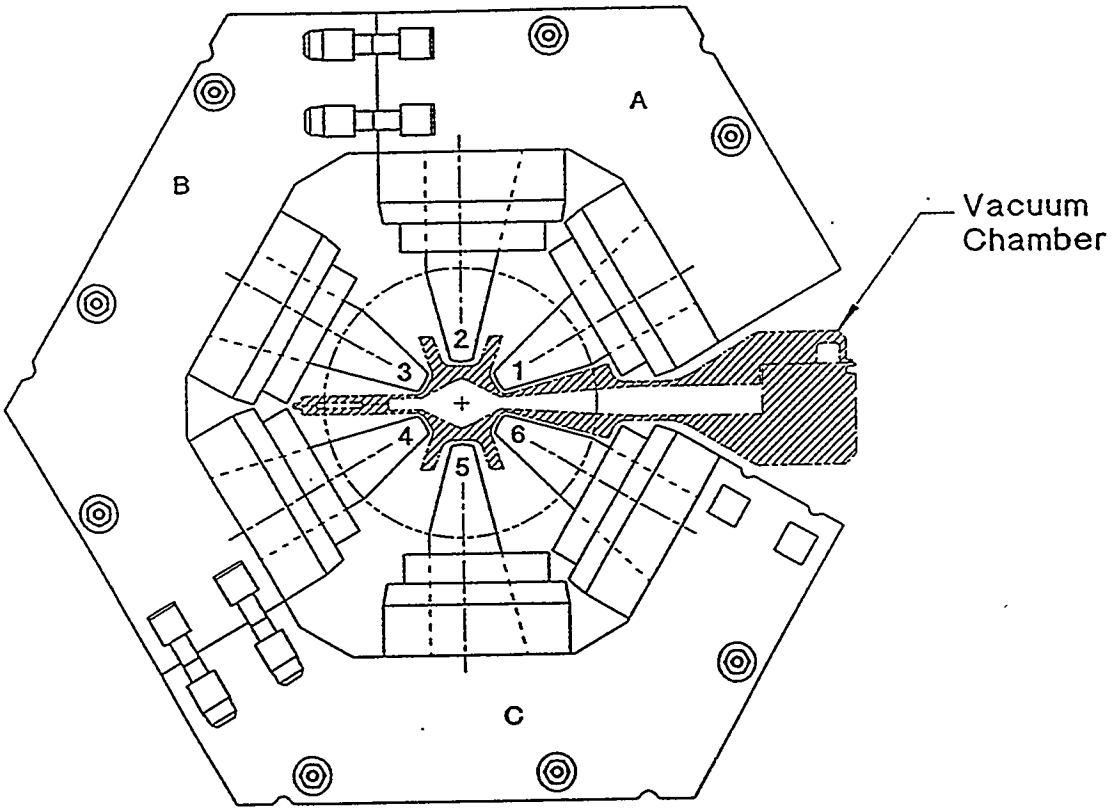

Figure 1: ALS Storage Ring Sextupole

of Klaus' contributions in general. As will be illustrated in the example discussed here, the theory contains not only information required for quantitative evaluation, but also contains valuable qualitative information to guide design practice. Indeed, for the case of the ALS sextupole design, the Halbach perturbation theory represents a unique and essential tool; I don't believe the multi-function aspect of the design would have been conceived and successfully implemented without this theory.

1.2 Features of the ALS Sextupole

Fig. 1 shows a cross-section view of the ALS sextupole. Several prominent features are evident. The magnet is constructed from laminations in three separate sections labeled as A, B, and C in the figure. The return yoke has an asymmetric gap at the midplane; *i.e.*, it is a C-magnet. This is to allow for vacuum chamber clearance. Despite this asymmetry, which results in section A being different than sections B and C, a single lamination is used. The laminations for section A are sheared to produce the required vacuum chamber gap.

Each pole has three coils. The inner coils produce the sextupole excitation. These consist of 15 turns of hollow, water-cooled conductor. The outer coil bundles shown in Fig. 1 consist of a single water cooling circuit with two solid core coils of 56 and 28 turns except for poles 2 and 5. The larger of the two coils in the outer coil package

is modified for poles 2 and 5. The coils have 54 instead of 56 turns. This is to compensate for the effect of the C-magnet asymmetry on horizontal steering. This point will be discussed in Section 4.2.

Note that the poles are asymmetric about their axes. Look at pole number 1. The pole contour near the vacuum chamber is different than that on the side away from the vacuum chamber. This geometry is required to avoid pole saturation at the base (the junction of pole and return yoke). The width at the pole base is what is required to avoid saturation at this location. The vacuum chamber clearance, in combination with the required coil dimensions does not allow for a symmetric pole base width. However, the poles are symmetric within the region designated by the dashed circle in Fig 1. Asymmetry beyond this radius is far from the magnetic axis and will therefore not have a significant influence. The pole geometry has three-fold symmetry, instead of the ideal six-fold symmetry. This arrangement provides the greatest possible symmetry consistent with a single lamination pattern.

The ALS sextupole features four primary asymmetries which will be discussed in the sections below: C-magnet asymmetry, and excitation asymmetries associated with horizontal steering, vertical steering, and skew quadrupole. Engineering design calculations for this magnet design are documented in several LBL Engineering Notes [2] [3]. The major parameters of of the magnet are summarized in Table 1.

2 Procedure for Calculating Perturbations

The Halbach perturbation theory develops perturbation coefficients for a reference pole centered on the horizontal axis at $\theta = 0$. The effect due to errors on a set of poles is calculated from this sensitivity coefficient, the strength of the perturbation, and a geometry factor which accounts for the actual position of the poles. The perturbation to the nth harmonic is formulated as

$$\frac{|H_n|}{|H_N|} = \frac{n}{N}\Delta C_n \tag{1}$$

where n designates the particular harmonic being considered, N designates the fundamental, and ΔC_n is the perturbation to the nth multipole coefficient

$$\Delta C_n = \Delta C_n(0) g_n \epsilon \tag{2}$$

$$g_n = \sum_j e^{-in\theta_j} \tag{3}$$

where $\Delta C_n(0)$ is the perturbation corresponding to the reference pole, g_n is the geometry factor for the nth harmonic, ϵ is the strength of the perturbation, and the θ_j are the angle locations of pole centers.

Normalized sensitivity coefficients can be calculated directly from a set of equations given in Halbach's paper or from tables which include values for the most important cases. The tables give values for

$$\frac{n}{N} j_n = \frac{n}{N}\frac{\Delta C_n(0)}{i\epsilon} \tag{4}$$

Parameter	Value
Magnet Aperture Radius	3.5 cm
Good Field Radius	3.0 cm
Sextupole Mode:	500 T/m^2
Pole Tip Field	0.6125 T
Amp-Turns	5868 (infinite permeability)
	5923 (finite permeability)
Horizontal Steering Mode:	
Field Strength	0.07 T
Current	42.9 Amps
Vertical Steering Mode:	
Field Strength	0.07 T
Current	35.7 Amps
Skew Quadrupole Mode:	
Field Strength	0.75 T/m
Current	29.1 Amps

Table 1: ALS Sextupole Parameters

For production of a particular multipole field, the required perturbation is

$$\epsilon = \frac{|H_n|}{|H_N|}\frac{N}{nj_n} \tag{5}$$

Perturbation values are calculated at the pole radius; values must be adjusted for other radii.

3 Effect C-Magnet Geometry

A break is made in the return yoke to accommodate the ALS vacuum chamber. This break violates sextupole symmetry and therefore represents a perturbation in the multipole signature of the magnet. In particular, a new set of "unallowed" multipoles will be present that would normally not be present if sextupole symmetry were preserved.

The perturbation results in a modification in the pole surface scalar potential values; *i.e.*, this is equivalent to a perturbation in excitation. The magnitude of the excitation error due to a gap of $2a$ can be determined by starting with an unbroken

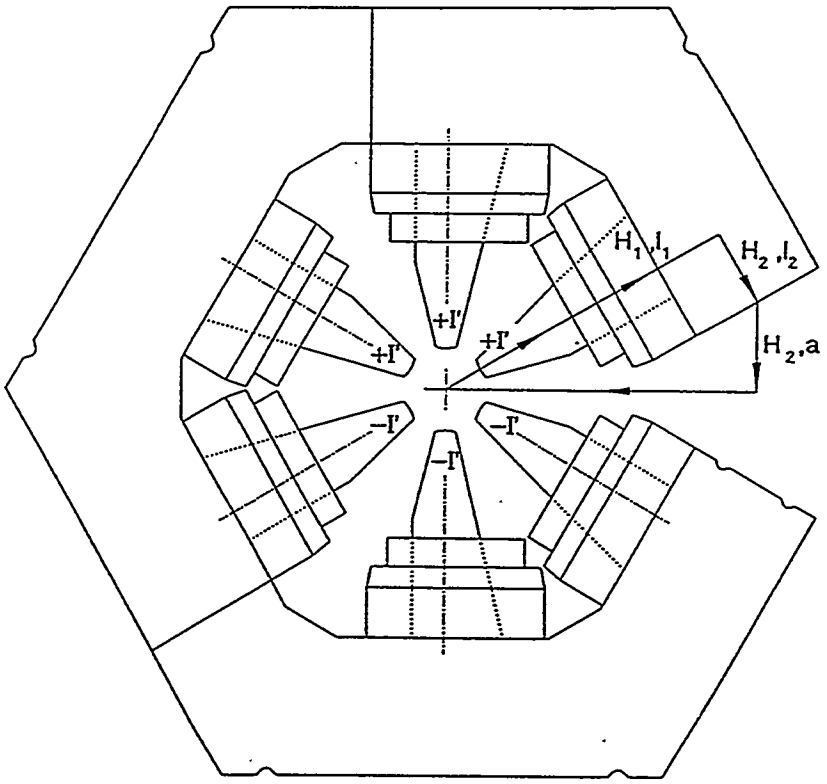

Figure 2: Perturbation due to C-magnet geometry

yoke. That is, assume that the yoke is continuous as indicated by the dashed line in Fig. 2. Now apply Ampere's law to the integral path represented in the figure.

$$\int H \cdot dl = \frac{1}{3} H_p r_p + H_1 l_1 + H_2 (l_2 + a) \tag{6}$$

where H_p is the pole tip field, r_p is the radius to the pole tip, H_1 and H_2 are the average field values in the pole and return yoke, respectively, as illustrated in Fig. 2, and l_1 and l_2 are the respective path lengths. The iron section corresponding to the gap can be removed and replaced by a coil with excitation $H_2 a$ without resulting in any change to the magnitude of the integral in Eq. 6 . Therefore it is clear that the magnitude of the excitation error, I resulting from the removal of the iron is

$$I = H_2 a \tag{7}$$

This will result in excitation errors $+I$ at poles 1, 2, and 3, and $-I$ at poles 4, 5, and 6.

An important qualitative result is evident from Eq. 7 without any further analysis. The magnitude of the perturbation is proportional to the average field level in the return yoke. Therefore the affect can be kept arbitrarily low by increasing the cross-section of the return yoke. It is particularly important to avoid saturation in the return yoke.

n	$\frac{n}{N}\frac{\Delta C_n(0)}{i\epsilon}$	g_n	$\frac{\lvert H_n\rvert}{\lvert H_N\rvert}$ @ 3.5 cm	$\frac{\lvert H_n\rvert}{\lvert H_N\rvert}$ @ 3.0 cm
1	9.79×10^{-2}	4.0	2.51×10^{-3}	3.42×10^{-3}
3	1.67×10^{-1}	2.0	2.14×10^{-3}	2.14×10^{-3}
5	7.09×10^{-2}	4.0	1.82×10^{-3}	1.34×10^{-3}
7	-1.34×10^{-2}	-4.0	3.43×10^{-4}	1.85×10^{-4}

Table 2: Multipoles due to C-Magnet Geometry

Now let us evaluate the change in multipoles due to C-magnet geometry. The geometry factor, to be inserted into Eq. 2 for this case is

$$g_n = 2i\left[\sin\left(\frac{n\pi}{6}\right)\sin\left(\frac{n\pi}{2}\right)\sin\left(\frac{5n\pi}{6}\right)\right] \tag{8}$$

From Poisson calculations the value of H_2 is 4.6 Oe for full sextupole excitation, and the half gap is about 10 cm. This gives a perturbation strength of

$$\epsilon = \frac{H_2 a}{NI} = 8.09 \times 10^{-3} \tag{9}$$

The results of calculations are summarized in Table 2. Relative multipole strengths are given at the pole tip radius of 3.5 cm and at the good field radius of 3.0 cm. Note that some multipoles are not allowed by symmetry. Only non-zero values are shown in the table. The dipole term represents a change in the magnetic center which can be eliminated by repositioning the magnet. The small perturbation in the sextupole term is also of no consequence. The higher order mulitpole errors are small enough to be acceptable.

4 Horizontal Steering

4.1 Elimination of Sextupole Coupling

We will now consider pole excitations for producing trim fields. The excitations should be such that the different modes are not coupled. Because of symmetry, the three trim fields are independent, however, care must be taken so that the trim modes do not produce a sextupole field. We will first consider the excitations required to produce a vertical dipole used for horizontal steering.

It is clear from symmetry that to produce a vertical dipole, the magnitude of excitations for poles 1, 3, 4, and 6 are equal, with that for 4 and 6 being of opposite polarity of that for 1 and 3. Let us call this I_{h1}. The magnitude of excitation in poles 2 and 5 must also be equal and opposite. Let us call this I_{h2}. We want to set the

ratio of the two excitations, I_{h1} and I_{h2}, to eliminate a sextupole component; that is, we want the sextupole contribution from the two excitations to cancel. The two sextupole contributions are proportional to the two geometry factors. The geometry factors for sextupole contributions, g_{31} and g_{32}, corresponding to excitations I_{h1} and I_{h2}, respectively, are given in Eqs. 10 and 11 below.

$$g_{31} = e^{i\pi/2} + e^{i5\pi/2} - e^{-i\pi/2} - e^{-5i\pi/2} = 4i \tag{10}$$

$$g_{32} = e^{3\pi/2} - e^{-3i\pi/2} = -2i \tag{11}$$

Therefore, in order that the horizontal steering mode not produce a sextupole, the strength of I_{h2} should be double that of I_{h1}. This is easily accomplished by connecting all coils in series and using twice as many turns in the coils for poles 2 and 5.

Now let us calculate the required value of the excitations. The value of the normalized dipole sensitivity coefficient is 0.0979. The geometry factor for $n = 1$ is

$$g_1 = 2i\left(\sin\frac{\pi}{6} + \sin\frac{5\pi}{6} + 2\sin\frac{\pi}{2}\right) = 6i$$

Using Eq. 5 we can calculate the perturbation, which multiplied by the normal sextupole excitation gives the required horizontal steering excitation.

$$\epsilon = \left(\frac{0.07}{0.6125}\right)\left(\frac{1}{0.0979}\right)\left(\frac{1}{6}\right) = 0.1946$$

Therefore the two excitations are

$$I_{h1} = (0.1946)(5688) = 1107 \text{ amp-turns}$$

$$I_{h2} = 2I_{h1} = 2214 \text{ amp-turns}$$

4.2 Effect of Return Yoke Gap on Horizontal Steering

During prototype measurements a coupling between the horizontal steering and sextupole modes was discovered. This was attributed to the effect of the return yoke gap which modifies the ideal two to one ratio between the two coil excitations. This effect was not taken into account in orginal design analysis, which is summarized in Section 4.1 above. A two turn reduction in the coil at poles 2 and 5 was empirically determined to effectively remove the sextupole coupling. This effect is analyzed below.

Consider an integration path through the top half of the sextupole. It passes through the return yoke gap, the return yoke, and then passes back along the horizontal midplane. The enclosed current in this loop is zero. Since all field components in the return yoke parallel to this path are in the same direction and there is no contribution from the part of the path along the midplane (symmetry requires that field lines are perpendicular to the midplane), application of Ampere's law produces the following requirement on field in the gap:

$$H_g a = H_1 l + H_2 l + H_3 \frac{l}{2} \tag{12}$$

n	$\frac{n}{N}J_n$	g_n	$\frac{\lvert H_n\rvert}{\lvert H_N\rvert}$ @ 3.5 cm	$\frac{\lvert H_n\rvert}{\lvert H_N\rvert}$ @ 3.0 cm
5	7.09×10^{-2}	3.0	8.28×10^{-2}	6.08×10^{-2}
7	-1.34×10^{-2}	-3.0	1.56×10^{-2}	8.42×10^{-3}
11	9.72×10^{-3}	-3.0	-1.14×10^{-2}	-3.32×10^{-3}
13	-1.01×10^{-3}	3.0	-1.18×10^{-3}	-2.52×10^{-4}

Table 3: Multipoles for Horizontal Steering Mode

where H_g is the gap field, a is the half gap, H_1, H_2 and H_3 are horizontal steering excitation field levels in the return yoke between poles 1 and 2, between poles 2 and 3, and pole 3 and the midplane, respectively, and l is the average path length in the return yoke between two poles. $H_g a$ represents an excitation perturbation that is equal for each pole.

Since we need to keep the horizontal steering excitation at poles 2 and 5 twice that at the other poles to eliminate sextupole coupling, the value of $H_g a$ is the magnitude of the required correction. From Poisson runs typical values for H_1, H_2 and H_3 are 0.7 Oe, 1.9 Oe, and 2.6 Oe, respectively for full horizontal steering excitation. The value of l is approximately 30 cm. These result in a value for $H_g a$ of 117 Oe-cm, which corresponds to 93 amp-turns. The full current value for the horizontal steering is 43 amps. So, the calculation is in close agreement with the required two turn reduction discovered in the prototype measurements.

4.3 Multipoles due to Horizontal Steering

Given the perturbation value from Section 4.1, a full set of multipoles can be calculated for the horizontal steering mode. The results are summarized in Table 3. Only the non-zero values are compiled. Notice that the relative values of the multipoles is fairly high. Also note that since the multipoles are not allowed by normal sextupole symmetry, pole shaping can not be used to cancel them. This is the primary negative feature of this method of producing auxiliary excitations.

5 Vertical Steering

Now consider excitation for production of a horizontal dipole field for vertical steering. From symmetry we know that this can be accomplished with an excitation of poles 1, 3, 4, and 6. The magnitude will be equal for all four poles, with the polarity at poles 3 and 4 opposite that at poles 1 and 6. Poles 2 and 5 are not excited.

We use the same dipole sensitivity coefficient 0f 0.0979 as for the horizontal steering

n	$\frac{n}{N}J_n$	g_n	$\frac{\lvert H_n\rvert}{\lvert H_N\rvert}$ @ 3.5 cm	$\frac{\lvert H_n\rvert}{\lvert H_N\rvert}$ @ 3.0 cm
5	7.09×10^{-2}	3.0	8.28×10^{-2}	6.08×10^{-2}
7	-1.34×10^{-2}	-3.0	1.56×10^{-2}	8.42×10^{-3}
11	9.72×10^{-3}	-3.0	1.14×10^{-2}	3.32×10^{-3}
13	-1.01×10^{-3}	3.0	-1.18×10^{-3}	-2.52×10^{-4}

Table 4: Multipoles for Vertical Steering Mode

mode. The geometry factor is

$$g_n = e^{in\pi/6} + e^{-in\pi/6} - e^{5in\pi/6} - e^{-5in\pi/6} \tag{13}$$

For $n = 1$, the value is 3.464. We use Eq. 5 to calculate the perturbation

$$\epsilon = \left(\frac{0.07}{0.6125}\right)\left(\frac{1}{0.0979}\right)\left(\frac{1}{3.464}\right) = 0.337$$

From this we can determine the required current.

$$I_v = (0.337)(5688) = 1917 \text{ amp-turns}$$

Using the value for ϵ, the full set of multipoles can be determined. The results are summarized in Table 4

6 Skew Quadrupole

A skew quadrupole mode is produced by excitation of poles 2 and 5 with the same magnitude and polarity. This arrangement is consistent with skew quadrupole symmetry. The geometry factor for this excitation is

$$g_n = e^{in\pi/2} + e^{-in\pi/2} = 2\cos\frac{n\pi}{2} \tag{14}$$

An alternative is to excite poles 1, 3, 4, and 6 with the same magnitude and polarity. The geometry factor for this case is

$$g'_n = e^{in\pi/6} + e^{-in\pi/6} + e^{5in\pi/2} + e^{-5in\pi/2} = 2\left(\cos\frac{n\pi}{6} + \cos\frac{5n\pi}{6}\right) \tag{15}$$

Examination of the two geometry factors for $n = 3$ shows that both modes are decoupled from sextupole excitation. By substituting $n = 2$ we see that the sign of the two modes is opposite. Therefore, they can be used in any combination to produce a skew quadrupole if their excitations are opposite in sign.

n	$\frac{n}{N}J_n$	g_n	$\frac{\lvert H_n\rvert}{\lvert H_N\rvert}$ @ 3.5 cm	$\frac{\lvert H_n\rvert}{\lvert H_N\rvert}$ @ 3.0 cm
4	1.33×10^{-1}	2.0	3.65×10^{-2}	3.13×10^{-2}
8	-1.07×10^{-2}	2.0	-2.94×10^{-3}	-1.36×10^{-3}
10	9.13×10^{-3}	-2.0	-2.51×10^{-3}	-8.53×10^{-4}

Table 5: Multipoles for Skew Quadrupole Mode

Because of the trim coil arrangement we chose to excite only poles 2 and 5 for skew quadrupole production. Each pole has two trim coils of 28 and 56 turns, except at poles 2 and 5, where the larger coils have 54 turns. Let us call these coils 1 and 2, respectively. For horizontal steering mode, coil 1 at poles 1, 3, 4, and 6 are connected in series with coil 2 at poles 2 and 5. The vertical steering mode uses coil 2 at poles 1, 3, 4, and 6 connected in series. This leaves coil 1 at poles 2 and 5 for the skew quadrupole mode.

Let us calculate the required excitation for this arrangement. The normalized quadrupole sensitivity coefficient is 0.156. The geometry factor is

$$g_n = e^{in\pi/2} + e^{-in\pi/2} = 2\cos\frac{n\pi}{2} \tag{16}$$

For $n = 2$ the value is -2. For the required field gradient of 0.75 T/m, the pole tip field is 0.02625 T. Using Eq. 5 we determine the perturbation value.

$$\epsilon = \left(\frac{0.02625}{0.6125}\right)\left(\frac{1}{0.156}\right)\left(\frac{1}{2.0}\right) = 0.1374$$

The required excitation then is

$$I_q = (0.1374)(5688) = 781 \text{ amp-turns}$$

The full set of multipoles are summarized in Table 5

7 Conclusion

Trim modes can be produced in a magnet by excitations that violate the magnet's natural symmetry. Halbach's theory of perturbations of iron core magnets [1] provides an indispensable design tool for accomplishing this. The procedure described in this paper for implementing vertical steering, horizontal steering and skew quadrupole trim modes in the ALS storage ring sextupole has proven to be successful. Prototype testing of the magnet demonstrated that the functions operated as expected from analysis using Halbach's theory. The only surprise was the discovery of a coupling between the horizontal steering and the sextupole modes. This was shown to be

due to the effect of the C-magnet geometry on the horizontal steering mode. This effect was not accounted for in the original design. However, calculations after the fact showed the effect can be fully accounted for. Corrections were made in the final design to eliminate the coupling.

References

[1] K. Halbach, "First Order Perturbation Effects in Iron-Dominated Two-Dimensional Symmetrical Multipoles", *Nuclear Instruments & Methods*, Vol. 74, 1969.

[2] S. Marks, "Multipoles for ALS Ring Sextupole", LBL Engineering Note M6599A, 1987.

[3] S. Marks, "Design Calculations for Storage Ring Sextupole", LBL Engineering Note M6671, 1987.

Working With Klaus Halbach: A Scientific Memoir

David Goldberg

Like many alumni of Halbach U., I welcome the opportunity to acknowledge my personal debt to a valued mentor as well as pay tribute to him. I suspect that many of Klaus's other former pupils have found themselves, as I did, wanting to write something that would give others a feeling of what it was like to work with Klaus, rather than presenting a formal scientific paper. Hence the following memoir.

Something over ten years ago, when I was affiliated with the Magnetic Fusion Energy group, I was working with Oscar Anderson and Bill Cooper on developing a high current accelerator for producing a high power neutral beam. Oscar had just come up with his invention of the Transverse-Field-Focusing (TFF) accelerator, a device which combined the strong (horizontal) focusing and multi-stage acceleration needed for a high-voltage, high-current beam, and was configured to accept a beam from what was then the highest current negative ion source available (a source developed by LBL's Ken Ehlers and Ka-Ngo Leung), which had a roughly 1 meter by 1 cm exit aperture. An alternate biasing scheme to the same TFF electrodes could also be used as a strong-focusing low-energy beam transport (LEBT) electrode system. For both the accelerator and the LEBT, there was concern about possible radial defocusing in the gaps between successive pairs of electrodes, so we needed to calculate the gap fields, preferably without resorting to a high-powered (read: expensive and time-consuming) field code.

When I brought the matter up at our weekly meeting, Bill suggested that a solution might be found through what at LBL was, in effect, the fifth Maxwell equation: "Klaus Halbach might be able to help you with that."[1] And indeed, when I presented the problem to Klaus, those were almost his exact words, "I think I may be able to help you with that," or something quite close to it. As I came to realize later, that was Klaus's wonderfully gentle way of saying that what you had brought him was a trivial problem whose solution he had worked out years earlier. Surely enough, when I came back a day or so later, he had written out the full solution, concluding with a simple analytic form for the solution of the fringe fields, all this on two single-sided hand written sheets of paper. These he handed to me, telling me that if there was anything about it that I didn't understand, I should feel free to get back to him.

At this point, a small digression is in order. As those who have worked with Klaus are well aware, when he is involved in solving electro- and magneto-statics problems, Klaus generally inhabits his alternate residence in the complex plane, a place to which he conformally maps himself by a mystical process known as the Schwarz-

[1] I subsequently came to learn that there were a number of variants of this law, obtained by substituting the names Glen Lambertson, Jackson Laslett, among others, but after all this is Klaus's *festschrift*.

Christoffel transformation. Those of us who have taken a graduate course in electrodynamics have all been exposed to the conformal mapping technique as a means of solving two-dimensional Laplace equation. However, I suspect that most of us regard this approach—particularly in the Age of the Chip—as something of a museum piece, a bit of arcane lore which one studies more out of deference to historical tradition than in the expectation of learning anything particularly useful. I learned otherwise from Klaus. Computational tools, like mechanical ones, may have become much more sophisticated in recent years. And if the desktop workstation is the physicist's equivalent of the numerically-controlled mill, then perhaps the conformal mapping technique is his/her Swiss army knife, a portable and wonderfully serviceable tool, particularly in the hands of an expert. And Klaus is such an expert.

To return to the story, when Klaus handed me his solution, he quickly went over what he had done, and I nodded dutifully at his references to such familiar objects as the Schwarz-Christoffel transformation and his descriptions of various steps in his derivation as "trivial," all the while thinking that there was a hell of a lot of physics in here, and I would really have to sit down and read this note over carefully when I got back to my office. When I did that, I quickly realized that the familiar was not at all familiar, and that the trivialities were anything but trivial. Well, Klaus had said that if there was anything I didn't understand about what he had done, I should get back to him; I decided to take him up on his offer.

It was not without some trepidation that I did so. It is not easy to admit to a colleague that you haven't understand something he has done, particularly a colleague you have only just met, and one who has described what he has done as "trivial." However, my desire to learn the power of this simple analytical tool was stronger than my fear of making a fool of myself, and so I presented myself once more at Klaus's office, and asked him in effect if he could go over with me exactly what he had done. He responded by asking me if I really wanted see what it was all about, because it might take some time; from the way he said it, it was clear that he would be more than happy to do it, in fact welcomed the opportunity, but was somewhat hesitant for fear of taking up more of my time than I had intended to give. Upon being reassured of my interest, he sat me down at the conference table with him, and he proceeded to give me what must have been a one-hour tutorial, not merely on the example at hand, but on conformal mapping in general, the electric vector potential, various tricks using the Schwarz-Christoffel transformation for a variety of geometries, and much, much more. And all delivered with the enthusiasm and excitement that I imagine he felt upon first learning it all himself. And far from making me feel foolish, Klaus made me feel almost as though I had done him a favor, by allowing him the pleasure of teaching.

This then was what it was like to work with Klaus. (The word "with" is probably a misleading description of the division of labor, but it was Klaus's nature to make you feel that you were a participant in the process, rather than, as was more nearly the case, a spectator.) One came with a question, and came away with an education. An education given gladly and unstintingly. He showed you all the wonderful physics—and he made it fun.

In his contribution to a *festschrift* for his teacher, Felix Bloch, Klaus paid Bloch the compliment of saying that in addition to being a fine physicist, "he was also exceptionally generous, gentle, and sensitive in his interactions with men [who] were less than his intellectual equals." Klaus has honored his mentor by carrying on that tradition in his own conduct towards those of us who have been privileged to study at Halbach U. And perhaps we can pay no higher honor to Klaus than by passing that tradition on to the next generation of our colleagues.

Your Magnet Disciples at GSI

Bernhard Langenbeck

Dear Professor Halbach,

The crew of the magnet laboratory is happy to have an opportunity not only to congratulate you on your 70th birthday and to express our good wishes for your future health and continuing professional success, but also to say thank you for all your help and advice at any time we needed it, especially during the early times of GSI.

To make it easier for you to remember our faces, we arranged a photo of our group and a measurement equipment whose design and construction traces back to a suggestion of yours in the early 1970s. On the left you see Klaus Zweig, who, soon after the foundation of GSI, was helping me powerful in setting up the facilities of the laboratory. For example, he constructed the multipole analysis for the drift tube quadrupoles of the UNILAC, which you see in front of us. First of all, the precise positioning and fixing of the wire bundles of the two coil system on the support has been very laborious. But the system was used very successfully and is still in operation as you see.

Next to Klaus there is Franz Klos. Perhaps you never met him during your much-to-rare visits to Darmstadt. We won him for work on the SIS/ESR magnets when the project became approved. He is a very good programmer and responsible for evaluation and preparation of the measurement results. He also has always a careful eye on the running measuring processes.

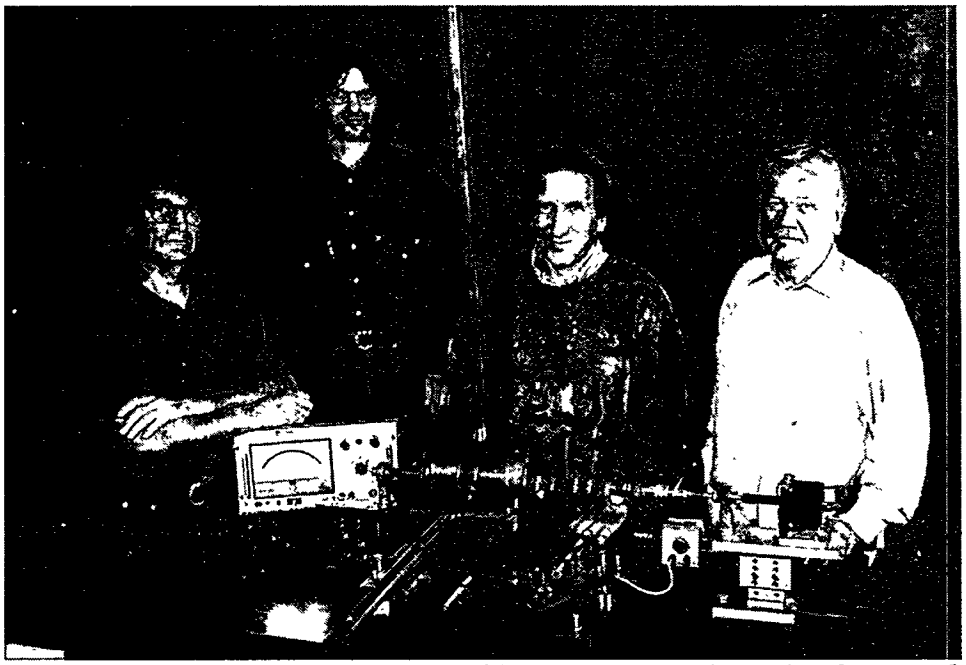

From left: Klaus Zweig, Franz Klos, Gebhard Moritz, and Bernhard Langenbeck.

The next in the row in Gebhard Moritz. You know, he is a member of the organizing and program committee of the IMMWs. Since the beginning of the SIS/ESR project, he takes care about the measurement tasks of the laboratory. He designed the equipment for the synchrotron and storage ring magnets, and also our big 3D field mapper is his work.

Finally, on the right you see whom you met as the proverbial greenhorn in magnet affairs in your lectures during September 1971 in Jülich. I tried to note down the lectures and to refine and supplement the text in the evenings. Perhaps you remember, once you trapped me at that work in my hotel room. At that time, as well as nowadays, I am very thankful for your start-up help into the magnet business. There has been also an earlier contact. As a beginner, I was doubtful about a first small quadrupole prototype for drift tubes and sent it to Berkeley "for a measurement" (that is, to get an experts opinion). It was in June or July 1971. To my relief, the magnet found grace in your eyes. The quadrupole jobs were running quite well also later, thanks to the Heaven and again to you. This may be the reason why it happened that I was addressed in GSI sometimes instead of with "hallo Langenbeck" by a "ha Quadrubeck!"

Once more, all the best wishes to you from your magnet disciples in Darmstadt!

Bernhard Langenbeck